



HAL
open science

Electronic structure of interfaces studied by in situ real-time XPS

Lucia Perez Ramirez

► **To cite this version:**

Lucia Perez Ramirez. Electronic structure of interfaces studied by in situ real-time XPS. Theoretical and/or physical chemistry. Sorbonne Université, 2020. English. NNT: 2020SORUS149 . tel-03278901

HAL Id: tel-03278901

<https://theses.hal.science/tel-03278901v1>

Submitted on 6 Jul 2021

HAL is a multi-disciplinary open access archive for the deposit and dissemination of scientific research documents, whether they are published or not. The documents may come from teaching and research institutions in France or abroad, or from public or private research centers.

L'archive ouverte pluridisciplinaire **HAL**, est destinée au dépôt et à la diffusion de documents scientifiques de niveau recherche, publiés ou non, émanant des établissements d'enseignement et de recherche français ou étrangers, des laboratoires publics ou privés.

THÈSE DE DOCTORAT
de l'Université Sorbonne Université

Spécialité : Chimie Physique

École doctorale n°388: Chimie physique et chimie analytique de Paris Centre

réalisée

au Laboratoire de Chimie Physique - Matière et Rayonnement

sous la direction de Jean-Jacques GALLET
co-encadrant François ROCHET

présentée par

Lucía PÉREZ RAMÍREZ

Sujet de la thèse :

**Electronic structure of interfaces studied by in
situ real-time XPS**

soutenue le 18 Décembre 2020

devant le jury composé de :

M.	WINTER Bernd,	Professeur	Rapporteur
M.	BLUHM Hendrik,	Professeur	Rapporteur
Mme	MARRY Virginie,	Professeur	Examinatrice
Mme	PÉREZ DIESTE Virginia,	Docteur	Examinatrice
M.	MUN Bongjin Simon,	Professeur	Examinateur
M.	NICOLAS Christophe,	Docteur	Examinateur
M.	ROCHET François,	Professeur	Examinateur
M.	GALLET Jean-Jacques,	Docteur	Directeur de thèse

Contents

Introduction	1
I X-ray Photoelectron Spectroscopy	5
I.1 Basic Principle	5
I.2 Sampling Depth	7
I.3 Instrumentation	8
I.3.1 Vacuum System	9
I.3.2 X-ray Source	10
I.3.3 Analyser	12
I.4 Interpretation of Spectra	14
I.4.1 Theory	14
I.4.2 Energy Loss Phenomena	15
I.4.3 Core-Level Shifts	16
I.5 Advanced XPS Techniques	20
I.5.1 Near-Ambient Pressure XPS	20
I.5.2 Liquid-jet XPS	23
II The Reference Level Problem	27
II.1 The Electrochemical Potential of the Electron	27
II.1.1 Revisiting the Work Function	28
II.2 Energy Calibration for Solid Samples	31
II.2.1 Measuring the work function of the sample	33
II.3 Energy Calibration for Liquid Samples	34
II.3.1 The Vacuum Level as Reference	34
II.3.2 The Fermi Level as Reference	37
III Band Alignment at a Solid/Gas Interface	39
III.1 The oxidation of metals	40
III.1.1 The Cabrera–Mott model	40
III.2 Experimental	43
III.3 The electronic band model of the Al/Al ₂ O ₃ interface	44

III.4 Results	46
III.4.1 Evolution of the band structure and the oxidation species	46
III.4.2 Growth kinetics	48
III.4.3 Discussing the validity of the CM model for the aluminium case	52
III.5 Conclusion	58
IV Band Alignment at a Metal/Redox Solution Interface	59
IV.1 Thermodynamic treatment of the metal/liquid interface in the presence of a redox couple	60
IV.1.1 Ionisation in the solution	60
IV.1.2 Ionisation in the metal	61
IV.1.3 Equilibrium between the solution and the electrode	61
IV.1.4 The absolute electrode potential	62
IV.2 Experimental	64
IV.2.1 The setup	65
IV.2.2 Calibration of the spectrometer	67
IV.2.3 Zobell solution in the absolute scale	68
IV.2.4 Measuring the work function of the liquid sample	69
IV.2.5 Measuring the ionisation energy of the $1b_1$ liquid phase peak	71
IV.2.6 Measuring the reorganisation energy	72
IV.3 Results	74
IV.3.1 Secondary electron cutoff and valence band	74
IV.3.2 Effect of a surfactant	77
IV.3.3 Reorganisation energy	81
IV.4 Conclusion	82
V A Model Surface to Study Hydrogen Bonding and Energy Shifts	85
V.1 The clean Si(100)- 2×1 surface	86
V.2 The water-terminated Si(100)- 2×1 surface	86
V.3 Methods	88
V.3.1 DFT slab periodic calculations	89
V.3.2 Cluster quantum chemistry (QC) DFT calculation of N 1s core ionisation potentials	89
V.3.3 Real-time core-level XPS	91
V.4 Results	92
V.4.1 Ammonia (NH_3) as probing molecule	92
V.4.2 Trimethylamine (TMA) as probing molecule	103
V.5 Conclusion	109

Conclusion and Perspectives	111
Appendix A	113
A.1 A Small Review in Thermodynamics	113
A.1.1 The Chemical Potential	114
A.1.2 The Electrochemical Potential	115
Appendix B	117
B.1 A thermodynamic approach of the Cabrera-Mott potential	117
B.2 Data treatment	119
B.2.1 Photon energies, inelastic mean free paths according to kinetic energy	119
B.2.2 Curve fitting	119
B.2.3 Calculation of thicknesses	121
B.3 Measurement of $E_{b,Al\ 2p_{3/2}}^{Al_2O_3} - E_{bVBM}$	122
B.4 Measurement of the oxide gap	123
B.5 Weight of the oxide surface plane in the O 1s spectrum	124
B.6 Effect of band bending on the measured binding energies	124
B.7 Uniform E and limit concentration of donors in the oxide	125
B.8 Kirk and Huber data (Kelvin probe measurement, 1968)	128
B.9 Fitting the oxide growing rate in the low-pressure regime	129
Appendix C	131
C.1 Cyclic voltammetry measurements of the Zobel solution after XPS exper- iments	131
C.2 Effect of applied bias on a liquid jet	133
C.3 Electrical properties of n-butyl alcohol isomers at the free surface of water Solution	134
C.4 Crystal field theory applied to ferricyanide and ferrocyanide complexes . .	134
Appendix D	137
D.1 XPS characterisation of the water-covered Si(100) surface	137
D.2 O 1s and N 1s normalisation with respect to Si LVV	138
D.3 Cluster QC DFT O 1s ionisation energies ($E_{i,QC}^{th}$)	139
D.3.1 Single dimer clusters	139
D.3.2 Adsorption on Si ₉ H ₁₂ (H,OH)	141
D.3.3 Adsorption on Si ₉ H ₁₂ (2OH)	141
D.4 Experimental O 1s XPS spectra and their interpretation	142
Bibliography	145

List of Figures

I.1	Sketch of an XPS experiment.	6
I.2	Compilation of electron IMFP values for different elements.	8
I.3	Schematic diagram of a synchrotron.	11
I.4	Schematic view of the photoelectron spectrometer with a hemispherical electron energy analyser.	12
I.5	Pass energy and energy resolution explained.	13
I.6	Illustration of the three-step and the one-step model of XPS.	15
I.7	Survey spectrum of an ammonia covered (H,OH)-Si(100) surface showing main XPS features.	16
I.8	Overview of the TEMPO NAP-XPS station at SOLEIL.	22
I.9	Schematic layout of in situ measurement cells currently used in NAP-XPS systems.	23
I.10	Illustrative sketch of the liquid jet XPS setup.	24
II.1	Energy level diagram for a conductor.	30
II.2	Energy level diagram for a sample in electrical equilibrium with an electron spectrometer.	31
II.3	Illustration of the measurement of the work function on a metallic sample.	33
II.4	Energy level diagram for a liquid solution in electrical contact with a grounded electron spectrometer.	35
III.1	Ionic transport and thermodynamic equilibrium during the formation of an oxide film according to Cabrera and Mott model.	41
III.2	The metal/oxide band structure accessible to XPS.	45
III.3	Evolution of the Al 2p, O 1s, valence band and secondary electron cutoff spectra during the in situ monitoring of aluminium oxidation.	47
III.4	Time evolution of the intensities of the various oxidation components of the Al 2p spectra, in UHV and when the surface is exposed to the 10^{-6} and 10^{-2} mbar pressure steps.	49
III.5	Evolution of the aluminium oxide thickness and band structure parameters of the Al/Al ₂ O ₃ interface versus time.	50

III.6	Aluminium oxidation growth rate (with the corresponding fit parameters) and calculated Cabrera-Mott potential plotted against time during the NAP regime.	51
IV.1	Equilibrium between a metal and a solution with a redox couple.	62
IV.2	Steady-state OCP values with increasing concentration of added redox molecules $\text{Fe}^{\text{III}}(\text{CN})_6^{3-}(\text{aq})/\text{Fe}^{\text{II}}(\text{CN})_6^{4-}(\text{aq})$ in a $100 \text{ mmol} \cdot \text{L}^{-1}$ KCl solution.	64
IV.3	Schematic energy level diagram illustrating the measured elements during the liquid-jet XPS experiment.	65
IV.4	Configuration of the liquid jet setup in PLEIADES beamline.	66
IV.5	Determination of the true photon energy value using the first and second diffraction order method.	67
IV.6	Conversion of relative electrode potentials into electrochemical potentials for aqueous systems.	69
IV.7	Cl 2p core-level spectra of a 0.1 KCl solution under the effect of several values of applied bias.	70
IV.8	O 1s core-level spectra of a 0.1 KCl solution under the effect of several values of applied bias.	71
IV.9	Estimation of the ionisation potential of liquid water via XPS.	72
IV.10	Energy-level diagram for aqueous $\text{Fe}^{2+/3+}$ -hexacyano redox pairs illustrating the definition of vertical ionisation energy and reorganisation energy.	74
IV.11	Valence band maximum and secondary electron cutoff of a $0.1 \text{ mol} \cdot \text{L}^{-1}$ KCl solution and a commercial Zobell solution.	75
IV.12	C 1s spectra of the Zobell solution (red) and the Zobell + butanol solution.	78
IV.13	Valence band maximum and secondary electron cutoff of the Zobell solution and the Zobell + butanol solution.	80
IV.14	Fe 3d valence level and secondary electron cutoff spectra of the Zobell solution.	81
V.1	The dimers of the Si(100)- 2×1 surface reconstruction.	87
V.2	Ball and stick views of (H,OH)-Si(001).	88
V.3	NH_3/OH equilibrium geometries calculated via the periodic DFT approach.	93
V.4	NH_3/OH equilibrium geometries calculated via the cluster QC DFT approach.	95
V.5	Measured time-resolved N 1s spectra and calculated nitrogen coverage during NH_3 adsorption on (H,OH)-Si(001)- 2×1 at 120 K under 5×10^{-9} mbar of ammonia.	98
V.6	NH_3 desorption curves in vacuum plotted against time.	101

V.7	Cluster QC DFT optimised geometries.	103
V.8	Measured real-time N 1s spectra and calculated nitrogen coverage during TMA adsorption on (H,OH)-Si(001)-2×1 at 130 K under 5×10^{-9} mbar of TMA.	106
B.1	Al 2p _{1/2} spin-orbit stripping.	120
B.2	Al 2p spectrum of the Al(111) surface during exposure to 10 ⁻⁶ mbar of O ₂ , after background subtraction and stripping of the 2p _{1/2} component.	120
B.3	Measurement of $E_{b,Al\ 2p_{3/2}}^{Al_2O_3} - E_{bVBM}$ against oxide thickness.	122
B.4	O 1s energy-loss spectra for a 3.0-nm-thick Al ₂ O ₃ oxide film indicating the calculated bang gap $E_g = 7.1$ eV.	123
B.5	Plot of the $G(X, \lambda_{ox})$ function for $\lambda_{ox} = 0.7$ nm and comparison of $E_{bVBM}^{o/g}$ and the averaged measured E_{bVBM} versus X	125
B.6	Plot of contact potential difference ($\Delta\phi$ in the figure) between an aluminium film and a gold reference electrode in an oxygen atmosphere versus time, t , with oxygen pressure as a parameter.	128
B.7	Aluminium oxidation growth rate (with the corresponding fit parameters) and calculated Cabrera-Mott potential plotted against time during the low pressure regime.	129
C.1	Voltammogram of an unused Zobell solution compared to a Zobell solution recovered after liquid-jet measurements.	132
C.2	Voltammogram of an unused Zobell solution compared to a Zobell + butanol solution recovered after liquid-jet measurements.	132
C.3	Energy level diagram depicting the effect of applied bias on the liquid jet and the corresponding response in the gas phase O 1s spectra.	133
C.4	ΔV vs concentration for several n-butyl alcohol isomers and calculated molecular surface density.	134
C.5	Octahedral CFT splitting and configuration of ferricyanide and ferrocyanide ligands.	135
D.1	XPS Si 2p spectrum ($h\nu = 175$ eV) of the (H,OH)-Si(001)-2×1 surface.	138
D.2	Si Auger LVV and N 1s core level peak recorded at $h\nu = 530$ eV from the NH ₃ -covered silicon surface and the NH ₃ -(H,OH)-covered surface.	139
D.3	Si Auger LVV and O 1s core level peak recorded at $h\nu = 595$ eV from the silicon surface after water saturation at room temperature, then cooling down to 130 K, and after NH ₃ dosing under a pressure of 5×10^{-9} mbar.	140
D.4	O 1s spectra of the clean, the (H,OH)-Si(001) and the NH ₃ -(H,OH)-Si(001) surface, measured at $h\nu=595$ eV.	143

D.5	Normalised O 1s spectra of the (H,OH)-Si(001) surface at 130 K covered by ammonia.	144
-----	--	-----

List of Tables

IV.1	Kinetic energy shifts of the Cl 2p _{3/2} peak as a function of the applied potential.	70
IV.2	Kinetic energy shifts of the O 1s liquid phase peak as a function of the applied potential.	71
IV.3	Binding and ionisation energy, work function, width of the SEEDC, and outer potential values for 0.1 KCl, Zobell and Zobell + butanol solutions.	75
IV.4	Electron ionisation energies of liquid H ₂ O ($E_{b,1b_1(\text{liq})}$).	76
V.1	Periodic DFT Geometries, Adsorption Energies (E_{ads}), and N 1s Binding Energy Core-Level Shifts ($\text{CLS}_{\text{per}}^{\text{th}}$) with Respect to Si-NH ₂ for Structurally Relaxed Configurations (at 0 K).	94
V.2	Theoretical N 1s ionisation potential energies $E_{i,\text{QC}}^{\text{th}}$ calculated via a DFT QC silicon cluster approach for ammonia adsorption.	96
V.3	Theoretical N 1s ionisation potential energies $E_{i,\text{QC}}^{\text{th}}$ calculated via a DFT QC silicon cluster approach for TMA adsorption.	104
B.1	Inelastic mean free path values for metallic Al (λ_{m}) and Al ₂ O ₃ (λ_{ox}) calculated with Tanuma’s TPP-2 formula [124].	119
B.2	Binding energy positions (eV), Lorentzian and Gaussian widths of each component shown in Figure B.2.	121
C.1	Results from cyclic voltammetry measurements.	133
D.1	Surface core-level shifts referenced to the bulk component binding energy, widths, and spectral weights of the Voigt components used to fit the Si 2p experimental spectrum of the (H,OH)-Si(001) surface.	138
D.2	Theoretical O 1s ionisation potential energies $E_{i,\text{QC}}^{\text{th}}$ calculated via a DFT QC silicon cluster approach (Si ₉ H ₁₂ , the “one-bare-dimer” cluster).	141

Introduction

Interfaces are in nearly every naturally conceived or engineered system. They play an essential role in a wide range of phenomena and applications ranging between heterogeneous catalysis [1], energy conversion and storage [2], metal corrosion [3], and other environmental processes [4]. In fact, interfaces usually determine functionality and efficiency of a material involved in a particular process.

Let us take the distinctive example of microelectronic devices: the increasing demand for further miniaturisation and higher performance, as typified by Moore's law, has led to the implementation of several strategies that enable the conception of better materials that can work in extreme conditions. One of these strategies is the use of high- κ dielectric materials, usually manufactured via atomic layer deposition (ALD) (a subclass of chemical vapour deposition (CVD)), to replace silicon dioxide gate layers on silicon substrates. Several authors agree on that that interfacial quality (bonding, stability, etc.) drastically affects the performance of the final transistor [5, 6]. In this sense, a clear view of the physico-chemical phenomena that occur during the first steps of ALD manufacturing is key for an efficient design of most electronic devices. This includes not only the knowledge of the chemical intermediary active species that are formed, but also the understanding of how the electronic structure is affected when thermodynamic equilibrium prevails, i.e. when the electron electrochemical potential (i.e. the Fermi level in the language of solid-state physics) is constant throughout the interface. In this sense, an analysis of the interfacial electronic level alignment (affected by charge transfer phenomena) must be included if one aims at acquiring a comprehensive view of any particular process.

The necessity of a fundamental understanding of energy level alignment within an interface is not restricted to the classic cases where bulk solids are protagonists, but it also encompasses a lately increasingly attractive category of material: nanoparticles (NPs). In fact, nanomaterials are used in a wide range of applications in every possible field (medicine, high-tech industry, environmental sciences, etc. [7, 8]). Some authors

have reported that a range of important properties in NPs (such as photocatalysis and conduction) are dominated by charge transfer phenomena [9] and they have even come to say that level alignment could be deliberately engineered to improve their performance in technological applications, like solar cells [10].

In any case, characterisation of interfaces is not often a simple task (an affirmation considerably more valid when it comes to the analysis of materials at the nanometer scale) and it comes accompanied by a series of challenges, both from the instrumental and the theoretical point of view. The instrumental challenge is associated to the need of emulating “real-life” conditions during the study of interfacial reactions; in other words, being able to work under moderate to high pressure gaseous environments. Indeed, most classic surface characterisation techniques were limited to work under ultra-high vacuum (UHV) environments given the short inelastic mean free path of photoelectrons in the gas phase. This limitation, known as the “pressure gap”, hinders the understanding of processes in high pressure conditions; for instance, those of catalysis or environmental chemistry. It was not until recent developments that the community could bridge this gap and make it possible to reach working pressures of ~ 20 mbar. The introduction of Near-ambient pressure X-ray photoemission spectroscopy (NAP-XPS) was possible thanks to two modifications to the conventional instrumental design: (i) a very short distance between the surface under study and the analyser (~ 1 mm) to minimise inelastic scattering of photoelectrons in the gas phase and (ii) a highly efficient differential pumping system of the analyser lenses. The technique opened the possibility to study surface reactions under *operando* conditions. Surely, probing solid/gas interfaces was already possible under very low pressures, usually up to 10×10^{-6} mbar; a good example of that is given in this thesis by studying the reactivity of silicon at low temperature (Chapter V), where molecular condensation is obtained by keeping the substrate at cryogenic temperatures. Nevertheless, NAP-XPS expanded the operating pressure to a range much closer to ‘real-like’ environments, as it also allows molecular adsorption and condensation at temperatures of 300 K and above.

The theoretical challenge is associated to a sometimes misleading (or even absent) approach to the electronic level alignment phenomena that take place during a chemical reaction. Although great relevance is given to the chemistry-related retrievable information (i.e. the nature and the chemical environment of the species present during a reaction) that can be obtained from an XPS experiment, much of the electronic-structure related knowledge (e.g. the changes in the sample’s work function and other key energy parameters) is often overlooked. Indeed, one should not forget that the basic governing principle of any reaction: the equality of electrochemical potentials, which can be trans-

lated as an alignment of the Fermi levels involved in a system. In this sense, another great example of a modern XPS technique that comes handy for the study of interfaces is liquid-jet XPS, a technique originally designed to study highly volatile liquids, but that (we will see in Chapter IV) serves as a convenient setup to examine the level alignment within an electrode-liquid-gas interface.

In this thesis, I make use of advanced XPS techniques to characterise three kinds of interfaces, each one of particular importance in a specific domain. The three projects are named as “Band Alignment at a Solid/Gas Interface”, “Band Alignment at a Metal/Redox Solution Interface” and “A Model Surface to Study Hydrogen Bonding and Energy Shifts”. The first two chapters of this thesis are dedicated to a general review of the theoretical background behind XPS and electrochemical equilibria, while the last three chapters expose each of the mentioned experiments.

In chapter one, “X-ray Photoelectron Spectroscopy”, the basic aspects related to XPS, including its underlying principle, instrumentation and the interpretation of the spectra, are described. Since the experiments of this thesis were all carried out at synchrotron-based setups, a small introduction to synchrotron radiation is also provided. The special features related to the mentioned advanced XPS technique, namely NAP-XPS and liquid-jet XPS, are also detailed.

In chapter two, the elements necessary to understand the electronic level alignment within interfaces are explained, making a particular emphasis on the difference between two often misinterpreted concepts, the electrochemical potential and the work function, a confusion that has led to what is referred to as ‘the reference level problem’ [11]. This misunderstanding can be translated to the often mixed ‘vacuum levels’, the one local to a specific material ($E_{\text{vac}}^{\text{s}}$) and the thermodynamic one (E_{vac}^{∞}). A discussion is also made on how energy calibration is usually performed among both solid-phase and liquid-phase experimentalists, who use different references for their binding energy scale, the Fermi level E_{F} and the vacuum level $E_{\text{vac}}^{\text{s}}$, respectively. Special attention should be given to Section II.3.1 as it is explained why $E_{\text{vac}}^{\text{s}}$ is an inconvenient reference, since it is affected by uncontrolled features (e.g. surface dipole modification). Section II.3.2 explains the advantages of using the Fermi level as common reference point (either in solid phase and liquid phase experiments).

Chapter three, “Band Alignment at a Solid/Gas Interface”, discloses in great detail the capabilities of XPS to access a considerable quantity of features about the electronic band structure during an archetypical solid-solid interface formation process: the oxidation of aluminium. By monitoring in real-time the oxide growth process, it is possible to obtain

detailed energetic information on the metal/oxide/gas system and debate the validity of the landmark model for oxidation of metals developed by Cabrera and Mott in 1949 [12]. The reader will notice how the so-long unfortunate habit of mixing up $E_{\text{vac}}^{\text{s}}$ and E_{vac}^{∞} has often led to wrong interpretation of the model.

Chapter four, “Band Alignment at a Metal/Redox Solution Interface”, describes the electronic level alignment of a simple electrochemical system: an electrode/liquid interface in the presence of a redox couple. A complete methodology on how to perform energy calibration in liquid samples using the common Fermi level as reference is explained, as it is proved how the loose reference used by liquid-phase experimentalists, $E_{\text{vac}}^{\text{s}}$, is affected when the surface dipole is modified and can not be relied on. A solution with a known electrochemical potential is used to establish the position of the thermodynamic vacuum level (E_{vac}^{∞}) with respect to E_{F} and determine other relevant thermodynamic parameters, namely, the adiabatic ionisation energy and the reorganisation free energy parameter described in the well-known electron-transfer theory developed by Rudolph A. Marcus [13].

Finally, chapter five, “A Model Surface to Study Hydrogen Bonding and Energy Shifts”, exposes how XPS can be also used to perform studies on the reactivity of surfaces. By combining experimental measurements and *ab initio* quantum chemistry calculations, the nature of the bonding of two Lewis bases onto a water-saturated Si(001) surface is revealed. Again, the remarkable features of XPS as *in situ* technique are acknowledged on account of the complete picture of both reaction kinetics and bonding mechanisms that is presented.

Chapter I

X-ray Photoelectron Spectroscopy

X-ray Photoelectron Spectroscopy (XPS) is a technique widely used in surface science to investigate chemical composition and electronic properties of materials. It is based on the photoelectric effect, a phenomenon firstly observed by Heinrich Hertz in 1887 [14] and then successfully explained by Einstein using the new quantum mechanics in his classic paper of 1905, “On a Heuristic Viewpoint Concerning the Production and Transformation of Light” [15]. Although the basic concept of the technique was actually conceived as early as 1914 [16], present-day high-resolution photoelectron spectroscopy was initially developed in the mid-1960s by Kai Siegbahn and his co-workers at the University of Uppsala under the acronym of ESCA (Electron Spectroscopy for Chemical Analysis) [17, 18]. The acronym XPS was later naturally coined in order to indicate the nature of the photon source [19].

I.1 Basic Principle

The principle of XPS is illustrated in Figure I.1. When a sample is irradiated with photons of sufficient energy ($h\nu$), photoelectrons from inner shells get excited and can be ejected into vacuum with a kinetic energy (E_k) equal to

$$E_k = h\nu - E_i, \quad (\text{I.1})$$

where E_i corresponds to the ionisation energy of the photoelectron. The kinetic energy distribution of the emitted photoelectrons can be measured using an electrostatic analyser, and a spectrum can thus be recorded.

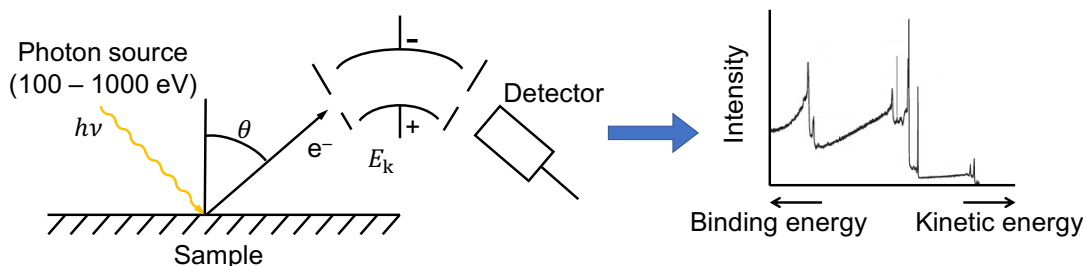


Fig. I.1 Sketch of an XPS experiment.

Equation (I.1) is only valid for free molecules, as in a gas, where the electron energy is naturally referenced to the vacuum level corresponding to the least bound valence orbital. In the case of liquid and solid samples, the main difference in photoelectron analysis arises from the presence of a band structure and, consequently, a Fermi edge¹ [20]. Now electrons have to overcome a potential barrier before being ejected from the surface. This potential is mainly a result of electron-electron interactions [21] and is known as the work function, $q\Phi$, with q being the electronic charge (a negative value)².

Namely, the work function corresponds to the minimum thermodynamic work needed to remove an electron from the Fermi level (E_F) of the sample and place it at rest at a point in free space just outside the surface [22]. General consensus has been reached regarding the fact that “just outside the surface” means far enough so that the electron’s image potential³ is zero, but close enough so that its distance from the surface is much smaller than the dimensions of the surface [11, 24, 25]. The electron energy is thus conveniently measured with respect to the Fermi level rather than to the vacuum level, and is referred to as ‘binding energy’, E_b . Equation (I.1) becomes⁴

$$E_k = h\nu - E_b - q\Phi. \quad (\text{I.2})$$

¹The usual definition of the Fermi level regards it as an energy level below which the electron levels are occupied and above which they are unoccupied in the ground state of a material. However, the reader will agree on the oversimplified character of this definition given that in a semiconductor this would correspond to any energy in the band gap. E_F can also be thought of as the level at which the probability of occupancy of states with electrons is 1/2 (at $T > 0$). Chapter 2 gives a more detailed overview on why we should simply consider it as nothing more than a synonym for “electrochemical potential”.

²By the notation used along the entire text, a clear distinction is made between an electrical potential and an energy: an electrical potential times a charge is a potential energy.

³The image potential is the static and local description of the many particle screening response of the solid to the electron near its surface [23].

⁴Note that E_i has been used to indicate the electron energy referenced against the vacuum level, whereas E_b is used when the reference is the Fermi level.

Three main aspects make of XPS one of the most established techniques in surface science for analysing elemental composition: elemental specificity, surface sensitivity, and chemical/electronic state sensitivity.

I.2 Sampling Depth

When an electron with kinetic energy E_k moves through matter, it has a probability of traveling a certain distance before losing all or part of its energy due to an inelastic collision. The average distance traveled between two inelastic collisions is known as the inelastic mean free path (IMFP, λ) [26], and it depends mainly on two parameters: the electron's energy and the nature of the medium interacting with this electron. Surface sensitivity of XPS (and of most electron spectroscopies) is attributed to the short IMFP of electrons within a solid sample. This is equal to saying that photoelectrons originating deep within a solid undergo more scattering events, losing enough E_k so that they are not likely to escape from the surface and be detected.

If elastic scattering is neglected, the intensity of an emergent electron flux from a given material, I , (this is, the number of photoelectrons that reach a surface without suffering energy loss through collisions) can be calculated using the Beer-Lambert law, as follows [27]:

$$I = I_0 \cdot e^{-d/\lambda \cos \theta}, \quad (\text{I.3})$$

where I_0 is the flux of electrons originating at depth d , θ is the angle formed between the normal to the surface and the analyser's direction, and thus, $d/\cos \theta$ is the distance traveled through the solid. Although not explicitly written in the equation, the intensity of the electron flux will be a function of the photon energy, $h\nu$. The product $\lambda \cos \theta$ is known as the mean escape depth (MED). Evidently, the MED of a photoemission experiment is maximised when the take-off angle is equal to 0° . From equation (I.3) one can deduce that 63% of all photoelectrons will come from within $1 \cdot \lambda \cos \theta$ of depth, while the majority (95%) of photoelectrons will come from $3 \cdot \lambda \cos \theta$. This is why the information depth (ID) of a photoemission experiment is usually said to be “three times the MED” [28].

Figure I.2 shows a compilation of published data on experimental determinations of IMFP⁵. The data indicates that the IMFPs of electrons in solids obey a universal curve

⁵The term IMFP is often mixed up with the attenuation length (EAL). Although both terms are usually used interchangeably, the IMFP is usually derived from theoretical calculations while the EAL

with a minimum around 2–5 Å. Thus, the information depth of a typical photoemission experiment will be of the order of 6–15 Å⁶.

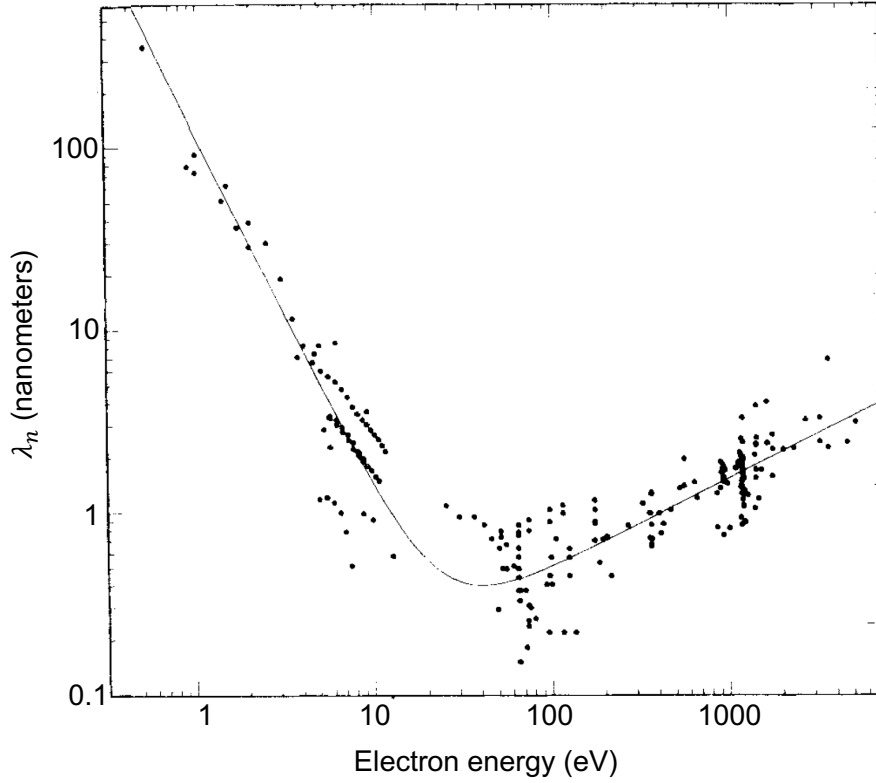


Fig. I.2 *Compilation of electron IMFP values for different elements. Reprinted with permission from [30]. Copyright 2020 John Wiley and Sons.*

I.3 Instrumentation

Two parameters determine a reliable spectrum for quantitative analysis in photoemission: resolution and intensity of the peaks. Assuming that the peak shapes can be described using Voigt functions, resolution (ΔE) can be calculated using the formula:

$$\Delta E^2 = \Delta E_{\text{peak}}^2 + \Delta E_{\text{instrum}}^2 = \Delta E_{\text{peak}}^2 + \Delta E_{\text{x}}^2 + \Delta E_{\text{ana}}^2, \quad (\text{I.4})$$

is determined experimentally and it ignores the effects of elastic scattering. This is why the EAL is less than the IMFP. Monte Carlo simulations can be used to calculate the effective attenuation length from a given IMFP [29].

⁶This is a typical value for excitation energies in the soft x-ray regime. For the hard x-ray regime, the ID will be around 40–100 Å.

where ΔE_{peak} is the natural line width of the XPS peak, generally described by a Lorentzian, and $\Delta E_{\text{instrum}}$ is the instrumental resolution, described by a Gaussian. This last one is affected by the finite energy resolution of the analyser (ΔE_{ana}) and the line width of the incident X-rays (ΔE_x). As for the measured intensity, it follows the formula:

$$P_i = c\sigma_i\Phi\lambda Tn_i, \quad (\text{I.5})$$

where P_i is the peak intensity, c a factor of proportionality, σ_i the cross section for photoemission for core level i , Φ an angular distribution factor, λ the IMFP of the electrons in the sample, T the analyser transmission efficiency and n the number of atoms in the analysed volume [31]. The parameters σ_i , λ and T depend on the photon energy.

The choice of the appropriate instrumentation for an XPS device, which includes i) an x-ray source, ii) an Ultra High Vacuum (UHV) system, and iii) an electron analyser (coupled with a detector), will naturally affect the resolution and intensity parameters.

1.3.1 Vacuum System

The vacuum system of electron spectrometers serves two purposes: avoiding electron scattering in the gas phase and minimising surface contamination from residual gases [32]. Scattering in the gas phase reduces the signal intensity and increases the background noise in the spectra. A pressure of the order of 10^{-6} mbar would be sufficient to overcome scattering effects [33]. At this pressure, however, the equivalent of about a monolayer of gas is delivered to the surface every second, a very short period of time compared with that required for a typical spectral acquisition [34]. This means that the surface will be contaminated with several monolayers before probing it. Hence, all vacuum systems for commercial electron spectrometers are designed to operate in the UHV range ($<10^{-9}$ mbar), an adequate pressure to accomplish both objectives.

Modern UHV systems consist of a combination of turbomolecular pumps, ion pumps, and multiple gauges and valves. Titanium sublimation pumps, Non-Evaporable Getter (NEG) pumps, cryogenic pumps and liquid nitrogen traps (LN2), are additionally used to improve the ultimate achievable vacuum or to reduce the pumping time. All UHV systems need occasional ‘bakeout’ in order to remove adsorbed molecules of residual gas from the chamber walls, mainly water. This basically refers to raising the temperature of the whole machine to about 180–200°C for a few days to improve the base vacuum⁷.

⁷The bakeout time and temperature depend on the desired final pressure and on how dirty is the

This is why all equipment must be fabricated from materials with high mechanical and thermal resistance [35].

1.3.2 X-ray Source

X-rays can be generated by x-ray tubes or synchrotrons. Other options are ultra fast laser with harmonic generation system or free electron lasers. As seen from eq. (I.4), one of the most important considerations when choosing an x-ray source, after taking into account the desired excitation energy range or value, is energy resolution. This means that the line width of the x-ray source should be significantly smaller than 1.0 eV if the resolution required is not to be limited by the source itself [33]. X-ray tubes are convenient radiation sources for home laboratories; they are easily accessible, relatively cheap, and can give reliable results. However, they have moderate intensity and are hardly polarised. Dedicated synchrotron radiation sources offer an alternative for high-quality x-ray beams production.

Synchrotrons constitute a particular class of particle accelerators that generate intense radiation extending from the infrared through the X-ray region of the electromagnetic spectrum. Their operation is based on a simple principle: charged-particles radiate electromagnetic energy when accelerated. For most synchrotrons, the charged-particles correspond to electrons although positrons were used before, because they were less interacting with the residual molecules remaining in the storage ring (as it was the case for LURE [36]). With the new vacuum techniques there is no need for positrons anymore.

The typical process for light generation is described as follows⁸. Electrons emitted by an electron gun are first accelerated in a linear accelerator (linac) in order to reach a very high speed and an initial energy level of 100 MeV, and group them in bunches. These are then transmitted to a circular accelerator (booster), which brings the energy level up to a standard operating value (2.75 GeV for SOLEIL) so that the electrons can be injected to the storage ring. Electrons circulate several hours in the storage ring, where magnetic devices such as dipoles (bending magnets) and undulators or wigglers (a succession of alternating magnets) control their trajectory to make them oscillate. Whenever their trajectory is changed, the electrons lose energy in the form of light: the synchrotron radiation. This radiation is then diverted, selected, and shaped by optic systems in experimental stations called beamlines, where it can be used for several experiments. A general schema can be found at Figure I.3.

chamber.

⁸The process outlined here applies for third generation synchrotrons, as it is the case for SOLEIL.

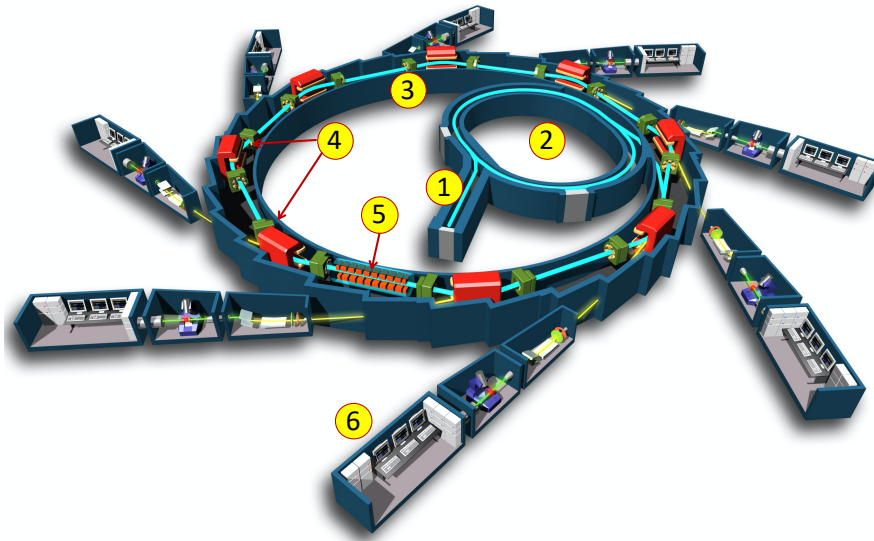


Fig. I.3 Schematic diagram of a synchrotron, (1) linac (2) booster (3) storage ring (4) bending and focusing magnets (5) undulators and wigglers (6) beamlines.

Synchrotron radiation has several advantages in comparison with a typical laboratory x-ray source. The most important one is its brilliance, a term that describes both the brightness and the angular spread of the beam ($\text{photons} \cdot \text{s}^{-1} \cdot \text{mrad}^{-2} \cdot \text{mm}^{-2}$ per 0.1% of radiation bandwidth) [37]. The greater the brilliance, the more photons of a given wavelength and direction are concentrated on a spot per unit of time. Other major advantage is its energy tunability, which means that the desired wavelength can be selected from a continuous range. Also, being a pulsed light emission, synchrotron radiation can be exploited to perform in situ and time-resolved measurements. High collimation and the ability to choose the radiation polarisation (linear, circular or elliptical) are notable properties as well [38].

To date there exist more than 50 synchrotron facilities in operation all over the world [39]. The experiments of this thesis were carried out at three different beamlines in two synchrotrons:

- SOLEIL, which is the French synchrotron and has an energy level of 2.75 GeV. The NAP-XPS experiments were done at TEMPO beamline, while the liquid jet experiments were carried out at PLEIADES.
- ELETTRA, the Italian synchrotron light source, which operates at two different electron energies: 2.0 GeV for enhanced extended ultraviolet performance and spectroscopic applications, and 2.4 GeV for enhanced x-ray emission and diffraction

applications. XPS experiments were done at BACH beamline.

I.3.3 Analyser

An electron energy analyser has to satisfy two main criteria: i) high finite energy resolution (ΔE_{ana}) and ii) high collection efficiency (the highest possible fraction of electrons leaving the sample should be energy-analysed and detected at the same time). The hemispherical sector analyser (HSA), also known as a concentric hemispherical analyser (CHA), satisfies both criteria and is the most popular among the modern XPS systems [33, 40].

Figure I.4 shows the schema of a typical spectrometer with an HSA. The hemispherical analyser consists of two concentric hemispheres of radii R_1 and R_2 . Electrons are collected and focused onto the entrance slit of the analyser by an input lens, which adjusts the kinetic energy of the electrons to match a user-selected value known as the pass energy E_p of the analyser. A potential difference is then applied across the two hemispheres (the inner is grounded so that a negative bias is applied to the outer one) in order to disperse the electrons according to their kinetic energy. Finally, the electrons cross the exit slit of the HSA to be detected [31].

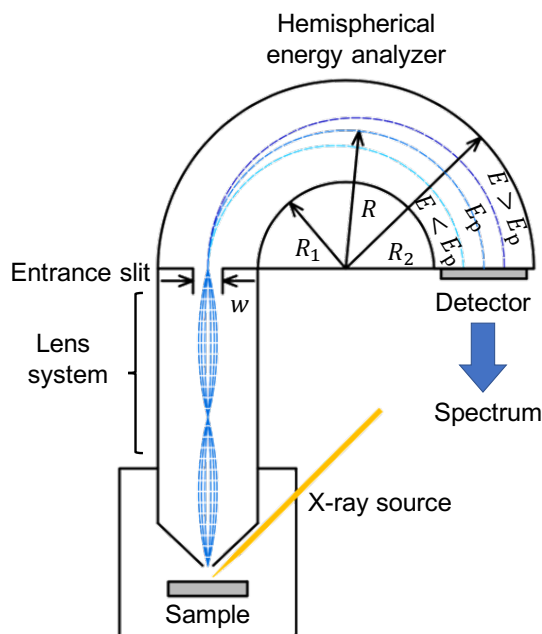


Fig. I.4 Schematic view of the photoelectron spectrometer with a hemispherical electron energy analyser.

The relation between the pass energy and the applied potential is given by

$$e\Delta V = E_p \cdot \left(\frac{R_2}{R_1} - \frac{R_1}{R_2} \right), \quad (\text{I.6})$$

where ΔV is the potential difference between the two hemispheres. The energy resolution of the analyser will be given by

$$\Delta E_{\text{ana}} = E_p \left(\frac{w}{2R} + \frac{\alpha^2}{2} \right), \quad (\text{I.7})$$

which shows that the energy resolution of the analyser, depends on the entrance slit width, w , the mean radius, R , the pass energy, E_p , and the acceptance angle, α . The choice of a pass energy sets a constant resolution for the whole spectrum [41].

Lower pass energies will yield better resolutions. This is because a higher pass energy mixes spatial and energy information to a greater extent than a lower pass energy. This principle is illustrated in Figure I.5; the resolving power is better for the case of low pass energies. However, a greater resolution is gained at the cost of a higher signal-to-noise ratio and a lower count rate. An alternative way to improve energy resolution is to reduce the width of the entrance slit to the HSA or simply having a larger analyser. Unfortunately, as the size increases, so does the vacuum and mechanical requirements [42].

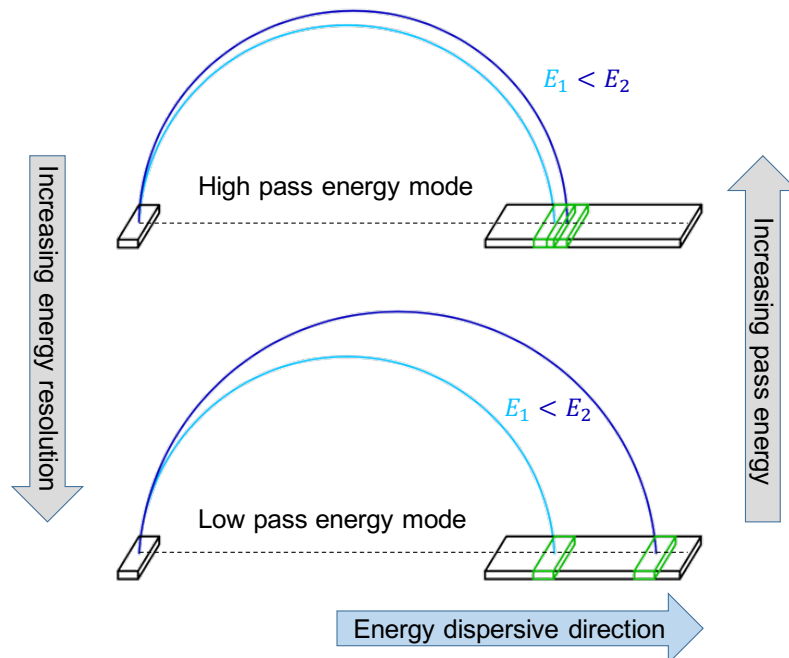


Fig. I.5 Pass energy and energy resolution explained.

The HSA can be operated in two modes, fixed analyser transmission (FAT) and fixed

retardation ratio (FRR). In the FAT mode, the analyser varies the electron retardation potential but keeps the pass energy constant. This keeps a uniform resolution during the whole spectrum. In the FRR mode, the pass energy is varied along with the retardation potential so that the ratio E_p/E_k is held constant. The FAT mode is a more usual practice in XPS [43].

Once the electrons traverse the exit slit of the analyser, they need to be counted by a detector. Modern XPS systems usually use 2D detectors based on micro-channel plates (MCP), combined with a read-out method which can be a charge-coupled device (CCD) camera or a delay-line detector (DLD). Detection can be carried out in two modes: swept mode and snapshot mode. In the swept mode, the analyser is swept over kinetic energy with a step width smaller than the energy window on the detector. In the snapshot mode, all voltages are kept fixed and the width of the energy window on the detector is determined by the pass energy [44].

1.4 Interpretation of Spectra

1.4.1 Theory

Note that so far the photoemission process in a solid sample has been implicitly described as a sequence of three independent steps: (i) optical excitation of a core electron in the solid, (ii) transport of the electron to the surface, (iii) escape of the electron into vacuum. This is the so-called three-step model, developed by Berglund and Spicer [45], and it is the simplest model for interpretation of XPS spectra. Being a semi-classical approach, the three-step approach completely neglects, however, many-electron and surface effects which induce energy-loss structures and energetic shifts in XPS spectra.

To overcome the deficiencies of the three-step model, Pendry and co-workers [46] suggested a more rigorous one-step approach based on the quantum-mechanical description of the perturbation induced by the photoexcitation process of the electron states of the solid. The one-step model describes photoemission as a single quantum-mechanically coherent process including all multiple-scattering events [47]. Figure I.6 illustrates both models.

Despite being a purely phenomenological approach, the three-step model has proven to be more intuitive in the interpretation of XPS spectra than the ‘correct’ one-step model approach. Many of the practical applications of XPS for quantitative determination can

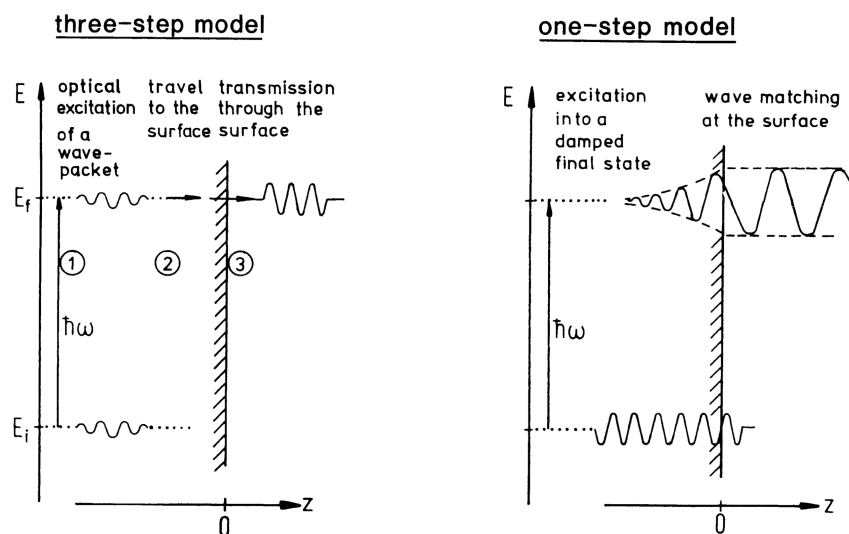


Fig. I.6 Illustration of the three-step and the one-step model of XPS. Reprinted with permission from [48], adapted from [49]. Copyright 2020 IOP Publishing.

actually be quite well explained by the one-step model.

I.4.2 Energy Loss Phenomena

Figure I.7 shows the main features on an XPS spectrum. The primary peaks are shaped by photoelectrons that come out of a sample without having suffered inelastic scattering. These include both photoemission and Auger⁹ peaks. Most of the photoelectrons detected, however, do not in fact contribute to the main peaks of a spectrum, but suffer ‘extrinsic’ or ‘intrinsic’ energy losses, and form the secondary structure (secondary background and satellite peaks).

“Extrinsic” losses occur when the photoelectrons lose energy in their passage from the site of excitation to the solid surface, and possibly in escaping through the surface. They are caused by interaction of the electric field from the photoelectron with other electrons. They shape the main feature of the secondary structure: the continuous background on the low kinetic energy side of the spectrum.

“Intrinsic” losses arise from the additional (many-electron, or many-bodied) excitations that accompany the main photoexcitation process, and reduce the observed kinetic

⁹When a photoelectron is ejected and leaves a vacancy, an electron from a higher energy level may fall into the vacancy, releasing enough energy to provoke the emission of another electron. This is known as the Auger effect

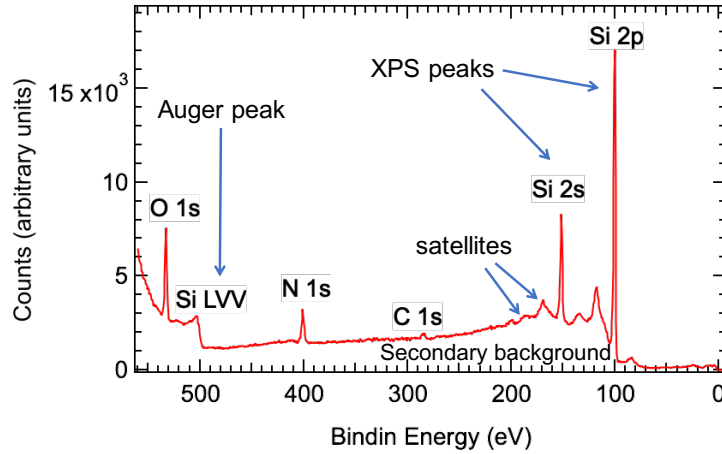


Fig. I.7 Survey spectrum of an ammonia covered (H,OH)-Si(100) surface showing main XPS features.

energy of the “parent” electrons. They are due to the sudden creation of an electric field from the core-hole which acts as a perturbation to valence electrons. Examples include shake-up satellites, in which a valence electron is excited to an unfilled level above, and shake-off satellites, in which a valence electron is completely removed. Shake-up features will be observed as satellite peaks at the high binding energy side of the main photoelectron line. Shake-off features fall in the region of broad inelastic tail and are not usually observed experimentally [50,51].

Additional features in an XPS spectrum are plasmons, which refer to collective oscillations of delocalised valence band electrons. Plasmon satellites are specific to materials which have a free-electron-like band structure and they can either be intrinsic or extrinsic [52]. It is often hard to distinguish between intrinsic and extrinsic features in an actual spectrum. Tougaard [47] affirms, however, that they can be distinguishable in the basis of shape differences [53].

I.4.3 Core-Level Shifts

Rigorously speaking, a core-level binding energy, ξ , is given by the energy difference between the ground state and the core-hole final state of the system. For a system containing N electrons,

$$\xi = E_{\text{fin}}^{\text{exact}}(N-1) - E_{\text{in}}^{\text{exact}}(N), \quad (\text{I.8})$$

where E_{fin} and E_{in} are the exact *total energies* of the system after and before ionisation,

respectively. Total energies can be computed using the Hartree-Fock (HF) method to solve the electronic Schrödinger equation¹⁰. The starting point of the HF theory is the assumption that the motion of each electron can be treated as if it were independent of the motions of other electrons. The original wave function is represented as a Slater determinant and its calculation is reduced to solve a set of interdependent single-particle eigenvalue equations. However, the electron-electron interaction must be accounted for in some kind of approximate way. Consequently, the kinetic energy, the Coulomb, and the exchange terms for each electron are calculated as if all other electrons in the system formed an effective electric field.

It is only natural that the energy calculated by the HF does not match the exact total energy of the system; electrons are not really moving independently from one another. Their motion is correlated and this results in a lowering of the energy with respect to the fictitious uncorrelated situation. Hence, the total energy calculated by the HF method must be corrected by adding up a correlation energy term, E^c :

$$E^{\text{exact}} = E^{\text{HF}} + E^c . \quad (\text{I.9})$$

Equation (I.8) then becomes

$$\xi = E_{\text{fin}}^{\text{HF}}(N - 1) - E_{\text{in}}^{\text{HF}}(N) + \Delta E^c . \quad (\text{I.10})$$

Bear in mind that one-electron eigenvalues obtained by the HF method do not actually represent initial-state properties of a system. They should be rather viewed as a first-order approximation to electron binding energies. Koopmans' theorem is a central concept to understand the physical significance of this. Also called the frozen orbitals approximation, Koopmans' theorem is based on the assumption that when one electron is removed from a system the wave functions of the other electrons are unchanged. Under this premise, the initial-state HF eigenvalue, ε_i (by convention a negative quantity), exactly equals the difference between final and initial HF total energies of the system,

$$-\varepsilon_i = E_{\text{fin}}^{\text{HF}}(N - 1) - E_{\text{in}}^{\text{HF}}(N) . \quad (\text{I.11})$$

Nevertheless, after the photoionisation process, the surrounding orbitals relax around

¹⁰Remember that the electronic part of the Schrödinger equation is obtained after applying the Born–Oppenheimer (BO) approximation, which assumes that the motion of atomic nuclei and electrons in a molecule can be treated separately.

the core hole to screen it and this relaxation term should be added to make the equation hold exactly:

$$-E^{\text{R}} - \varepsilon_i = E_{\text{fin}}^{\text{HF}}(N-1) - E_{\text{in}}^{\text{HF}}(N). \quad (\text{I.12})$$

Equation (I.10) can be then simplified to

$$\xi = -\varepsilon_i + \Delta E^{\text{c}} + E^{\text{R}}. \quad (\text{I.13})$$

Since the common practice with solid materials in XPS is to reference the binding energy to the Fermi level of the sample, the binding energy of a core-level i can be then written as

$$E_{\text{b}}(i) = -\varepsilon_i + \Delta E^{\text{c}} + E^{\text{R}}(i) + E_{\text{F}}. \quad (\text{I.14})$$

Hence, following the initial-state-final-state approach, one can represent any shift in the binding energy as

$$\Delta E_{\text{b}}(i) = \underbrace{-\Delta\varepsilon_i}_{\text{initial-state contribution}} + \underbrace{\Delta(\Delta E^{\text{c}}) + \Delta E^{\text{R}}(i)}_{\text{final-state contribution}} + \Delta E_{\text{F}}, \quad (\text{I.15})$$

where $\Delta(\Delta E^{\text{c}})$ is usually ignored and set equal to zero [11, 49].

1.4.3.1 Initial-state Effects

Initial-state contributions, also called chemical shifts, refer to any change in the initial-state charge density of the system. Therefore, anything that changes the electrostatic potential at the atom under study takes the form of an initial-state contribution and will induce a shift in the core-level eigenvalue. One can assume that the electrostatic potential at the atom is dominated by the Coulombic interactions of the valence electrons, so it will be affected by the formal oxidation state of the atom and the local chemical and physical environment. For example, a higher negative oxidation state (an excess negative charge in the valence shell) will raise the electrostatic potential at the core and thereby reduce the energy required to remove a core electron [54].

I.4.3.2 Final-state Effects

Final-state contributions always refer to core-hole screening or relaxation. For solid-state systems, the term ΔE^R is conveniently broken down into contributions from intra-atomic screening and extra-atomic screening. For most cases, it is assumed that the intra-atomic part is unchanged and cancels out. The energy associated with the extra-atomic part is given by the classical equation for the electrostatic polarisation of a dielectric medium by a point charge [55],

$$E_{\text{extra}}^R = (1 - \varepsilon_0^{-1}) e^2 / 2r_0, \quad (\text{I.16})$$

where e is the point charge, r_0 is the radius of the effective electron screening distance, and ε_0 is the static dielectric constant. Hence, a shift of the relaxation energy ΔE^R can be obtained by computing the change of the extra-atomic relaxation energy between the two different environments, $\Delta E_{\text{extra}}^R$.

I.4.3.3 Shift of the Fermi Level

The Fermi level of any sample is given by the electrochemical potential of electrons [56], $\bar{\mu}$; it is thus determined by the chemical nature of the sample studied. In the case of extrinsic semiconductors, for example, the chemical nature is affected by the presence of doping impurities, so their concentration usually dictates the position of the Fermi level within the gap. A shift of the Fermi level can be then caused by a change on the nature of the material. One of the classic examples in XPS is the study of oxidation processes in metals, where core-level shifts respond to a variation in the surface Fermi level position due to the creation of an oxide film.

Core-level shifts can be also induced by Fermi level pinning. On a clean semiconductor, surface states may exist due to the termination of lattice periodicity. They will induce a charge transfer between the bulk and the surface causing a band bending. Since the density of surface states is usually larger ($\sim 10^{15} \text{ cm}^{-2}$) in comparison with the bulk dopant states in regions of the bulk semiconductor parallel to the surface ($\sim 10^8 - 10^{12} \text{ cm}^{-2}$), the Fermi level of the semiconductor is almost independent of the bulk dopant concentration and is pinned by the surface states [57].

I.5 Advanced XPS Techniques

As mentioned in Section I.3.1, conventional XPS experiments must operate in the UHV range, which basically limits the technique to the study of clean model surfaces. This makes most liquids incompatible with the technique (due to an elevated vapour pressure), and makes the investigation of interfaces at “real-life” conditions particularly hard. Some of the developments in advanced XPS instrumentation have allowed the study of liquids (liquid-jet XPS) and solid samples in gaseous environments (NAP-XPS).

I.5.1 Near-Ambient Pressure XPS

Near-Ambient Pressure XPS (NAP-XPS) is an advanced form of XPS designed to probe surfaces under “real-like” conditions, i.e. gaseous environments. Not only it allows the study of specific interfaces, but it also makes it possible to perform real-time measurements during chemical reactions, making the technique particularly interesting for applications in environmental and catalytic sciences. Unlike conventional XPS systems, NAP-XPS spectrometers are designed to reach working pressures of several mbar. This is achieved by means of two modifications: (i) a very short distance between the analyser nozzle and the sample, to minimise the inelastic scattering of the photoelectrons by the gas phase, and (ii) a specific additional lens design with a highly efficient differential pumping.

The maximum pressure achievable in an NAP-XPS experiment p_{\max} is set by the aperture between sample and analyser D_0 , and scales as D_0^{-1} . As a rule of thumb, the optimum sample distance from the aperture should be $2D_0$ to minimise the perturbation of the gas environment at the sample surface. This means that small aperture values not only imply higher working pressures but also a shorter distance for electrons to travel within the gas phase before reaching the analyser. This would also entail, however, a reduction of the acceptance angle of the electrons, consequently decreasing the total count rates. A value of $D_0 = 0.3$ mm is the standard aperture size in most NAP-XPS setups, limiting p_{\max} to ~ 10 mbar and defining the aperture-sample distance to less than 1 mm [58, 59].

As for the instrumentation, working in the millibar regime requires the implementation of some additional constraints in order to protect the X-ray source and the detection system. For the X-ray source, either Si_3N_4 or Al thin windows, or a differential pumping system can be used. When the X-rays are produced by synchrotron radiation, this prevents the UHV environment of the beamline from possible pressurisation. For the de-

tection system, a typical modern NAP-XPS spectrometer features an analyser with four pumping stages: the first three consist of the differentially pumped electrostatic pre-lens system, and the fourth contains the hemispheres and detector. The electrostatic lenses make possible the collection of a substantially larger fraction of electrons that would otherwise be lost due to the diverging nature of their trajectories and the small apertures separating the pumping stages [60].

Figure I.8 (a) illustrates the TEMPO NAP-XPS setup at SOLEIL. It is a modular design with a backfilling configuration that features several chambers:

- A loadlock, which allows easy introduction of samples with minimal perturbation of the base pressure, thanks to an easy venting system with liquid nitrogen and a fast-entry door.
- A transfer chamber, which serves as an intermediary station between the loadlock, the catalysis chamber, and the preparation chamber.
- A catalysis chamber, equipped with two gas lines connected to two leak valves and two different systems for sample heating (a class 4 laser and a button heater). The pressure inside the catalysis chamber can be as high as 1 bar in static mode.
- A preparation chamber for sample pre-treatment, equipped with a five-axis (x , y , z , θ , φ) manipulator, an argon sputter gun, an electron gun for low-energy electron diffraction (LEED), and two gas inlets through variable leak valves; it can be optionally equipped with additional surface science instruments for UHV sample preparation like molecule evaporators and e-beam heater.
- An analysis chamber for XPS experiments, made from mu-metal and coated with gold. It is equipped with 7 lines inlets; five of them are dedicated to gas dosing (four for pure gas and one for mixed gas), while the other two are restricted to liquid dosing. It has a five-axis manipulator which can be used along with two different heads. The first one is designed to heat the sample up to 1000°C in the presence of gases which pressure can reach several mbar. The second one comprises a Peltier cooler which allows to go down to -20°C , making it ideal for environmental chemistry applications since it allows to lower the gas vapour pressure and to study, for example, interfaces involving condensed liquid water. The sample is electrically connected with the manipulator, which is isolated from common ground, so it can be biased or grounded through dedicated connection.

All chambers are separated by gate valves and the use of linear sticks and wobblesticks allows sample transferring between them.

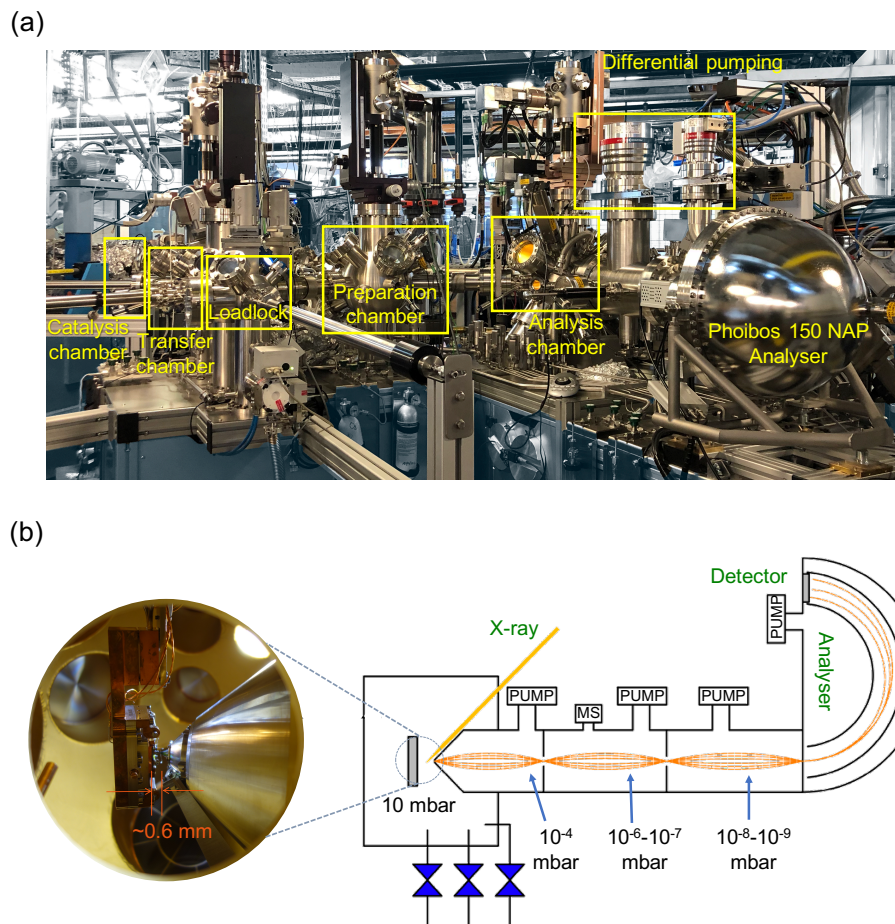


Fig. I.8 (a) Overview of the TEMPO NAP-XPS station at SOLEIL (b) Schematic diagram of the analysis chamber, differential pumping stages and electrostatic lenses in the NAP-XPS system.

Finally, the setup at TEMPO is equipped with a Phoibos 150 hemispherical analyser manufactured by SPECS [44]. A simplified diagram of the analyser can be seen in Figure I.8 (b). Note that the first two stages of the analyser create a pressure drop from the mbar to high vacuum while the third and fourth ones create a stable high/ultrahigh vacuum in the lens, analyser and detector region. A mass spectrometer (MS) is also added for gas phase characterisation.

A major advantage of the NAP-XPS technique is the parallel acquisition of information coming from the gas and the substrate species, leading to a comprehensive view of any chemical process. Fortunately, the binding energies of gas phase species are usually separated by several eV from the energies of adsorbed and condensed phase species. One can then, for example, follow in real time the gas composition of reactants and products during an heterogeneous catalytic reaction, as well as the possible intermediary

adsorbed species. Gas phase x-ray absorption has another consequence; the ionisation of gas molecules provides a local source of electrons for surface charge compensation during experiments on insulating or semiconductor samples [58].

Most NAP-XPS instruments operate using a standard vacuum chamber as the sample environment (Fig I.9 (a)). This is the case of the setup located at the TEMPO beamline at synchrotron SOLEIL. During an experiment, the whole chamber is exposed to the gas atmosphere. Although it is a conveniently simple design, it is not recommended when a fast change between gas atmospheres is desired. Custom-designed in situ cells have recently been developed to overcome this difficulty; they are docked to the analyser and the sample is introduced using special manipulators. Fig I.9 (b) shows the design of an in situ cell placed inside a vacuum chamber. During the measurement, the cell is sealed off from the surrounding UHV chamber so that the gaseous sample environment is limited to the volume of the cell. After the measurement, the sample is taken out and the cell is retracted and valved off again. Hence, the analysis chamber is then left in its UHV state. Other designs use independent exchangeable in situ cells without a surrounding UHV environment (Fig I.9 (c)) [59].

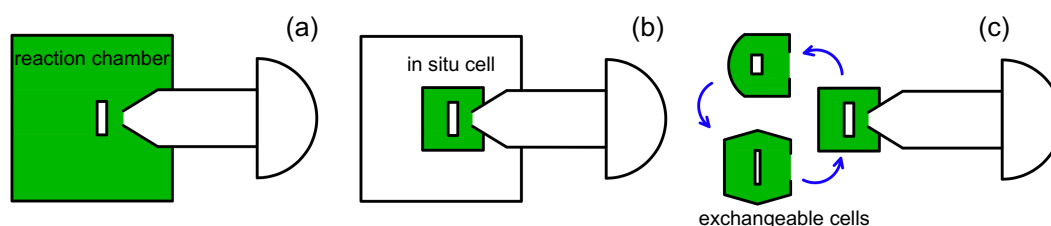


Fig. I.9 Schematic layout of in situ measurement cells currently used in NAP-XPS systems. (a) The standard vacuum chamber is backfilled with the gas. (b) The in situ cell is located inside a larger vacuum chamber. Only the in situ cell is exposed to gases during measurements. (c) Alternative cell setup without the standard vacuum chamber. Exchangeable in situ cells, tailored to a particular experiment, are attached to the analyser. Modified from [61].

I.5.2 Liquid-jet XPS

The earliest studies on liquid surfaces by means of XPS were performed K. Siegbahn and co-workers [62]. Their arrangement was based on the creation of a “beam” of the liquid sample to investigate. Most of the common liquids are highly volatile, with vapour pressures that can extend up to several hundred mbar. A dense vapour phase not only represents a hazard for the vacuum instrumentation but it also implies a higher attenuation of the photoelectron signal due to inelastic scattering. This is why Siegbahn’s

experiments were limited to the study of low-vapour pressure liquids (<1 torr). High volatility had still remained the main inconvenient for further investigation of liquid surfaces, until the development of the vacuum liquid microjet technique for XPS introduced by M. Faubel and co-workers [63].

Faubel’s approach is based on a simple statement: the introduction of high vapour pressure liquids into the high vacuum environment could only be achieved by satisfying the Knudsen condition of molecular flow [64],

$$\text{Kn} = d_{\text{jet}}/\lambda_{\text{gas}} > 0.5. \quad (\text{I.17})$$

Thus, the diameter of the liquid “beam”, d_{jet} , must be of the order of several μm . This jet is generated by pushing the liquid through a glass nozzle with high backing pressure and injecting into an evacuated chamber. It is generally cooled down with the aid of liquid nitrogen to reduce its equilibrium vapour pressure. It has a velocity of $\sim 100 \text{ m} \cdot \text{s}^{-1}$, this fast flow prevents the surface from early freezing despite its low temperature. It also ensures local thermodynamic equilibrium because liquid-liquid molecule collisions occur on a much slower time scale. A diagram of the setup can be found in Figure I.10. The technique allows the constant renewal of the liquid sample, making it free from contamination or beam damage.

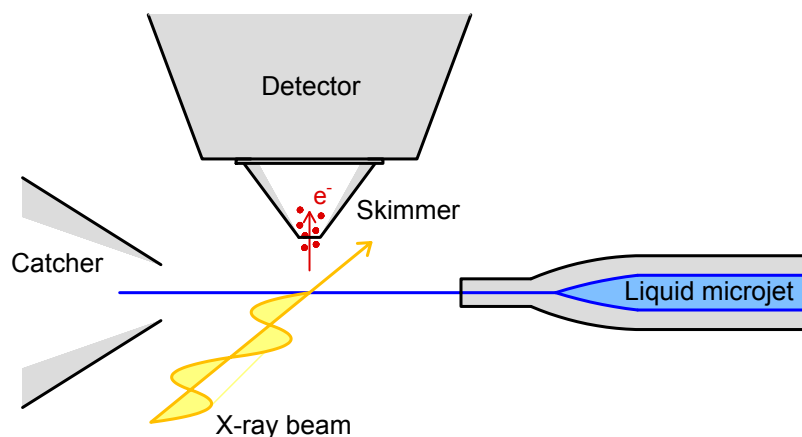


Fig. I.10 *Illustrative sketch of the liquid jet XPS setup.*

The development of the technique brought its own drawbacks, of course. In 1992, Faubel and Steiner [65] noticed “unexpectedly large streaming currents and electrokinetic charging” which could provoke errors in the apparent photoelectron energy when studying

a thin jet of pure water. Electrokinetic charging can be explained as a consequence of the fast flow of the liquid through the small nozzle, which induces a shearing of the electrical double layer (EDL) [66] and a net separation of charges. This creates a potential difference between the liquid jet and the electron spectrometer that can accelerate or retard emitted electrons, and is known as the streaming potential, ϕ_{str} . Preissler and co-workers [67] affirm that for a flow rate of $0.5 \text{ mL} \cdot \text{min}^{-1}$, electrokinetic charging can be suppressed by the addition of salts in the millimolar concentration regime.

Chapter II

The Reference Level Problem

It has now been clearly stated how the major strength of the photoemission spectroscopy technique is the possibility of both retrieving the ‘chemical’ information of the probed sample (associated to the elements present within and their chemical environment), as well as having an insight on its electronic environment and its changes over time (given, for example, as the form of changes in the work function). The accuracy of these determinations clearly relies on an appropriate calibration of the energy scale, a task performed quite differently for solid, liquid and gas samples. This chapter addresses the basic notion underlying thermodynamical equilibria and its relevance for energy calibration in XPS measurements.

II.1 The Electrochemical Potential of the Electron

In order to understand all the essential elements of the reference level problem, it is necessary to begin with the concept of the electrochemical potential. According to its original definition derived from the phenomenological equation of thermodynamics¹, the electrochemical potential is expressed mathematically as

$$\tilde{\mu} = \left(\frac{\partial G}{\partial n} \right)_{T,p} . \quad (\text{II.1})$$

This is, the work (Gibbs energy) entailed by a change in the number of particles of a

¹A more detailed treatment starting from the First Law of Thermodynamics can be found in Appendix A, if the reader is interested.

system as the temperature T and pressure p are held constant, except for the volume work. The general theory [68] states that for two phases to be in equilibrium, their electrochemical potentials must be the same:

$$\tilde{\mu}_1 = \tilde{\mu}_2. \quad (\text{II.2})$$

In the event of dealing with charged particles (electrons), the work must include a term that accounts for the electrostatic potential energy of the region to which electrons are added, qV . This electrostatic potential can be affected by external factors (shifting charges outside the body, depositing a layer of dipoles on its surface, etc.), which means that $\tilde{\mu}$ is not a function of the internal state of the body alone [69]. The electrochemical potential can then be conveniently separated in a quantity that depends exclusively on the ‘chemical nature’ of the material (its constitution and the electron density), and a quantity for the electrostatic potential [70–73]:

$$\tilde{\mu} = \mu + qV. \quad (\text{II.3})$$

The term μ is commonly referred to as the chemical potential. For an uncharged particle the electrochemical potential is equivalent to the chemical potential, that is, for an atom in field-free space [74]. It can be shown that $\tilde{\mu}$ is identical to the energy parameter occurring in the Fermi-Dirac distribution function,

$$f(E) = \frac{1}{(1 + e^{(E-\tilde{\mu})/k_B T})}, \quad (\text{II.4})$$

provided that the energy is measured from a zero representing an electron at rest at infinity, E_{vac}^∞ [11, 56, 69]. Here, $f(E)$ is the probability that a state of energy E is occupied according to the Fermi-Dirac equation, T is the temperature and k_B is the Boltzmann constant. Under this circumstances, $-\tilde{\mu}$ is equal to the binding energy of a Fermi-level electron with respect to E_{vac}^∞ [11]. This is why it is customary to refer to $\tilde{\mu}$ as the Fermi level.

II.1.1 Revisiting the Work Function

As already mentioned in Section I.1 when discussing the photoelectric effect, the work function can be defined as a threshold energy which accounts for the difference between the total energy of an incident photon and the residual kinetic energy of the ejected

electron [56]. From the thermodynamic point of view, Herring and Nichols [69] express the definition of what they call the “true work function” using the equation

$$q\Phi = q\phi_{\text{out}} - \tilde{\mu}. \quad (\text{II.5})$$

in which q is the electronic charge, and ϕ_{out} is the electrostatic potential in the vacuum just outside² of an electronic conductor. Both ϕ_{out} , and $\tilde{\mu}$ are conveniently referenced to the same level³.

Now, if ϕ_{in} is the electrostatic potential in the bulk of the conductor, we may write, using the definition of the electrochemical potential (II.3),

$$\tilde{\mu} = \mu + q\phi_{\text{in}}. \quad (\text{II.6})$$

When substituted into eq II.5, eq II.6 yields

$$q\Phi = q\phi_{\text{out}} - q\phi_{\text{in}} - \mu. \quad (\text{II.7})$$

The difference between the outer potential and the inner potential⁴ is known as the surface dipole layer or potential barrier, $q\Delta\phi$. This potential barrier is the consequence of electrons partly spilling-out into vacuum, which creates a surface dipole layer with an excess negative charge above the surface and an excess positive charge below [76]. It will also depend on the peculiar condition of the surface because of adsorption, orientation, relaxation, and other effects [56]. The work function can be then re-written as:

$$q\Phi = q\Delta\phi - \mu, \quad (\text{II.8})$$

where

$$q\Delta\phi = q\phi_{\text{out}} - q\phi_{\text{in}}. \quad (\text{II.9})$$

²The outer potential is to be evaluated at a distance large enough from the surface so that the image potential is negligible, but small enough compared with macroscopic dimensions.

³All potentials discussed here are referred to the vacuum level at infinity.

⁴It should be noted that the inner potential defined here is not the same as the ‘inner potential’ (V_o) of a metal which is usually referred to in the solid state physics theory for metal surfaces [75]. The latter is the mean potential energy of an electron in a metal as a result of its interaction with the lattice of positive ions. In the following, we shall assume that this inner potential (V_o) is accounted for in the bulk chemical potential term (μ).

Equation (II.8) shows explicitly that the work function is the sum of the energy required to take an electron through the surface dipole layer, $q\Delta\phi$, and a bulk chemical potential μ independent of the surface. Since this dipole moment may be expected to be different for different faces of a single crystal, the work function will vary from face to face. On the other hand, the chemical potential μ is a volume property independent of the structure of the surface.

The energy level diagram for a metal crystal is illustrated in Figure II.1. The graphic representation of the discussed potentials makes it easier to understand why $\tilde{\mu}$ is not equal to $q\Phi$. Note that being referenced to E_{vac}^∞ , the electrochemical potential does not depend on the metal's crystal plane through which the electron is added or removed. This can also be explained by the simple fact that $\tilde{\mu}$ is a thermodynamic state function whose value is path independent. On the other hand, the work function is referred to a 'vacuum level' local to the surface, E_{vac}^s ; its value clearly depends on the electronic structure of the surface under study, which will vary according to the exposed crystal plane of the metal. This is the reason why we cannot talk about the work function as an intrinsic property. It is a misfortunate practice to express 'isotropic' values of the work function of a material. Although it is true that an average value over the entire sample can be computed, such an average will be different for the particular technique by which the work function is measured. This explains why the values for the thermionic work function (the energy required to boil an electron out of a heated metal filament) and the photoelectric work function (the energy required to eject an electron from a metal that is struck by light) differ slightly.

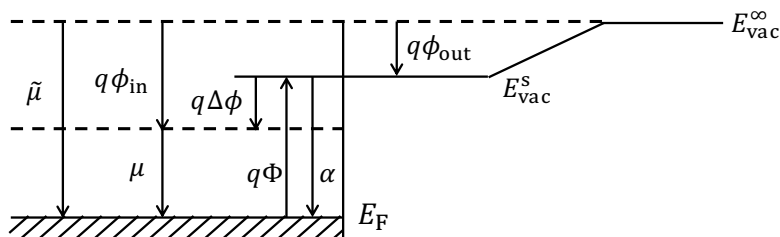


Fig. II.1 Energy level diagram for a conductor. Based on [77].

The negative of the work function is known as the real potential⁵,

$$\alpha = -q\Phi. \quad (\text{II.10})$$

⁵Note that the symbols $\tilde{\mu}$, μ and α are used as energies with the understanding being that the multiplication by a unitless particle number (an electron in this case) is implicit. This, to follow the usual nomenclature found in the literature [11, 56, 78].

II.2 Energy Calibration for Solid Samples

As already stated in seen in Section I.1, binding energies within solid XPS measurements are usually expressed relative to the Fermi level. This choice can be attributed to E_F being the most easily accessible reference, at least in metals. The binding energy calibration is based on a simple principle: the sample and the analyser are in equilibrium ($\tilde{\mu}_s = \tilde{\mu}_a$), which is equivalent to saying that their Fermi levels are aligned ($E_F^s = E_F^a$). This latter statement implies a good electrical contact between the sample and the spectrometer in order to ensure electron transport. An energy-level diagram illustrating the calibration principle is shown in Figure II.2.

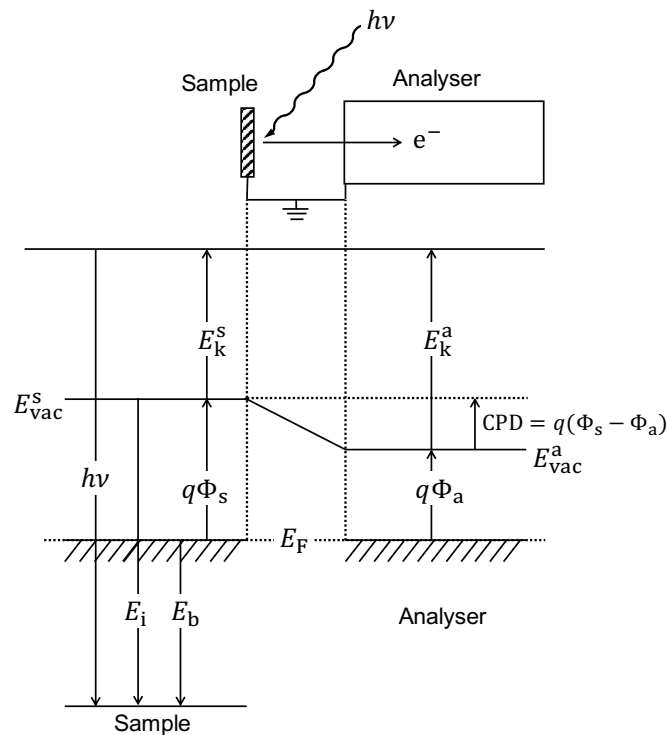


Fig. II.2 Energy level diagram for a sample in electrical equilibrium with an electron spectrometer.

A photoelectron coming out from the Fermi level of a material must first overcome the sample's work function ($q\Phi_s$) before being ejected and sent through the analyser in order to measure its kinetic energy. The analyser will have its own work function ($q\Phi_a$) as well, which suggests that the electron will experience a contact potential difference ($CPD = q\Phi_s - q\Phi_a$) that will result either in its acceleration or deceleration. If the kinetic energy of an electron coming out of the sample is given by

$$E_k^s = h\nu - E_b - q\Phi_s, \quad (\text{II.11})$$

then, the kinetic energy measured by the analyser will be E_k^s plus the contact potential difference⁶,

$$\begin{aligned} E_k^a &= h\nu - E_b - q\Phi_s + (q\Phi_s - q\Phi_a) \\ &= h\nu - E_b - q\Phi_a. \end{aligned} \quad (\text{II.12})$$

Equation (II.12) indicates that the measured kinetic energy of a photoelectron depends only on $q\Phi_a$, presumably a constant, so one should not worry about knowing the work function of the sample. Thus, if the true photon energy⁷ and the work function of the analyser are known values, a proper binding energy calibration with respect to the Fermi level can be achieved.

In the practical sense, especially for synchrotron-based measurements, it becomes more convenient to simply measure the Fermi edge of the sample (or of a metal surface in contact with the sample if dealing with a semiconductor or an insulator) to calibrate the energy scale. The calibration procedure is relatively straightforward when working with conducting samples that allow a continuous electron flux for quick neutralisation of the positive charges left by the photoionisation process. Contrarily, when working with low-conductivity samples like an insulator or a semiconductor, electrons are not replenished at a sufficiently high rate and a significant net positive charge may accumulate at the surface. The sample's surface will acquire a positive potential which decreases the kinetic energy of escaping photoelectrons, and its Fermi level will no longer be aligned with that of the spectrometer. This potential can vary from several eV to several hundreds of eV for insulators [79]. Surface charging can be compensated by several methods. One of them is to use a flood gun to irradiate the sample with low energy electrons. A perfect neutralisation will be achieved if the electron current is appropriate. Another method requires the use of a residual gas at pressures equal or above 1 mbar, as it is the case for NAP-XPS experiments. The X-rays will ionise the gas, producing positive ions and electrons in front of the sample so that a self compensation occurs.

⁶In the case exposed here $q\Phi_a < q\Phi_s$, the CPD ($q\Phi_s - q\Phi_a$) results in the acceleration of electrons and it must be added to the equation. If $q\Phi_s < q\Phi_a$, the CPD ($q\Phi_a - q\Phi_s$) results in a deceleration and must be subtracted.

⁷The X-ray photon energy is a fixed, known value for laboratory sources. In the case of synchrotron sources, although one is able to set a desired photon energy, this will not always be a 'true' value due to small variations in the monochromator configuration. The true photon energy can be accurately determined by measuring the kinetic energy of a chosen photoline using the first and second diffraction order of the monochromator's grating, and applying the equation $h\nu = E_k(2\text{nd-order}) - E_k(1\text{st-order})$.

II.2.1 Measuring the work function of the sample

Although not necessary for energy calibration, the work function can bring additional insight into the condition of a sample. This property is highly sensitive to chemical changes on a given surface; it is known that it may change substantially by the occurrence of surface reactions, but the same effect can also be expected even by the presence of very small amounts of contamination (less than a monolayer of atoms or molecules). Changes of the order of 1 eV are common for metals and semiconductors, depending on the surface condition. These changes are a result of the formation of electric dipoles at the surface, which modify the energy an electron needs to leave the sample.

Once the energy position of the Fermi level is known, the work function of a sample can be simply determined by measuring the onset of the photoemission signal stemming from the secondary background (see Section I.4.2), known as the secondary electron energy distribution cutoff (SEEDC). This cutoff determines the vacuum level of the sample, $E_{\text{vac}}^{\text{s}}$. Note, however, that the cutoff of the sample may not be visible if the work function of the analyser is greater than that of the sample (see Figure II.3 (a)). In order to solve this, an accelerating potential (resulting in additional kinetic energy E_{bias}) between sample and analyser is applied. This pushes the sample's spectrum to higher kinetic energies and accords a clear 'view' of the sample's cutoff, as shown in Figure II.3 (b).

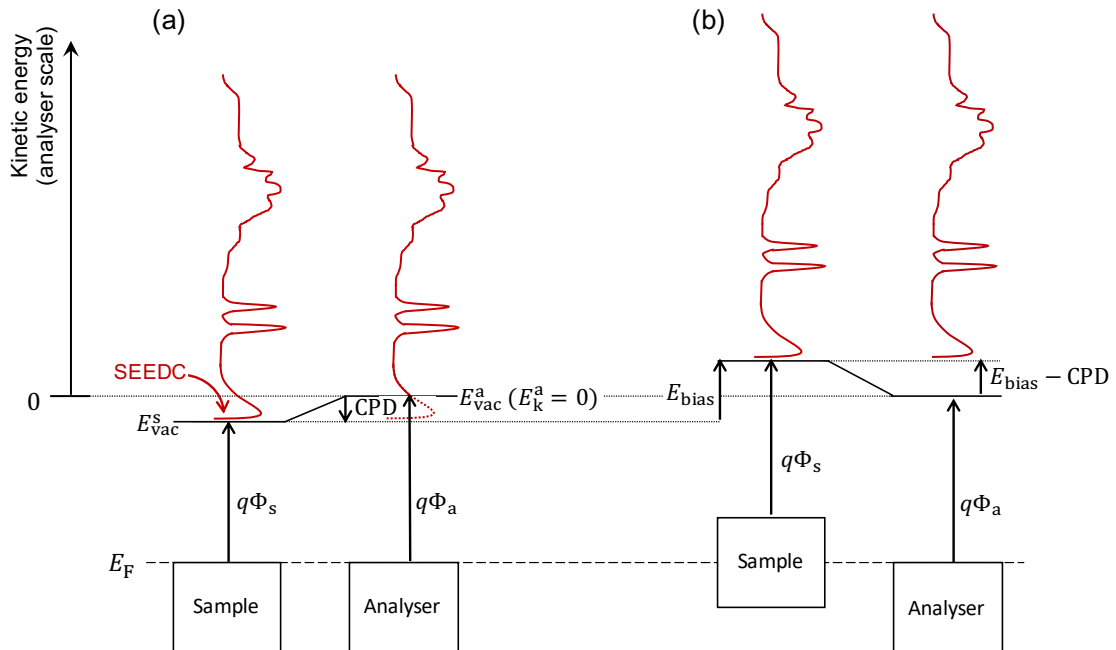


Fig. II.3 Illustration of the measurement of the work function on a metallic sample. (a) Grounded sample. (b) Negative bias applied.

II.3 Energy Calibration for Liquid Samples

II.3.1 The Vacuum Level as Reference

Contrary to the case of solid samples, energy calibration for liquid jet experiments becomes a bit more tricky as no reference level (such as a Fermi edge) is available. Instead of having ‘binding energies’ (E_b), most articles express ‘ionisation energy’ (E_i) values, which are referenced against the vacuum level local to the sample. Before explaining the calibration procedure, it is important to first have a clear picture of the equilibrium between the liquid jet and the analyser, and take into account the possible artefacts that may affect the measured kinetic energies.

Starting on the basis of the Fermi level alignment principle at equilibrium, there exists an energetic offset between the vacuum levels of the liquid and of the analyser. The main contribution to this offset is the difference between the work functions of the aqueous solution and the analyser, $q\phi_o$ (similar to the CPD in solid samples) (Figure II.4 a). An additional contribution can be caused by a possible charging of the jet surface. This may include both (i) the charging due to the photoemission process (water is an insulator), and (ii) the electrokinetic charging due to the shearing of the electrical double layer. The first effect can be completely neglected, given the very small diameter of the jet and its large velocity [80]. The second one induces a streaming potential ϕ_{str} , which depends on the flow rate of the jet. In any case, surface charging causes a displacement of the liquid’s Fermi level with respect to the analyser’s Fermi level; this shift has to be consequently added to the offset of the vacuum levels, as shown in Figure II.4 b.

Thus, the total vacuum level offset can be calculated as:

$$\Delta E_{vac} = E_{vac}^a - E_{vac}^{liq} = q\phi_o + q\phi_{str}. \quad (\text{II.13})$$

If electrokinetic charging is handled appropriately, which is usually the case and can be simply done by the addition of salts in the millimolar regime, equation (II.13) simply becomes the difference between the work functions,

$$\Delta E_{vac} = q\Phi_s - q\Phi_a. \quad (\text{II.14})$$

Taking into account the vacuum level offset, the ionisation energies of the liquid are given

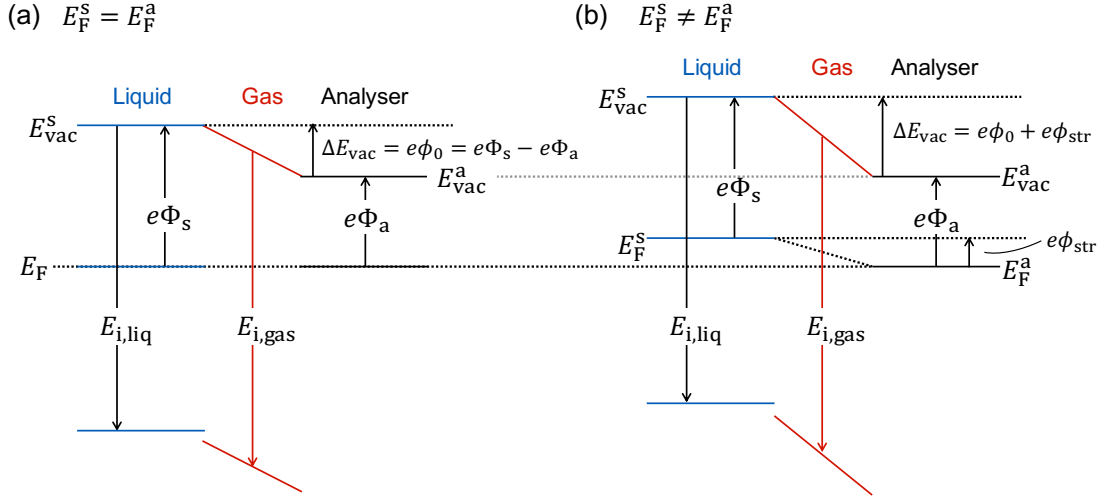


Fig. II.4 Energy level diagram for a liquid solution in electrical contact with a grounded electron spectrometer. (a) No surface charging. (b) Surface charging.

by the equation:

$$E_{i,\text{liq}} = h\nu - E_{\text{k}}^{\text{a}} + \Delta E_{\text{vac}}, \quad (\text{II.15})$$

where the zero of the kinetic energy E_{k}^{a} is defined at the vacuum level of the analyser.

Keeping in mind the above-explained, one possible option to perform the calibration procedure of the absolute (ionisation) energy scale is to select a peak whose ionisation energy is accurately known, and use it as internal energy reference. This would account for energy shifts along the whole measurement process caused by a possible change in ΔE_{vac} over time. Under this premise, it is natural to understand why the experimental energies of liquid samples and solutions are commonly calibrated by aligning the $1b_1$ liquid-phase water peak to a fixed value⁸. The real matter of controversy is knowing the precise value of this peak position, which would initially need the use of an external reference.

The first ones to identify the valence orbital energies of liquid water were Winter and co-workers. Their pioneering study was conducted using a laboratory UV source [80]; however, the determined position values were imprecise due to large background of secondary electrons in the spectra and limited statistics. This was later improved using a synchrotron-based source in 2004 [82]. They found the $1b_1$ liquid peak to be at 11.16 eV (top of the peak) by using the known $1b_1$ gas-phase ionisation potential of water (denoted $1b_{1\text{g}}$, with a value of 12.6 eV) as external reference [83]. Winter and

⁸The ground-state electronic configuration of water is $(1a_1)^2(2a_1)^2(1b_2)^2(3a_1)^2(1b_1)^2$ with $1b_1$ being the orbital associated to the highest energy electrons [81].

co-workers state that this corresponds to a convenient and precise energy reference given that, during their jet measurements, “its position and width are found to remain constant in the spectra as the jet was moved off-sight from the spectrometer direction axis by about 100 micro meter” [82], implying that “gas-phase and liquid-phase signals originate from identical potentials” [84]. It is not clear whether the streaming potential due to electrokinetic charging is taken into account or handled, as they say they used ‘highly demineralised water (conductivity ca. $0.2 \mu\text{S} \cdot \text{cm}^{-1}$)’ in their experiments; no adding of salt is mentioned.

Additional studies where the $1b_{1g}$ peak is used as external reference to determine the position of the $1b_1$ liquid water peak are the ones done by the group of Suzuki [85, 86]. However, a key difference is introduced: the use of an electrolyte to (apparently) eliminate electrokinetic charging effects. Initially, in 2011, Nishizawa et al. conducted the experiment ‘adding $140 \text{ mmol} \cdot \text{L}^{-1}$ NaCl to water to reduce the streaming potential’, and reported a value of 11.23 eV ⁹. Later, in 2014, Kurahashi et al., indicated a value of 11.31 eV using a $30 \text{ mmol} \cdot \text{L}^{-1}$ NaI aqueous solution to eliminate electrokinetic charging.

As the reader may notice, all the values found by each separate study differ by $11.23 \pm 0.10 \text{ eV}$. Olivieri and co-workers attribute this discrepancies to the fact that the deduction of the position of the $1b_1$ liquid peak using the $1b_{1g}$ gas-phase peak as reference completely ignores the vacuum-level offset between the liquid and the analyser (ΔE_{vac}). This assertion would explain the small variations between the reported values, since ΔE_{vac} depends on the work function of the analyser and it would be only natural for analysers in different laboratories to have different work functions. According to Olivieri, another source of variation can be due to the ionisation energy of liquid water depending on the chemical composition of the solution [87], although this latter statement was disproven by Pohl and co-workers [88], as they re-examine in detail the concentration dependance of the photoelectron spectra. Pohl et al. show that for concentrations even as high as 8 M, shifts of only less than $150 \pm 60 \text{ meV}$ were observed, abating Olivieri’s conjecture that an energetic shift of the water $1b_1$ peak position of up to 0.57 eV could be expected in going from (nearly) neat water to a 1 M NaCl solution.

Although the study done by Pohl and co-workers validates the common calibration procedure of using the $1b_1$ liquid phase peak as reference if expressing relative energy values, the method does not seem to be applicable if absolute energy values are to be reported. Inspired by the necessity of having a proper calibration of the absolute energy scale, an alternative procedure was proposed by Olivieri, which consisted in applying a

⁹It is not clear whether the final composition of the solution was 0.14 M or some quantity of a 0.14 M NaCl solution was added to water.

variable external voltage on the liquid microjet so that both the offset potential and the streaming potential are compensated. Perry’s group [89] recently re-visited ionisation energy of liquid water using this technique and reported the vertical ionisation energy of liquid water ($1b_1$) to be 11.67 eV. Nishitani et al. confirmed that the procedure effectively ‘flattens the vacuum level potential around the microjet’ although ‘recalibration is indispensable after the application of an external voltage for accurate measurements’ [90].

II.3.2 The Fermi Level as Reference

The disagreements between the ionisation energy values given by different research groups can be simply attributed to one main problem: the lacking of physical means to access the default thermodynamic universal energy reference, the vacuum level at infinity E_{vac}^{∞} . A secondary issue comes from the fact that many people confuse this latter one with the local vacuum level of a finite-sized sample [91]. By this point, the reader should now be aware that ionisation energies of liquids determined via XPS experiments are referred to the sample’s local vacuum level $E_{\text{vac}}^{\text{s}}$. The difference between $E_{\text{vac}}^{\text{s}}$ and E_{vac}^{∞} is known as the outer potential of the sample, $q\phi_{\text{out}}$, as shown in Figure II.1 of Section II.1.1. The fact that Pohl and co-workers [88] had shown that considerable composition changes produced barely no energetic shift in the ionisation energy of water could be an indicator of a negligible value of $q\phi_{\text{out}}$ in the liquid phase. This would lead us to say that both vacuum levels (local and thermodynamic) almost equate, at least for the case of liquid samples.

One could just avoid all the inconveniences brought by the unknown vacuum level offset in liquid jet experiments by referencing the binding energy scale with respect to the Fermi level. Although not distinguishable in the liquid phase, a Fermi edge can be made readily available if measuring it from a metal in contact with the jet, assuming equilibrium between both ($\tilde{\mu}_{\text{metal}} = \tilde{\mu}_{\text{solution}}$). In their recent work, Tissot and co-workers performed photoemission measurements of liquid droplets of saturated solutions of sodium chloride and sodium iodide on a gold substrate in a NAP-XPS system, and confirmed that the Fermi levels of both phases are aligned [92]. Still, this does not solve the problem for having uniform measurements among different laboratories.

Similar to a semiconductor, the Fermi level of a liquid solution, which is fixed by its electrochemical potential, will be found somewhere between the gap of the HOMO and LUMO levels. Percival and Bard [93] observed that, in the absence of a redox couple, $\tilde{\mu}$ is set by the so-called ‘mixed potential’ of the system, whose value is determined by and very sensitive to the background reactions taking place within. In the case of water, the

main background reactions are water oxidation and oxygen reduction, which naturally depend on the oxygen concentration and can be additionally affected by the presence of an electrolyte. This leads to an ill-defined electrochemical potential and, consequently, variations of Fermi level positioning within the gap of the liquid phase depending on the solution to be used. In other words, seeing it from the perspective of the $1b_1$ peak positioning calibrated against the Fermi level, its binding energy will not be the same when determined for a solution with E_F closer to the HOMO band than for a solution with E_F closer to the LUMO band. If the system contains a reversible redox couple, $\tilde{\mu}$ is equivalent to the absolute redox potential of the couple and is said to be poised, independent of the background reactions taking place within. Now, the Fermi level will be fixed to a known stable value with respect to the vacuum level at infinity (the ultimate reference).

In chapter 4, we show our preliminary studies in attempting to determine the electronic level alignment at the metal/liquid interface considering a well-defined redox couple using the liquid-jet photoemission setup at PLEIADES beamline at SOLEIL. Along with the determination of the binding energy of the liquid $1b_1$, the measurement of the secondary electron energy distribution cutoff provides the energy position of the vacuum level of the sample and serves to estimate its work function.

Chapter III

Band Alignment at a Solid/Gas Interface

Using the nascent band theory of solids, N. Cabrera and N.F. Mott designed in the late 1940s a model for the low-temperature oxidation of metals that still stands today as a landmark. The core assumption is that an electric field set up in the growing oxide at thermodynamic equilibrium drives the transport of the ionic species responsible for the oxidation process. Although the existence of an electrostatic potential has long been sought experimentally in the in situ measurement of the work function changes in the presence of gaseous O_2 , it is demonstrated here that the measurement of the work function is itself insufficient to test the model, and the oxide band structure characteristics (surface dipole energy barrier and band bending) that should be followed instead are pointed. Addressing the paradigmatic case of the oxidation of the Al(111) single crystal surface in O_2 using a modern spectroscopic tool, i.e. near ambient pressure X-ray photoemission spectroscopy (operated up to a pressure of 1 mbar), the oxide growth is monitored in real time and detailed energetic information on the metal/oxide/gas system that allows to validate the central hypothesis of the Cabrera-Mott (CM) model is obtained. The original assumption that oxygen anions are adsorbed at the oxide/gas interface is also discussed.

Al oxidation has been considered because of its historical role in the establishment of the oxidation models [94–96], and because it keeps attracting a considerable attention both experimentally [97–100] and theoretically [101–107]. More specifically, the present in situ study of the electronic structure of a growing film can be compared to the theoretical work of Baran et al. [102] that is the only one addressing the central issue of the Cabrera-Mott potential with the modern DFT tools by considering the attachment of O_2 molecules

onto α -Al₂O₃ layers supported on an Al(111) substrate. Finally, it has been chosen to study the oxidation of the (111) face of an aluminium single crystal to avoid unnecessary complications due to the presence of grains with different orientations. The in situ, real-time spectroscopic methodology used here is effective and can be generalised far beyond the specific case of aluminium oxidation.

III.1 The oxidation of metals

Oxidation phenomena on metal surfaces are a vast field of basic scientific research and play a key role in many technological fields, from corrosion science to nano-devices. Oxidation is the typical chemical process that needs the physical insights of solid state physics, both at a macroscopic level, the classical oxidation models and their refinements [12, 94, 95, 108], and, in more recent years, at an atomic level thanks to the development of density functional theory (DFT) techniques, including molecular dynamics, and reactive force field-based molecular dynamics, which have brought a fresh vision on the mechanisms at stake (see e.g. refs. [101, 102, 104, 104–107] just for the specific case of Al oxidation).

III.1.1 The Cabrera–Mott model

With regards to the oxidation of metals at low temperature, the model presented by N.F. Mott and N. Cabrera in 1949 [12] was a landmark. Its application to the oxidation of metals is widespread [109], including nano-fabrication, where its key tenets are harnessed [110]. The core idea of the CM model is that the transport of ions (e.g. metal cations) is the limiting step and that the built-in electric field \mathbf{E} that appears in the oxide, helps moving metal cations towards the oxide/gas interface (or conversely oxygen anions towards the metal/oxide interface), see Figure III.1(a). In terms of band structure, the orientation of \mathbf{E} implies that the oxide bands are bent upward [57]. Cabrera and Mott found a simple explanation for the band bending qV_{bb} . They assumed that when thermodynamic equilibrium prevails, electrons are transferred from the metal to oxygen adsorbate acceptor levels at the oxide/gas interface. Then the Fermi level (E_F) is constant from the metal to the oxide surface (see Figure III.1(b)). The absence of charge space in the oxide (q is the charge of the electron and is negative) was also assumed. As a consequence, the negative excess charge is concentrated at the oxide/gas interface where the oxygen anions sit, and the positive one (of equal magnitude) at the metal/oxide interface. As in a condenser with a dielectric layer of thickness X , a uniform electric field $|\mathbf{E}| = (qV_{bb})/X$ is established in the film. To set ideas, 1/10 of a monolayer (10^{14} cm⁻²)

of singly charged anions on top of an oxide of thickness $X=1$ nm and of relative dielectric constant $\epsilon_r=10$ gives a high field of $1.8 \text{ V} \cdot \text{nm}^{-1}$ and a qV_{bb} value as large as 1.8 eV. Naturally, with a constant qV_{bb} , the electric field will vanish when the film thickens, which explains why oxidation stops at some limiting thickness at low temperature.

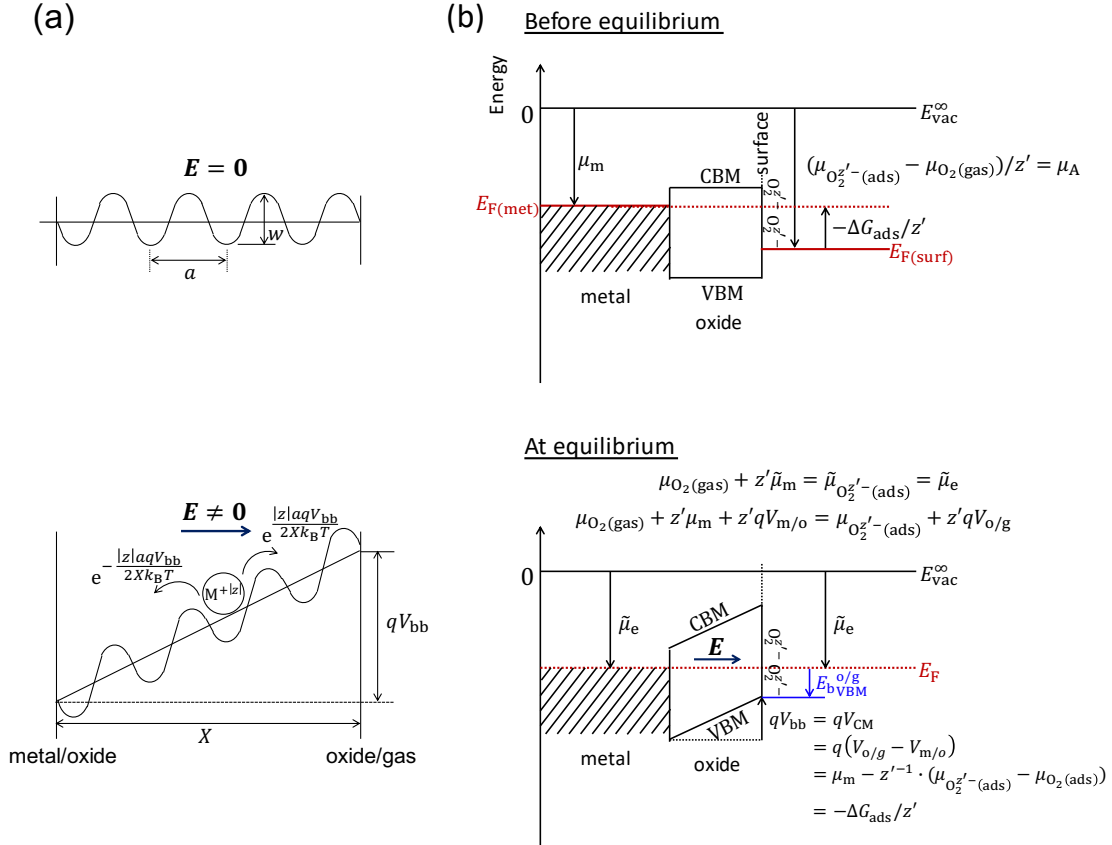
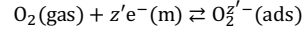


Fig. III.1 (a) Ionic transport in the presence of an electric field according to Cabrera and Mott (1949). It is assumed that the rate-limiting step is the ion movement of charge $z|q|$ (where z is a relative integer) within the oxide film. Here the ion is a metal cation $M^{+|z|}$. (b) Establishment of the Cabrera–Mott potential for the reaction $\text{O}_2(\text{gas}) + z'e^-(\text{m}) \rightleftharpoons \text{O}_2^{z'-}(\text{ads})$ at thermodynamic equilibrium, where z' is a positive integer equal to 1 or 2. E_{vac}^∞ is the thermodynamic reference energy for the electrons (the so-called vacuum level at infinity, distinct from the vacuum level in the vicinity of the surface E_{vac}^s). E_{F} is the Fermi level. VBM and CBM are the oxide valence band maximum and conduction band minimum, respectively.

It is shown in Section B.1 of the Appendix B that at thermodynamic equilibrium, the band bending qV_{bb} , denoted the ‘‘Cabrera-Mott potential’’ qV_{CM} in this case¹, is simply related to the Gibbs energy of adsorption of the molecule ΔG_{ads} corresponding to the reaction $\text{O}_2(\text{gas}) + z'e^-(\text{m}) \rightleftharpoons \text{O}_2^{z'-}(\text{ads})$ via the Nernst-like equation:

$$qV_{\text{CM}} = \frac{\mu_{\text{O}_2(\text{gas})} + z'\mu_{\text{m}} - \mu_{\text{O}_2^{z'-}(\text{ads})}}{z'} = -\frac{\Delta G_{\text{ads}}}{z'} \quad (\text{III.1})$$

where z' (an integer number equal to 1 or 2) is the number of electrons transferred from the metal to the adsorbate (e.g. an $\text{O}^{z'-}$ anion is formed). μ_{m} , $\mu_{\text{O}_2(\text{gas})}$, $\mu_{\text{O}_2^{z'-}(\text{ads})}$ are the chemical potentials of the electron in the metal, of the gas phase O_2 molecule and of the adsorbed molecular anion $\text{O}^{z'-}$, respectively. The equation $qV_{\text{CM}} = -\frac{\Delta G_{\text{ads}}}{z'}$ is general and is still valid for dissociative chemisorption (see Section B.1 of the Appendix B). The alignment of the Fermi levels (i.e. of the electrochemical potentials) at equilibrium is depicted in Figure III.1(b).

Equation (III.1) portrays qV_{CM} as a purely thermodynamic quantity and, as such, it must be referenced to the thermodynamic vacuum level at infinity E_{vac}^∞ [11]. Nevertheless, in their original paper of 1949, Cabrera and Mott equated qV_{CM} to the energy difference between the electron affinity of the oxygen acceptor level at the oxide surface and the work function of the clean metal surface, or, in other words, to the work function change between the clean and oxidised surface. This comes from a confusion between the E_{vac}^∞ and the vacuum level local to the sample $E_{\text{vac}}^{\text{s}}$ (that depends on the surface dipolar layer, affected by crystal orientation, adsorbates etc. see Section II.1.1), which led Cabrera and Mott to mistakenly assimilate $-\mu_{\text{m}}$ with the work function of the clean metal and $-\mu_{\text{A}}$ with the electron affinity of the adsorbate at the oxide surface. Therefore, despite the statement of Fehlner and Mott [94], ‘‘surface potential measurements [i.e. work function measurements] have confirmed the Cabrera-Mott prediction of a voltage V across an oxide film growing at low temperature’’, work function changes cannot be used to quantify qV_{CM} .

Indeed, many metals display negative work function changes upon oxidation [94, 111], which would suggest that a negative qV_{CM} opposes to the motion of ionic species. This simply ignores that work function variations are due to changes both in band bending and in the surface dipole energy barrier [112], the latter being highly sensitive to surface adsorbates, including water contaminant. As the work function is definitely not a good proxy, Figure III.1(b) shows that the determination of qV_{CM} must rather involve the measurement of the energy distance between E_{F} and the valence band maximum (VBM).

¹Note that qV_{bb} is used to refer to a measured experimental band bending while qV_{CM} would be its value at thermodynamic equilibrium according to the Cabrera-Mott model.

This is just the binding energy of the valence-band maximum, E_{bVBM} .

The strength of the electric field \mathbf{E} directly impacts the oxide growth rate. It is clear from Figure III.1(b) that \mathbf{E} increases (decreases) the jump probability of a cation with a charge number $|z|$ moving towards the oxide/gas (metal/oxide) interface by a factor $e^{\frac{|z|aqV_{\text{bb}}}{2Xk_{\text{B}}T}}$ ($e^{-\frac{|z|aqV_{\text{bb}}}{2Xk_{\text{B}}T}}$), where a is the distance between two minima of the diffusion potential, X the oxide thickness, k_{B} the Boltzmann constant, and T the temperature. A similar picture can be given for a moving anion. Therefore, any change in qV_{bb} will affect the kinetics through the Boltzmann factors here above and, at the same time, the oxide binding energies referenced to E_{F} , such as E_{bVBM} . In principle, such measurements can be performed using valence band or core-level X-ray photoemission spectroscopy (XPS) [112, 113]. In practice, however, it was not until the invention of NAP-XPS [114, 115] that in situ monitoring of oxidation in realistic conditions (from 1 mbar to 1 bar) was possible. Indeed, NAP-XPS enables to make a correlation, in real conditions, between changes in qV_{bb} and the growth kinetics. Therefore, with respect to the in situ experiments of half a century ago that combined smartly the measurement of $q\Phi_{\text{ox}}$ (via the Kelvin probe) with that of the oxide thickness (via a quartz balance) [111, 116–118], present day NAP-XPS provides a much more complete description of the electronic structure of the growing oxide, as E_{bVBM} can be determined, which is impossible with a Kelvin probe. Moreover, the metal/oxide interface chemistry can be monitored in great detail, at least in the initial growth regime when oxide thicknesses compare with the inelastic mean free path, and information can be gained on the species adsorbed at the oxide/gas interface, including contaminants like water. More generally, gas phase oxidation studies have seen a renewal by the implementation of in situ, real-time techniques, like NAP-XPS [119, 120], and environmental high resolution transmission electron microscopy (E-HRTEM) [100].

III.2 Experimental

The experiment was carried out using the NAP-XPS setup of the TEMPO beamline in synchrotron SOLEIL (described previously in detail in Section I.5.1). First, the Al (111) crystal face was cleaned in the preparation chamber of the NAP-XPS setup by cyclic of Ar^+ bombardment followed by annealing in vacuo. The sample was subsequently transferred to the analysis chamber and surface cleanliness was checked with XPS. O_2 gas of purity 99.9995%, was introduced into the reaction chamber through a variable leak valve, and the photoemission spectra were recorded in “swept mode”.

The water content in the O_2 controlled by mass spectrometer set on the second dif-

ferential stage of the analyser lens was less than 3 ppm, but in NAP conditions the coadsorption of water must be considered. As a matter of fact, for $p_{\text{O}_2} = 10^{-2}$ mbar the maximum partial pressure of water $p_{\text{H}_2\text{O}}$ is 3×10^{-8} mbar, and for an oxidation step duration of 600 s, the maximum water dose is ~ 13 L.

The study consists in combining an oxygen pressure program (at 300 K) with real-time NAP-XPS. The oxygen pressure program (at 300 K) consists in four successive oxidation steps of 600 s each under 10^{-6} , 10^{-2} , 10^{-1} and 1 mbar of O_2 pressure p_{O_2} . The reversibility of the observed phenomena is examined after the 1 mbar step, by reducing the pressure to 10^{-1} mbar, and then by pumping the analysis chamber to 10^{-8} mbar. Such programs were previously used to determine pressure dependent kinetics, possibly in relation to in situ work function monitoring using the Kelvin probe [94, 97, 117]. The aim of the 10^{-6} mbar step is to produce an amorphous Al_2O_3 layer of thickness ca 1.5 nm, in conditions similar to the in situ E-HRTEM study of ref. [100]. Thus the conditions to test the Cabrera-Mott model are met, as a continuous film of sufficiently small thickness (< 3 nm) is prepared [94, 96]. Then starting from this low pressure grown film, it is explored how the NAP conditions impact both the oxidation kinetics and the electronic structure.

The monitoring of the Al 2p transformation is central to this study because it enables an estimation of the oxide thickness (see Section B.2.3 of the Appendix B) on the one hand, and because it provides information on the interface chemistry and the value of E_{bVBM} , on the other hand. Thus, the measurement of the Al 2p core level is systematically coupled to that of the secondary electron energy distribution curve (SEEDC) (to get $q\Phi_{\text{ox}}$), to that of the O 1s core-level, or, finally, to that of the valence band spectrum. Moreover, the oxide gap E_g (see section B.4 of Appendix B) is measured from the onset of the band-to-band losses at lower kinetic energy from the O 1s core-level peak [121].

III.3 The electronic band model of the Al/ Al_2O_3 interface

The information on the electronic band structure accessible to XPS is illustrated in Figure III.2. The substrate being a metal, its Al 2p binding energy referenced to E_{F} ($E_{\text{bAl}2\text{p}_{3/2}}^{\text{Al}^0}$) remains constant. In contrast, the E_{b} of Al_2O_3 will change whenever E_{F} moves in the oxide gap, responding to variations in the O_2 pressure. Therefore as in ref. [122], the good proxy to follow changes in qV_{bb} is the Al $2\text{p}_{3/2}$ binding energy of the oxide referenced to E_{F} , $E_{\text{bAl}2\text{p}_{3/2}}^{\text{Al}_2\text{O}_3}$. This is equivalent to follow the binding energy of the valence band maximum E_{bVBM} . Indeed,

$$E_{i\text{Al}2\text{p}_{3/2}}^{\text{Al}_2\text{O}_3} = E_{\text{kcutoff}}^{\text{SE}} + E_{\text{bAl}2\text{p}_{3/2}}^{\text{Al}_2\text{O}_3} \quad (\text{III.3})$$

As illustrated by Figure III.2, $E_{i\text{Al}2\text{p}_{3/2}}^{\text{Al}_2\text{O}_3}$ is unaffected by changes in the position of the Fermi level. Thus, it is an unambiguous proxy to examine intrinsic changes in the surface dipole energy barrier, especially when such changes could be related to varying concentrations of charged adsorbates at the oxide surface, as the Cabrera-Mott model supposes it, or of contaminants unwillingly adsorbed on the surface like water [116]. It should be added that $E_{i\text{Al}2\text{p}_{3/2}}^{\text{Al}_2\text{O}_3}$ is immune from possible charging [11] effects.

III.4 Results

III.4.1 Evolution of the band structure and the oxidation species

Some illustrative NAP-XPS spectra of the successive aluminium oxidation steps during the oxygen pressure program are shown in Figure III.3. In panel (a) the Al $2\text{p}_{3/2}$ core level spectra (the $2\text{p}_{1/2}$ component has been numerically stripped [123], see Section B.2.2 of the Appendix B) are presented. The spectra are measured in surface sensitive conditions at $h\nu = 149.95$ eV, as photoelectrons of kinetic energy (E_{k}) ~ 74 eV have inelastic mean free paths of 0.48 nm in the metal (λ_{m}) and 0.70 nm in alumina (λ_{ox}) [124]. The component corresponding to metallic aluminium, denoted Al^0 , is observed at a constant binding energy value of 72.68 eV. Oxidation components at higher binding energies are also identified, i.e. Al(I), Al(II) and Al(III), positioned at 0.45 eV, 0.88 eV and 1.42 eV, respectively from Al^0 . The increasing chemical shifts are interpreted in refs [125, 126] as due to Al atoms bonded to an increasing number of oxygen atoms, from one to three. The fourth oxide component, shifted by 2.18 – 2.81 eV from Al^0 , is related to amorphous Al_2O_3 . The parallelly acquired SEEDCs are shown in panel (b) against a kinetic energy scale referenced to E_{F} ($q\Phi_{\text{ox}} = E_{\text{kcutoff}}^{\text{SE}}$ in the absence of sample charging).

The Al $2\text{p}_{3/2}$ spectrum of the starting surface in Figure III.3(a) shows it is already (slightly) partially oxidised. This is a consequence of the stay in the NAP-XPS analysis chamber whose base pressure is 10^{-8} mbar. The measured $q\Phi_{\text{ox}}$ for this starting surface is 4.02 eV. This value is only ~ 0.2 lower than the work function of the clean surface in UHV (4.24 [127]–4.26 eV [128]). A 0.2 eV decrease of the work function is reported upon exposure to 50 L of O_2 [129].

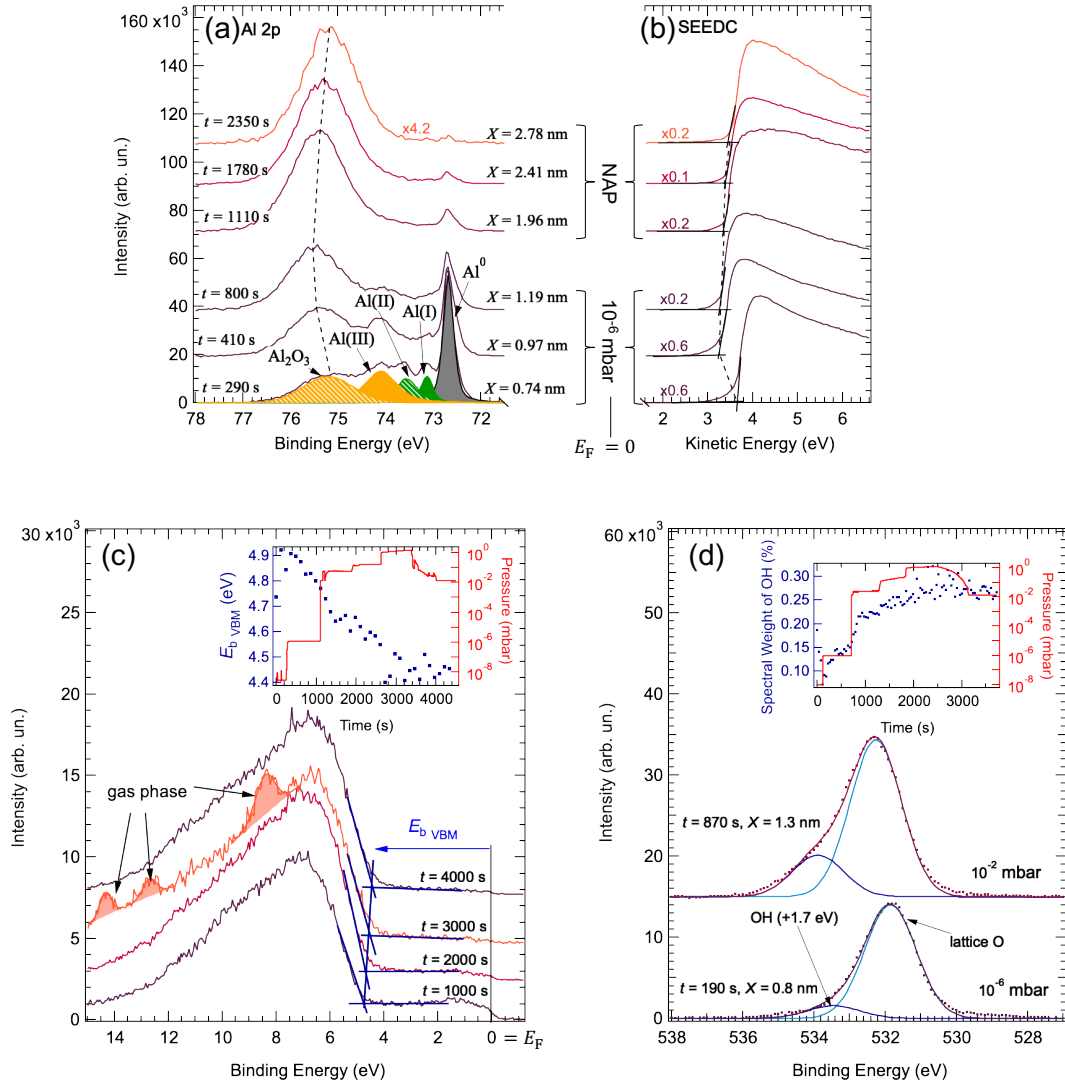


Fig. III.3 (a) Al $2p_{3/2}$ spectra after numerical $2p_{1/2}$ stripping ($h\nu = 149.95$ eV). The “unstripped” $2p$ core-levels are given in Section B.2.2 of Appendix B. The spectra acquired in real time under 10^{-6} mbar and under 10^{-2} , 10^{-1} and 1 mbar (this last one is rescaled in height) are shown. (b) SEEDC curves (rescaled in height) corresponding to the Al $2p_{3/2}$ core-levels shown in panel (a). (c) O $2p$ valence band spectra ($h\nu = 149.95$ eV) and determination of the valence band maximum (VBM) binding energy $E_{b\text{VBM}}$. (d) Illustrative O $1s$ core-levels ($h\nu = 600$ eV). Fits with sums of Gaussians are shown for the Al $2p_{3/2}$ and O $1s$ spectra (in the inset the evolution of the OH/H₂O spectral weight according to the oxygen pressure program). Calculated thicknesses are also indicated.

Valence bands ($h\nu = 149.95$ eV) are presented in panel (c). The O 2p level constitutes the top of the valence band, and its extrapolated leading edge could be used to directly determine E_{bVBM} (inset of Figure III.3(c)), but when changes ΔE_{bVBM} are of concern, the monitoring of $E_{\text{bAl}2\text{p}_{3/2}}^{\text{Al}_2\text{O}_3}$ is more precise. Then E_{bVBM} can simply be obtained from equation (III.2). Note that it is not correct to say that the measured energy value of the valence band maximum corresponds exactly to its value at the oxide/gas interface ($E_{\text{bVBM}} \neq E_{\text{bVBM}}^{\text{o/g}}$). In fact, the measured E_{bVBM} is an average value of $E_{\text{bVBM}}(X)$ which depends on the inelastic mean free path of the photoelectrons in the oxide, λ_{ox} . As discussed in Section B.6 of Appendix B, the real $E_{\text{bVBM}}^{\text{o/g}}$ can be calculated using a correction parameter.

Illustrative O 1s spectra ($h\nu = 600$ eV, $E_{\text{k}} \sim 70$ eV, i.e. in surface sensitive conditions identical to the Al 2p spectra) are shown in panel (d). The O 1s spectrum measured under $p_{\text{O}_2} = 10^{-6}$ mbar is fitted with two components, a major one at a E_{b} of 531.7 eV attributed to O_2^- ions in alumina, and a smaller one positioned at 533.4 eV (14% of the spectral weight at the end of the oxidation step), attributed to surface hydroxyls, or adsorbed water molecules (OH/H₂O) whose E_{b} cannot be distinguished clearly [130].

III.4.2 Growth kinetics

Figure III.4 shows the time evolution of the intensities of the various oxidation components resulting from the fitting of the Al 2p spectra, when the surface is under vacuum or exposed to the p_{O_2} steps of 10^{-6} and 10^{-2} mbar. Once the pressure is increased to 10^{-6} mbar, oxidation starts, as shown by the immediate intensity rise of the Al_2O_3 component. This initial rapid growth is followed by a slower growth. During the rapid growth regime, the Al(I), Al(II), and Al(III) component intensities successively reach a maximum, in this order. The maximum of the Al(III) peak intensity is concomitant with the change in growth rate, and in the successive slow growth regime the Al(I) and Al(II) components almost vanish. While the Al(III):Al⁰ intensity ratio remains constant and equal to ~ 1 , the intensities of both components diminish while that of Al_2O_3 increases. This behaviour suggests that a continuous Al_2O_3 layer is formed at this point ($t \approx 350$ s).

Knowing the intensities of each oxidation component, it is possible to calculate the oxide thickness over time (see section B.2.3 of Appendix B) as shown in Figure III.5(a). Panel (b) shows the evolution of the band structure proxies, $q\Phi_{\text{ox}}$, $E_{\text{iAl}2\text{p}_{3/2}}^{\text{Al}_2\text{O}_3}$, and $E_{\text{bAl}2\text{p}_{3/2}}^{\text{Al}_2\text{O}_3}$ measured during the same “pressure program” at $h\nu = 149.95$ eV. E_{bVBM} is also depicted, knowing that, from the moment when a continuous film is formed (at the end of the oxidation step under 10^{-6} mbar), equation (III.2) establishes $E_{\text{bVBM}} = E_{\text{bAl}2\text{p}_{3/2}}^{\text{Al}_2\text{O}_3} - \text{constant}$.

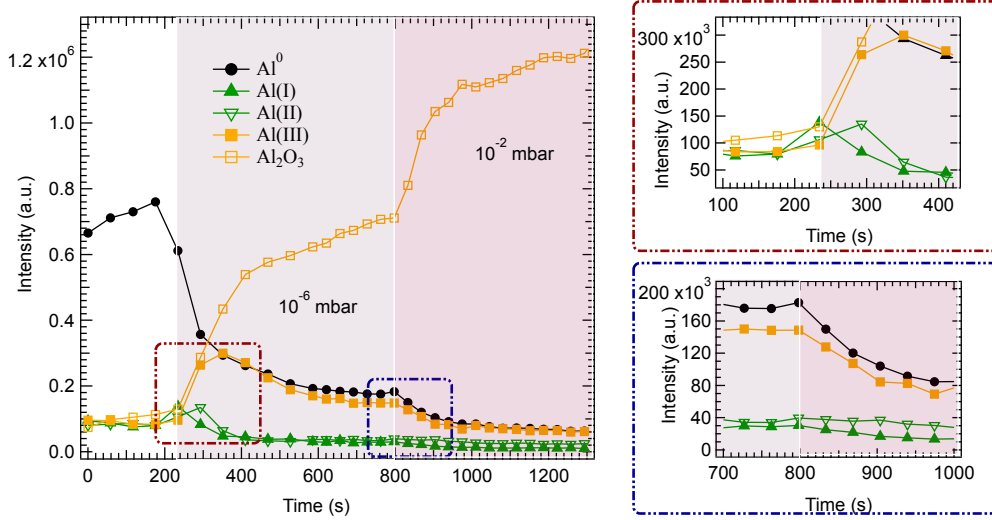


Fig. III.4 Time evolution of the intensities of the various oxidation components of aluminium (Al^0 , $Al(I)$, $Al(II)$, $Al(III)$, Al_2O_3) of the Al 2p spectra, in UHV and when the surface is exposed to the 10^{-6} and 10^{-2} mbar steps. Under 10^{-2} mbar the attenuation of the photoelectron intensity by inelastic scattering in the gas layer is still negligible.

In this case, the constant is worth 70.70 eV (standard deviation $\sigma = 0.04$ eV, see B.3 of Appendix B for its determination).

Figure III.5(a) indicates that the kinetic breakpoint of the above-mentioned initial rapid growth regime corresponds to a thickness $X = 0.8$ nm. Indeed, one can say that a continuous Al_2O_3 layer is formed for $X > 0.8$ nm, with an interface layer characterised by the dominance of the $Al(III)$ component. This observation is coherent with the recent E-HRTEM experiment [100] carried out in the same range of pressure which shows that a continuous, amorphous film of $X = 1.5$ nm covers the Al(111) surface, after an initial rapid growth regime where oxide formation is not uniform. The value of $E_{b_{Al_2O_3}^{Al_2O_3}}^{Al_2O_3}$ is maximal when the continuous film is completed ($X = 1.1$ nm) and reaches 75.49 eV (Figure III.5(b)). This corresponds to a chemical shift of 2.81 eV with respect to the metallic component, in agreement with other low pressure oxidation data [122, 126]. $E_{b_{VBM}}$ deduced from equation (III.2) (Figure III.5(b)), reaches a maximum of 4.79 eV at the end of the 10^{-6} mbar oxidation step. This value coincides with that reported in ref [131] (UHV measurement). For his part, $q\Phi_{ox}$ reaches 3.27 eV at the end of 10^{-6} mbar oxygen step, in excellent accord with ref. [131] (UHV measurement). The large drop in the work function with respect to the clean aluminium value (4.26 eV) can be explained by oxygen species penetrating into Al(111) subsurface sites [100, 132, 133], and by the presence of OH/ H_2O [116] (see Figure III.3(d)).

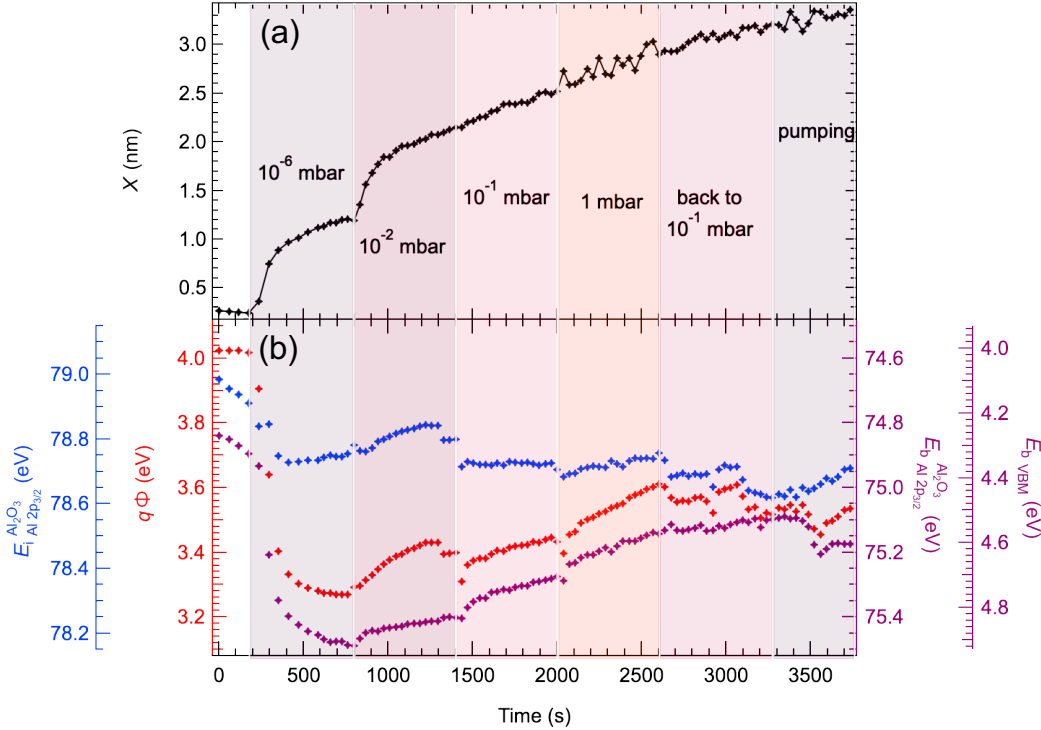


Fig. III.5 (a) Oxide thickness versus time. (b) Time dependence of the measured $q\Phi_{\text{ox}}$, $E_{i \text{ Al } 2p_{3/2}}^{\text{Al}_2\text{O}_3}$, and $E_{b \text{ Al } 2p_{3/2}}^{\text{Al}_2\text{O}_3}$. The binding energy position of the valence band maximum $E_{b \text{ VBM}}$ has also its own scale ($E_{b \text{ VBM}} = E_{b \text{ Al } 2p_{3/2}}^{\text{Al}_2\text{O}_3} - 70.70$ eV, see Section B.3 of Appendix B).

The growth rate r_{ox} , i.e. the time derivative of the oxide thickness X ($\frac{dX}{dt}$) is plotted against X in Figure III.6(a) for X values corresponding to a continuous oxide ($X > 1.1$ nm). Increasing p_{O_2} from 10^{-6} to 10^{-2} mbar increases the growth rate r_{ox} by a factor of 10, from $\sim 5 \times 10^{-4}$ nm s $^{-1}$ (at 1.2 nm) to $\sim 4 \times 10^{-3}$ nm s $^{-1}$. Under 10^{-2} mbar, the kinetic breakpoint is reached at ~ 1.9 nm (Figure III.5) when r_{ox} is reduced to $\sim 8 \times 10^{-4}$ nm s $^{-1}$. The following pressure surges (10^{-1} mbar and 1 mbar) do not lead to marked steps in X ; r_{ox} is little affected ($\sim 7 \times 10^{-4}$ nm s $^{-1}$) while X increases considerably, up to 2.9 nm. Therefore, increasing the pressure makes that the “limiting thickness”, defined by Cabrera and Mott [134] when r_{ox} is 0.1 nm day $^{-1}$ (or 10^{-6} nm s $^{-1}$), is not reached, contrary to what is expected from the effects of a driving force decaying as $1/X$. The growth kinetics strongly suggest that qV_{bb} is an increasing function of pressure and thickness. In this context, the relevance of NAP-XPS in testing the oxidation models will be better appreciated when information on oxidation kinetics will be related to information on the electronic structure.

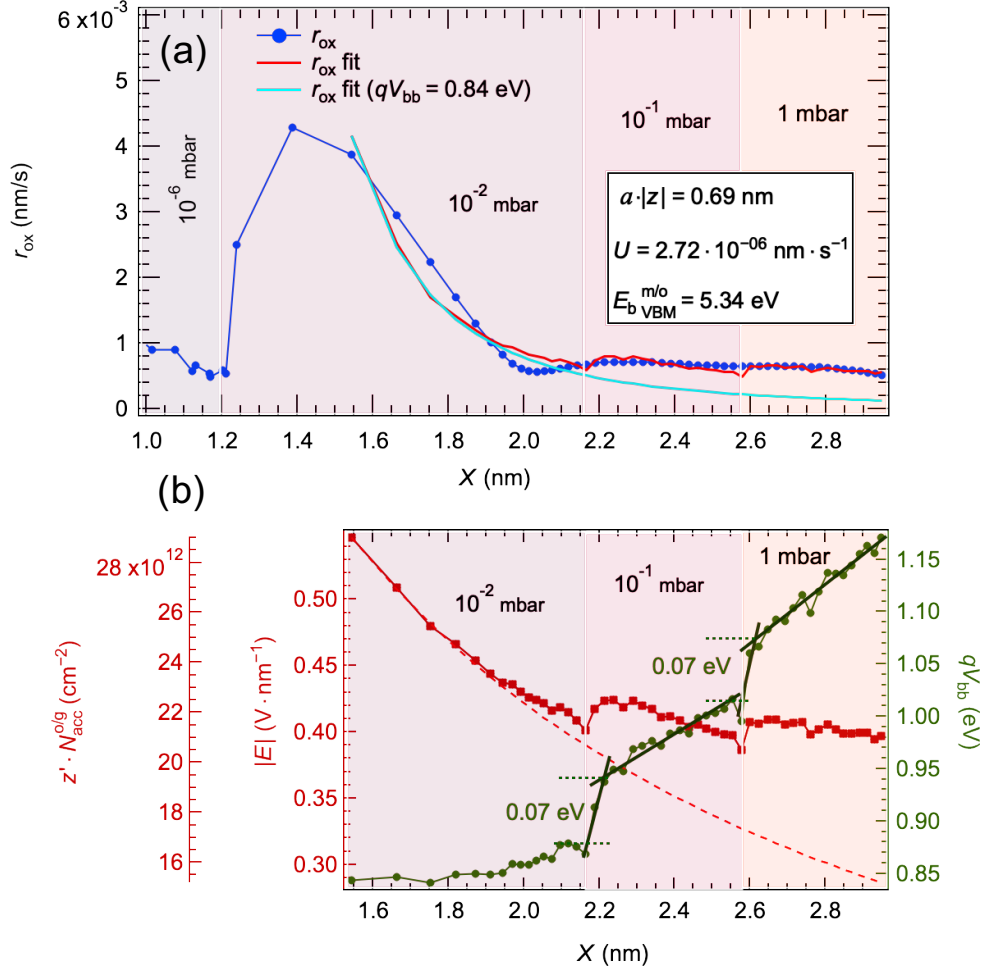


Fig. III.6 (a) Blue dots: oxide growth rate r_{ox} plotted against thickness X . Cyan line: fit of the high-pressure regime using a constant qV_{bb} of 0.84 eV (valid under 10^{-2} mbar for $X = 1.5$ nm). Red line: fit of the growth rate in the high-pressure regime using the Cabrera-Mott rate law (the three independent fit parameters $E_{\text{bVBM}}^{\text{m/o}}$, $|z| \times a$, and U are shown in the box). Panel (b) evolution of $qV_{\text{bb}} = E_{\text{bVBM}}^{\text{m/o}} - E_{\text{bVBM}}^{\text{o/g}}$ and $|\mathbf{E}| = \frac{|V_{\text{bb}}|}{X}$ with pressure and oxide thickness X . The surface density of the negatively charged acceptors $z' \times N_{\text{acc}}^{\text{o/g}}$ (proportional to $|\mathbf{E}|$) has its own scale (left side of the plot). The dashed red curve (0.84 eV/ X) extrapolates the values of electric field calculated at the beginning of the 10^{-2} mbar exposure to the higher pressure ranges.

III.4.3 Discussing the validity of the CM model for the aluminium case

From Figure III.5, it is striking to see that $-E_{\text{bAl}2\text{p}_{3/2}}^{\text{Al}_2\text{O}_3}$ and $q\Phi_{\text{ox}}$ exhibit rather parallel behaviours, specially when moving into the NAP regime (10^{-2} to 1 mbar). Thus, changes in $E_{\text{bAl}2\text{p}_{3/2}}^{\text{Al}_2\text{O}_3}$ (i.e in E_{bVBM}) that are due to pressure surges determine in large part the observed changes in $q\Phi_{\text{ox}}$. However, $E_{\text{iAl}2\text{p}_{3/2}}^{\text{Al}_2\text{O}_3}$ remains the right proxy to follow variations in the surface dipole energy barrier of the oxide (since it is unaffected by changes in the position of E_{F}). These variations are due to the adsorption of molecules or molecular fragments, which accept electron charge (e.g. oxygen anions) or bear a dipole moment (water molecules/hydroxyls). When p_{O_2} varies from 10^{-6} mbar to 10^{-2} mbar, $E_{\text{iAl}2\text{p}_{3/2}}^{\text{Al}_2\text{O}_3}$ increases by about +0.1 eV. At the same time, the O 1s spectrum in Figure III.3(d) shows that the OH/H₂O component increases from 15% to 22% of the spectral weight. At $h\nu = 600$ eV ($E_{\text{k}} \sim 70$ eV), the contribution of the surface plane is about 25% of the spectral weight (see Section B.5 in the Appendix B). Thus, the coverage of OH/H₂O on the alumina film should be of the order of one monolayer! OHs with their protons pointing outward are expected to decrease the surface dipole energy barrier, not to increase it. So, with the observed slight increase of $E_{\text{iAl}2\text{p}_{3/2}}^{\text{Al}_2\text{O}_3}$, passing from 10^{-6} to 10^{-2} mbar, it is admitted that negative oxygen anions are formed on the top of the oxide surface, but their real contribution to the surface dipole energy barrier is masked in part by the increase of the OH coverage. This masking effect was already suggested by Fehlner and Mott [94]:

“The increase in surface potential [i.e. the decrease in qV_{CM}] does not mean that the C-M [Cabrera-Mott] mechanism is no longer applicable. It may simply mean that the potential across the oxide due to oxygen ions is masked by the effect of water dipoles adsorbed at the oxide-gas interface”.

The pressure surges to 10^{-1} and to 1 mbar will further increase the OH contribution to $\sim 25\%$ of the O 1s spectral weight (inset of Figure III.3(d)), which likely corresponds to saturation. Pumping down does not affect the OH/H₂O component weight, therefore the water-related species are tightly bound on the surface. Small drops in $E_{\text{iAl}2\text{p}_{3/2}}^{\text{Al}_2\text{O}_3}$ followed by a recovery, are also clearly seen (Figure III.5) when p_{O_2} increases from 10^{-2} mbar to 10^{-1} mbar (-0.09 eV), from 10^{-1} to 1 mbar (-0.05 eV), and when the gas is pumped down (-0.05 eV). This may be due to positive spikes in the water partial pressure due to opening or closing the leak valve. Water molecules may be released, making H bonds with the surface hydroxyls for a short while, and then leaving it, which makes that $E_{\text{iAl}2\text{p}_{3/2}}^{\text{Al}_2\text{O}_3}$ recovers its value.

Now, the right proxy for studying changes in the band structure that depend on p_{O_2} is $E_{\text{bAl}2\text{p}_{3/2}}^{\text{Al}_2\text{O}_3}$, or equivalently E_{bVBM} . It is clear in Figure III.5(b) that for $p_{\text{O}_2} \geq 10^{-2}$ mbar,

E_{bVBM} tends to decrease. From 10^{-6} mbar to 1 mbar, the overall variation in E_{bVBM} is -0.37 eV. The observed decrease is certainly not due to the mitigation of a charging effect by the elevation of pressure. First, pumping down to high vacuum does not lead to a reversal to the value found at 10^{-6} mbar, as the increase of $E_{\text{bAl}2\text{p}_{3/2}}^{\text{Al}_2\text{O}_3}$ (E_{bVBM}) is only $+0.1$ eV. The evolution under increasing pressure shown in Figure III.5(b) was obtained while biasing the substrate negatively by -20 eV, which is not a favourable situation to collect negatively charged species created in the gas phase (electrons, anions). Second, Ocal et al. [122] have made a similar observation, highly relevant for the present room temperature NAP study. The adsorption of O_2 at 80 K on a thin alumina layer grown on Al(111) also led to a decrease of -0.43 eV in $E_{\text{bAl}2\text{p}_{3/2}}^{\text{Al}_2\text{O}_3}$, a value close to the one found here (-0.37 eV) for a pressure excursion of 6 orders of magnitude at room temperature. Third, the ‘‘staircase’’ behaviour of $-E_{\text{bAl}2\text{p}_{3/2}}^{\text{Al}_2\text{O}_3}$ ($-E_{\text{bVBM}}$) with pressure surges reported in Figure III.5(b) and especially the magnitude of the steps per decade of pressure is nearly equal to the changes in $q\Phi_{\text{ox}}$ observed by Kirk and Huber [117], who used in the late 60s a Kelvin probe to monitor the oxidation of aluminium films in the presence of the gas phase (their data are reported in Section B.8 of the Appendix B). Remarkably, they found that $q\Phi_{\text{ox}}$ increases by ~ 0.3 eV when the pressure increases from 10^{-9} mbar to 1 mbar. The present experiment suggests that the change in $q\Phi_{\text{ox}}$ they observed is essentially due to a change in E_{bVBM} and not to a change in the surface dipole energy barrier.

The question that arises now is the following: is there a driving force (i.e. an electric field) for ions transported through the growing film. In other words, can we prove that a positive qV_{bb} appears in the oxide in the presence of the gas phase? The profiling of the potential would be possible if it were possible to change appreciably the inelastic mean free path λ_{ox} in the oxide, e.g by pushing the photon energy up to the tender/hard X-ray range. This is unfeasible here as the beamline energy range is limited to soft X-rays. With short λ_{ox} values (0.7 nm for a photoelectron kinetic energy of 70 eV) the binding energies of the oxide surface layers have a major weight when binding energies are measured.

However, combining information on the electronic structure (the measured E_{bVBM}) and on the kinetics (shown in Figure III.6) enables to determine the strength of the electric field in the oxide and its response to changes in the oxygen pressure. As stressed earlier, the measured E_{bVBM} is an averaged value that slightly underestimates the real value at the oxide/gas interface $E_{\text{bVBM}}^{\text{o/g}}$ by $\sim 0.2 - 0.3$ eV. The correction to be made is dealt with in Section B.6 of the Appendix B, where the real $E_{\text{bVBM}}^{\text{o/g}}$, is expressed as a function of the measured ‘‘proxy’’ E_{bVBM} knowing the band bending and λ_{ox} .

With $E_{\text{bVBM}}^{\text{m/o}}$ (the binding energy of the valence band maximum at the metal/oxide

interface), the sought built-in potential qV_{bb} states that:

$$qV_{\text{bb}} = E_{\text{bVBM}}^{\text{m/o}} - E_{\text{bVBM}}^{\text{o/g}}, \quad (\text{III.4})$$

The electronic structure data at hand will help to examine whether the CM assumption on the absence of space charge is relevant or not in the present case. If true it will greatly simplify the analysis, as with excess negative (positive) charge distributed at the oxide/gas interface (at the metal/oxide interface) the electric field is uniform throughout the film. This situation occurs when the thickness of a depletion layer w_{d} in amorphous Al_2O_3 (for a given concentration of dopants) is considerably greater than the oxide film thickness X . The measured E_{bVBM} in the range 4.8 eV (10^{-2} mbar) to 4.4 eV (1 mbar) is above mid-gap ($E_{\text{g}} \sim 7.1$ eV), therefore the amorphous oxide is n -type. Donors could be 2+ ionised oxygen vacancies leaving the electrons to the conduction band. The condition $w_{\text{d}} \gg X$ implies that the concentration of donors (and of electrons in the conduction band) is much less than 10^{20} cm^{-3} (see Appendix B Section B.7). It is shown that the density of conduction band electrons is vanishingly small given the large energy distance between the conduction band minimum and E_{F} . Therefore, there is no space charge in the oxide, and consequently $|\mathbf{E}|$ is uniform throughout the oxide layer. $q|\mathbf{E}|$ is worth:

$$q|\mathbf{E}| = \frac{qV_{\text{bb}}}{X} = \frac{E_{\text{bVBM}}^{\text{m/o}} - E_{\text{bVBM}}^{\text{o/g}}}{X}, \quad (\text{III.5})$$

Therefore, the Cabrera-Mott law (1949) that accounts for a field-assisted oxidation rate in all generality can be applied. The rate writes [12]:

$$r_{\text{ox}} = \frac{dX}{dt} = 2 \times U \times \sinh \left(\frac{a|z|q|\mathbf{E}|}{2k_{\text{B}}T} \right), \quad (\text{III.6})$$

with $U = \Omega N \nu_j \exp -\frac{W}{k_{\text{B}}T}$, where Ω is the volume of oxide per mobile ion, N the surface density of mobile ions, ν_j a jump frequency, and W an activation energy for the motion of the ion in the oxide.

From equations (III.5) and (III.6), one obtains:

$$r_{\text{ox}} = 2U \sinh \left(\frac{a|z|(E_{\text{bVBM}}^{\text{m/o}} - E_{\text{bVBM}}^{\text{o/g}})}{2Xk_{\text{B}}T} \right). \quad (\text{III.7})$$

It is assumed that $E_{\text{bVBM}}^{\text{m/o}}$ in equation (III.7) remains independent of X and oxygen pressure. Indeed, the “pinning” of E_{F} at the metal/oxide interface is a reasonable assumption, as the chemistry of the metal/oxide (the Al(III)/Al⁰ ratio in Figure III.4) does not change while the oxide grows. Then the values of the three independent parameters $E_{\text{bVBM}}^{\text{m/o}}$, $a \times |z|$ and U that best simulate the experimental r_{ox} curve are obtained. The derivative form (III.7) is preferred instead of the “integrated” inverse logarithmic function (used by Na Cai et al. [97, 99]) first, because this approximate law is not an asymptotic form of $X(t)$ [135] and, second, because the values of qV_{CM} extracted from the fits depend on the a priori choice of the parameters a , $|z|$, ν_j and Ω .

The growth mechanisms at low pressures and for layers below ~ 1 nm have been addressed in a recent E-HRTEM work [136]. Under 10^{-6} mbar, oxide islands form first at kinks and O atoms penetrate the aluminium lattice (that swells by 21%) in between these islands before amorphisation occurs. Therefore, the mechanisms involved (O diffusion in the metal and oxide nucleation) are not considered by Cabrera and Mott’s approach, which was thought for continuous, stable films. Indeed, it is shown in Section B.9 of Appendix B that under 10^{-6} mbar the fitting parameters of r_{ox} using equation (III.7) are strikingly different from those obtained in the NAP regime (10^{-2} to 1 mbar). Consequently, the discussion of the changes in r_{ox} with pressure and thickness, presented in Figure III.6(a), is limited to the NAP regime.

The cyan curve in Figure III.6(a) is a first attempt to fit r_{ox} keeping qV_{bb} constant (as in the Cabrera-Mott model) at a value of 0.84 eV. This is a rather good fit under 10^{-2} mbar, in the thickness range 1.5 to 2.0 nm. However, the extrapolated value of r_{ox} at $X = 2.9$ nm, under 1 mbar, is $\sim 10^{-4}$ nm s⁻¹, instead of the measured 10^{-3} nm s⁻¹. This shows that qV_{bb} necessarily depends on pressure. The fit that includes the measured E_{bVBM} that decreases with pressure and thickness, is displayed as a red line in Figure III.6(a). Then the values of r_{ox} in the whole pressure range, from 10^{-1} mbar to 1 mbar, are correctly reproduced.

The parameter $|z| \times a$ found from the fit is equal to 0.69 nm. The jump distance is related to the type of atomic transport during oxidation. There are apparently conflicting reports concerning the nature of the species involved in the low-temperature oxidation of aluminium in O₂ atmosphere. On the one hand, a four-point probe scanning tunnelling measurement [137] performed in Yates’ group indicated that the aluminium ion is the only mobile species when oxidation occurs at room temperature. On the other hand, by combining a ¹⁸O marker experiment with medium energy ion scattering analysis, Starodub and Garfunkel [138] demonstrated that oxygen ions are mobile during the oxidation of Al(110) in O₂ at 300°C. In addition, the electric field strength (Figure III.6(b)) and the

discussion below) compares with the fields of anodic oxidation (a typical bias of 125 V for a film of $45 \mu\text{g} \cdot \text{cm}^{-2}$ gives a field of $0.8 \text{ V} \cdot \text{nm}^{-1}$ [139]). During the anodic growth of alumina, both Al^{3+} cations and oxygen-containing anions (e.g., O_2^- or OH^-) are mobile within the oxide [139,140] under high electric field. Consequently, the motion of both ionic species must be envisaged. The experimental pair distribution functions of amorphous alumina show O–O and Al–Al peaks at around 0.28, and 0.32 nm, respectively [141], which would position $|z| \times a$ between 0.56 nm for a mobile O_2^- and 0.96 nm for a mobile Al^{3+} . The value of the parameter $|z| \times a$ obtained in the fitting of r_{ox} (0.69 nm) falls into this range. This validates the fitting procedure but does not allow to favour one mobile species over the other.

The fitting procedure also shows that U can be kept constant at $2.72 \times 10^{-6} \text{ nm} \cdot \text{s}^{-1}$ in the 10^{-2} to 1 mbar pressure range. This means that the surface concentration of the mobile species injected either at metal/oxide or at the oxide/gas interface depends little on pressure (in fact only qV_{bb} depends on pressure). This is understandable if cations are moving, but this would need a further examination if the oxygen anions are also mobile.

After validating the structural parameters of the r_{ox} fit, we can now focus on the energetic information drawn from it (Figure III.6(b)). The fit gives a value of $E_{\text{bVBM}}^{\text{m/o}}$ equal to 5.34 eV, which verifies the necessary condition of being less than the measured band gap (7.1 eV). The values of qV_{bb} are in the 1 eV range, a typical value expected for a CM potential [97, 102, 134]. Considering equation (III.1), at equilibrium $qV_{\text{bb}} = qV_{\text{CM}} = -\frac{\Delta G_{\text{ads}}}{z'}$, where z' is the number of transferred electrons. Therefore, it is interesting to know whether the measured experimental changes in qV_{bb} enter within the thermodynamic framework. Under 10^{-2} mbar and for $1.5 \text{ nm} < X < 2.2 \text{ nm}$, qV_{bb} tends to remain practically constant (it increases by only 0.02 eV). This quasi-constancy while X increases by 0.7 nm contrasts with the outputs of the DFT calculation of O_2 adsorption on the undercoordinated Al atoms of (0001)-oriented $\alpha\text{-Al}_2\text{O}_3$ layers supported on Al(111) [102]. Indeed Baran and coworkers found that ΔG_{ads} increases with increasing thicknesses until it becomes positive above a critical thickness (1.6-1.8 nm under 10^{-2} mbar). This is understandable, as the image interaction felt by the molecular anion decreases when thickness increases (this was the tenet of the Stoneham-Tasker model [142]). Therefore, the quasi constancy of ΔG_{ads} suggests that some reorganisation of the molecule on the surface may occur with time (see below).

For what concerns the pressure dependence of qV_{bb} , Figures III.5(b) and III.6(b) show that each pressure surge, from 10^{-2} to 10^{-1} and then from 10^{-1} to 1 mbar, leads to an immediate jump of ~ 0.07 eV, followed by a slow increase (with time and/or thickness). Considering the sole contribution of $\mu_{\text{O}_2(\text{gas})}$ in qV_{CM} (equation (III.1)), the latter should

vary as $\frac{k_B T}{z'} \ln(p_{\text{O}_2})$, which would correspond to an increase of 0.06 eV when the pressure increases by a factor of 10, assuming that $z' = 1$. Concerning the concentration of adsorbed anions, an increase of an order of magnitude in the pressure leads to an increase in surface concentration by a factor of about ~ 1.05 (Figure III.6(b)), corresponding to a decrease in qV_{CM} of $\frac{k_B T}{z'} \ln 1.05 \approx \frac{10^{-3}}{z'}$ eV (through $\frac{\tilde{\mu}_{\text{O}_2^{z'-}(\text{ads})}}{z'}$ in equation (III.1)), which negligibly contributes to the change in qV_{bb} . Thus, if the qV_{bb} steps measured immediately after the pressure surges can be explained by the thermodynamics of O_2 adsorption, the slow increase that follows (~ 0.05 eV) suggests that ΔG_{ads} slowly decreases with time as the molecule inserts into the amorphous alumina network or even decomposes. This process may take longer times than the experimental duration of the oxidation treatment.

Values of $|\mathbf{E}|$ (the parameter that governs r_{ox} , see equation (III.6)) are found between $0.54 \text{ V} \cdot \text{nm}^{-1}$ and $0.40 \text{ V} \cdot \text{nm}^{-1}$. This corresponds to a regime of high electric field, as $\frac{a|z|q|\mathbf{E}|}{2}$ is ~ 0.17 eV i.e. an order of magnitude greater than $k_B T$. Under 10^{-2} mbar, $|\mathbf{E}|$ practically follows the $1/X$ law expected in the CM model (see Figure III.6(b)), as qV_{bb} remains rather constant while X increases. However, the subsequent pressure surges at 10^{-1} and 1 mbar stop that decay with increasing X (compare the dashed curve in Figure III.6(b) with the actual fit). Indeed, qV_{bb} increases with pressure *and* time/thickness in such a way that $|\mathbf{E}|$ is kept practically constant under 1 mbar.

Commenting the data of Kirk and Huber [117] (see Figure B.6 of Appendix B), Fehlner and Mott [94] already noticed that “an increase in pressure causes the SP [the surface potential, in our case qV_{bb}] and X to increase to new equilibrium values”. When the field is uniform, the concentration of electron acceptors $N_{\text{acc}}^{\text{o/g}}$ with charge number z' at the oxide/gas interface is simply $\frac{\varepsilon_0 \varepsilon_r |\mathbf{E}|}{z' |q|}$ where ε_0 is the vacuum permittivity, and ε_r the relative permittivity of amorphous alumina ($\varepsilon_r = 9.6$). $z' \times N_{\text{acc}}^{\text{o/g}}$, reported in Figure III.6(b), is in the $\sim 2.5 \times 10^{13} \text{ cm}^{-2}$ range in the NAP regime. Using a plate capacitor model and Bader charges differences, Baran et al. [102] calculated that $qV_{\text{CM}} \sim 1$ eV corresponds to an oxygen coverage (O_2^-) of $4.8 \times 10^{13} \text{ cm}^{-2}$ (one of the nine undercoordinated Al atom of the $p3 \times 3$ cell is bonded an O_2 molecule). The coverage provided by the DFT calculation is close to the values reported in Figure III.6(b). However there is no surprise in this agreement because in our case qV_{bb} is also about ~ 1 eV, and because we use the same “condenser” model. Now, for what concerns the detection of the molecular anions by XPS, their density would be about 1/100th of the O^{2-} ion surface (on neutral $\alpha\text{-Al}_2\text{O}_3$ (0001) the density of surface oxygens is $\sim 1.5 \times 10^{15} \text{ cm}^{-2}$, see the SI of ref [102]). This coverage seems too small to be observed as a distinct surface component in the O 1s spectra, independently of the water contamination issue.

III.5 Conclusion

The Cabrera-Mott model has so far been tested essentially by a mathematical analysis of the oxidation kinetics. Electronic structure information obtained under the conditions of oxide growth has long been lacking to highlight what is at the heart of the model, namely the existence of an electric field that facilitates the transport of ionic species. This gap was filled by the present NAP-XPS study, as this approach enabled to relate the kinetics of the oxidation of the Al(111) surface in O₂ atmosphere with changes in the band energies. The key observation is the fact that the Fermi level in the oxide gets closer to the valence band maximum when pressure and thickness increase in the 10⁻² to 1 mbar domain. When the kinetic data (deduced from the changes in the Al 2p core-levels) are associated to the determination of the Fermi level position within the oxide gap, it was showed that the oxide bands are bent upwards, in accord with the core tenet of the Cabrera-Mott model. The spectroscopically-proven formation of a layer of oxygen anions at the surface of the oxide – the second tenet of the Cabrera-Mott model – could not find direct evidence, due to the low concentration of the charged adsorbates. However, the presence of co-adsorbed water was revealed. This is an unavoidable consequence of working in NAP conditions (considering water content in the ppm range in the gas phase). Finally, the observed changes in band bending with pressure and thickness were discussed in detail considering the thermodynamic grounds of the Cabrera-Mott potential. Hopefully, this chapter has been convincing in showing that the NAP-XPS instrument and the real-time electronic level analysis it provides can be profitably used in oxidation studies.

Chapter IV

Band Alignment at a Metal/Redox Solution Interface

The alignment of electronic energy levels at metal/liquid interfaces in the presence of redox species has proven to play an important role in determining the properties and functionality of electrochemical systems. This issue not only attracts a considerable attention, especially at the theoretical level [143–145], but is of utmost practical importance. Examples of this can be seen in the context of functional organic materials [146,147] and, more recently, suspended metallic nanoparticles in solution [148]. The latter case corresponds to a complex system of great interest in colloid science due to its wide variety of applications in chemical, physical, material and biological sciences, and is now possible to study thanks to the significant advances in surface science techniques [149]. In particular, XPS can provide detailed information on the electronic structure of these interfaces.

On this regard, liquid-jets XPS can be thought of as a versatile tool to study not only dissolved chemical species (molecules, ions) but also nano-objects [150], e.g. semiconducting nano-crystals with interesting properties in (photo-) catalysis, in relation to their electronic level alignment with the liquid (water) phase and more specifically with the redox levels [57]. As these experiments are carried out in the liquid phase, in most studies [151] the energy reference is only loosely related to the vacuum level of the solution, measured from water vapour valence band state ionisation energies, but unfortunately affected by uncontrolled variations of the contact potential difference between the liquid surface and the analyser (see Section II.3.1). Indeed, one needs to reference the measured binding energy in liquid experiments (especially in the context of dissolved “solid” nano-objects) to the Fermi level of the analyser, as it is the common practice for solids.

The aim of this work was to provide a way to reference the XPS binding energies in liquid solutions to the Fermi level of the analyser, as is done in the case of solids. On a more general viewpoint and with this in mind, a clear elucidation of the electronic structure at interfaces will lead to a better understanding of electrochemical systems, enabling their performance to be improved.

IV.1 Thermodynamic treatment of the metal/liquid interface in the presence of a redox couple

It is known that at thermodynamic equilibrium, the electrochemical potentials of a solution and of any solid in contact with this solution (i.e. an electrode, ‘dissolved’ solid particles, etc.) should be equal; this is equivalent to saying that their Fermi levels should align (see Section II.1). Under this premise, when doing liquid-jet XPS measurements, it is possible to connect electrically the liquid jet and the XPS analyser and measure the binding energies of the liquid phase component using the common Fermi level as energy reference. This section will explain in more detail the equilibrium governing this principle.

IV.1.1 Ionisation in the solution

Taking into account the equilibrium reaction of a redox couple in a liquid solution,



one can calculate the reaction Gibbs energy (at constant temperature and pressure) of the ionisation of the reduced species as

$$\Delta_{\text{r}}G_{\text{red/ox}}^{\text{sol}} = \tilde{\mu}_{\text{ox}}^{\text{sol}} + \tilde{\mu}_{\text{e}}^{\infty} - \tilde{\mu}_{\text{red}}^{\text{sol}}, \quad (\text{IV.2})$$

where $\tilde{\mu}_{\text{ox}}^{\text{sol}}$ and $\tilde{\mu}_{\text{red}}^{\text{sol}}$ are the electrochemical potentials of the oxidised and the reduced species, respectively, and $\tilde{\mu}_{\text{e}}^{\infty}$ is the electrochemical potential of the electron. Note that the superscript ‘ ∞ ’ indicates that the electron of the ionised species is placed at the thermodynamic vacuum level. If $\tilde{\mu}_{\text{e}}^{\infty}$ is set to zero, all electrochemical potentials can be defined with respect to it. Equation (IV.2) can then be rewritten as

$$\Delta_r G_{\text{red/ox}}^{\text{sol}} = \tilde{\mu}_{\text{ox}}^{\text{sol}} - \tilde{\mu}_{\text{red}}^{\text{sol}}, \quad (\text{IV.3})$$

where $\Delta_r G_{\text{red/ox}}^{\text{sol}}$ is positive and corresponds to an adiabatic ionisation energy.

IV.1.2 Ionisation in the metal

Similarly, we can consider the ionisation of a metal electrode: an electron pertaining to the highest occupied level (this is strictly true at $T = 0$ K) is removed and placed at the vacuum level at infinity. At constant T and p , its ionisation energy will be given by

$$\Delta_r G_{\text{ion.}}^{\text{m}} = \tilde{\mu}_{\text{e}}^{\infty} - \tilde{\mu}_{\text{e}}^{\text{m}}. \quad (\text{IV.4})$$

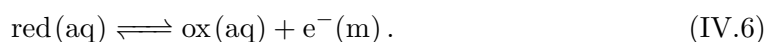
Again, taking $\tilde{\mu}_{\text{e}}^{\infty} = 0$, the ionisation energy simply becomes

$$\Delta_r G_{\text{ion.}}^{\text{m}} = -\tilde{\mu}_{\text{e}}^{\text{m}}, \quad (\text{IV.5})$$

where $\tilde{\mu}_{\text{e}}^{\text{m}}$ is the electrochemical potential of the electron in the metal. Note that having taken the electron at the vacuum level at infinity as reference implies that $\tilde{\mu}_{\text{e}}^{\text{m}}$ positions the Fermi level in the metal. $\Delta_r G_{\text{ion.}}^{\text{m}}$ is therefore the adiabatic ionisation energy.

IV.1.3 Equilibrium between the solution and the electrode

Now we consider the situation in which a metallic electrode is plunged in a solution with a redox couple red(aq)/ox(aq). We assume that the thermodynamic equilibrium is established between the metal and the redox couple that can exchange electrons at the metal/solution interface, following the reaction



where the reaction Gibbs function is given by

$$\Delta_r G = \tilde{\mu}_{\text{ox}}^{\text{sol}} + \tilde{\mu}_{\text{e}}^{\text{m}} - \tilde{\mu}_{\text{red}}^{\text{sol}}. \quad (\text{IV.7})$$

However, at equilibrium, the reaction Gibbs function is zero. Equation (IV.7) can then

be re-written as

$$-\tilde{\mu}_e^m = \tilde{\mu}_{\text{ox}}^{\text{sol}} - \tilde{\mu}_{\text{red}}^{\text{sol}}. \quad (\text{IV.8})$$

which is equivalent to

$$\Delta_r G_{\text{ion.}}^m = \Delta_r G_{\text{red/ox}}^{\text{sol}} \quad (\text{IV.9})$$

Equation (IV.9) indicates that the adiabatic ionisation energies are the same in the metal and in the solution in the presence of a redox couple. In other words, the electrochemical potential of the electron in the metal will be given by the redox potential of the solution. The principle is illustrated in Figure IV.1.

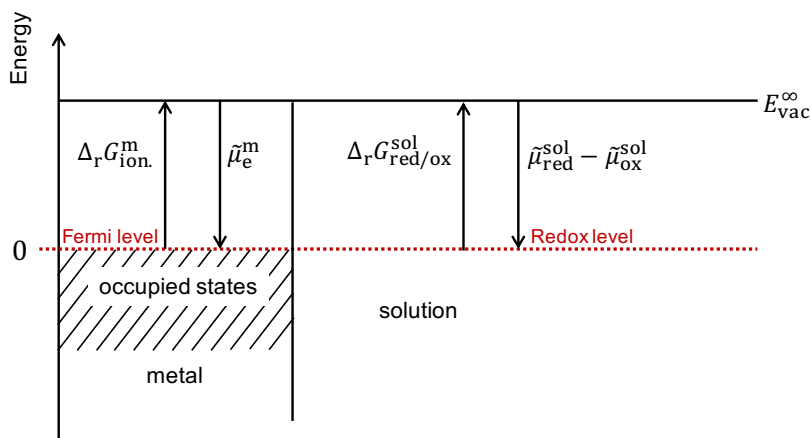
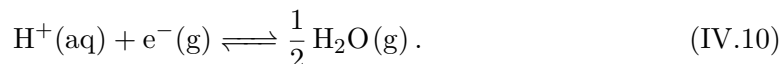


Fig. IV.1 Equilibrium between a metal and a solution with a redox couple.

IV.1.4 The absolute electrode potential

It has now been established that the electrochemical potential of a solution is given by its redox potential. In fact, one could say that these two concepts are identical except for their reference level [56, 78, 152, 153]. This can be made more clear in the light of the concept of the absolute electrode potential.

Since the ultimate thermodynamic reference (the vacuum level at infinity) is not physically accessible, an absolute value of the redox potential is not amenable of direct experimental determination. An accessible reference must be arbitrarily chosen as zero. For the electrochemical scale, the choice was set to the standard hydrogen electrode (SHE) ($E^\circ(\text{H}^+/\text{H}_2) = 0$), which corresponds to the half-cell reaction:



It is possible to convert all relative electrode potential values to an absolute scale if knowing the absolute SHE potential with respect to the universal reference system, the vacuum level at infinity. This has been subject of a thoroughgoing debate. Since 1986, the IUPAC recommendation indicates a value of 4.44 V [154] obtained from a thermodynamic analysis done by Sergio Trasatti¹. However, this result has been quite debated given the fact that its deduction involves the use of the real potential (see Section II.1.1 for its definition) $\alpha_{\text{aq}}(\text{H}^+)$ instead of the standard hydration free energy of the proton $\Delta G_{\text{aq}}^\circ(\text{H}^+)$. Indeed, the estimated $E^\circ(\text{H}^+/\text{H}_2)_{\text{abs}}$ depends on the reference state chosen for the electron. Three different reference states are possible, (i) free electron in the solution, (ii) free electron at rest in vacuum near the surface of the solution, and (iii) free electron at rest in vacuum at infinity, the latter one being the thermodynamic universal reference. Isse and Gennaro [155] remark some inconsistencies involved in Trasatti's calculations and highlight that the IUPAC electrochemical (absolute) scale assumes the electron in vacuum close to the solution surface as the zero level for electron energy. This differs from the vacuum level at infinity by the outer potential $q\phi_{\text{out}}$ of the solution (see Section II.1.1). For this reason, Isse and Gennaro argue that the value given by Trasatti “does not refer to a pure chemical potential of the proton”. The corrected value of the SHE absolute potential is then calculated in their paper on the basis of a thermodynamic cycle involving $\text{H}_2(\text{g})$ atomisation, ionisation of $\text{H}(\text{g})$ to $\text{H}^+(\text{g})$, and hydration of H^+ , obtaining a result of 4.281 V. The conversion of any relative electrode potential to an absolute value can be simply done by

$$-\tilde{\mu} = \Delta_{\text{r}}G_{\text{red/ox}}^{\text{sol}} = 4.281 + E_{\text{SHE}}. \quad (\text{IV.11})$$

where E_{SHE} is the redox potential relative to the standard hydrogen electrode.

The above-explained suggests that if one wants to determine the electronic level alignment at a metal/liquid interface a solution with a precisely known redox potential (i.e. with a well-defined redox couple) must be used. An aqueous solution with no redox molecules (or with a very low concentration of them) will have its electrochemical potential established by what is called the ‘mixed potential’, which is governed by (and very sensitive to) the background reactions taking place within. Percival and Bard [93]

¹According to the definition presented by Sergio Trasatti [154], the absolute electrode potential is the difference in electronic energy between a point inside the metal (Fermi level) of an electrode and a point outside the electrolyte in which the electrode is submerged (an electron at rest in vacuum). This is the same as the electrochemical potential.

illustrated this by performing a series of Open Circuit Potential (OCP) measurements on two $0.1 \text{ mmol} \cdot \text{L}^{-1}$ KCl solutions with increasing concentrations of the redox couple $\text{Fe}^{\text{III}}(\text{CN})_6^{3-}(\text{aq})/\text{Fe}^{\text{II}}(\text{CN})_6^{4-}(\text{aq})$. The two solutions only vary in that they have low (deaerated) and high (air-saturated) oxygen concentrations. For both cases, it is shown that at low concentrations of the redox couple, the OCP is dominated by the mixed potential of the other half reactions taking place within. In the deaerated case, the OCP is dominated by the oxygen reduction reaction (ORR) $\text{O}_2 + 2\text{e}^- + 2\text{H}^+ \rightleftharpoons \text{H}_2\text{O}_2$, while in the air-saturated case, it is the water oxidation reaction (WOR) $2\text{H}_2\text{O} \rightleftharpoons \text{O}_2 + 4\text{H}^+ + 4\text{e}^-$ that prevails. However, at high enough concentrations, the OCP moves toward the formal potential of the redox couple and eventually becomes ‘poised’ at this value. Figure IV.2 shows that, for both solutions, the OCP becomes poised with a value of 430 mV when the redox couple is at a concentration of $\sim 10^{-3}$ M.

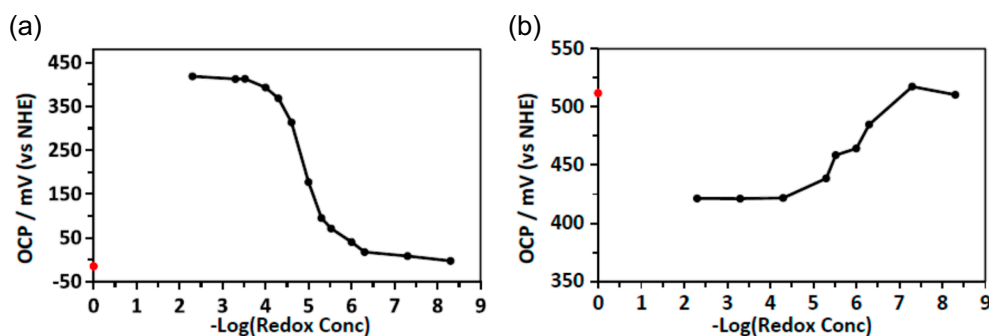


Fig. IV.2 Steady-state OCP values with increasing concentration of added redox molecules $\text{Fe}^{\text{III}}(\text{CN})_6^{3-}(\text{aq})/\text{Fe}^{\text{II}}(\text{CN})_6^{4-}(\text{aq})$ in a $100 \text{ mmol} \cdot \text{L}^{-1}$ KCl solution that is (a) deaerated by actively purging with argon and (b) air saturated. The red point indicates the OCP value when the concentration of the redox couple is vanishingly small. Reprinted with permission from [93]. Copyright 2020 American Chemical Society.

IV.2 Experimental

Based on the principle of Fermi level alignment (equality of electrochemical potentials), the objective of the present work was to measure the binding energies of a liquid phase containing a well-defined redox couple in contact with a metal, referred to the common Fermi level. We were particularly interested in the water valence band maximum (HOMO) and the work function of the sample, in order to be able to calculate the so-called ionisation energy associated to the water $1b_1$ level. Note that for the work function it was necessary to measure the secondary electron energy distribution cutoff (SEEDC) of the solution, as it is done for solid samples. All these elements are depicted in Figure IV.3.

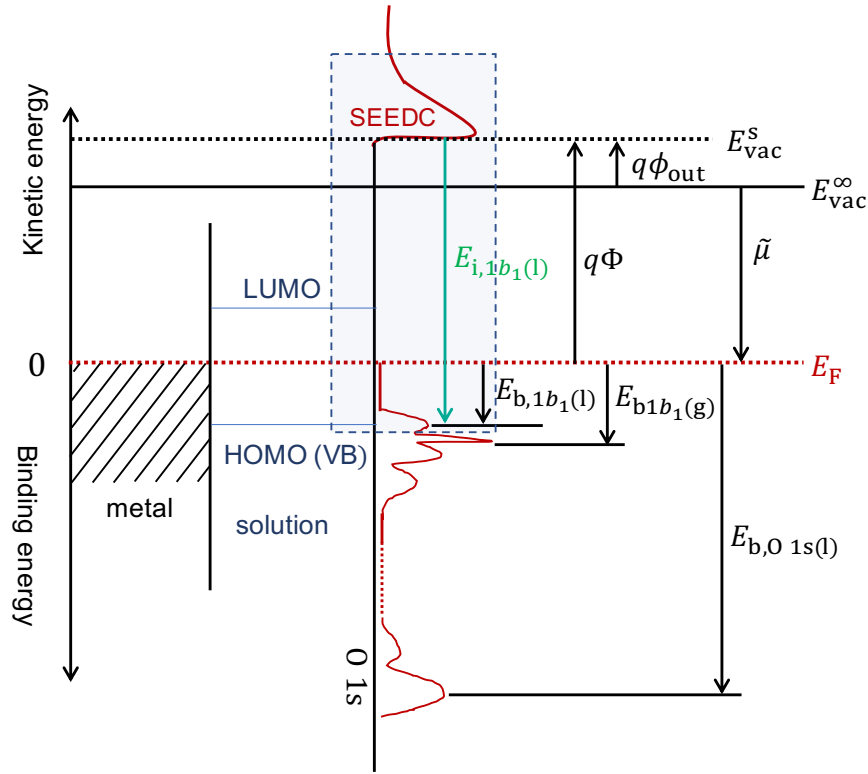


Fig. IV.3 Schematic energy level diagram illustrating the measured elements during the liquid-jet XPS experiment. The difference between the so-called XPS measured ‘binding energy’ E_b (referred to the Fermi level) and the ‘ionisation energy’ E_i (referred to the local vacuum level) becomes clear again. The definition of the ‘outer potential’ $q\phi_{\text{out}}$ is also reminded. In the case depicted here, $E_{\text{vac}}^s > E_{\text{vac}}^\infty$ giving a positive value for $q\phi_{\text{out}}$, but the contrary can also be possible ($E_{\text{vac}}^s < E_{\text{vac}}^\infty$ giving a negative value for $q\phi_{\text{out}}$).

The small section highlighted in the blue box serves to depict what is later shown in Figure IV.9 as a result from the experiment.

IV.2.1 The setup

The experiments were carried at PLEIADES² beamline in the french synchrotron SOLEIL. PLEIADES is an ultra-high resolution soft X-ray beamline that supports a variety of experiments studying photoionisation of dilute matter. It covers the photon energy range of 10-1000 eV with variable polarisation and has three branches providing light for experiments on gases, nanoparticles and liquid jets. The dedicated liquid-jet end-station is equipped with a Scienta R4000 electron analyser.

The introduction of the liquid samples into the jet requires special treatment. All

²Polarised Light source for Electron and Ion Analysis from Diluted Excited Species

solutions are connected via capillaries to a bubbler, which removes the small air pockets present in the line in order to maintain its uniformity. A switch makes it then possible to select the solution which will pass into the jet and change accordingly without having to modify the assembly. When the solution is transported to the analysis chamber, the liquid jet is created by a 40 μm diameter capillary. Once passed through the jet, the solution is recovered in a bottle kept in an ice bath, which allows to take voltammetry measurements that permit to check for the stability of the redox potential after the XPS experiments (see Section C.1 of Appendix C).

As already stated, electrical contact of the jet with the analyser was permanently required, in first place, to make sure that the Fermi levels of the solution and the analyser were aligned, in second place, to make possible the electrical biasing of the jet in order to measure the SEEDC of the sample. For this purpose, an insulated gold-plated ring in contact with the jet was used as electrode. In normal XPS operation, the ring was grounded, as the analyser. Since electrons can be easily transferred from the solution to the metal electrode and vice versa (as it was expected for a clean gold electrode), the Fermi level of the analyser is aligned with the (redox) electrochemical potential of the solution. A picture illustrating the position of this gold ring and the configuration of the jet is shown in Figure IV.4.

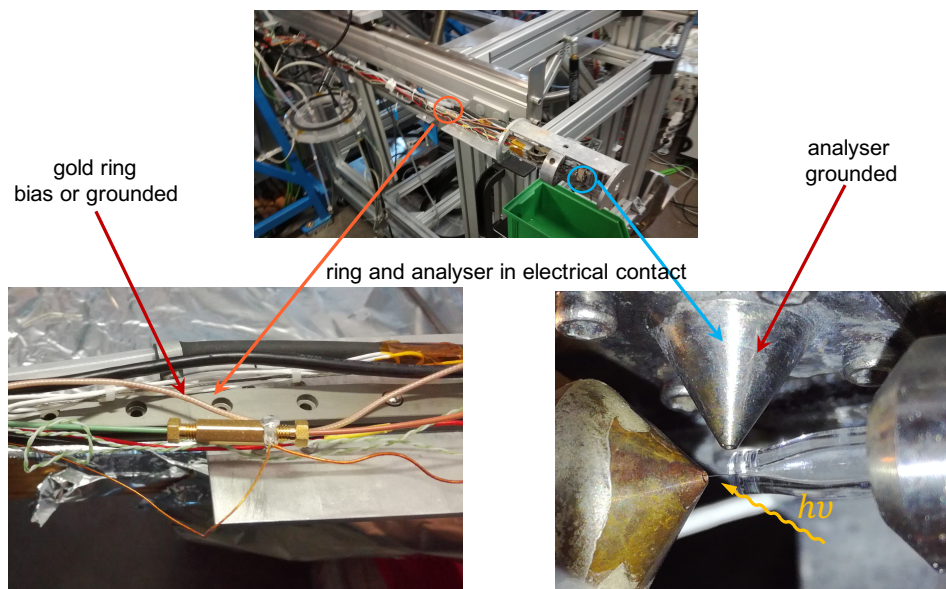


Fig. IV.4 Configuration of the liquid jet setup in PLEIADES beamline.

IV.2.2 Calibration of the spectrometer

In a first step, before performing the liquid-jet measurements, the XPS analyser was carefully calibrated placing a gold wire instead of the liquid jet. Since precision is particularly critical during this procedure, the calibration can be divided in three main steps: (i) precisely determining the true photon energy used during the calibration, (ii) measuring the kinetic energy of the Au 4f_{7/2} peak, and (iii) determining the analyser apparent work function (for a specific pass energy value) as

$$\Phi_a = h\nu - E_{b,\text{Au } 4f_{7/2}} - E_{k,\text{Au } 4f_{7/2}}^a, \quad (\text{IV.12})$$

where $E_{b,\text{Au } 4f_{7/2}}$ is the Au 4f_{7/2} ISO³ standard binding energy for metallic gold used for calibration is 83.95 eV [156].

Although the source was set to a photon energy of 400 eV, the true photon energy was determined by the energy difference between the E_k^a position of the Au 4f_{7/2} peak (with an uncertainty of ± 0.02 eV) in the first and second diffraction order of the monochromator (see Figure IV.5)⁴.

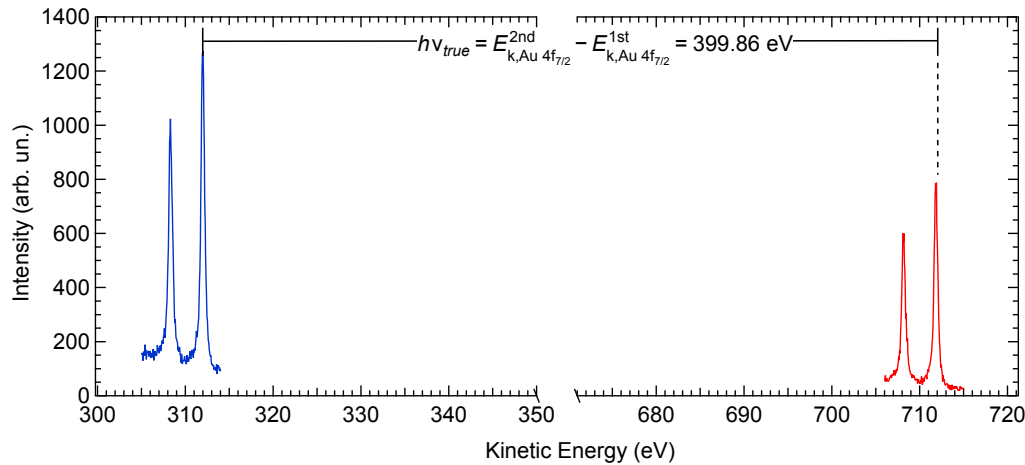


Fig. IV.5 Determination of the true photon energy value using the first and second diffraction order method.

Once the true photon energy value is known, the apparent work function of the analyser was calculated from equation (IV.12) as $\Phi_a = 399.86 - 83.95 - 311.98 = 3.93$ eV for

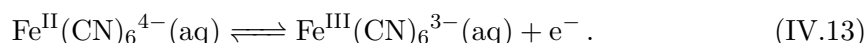
³International Organisation for Standardisation

⁴Note that the directly measured kinetic energy will always be naturally referenced to the vacuum level of the analyser. This is why the superscript ‘a’ is explicitly marked.

a pass energy of 20 eV⁵. Knowing the work function of the analyser allows to calibrate all further measurements with respect to the Fermi level.

IV.2.3 Zobel solution in the absolute scale

As it was imperative to use a solution with a precisely known redox potential, our choice was to work with a commercial ORP (oxidation reduction potential) reference standard⁶ known as ‘Zobell’s solution’. It consists of $3.33 \times 10^{-3} \text{ mol} \cdot \text{L}^{-1}$ $\text{K}_4\text{Fe}(\text{CN})_6$ (source of Fe^{2+} ions), $3.33 \times 10^{-3} \text{ mol} \cdot \text{L}^{-1}$ $\text{K}_3\text{Fe}(\text{CN})_6$ (source of Fe^{3+} ions), and $0.10 \text{ mol} \cdot \text{L}^{-1}$ KCl. Its controlling redox equilibrium is:



For a temperature of 21°C, the Zobell solution has a potential of 0.441 V referenced to the SHE [157, 158]. This was confirmed by the complementary voltammetry measurements done on the solution before the passage through the jet. The OCP SHE value obtained through voltammetry was 0.439 V for a temperature of 22°C. This is in good agreement if one considers the Zobell redox potential’s temperature dependance proposed by Nordstrom [159]⁷.

In the absolute scale, the redox potential at 21°C of the Zobell solution would give a value of the electrochemical potential equal to

$$\begin{aligned} -\tilde{\mu}_{\text{Zobell}} &= \Delta_{\text{r}}G_{\text{ferri/ferro}}^{\text{sol}} = 4.281 + 0.441 \\ &= 4.722 \text{ eV} . \end{aligned} \quad (\text{IV.14})$$

The equivalence between the electrochemical scale and the physical (absolute) scale is better illustrated in Figure IV.6.

⁵Combined with a monochromator slit of 600 μm , this gives a resolution of 100 meV.

⁶ORP standards are generally used for calibration of electrodes to ensure accurate and reliable results.

⁷Nordstrom proposed this formula to calculate the redox potential of Zobell at any temperature, $E(V) = E_{\text{SHE}}^{25^\circ} - 2.5157 \times 10^{-3}(t - 25) - 3.7979 \times 10^{-6}(t - 25)^2$ where $E_{\text{SHE}}^{25^\circ}$ is the potential at 25°C.

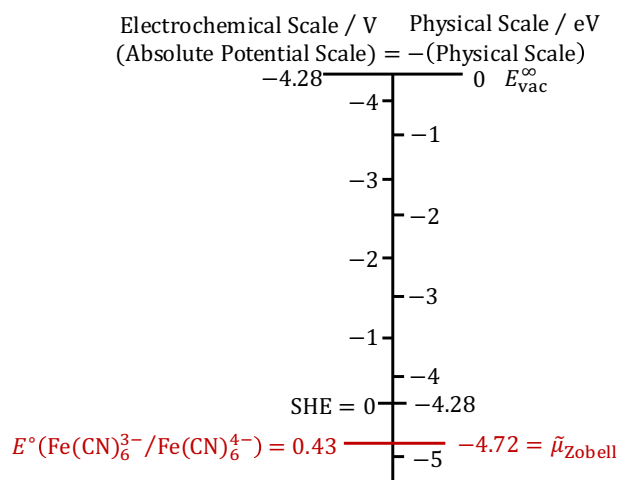


Fig. IV.6 Conversion of relative electrode potentials into electrochemical potentials for aqueous systems.

IV.2.4 Measuring the work function of the liquid sample

As the work function of the analyser was measured during the calibration procedure, the work function of the sample was deduced by measuring the secondary electron cutoff of the sample (recall Figure II.3 from Section II.2.1) and using the equation:

$$q\Phi_s = q\Phi_a + E_{k_{\text{cutoff}}}^{\text{SE}} - E_{\text{bias}}. \quad (\text{IV.15})$$

Note that this procedure relies on the possibility of applying a uniform negative bias to the entire jet. In order to evaluate the reproducibility and precision of the voltage applied, a 0.1 KCl solution was initially tested. The Cl 2p and O 1s core levels were observed as different polarisation values were applied to the sample. Both core-level peaks should have an intense and defined allure as there should not be any parasite signals that could distort our measurements.

The Cl 2p case is shown in Figure IV.7. The spectra were measured at a photon energy of 244.29 eV⁸ and a pass energy of 50 eV. Each curve in the figure is carefully shifted by the exact value of the potential applied in order to measure its position. For

⁸To determine the true photon energies used in the following measurements, the position of the resonance maxima of an element is measured and compared against its reference value. For Ar the reference position is 244.39 eV, for Xe, 674.00 eV, for N₂, 400.86 eV, and for Kr, 91.20 eV

every case, the chlorine 2p structure does not exhibit any noticeable deformation and the deviation values of the Cl 2p_{3/2} peak after correction with respect to the applied bias are within the incertitude of the peak position (see Table IV.1). With a maximum deviation of ± 0.04 eV in the measurement, the Cl 2p_{3/2} peak follows faithfully the bias.

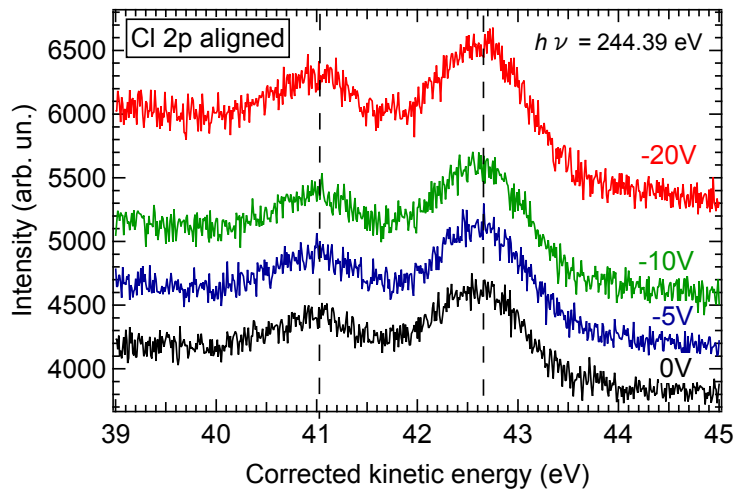


Fig. IV.7 Cl 2p core-level spectra of a 0.1 KCl solution under the effect of several values of applied bias.

Table IV.1: Kinetic energy shifts of the Cl 2p_{3/2} peak as a function of the applied potential. Spectra shown in Figure IV.7.

Applied bias (V)	Observed shift ΔE_k (eV)	Deviation (eV)
-4.98	4.97	0.01
-10.12	10.09	0.03
-20.56	20.52	0.04

The O 1s spectra are somewhat more interesting in that it is possible to see the gas phase peak along with the liquid phase one (Figure IV.8). This is only a natural consequence of the jet being surrounded by water vapour. In this case, the spectra were measured at a photon energy of 673.74 eV and a pass energy of 50 eV. Again, each curve in the figure is carefully shifted by the exact value of the potential applied in order to measure its kinetic energy position and the deviation values are within the incertitude of the peak position (Table IV.2). Note that, while the liquid phase peak remains practically unchanged in shape, the peak at lower kinetic energy corresponding to water vapour experiences an increasing broadening with the bias applied. As explained by Olivieri et. al. [87], this phenomenon is due to the X-ray spot size being broad and not matching exactly the diameter of the liquid jet, so it ionises (in addition to the jet)

all gas phase water molecules between the liquid and the entrance to the analyser. As a consequence, the measured ionisation energies are distributed over a range of kinetic energies (see Figure C.3 in Section C.2 of Appendix C).

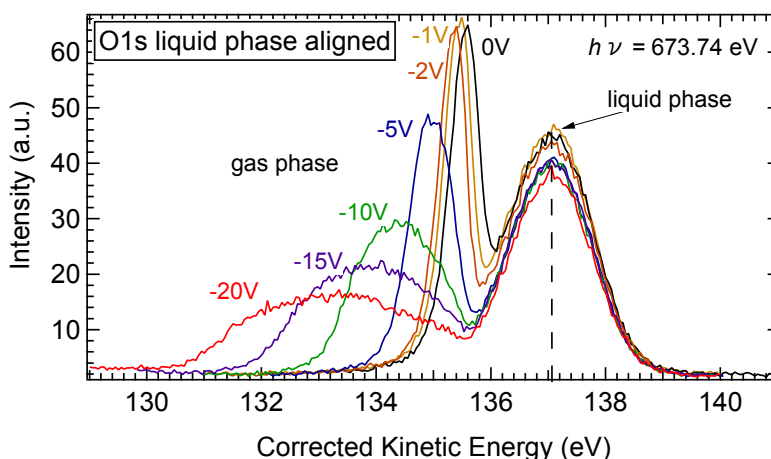


Fig. IV.8 *O 1s* core-level spectra of a 0.1 KCl solution under the effect of several values of applied bias.

Table IV.2: Kinetic energy shifts of the *O 1s* liquid phase peak as a function of the applied potential. Spectra shown in Figure IV.8.

Applied bias (V)	Observed shift ΔE_k (eV)	Deviation (eV)
-1.01	1.00	0.01
-1.98	1.94	0.04
-4.99	4.95	0.04
-10.12	10.07	0.05
-15.22	15.17	0.05
-20.58	20.58	0.00

All the secondary electron cutoffs shown in this chapter were measured applying a bias equal to -20.58 V. The SEEDC was measured in parallel with the corresponding HOMO band of each solution in the same negative bias conditions.

IV.2.5 Measuring the ionisation energy of the $1b_1$ liquid phase peak

If the kinetic energy position of the vacuum level of the sample is known (secondary electron cutoff) and the HOMO band of the liquid phase is measured (see Section IV.3.1), one is able to calculate the ionisation energy associated to the $1b_1$ liquid phase peak

referenced to the vacuum level local to a sample by simply measuring the energy distance between both, as shown in Figure IV.9. The SEEDC was fitted using a classic step function given by the following equation [160],

$$I_{\text{SEEDC}}(E) = H \left(\frac{1}{2} + \frac{1}{2} \operatorname{erf} \left(1.665 * \frac{E - P}{\gamma} \right) \right), \quad (\text{IV.16})$$

where H measures the magnitude of the step, P determines the mid-point (therefore, the position of the $E_{\text{vac}}^{\text{s}}$), and γ describes the broadening of the step⁹. As for $1b_1$ liquid phase peak of the HOMO band, there are two ways to proceed. The first one would be to consider the beginning of the vibrational series, which is given by the tangent to the inflexion point that intersects the zero intensity baseline. The second one would be to pick the centroid of the peak. Both approaches were considered and are discussed in the results section.

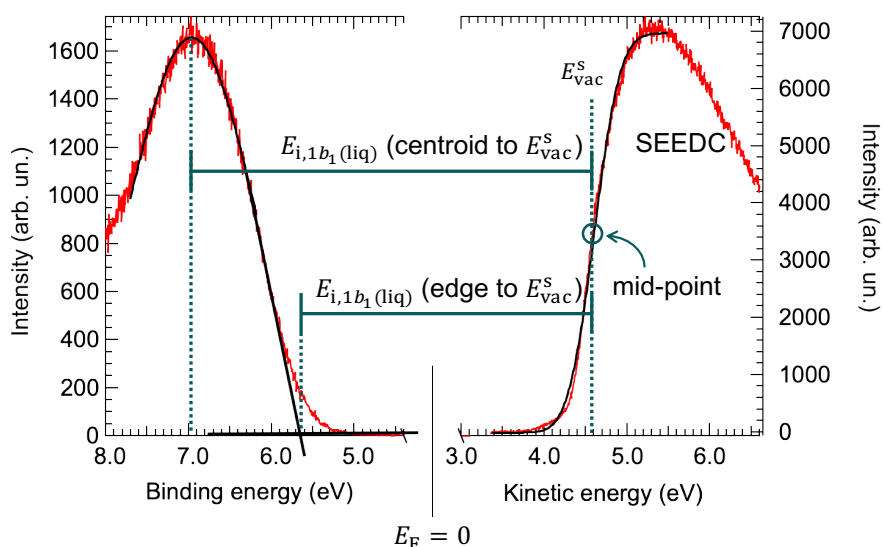


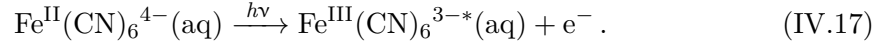
Fig. IV.9 Estimation of the ionisation potential of liquid water via XPS.

IV.2.6 Measuring the reorganisation energy

Note that the photoemission process is so fast that in solution the molecular environment does not have time to reorganise. We are thus dealing with a vertical ionisation process. Taking the specific case of the $\text{Fe}^{\text{II}}(\text{CN})_6^{4-}(\text{aq})$ ions in the Zobel solution, their valence ionisation (t_{2g} states, see Seidel [161]) will lead to a vertical ionisation energy,

⁹This would be the FWHM of a Gaussian resulting from the derivative of the function.

$E_i^{\text{vert}(\infty)}$. $E_i^{\text{vert}(\infty)}$ is a thermodynamic quantity (it is thus referenced to E_{vac}^∞)¹⁰. Naturally, $E_i^{\text{vert}(\infty)} > \Delta_r G_{\text{ferro/ferri}}^{\text{Zobell}}$, because during the photoexcitation process the surrounding molecules have no time to rearrange and find a ‘relaxed’ geometry. The valence photoemission process is represented by the equation



Valence photoemission will transform a ferrocyanide species $\text{Fe}^{\text{II}}(\text{CN})_6^{4-}$ into a ferricyanide* species $\text{Fe}^{\text{III}}(\text{CN})_6^{3-*}$; the star (*) indicates that the nuclei have not relaxed in response to the change in oxidation state. The free energy released by the subsequent reorganisation of the nuclei to the equilibrium configuration of the oxidised state is

$$\lambda_{\text{O}} = E_i^{\text{vert}(\infty)} - \Delta_r G_{\text{ferro/ferri}}^{\text{Zobell}} . \quad (\text{IV.18})$$

Knowing that $\Delta_r G_{\text{ferro/ferri}}^{\text{sol}}$ is the energy distance between the Fermi level and the thermodynamic vacuum level ($E_{\text{F}} - E_{\text{vac}}^\infty$), and $E_i^{\text{vert}(\infty)}$ the energy distance between the position of the t_{2g} valence photoemission state corresponding to the $\text{Fe}^{\text{II}}(\text{CN})_6^{4-}(\text{aq})$ complex and the thermodynamic vacuum level ($E_{\text{Fe } 3d(t_{2g})} - E_{\text{vac}}^\infty$), equation (IV.18) becomes

$$\begin{aligned} \lambda_{\text{O}} &= (E_{\text{Fe } 3d(t_{2g})} - E_{\text{vac}}^\infty) - (E_{\text{F}} - E_{\text{vac}}^\infty) \\ &= E_{\text{Fe } 3d(t_{2g})} - E_{\text{F}} \\ &= E_{\text{b,Fe } 3d(t_{2g})} . \end{aligned} \quad (\text{IV.19})$$

In other words and according to the general definitions and nomenclature used along this thesis, the reorganisation parameter λ_{O} is just the binding energy of the t_{2g} state corresponding to the $\text{Fe}^{\text{II}}(\text{CN})_6^{4-}(\text{aq})$ complex (i.e. the energy referred to the Fermi level). This highlights the interest of actually measuring the Fermi level of the system during a liquid-XPS experiment.

The estimation of λ_{O} via XPS can be explained by the fact that photoemission is, indeed, an oxidation process. One could also think about the exact opposite case, a hypothetical electron attachment experiment (thus, a reduction), for which we would have a vertical electron affinity $E_{\text{ea}}^{\text{vert}(\infty)}$ and a reorganisation energy associated to the reduced

¹⁰The superscript ∞ is added to stress out that the vertical ionisation energy is referenced to E_{vac}^∞ , the thermodynamic reference.

state, λ_R . However, these experiments are difficult to perform and for the moment we will stay with the photoemission case. The relation between all the mentioned parameters is depicted in Figure IV.10.

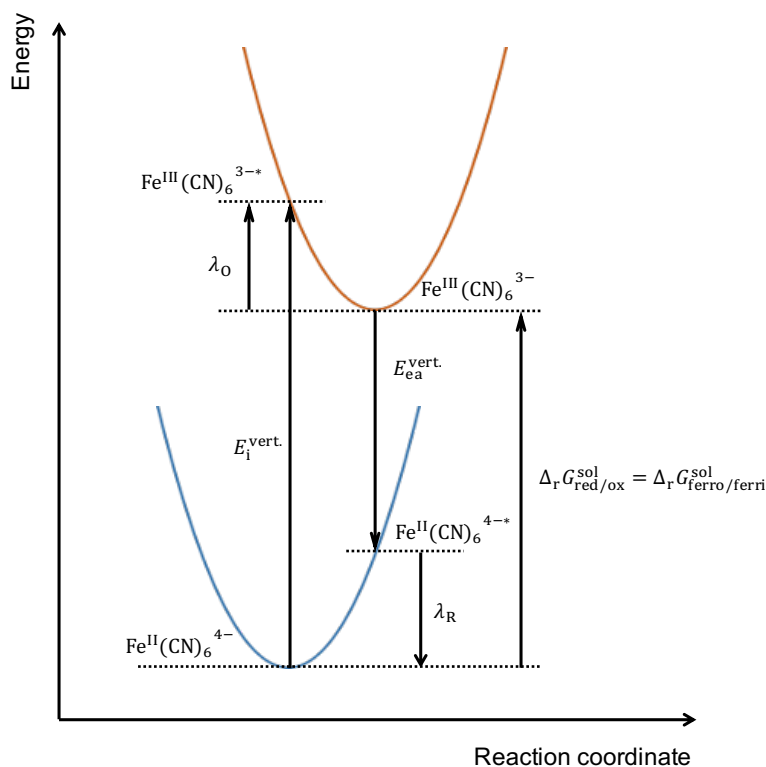


Fig. IV.10 Energy-level diagram for aqueous $Fe^{2+/3+}$ –hexacyano redox pairs illustrating the definition of vertical ionisation energy and reorganisation energy.

IV.3 Results

IV.3.1 Secondary electron cutoff and valence band

Figure IV.11 shows the secondary electron cutoff and the valence band spectra of the Zobell solution compared to a $0.1 \text{ mol} \cdot \text{L}^{-1}$ KCl solution alone, or, in other words, a solution with a well-defined redox potential compared a solution with an unknown redox potential (a mixed potential). The calculated binding and ionisation energies are specified in Table IV.3, as well as the work function (obtained from the position of the secondary cutoff, P parameter of equation (IV.16)), and the width of the SEEDC (γ parameter). Note that the binding and the ionisation energies were calculated using both the edge of

the tangent to the inflexion point intersecting the baseline of the $1b_1$ band ('edge') and the centroid of the Gaussian resulting from a peak fitting. It was also possible to calculate the so-called outer potential $q\phi_{\text{out}}$ from the difference between the work function and the electrochemical potential (see equation (II.5) from Section II.1.1).

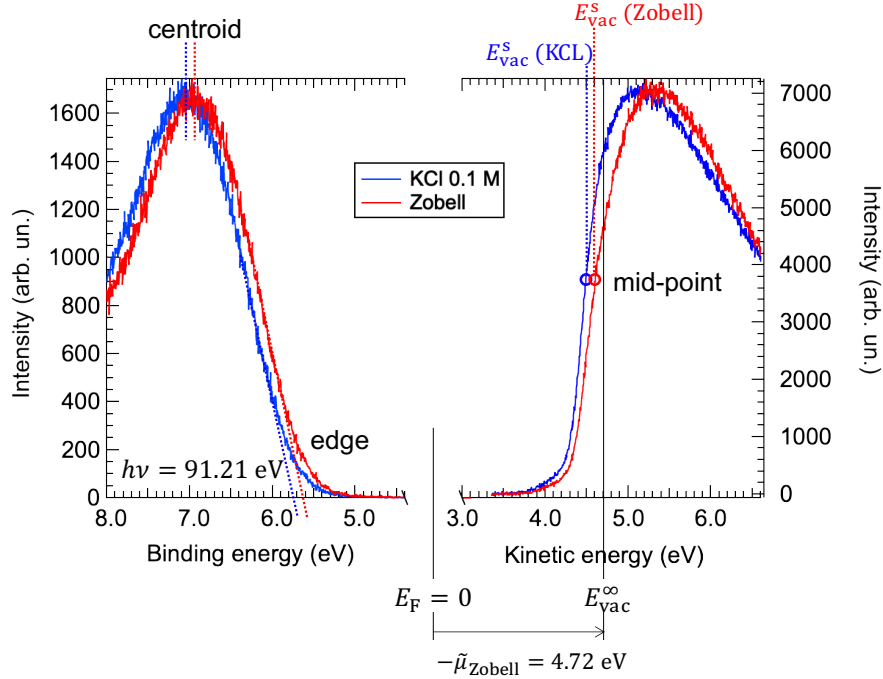


Fig. IV.11 Valence band maximum and secondary electron cutoff of a $0.1 \text{ mol} \cdot \text{L}^{-1}$ KCl solution (blue) and a commercial Zobell solution (red).

Table IV.3: Binding and ionisation energy, work function, width of the SEEDC, and outer potential values for 0.1 KCl, Zobell and Zobell + butanol solutions. All quantities are given in eV.

	KCl	Zobell	Zobell + ButOH
$E_{b,1b_1(\text{liq})}$ (edge to E_F)	5.73	5.66	5.66
$E_{b,1b_1(\text{liq})}$ (centroid to E_F)	7.06	6.94	6.91
$q\Phi$	4.53	4.60	4.43
SEEDC width	0.45	0.58	0.49
$E_{i,1b_1(\text{liq})}$ (edge to E_{vac}^s)	10.26	10.26	10.09
$E_{i,1b_1(\text{liq})}$ (centroid to E_{vac}^s)	11.59	11.55	11.37
$q\phi_{\text{out}}$	–	–0.12	–0.28

The first thing to highlight is that the position of the $1b_1$ is not the same in both solutions. If one refers to the diagram in Figure IV.3, such shift finds its cause in a change in the position of the Fermi level within the gap, which would be expected for different electrochemical potentials. Irregardless of the difference in the $1b_1$ binding energy, the

ionisation energy is equal for both cases. This was expected, given that the ionisation energy is independent of E_F and given also that the HOMO band and the SEEDC were both measured at the same conditions (same photon energy, same negative bias applied). A smaller energy of the HOMO band with respect to the E_F for the KCl solution with respect to Zobell indicates that E_F moves up within the gap (with a shift of ~ 0.1 eV), suggesting that $-\tilde{\mu}_{\text{KCl}} < -\tilde{\mu}_{\text{Zobell}}$. According to Bard et al. [93], this would correspond to a deaerated solution in which the electrochemical potential is dominated by the oxygen reduction reaction.

Using $q\phi_{\text{out}} = q\Phi + \tilde{\mu}$, the estimated outer potential of the Zobell solution is equal to -0.12 eV. In other words, considering the theoretical value of $E^\circ(\text{H}^+/\text{H}_2)$ given by Isse and Gennaro [155] to calculate the absolute electrochemical potential (and therefore the position of the thermodynamic vacuum level), we find $E_{\text{vac}}^{\text{s}} < E_{\text{vac}}^{\infty}$.

The obtained values for $E_{\text{b},1b_1(\text{liq})}$ in this work together with those reported earlier by other authors are summarised in Table IV.4 (see Section II.3.1 of Chapter II for a complete review). It should be noted that when the ionisation energy is calculated using the centroid of the $1b_1$ liquid phase, it differs by 0.43 eV with the one found by Winter and co-workers [82]. The best agreement is found with the more recently determined value by Perry et al. [89] (with a difference of 0.12 eV). Perry and co-workers are also the only ones to report a value using the ‘edge’ method (the tangent to the inflexion point that intersects the zero intensity baseline). Although they refer to it as an ‘adiabatic ionisation energy’ (given that the edge determines the beginning of the vibrational series), careful attention should be paid to the fact that this value does not account for the extra-atomic relaxation term. Therefore, the $E_{\text{b},1b_1(\text{liq})}$ determined using the edge of the $1b_1$ liquid peak should not be referred to as adiabatic. The results presented here are original in that the $E_{\text{b},1b_1(\text{liq})}$ is measured using the SEEDC to accurately determine the position of $E_{\text{vac}}^{\text{s}}$, while the others use the $1b_1$ ionisation energy of the gas phase as reference.

Table IV.4: Electron ionisation energies of liquid H_2O ($E_{\text{b},1b_1(\text{liq})}$). The energies are given in eV. All measurements, except the present one, are made using the $1b_1$ ionisation energy of the gas phase as reference.

	$E_{\text{b},1b_1(\text{liq})}$ centroid	$E_{\text{b},1b_1(\text{liq})}$ edge
This work (2020)	11.55	10.26
Winter et al. (2004)	11.16	–
Nishizawa et al. (2011)	11.23	–
Kurahashi et al. (2014)	11.31	–
Perry et al. (2020)	11.67	10.12

Another feature worth-discussing is the unexpected large broadening of the secondary electron cutoff. When dealing with solid samples it is normal to obtain quite steep cutoffs (if the surface is uniform) with small broadening parameters (γ is usually smaller than 0.1 eV). This was not the case in the present experiment, as for KCl and Zobell γ values of around 0.5 eV are found. A large γ could be indicative of a distribution of the surface potential, meaning that the surface dipole is not uniform along the whole liquid surface. This was already observed by Tissot et al. in their study on the electronic structure of saturated NaCl and NaI solutions in contact with a gold substrate [92], who observed broadening parameters of ~ 0.5 eV and interpreted them as due to thermal fluctuations. Therefore, the obtained $q\Phi$ value can be thought of as a *mean* work function. The broadening parameters presented here strongly contrast with the results from Olivieri et al. [87], who observed substantially narrower rising cutoff edges, with broadenings of around ~ 0.05 (an order of magnitude less).

IV.3.2 Effect of a surfactant

The fact of having obtained identical values for the ionisation potential of the $1b_1$ liquid phase peak in KCl and Zobell solutions would suggest that using the local vacuum level as reference for the calibration of liquid-phase XPS measurements would not be as problematic as explicitly aforementioned in Section II.3.1. However, this is only true if the sample's outer potential $q\phi_{\text{out}}$ remains relatively constant amongst measurements. $q\phi_{\text{out}}$ is in turn dominated by the surface dipole moment. It is only fair enough to wonder if a change in this surface dipole (i.e. a change in $q\phi_{\text{out}}$) would induce a significant difference in the ionisation energy. This change can be provoked by the presence of polar organic molecules in the solution which, in turn, should not change the redox potential. An alcohol fulfils the mentioned characteristics.

Hence, the original Zobell solution was then compared to one with a small quantity of 1-butanol that could act as a surfactant and induce a change in the surface dipole. Despite being soluble in water, alcohol molecules do not ionise in solution; the ionic strength should remain fairly constant meaning that the electrochemical potential should not change. In fact, 1-butanol appears as a more reasonable choice than the butylamine used by Olivieri et al. [87]. Organic bases like amines can dissociate in water and change the pH of the solution. Butylamine not only can have a large effect on the electron density and dipole orientation of the solution interface, as mentioned by Olivieri, but it will definitely induce a change in the redox potential, as well (an effect not considered in the article).

According to Werner [162], a concentration of $64 \text{ mmol} \cdot \text{L}^{-1}$ 1-butanol would ‘maximise’ the induced dipole change in the solution. Due to XPS sensitivity to chemical environment, one is able to distinguish the C 1s line corresponding to the methyl group C_C (lower binding energy) from the line corresponding to the oxygenated functional groups C_OH (higher binding energy), and thus, calculate the $\text{C}_\text{C}/\text{C}_\text{OH}$ ratio. A concentration of $64 \text{ mmol} \cdot \text{L}^{-1}$ leads to the highest $\text{C}_\text{C}/\text{C}_\text{OH}$ ratio, which Werner interprets as the alcohol molecules choosing to point their hydroxyl groups towards the bulk solution, while the alkyl-chains turn towards the vacuum side. At even higher concentrations the ratio decreases again due to the increasing contribution of the surface-near-bulk region, which is increasingly populated with molecules in random orientation.

Although being at a very small concentration, we are able to see a clear signal of butanol in the C 1s core level spectrum shown in Figure IV.12. In our case, the calculated $\text{C}_\text{C}/\text{C}_\text{OH}$ ratio corresponds almost exactly to the expected 3:1 stoichiometric ratio. Werner interprets this as the alcohol molecules at the surface being oriented with their alkyl chain parallel to the aqueous surface plane; thus, all carbon atoms contribute equally to the recorded photoemission signal [162]. However, this affirmation is only valid if the size of the molecule itself and the inelastic mean free path (λ) of the photoelectrons coming from the solution are comparable. Assuming that a molecule of n-butanol has a molecular size of less than 1 nm, and having a rough estimate of $\lambda \approx 3 \text{ nm}$ for photoelectrons traveling in water with a $E_\text{k} = 385 \text{ eV}$ (according to the scale proposed by Ottosson and co-workers [163]), one can judge that it is not possible to deduce the orientation of the molecule by relying only on the $\text{C}_\text{C}/\text{C}_\text{OH}$ intensity ratio.

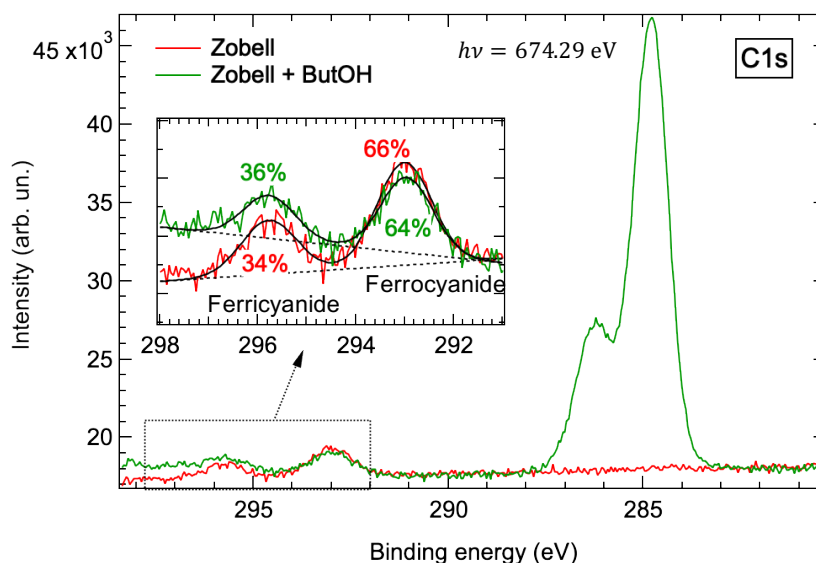


Fig. IV.12 C 1s spectra of the Zobell solution (red) and the Zobell + butanol solution (green).

If the molecule lies flat on the water surface, this would be contradictory with the Monte Carlo simulations performed by Chen et al. [164] who found substantial changes in the bonding and orientation of interfacial butanol and water in mixtures of butanol saturated in water and water saturated in butanol, as compared to neat solutions of either chemical. Their conclusion that the surface orientation of butanol is more perpendicular for small amounts of butanol in water than for neat butanol is consistent with evidence from surface potential experiments [165].

Figure IV.12 also illustrates the C 1s peaks associated to the cyano group in the ferrocyanide (292.95 eV) and ferricyanide (295.77 eV) complexes. Although both species have the same concentration and the peaks should have a 1:1 ratio, gaussian fitting reveals a major proportion of the $\text{Fe}^{\text{II}}(\text{CN})_6^{4-}$ complex, giving a $\sim 2:1$ ratio. Nevertheless, this does not have an impact on the reported redox potential, as evidenced by calculations that show that for a $\sim 2:1$ ratio the change in the redox potential is negligible. This is confirmed by the voltammetry measurements performed on the solutions before and after the passage through the jet that indicated a constant redox potential referred to the SHE of 0.439 V (for a temperature of 22°C, which is in agreement with a value of 0.441 V for 21°C).

Figure IV.13 shows the secondary electron cutoff and the valence band spectra of the Zobell solution compared to the Zobell + butanol solution. The calculated binding and ionisation energies can be found in the preceding Table IV.3. The general structure of the $1b_1$ band appears to be mildly affected by the presence of butanol, although there what it seems to be the presence of a new peak on its right side. The binding energy position of this new feature (~ 5.4 eV) agrees well with the reported value for the Cl 3p valence level [166]. The fact that we are able to see it only after the addition of butanol to the solution can be related to a redistribution of anions close to the vapour/gas interface.

In fact, segregation of ions in aqueous solutions has been well studied before. MD simulations show that big polarisable ions like Br^- and I^- tend to segregate at the water/vapour interface, while the cations are repelled away. In the case of the smaller Cl^- , the anion does not accumulate at the interface (see Jungwirth and Tobias [167]). This was confirmed by the NAP XPS study of Tissot *et al.* [168], and it explains the absence of a Cl 3p peak before the addition of 1-butanol.

Nevertheless, the enrichment of Cl^- ions at the surface after dissolution of the alcohol contrasts with previous calculations and XPS measurements on the effect of butanol with KI solutions. In fact, the increased iodide/potassium ratio at the liquid-vapour interface observed in aqueous KI solutions is suppressed upon the addition of butanol, as seen

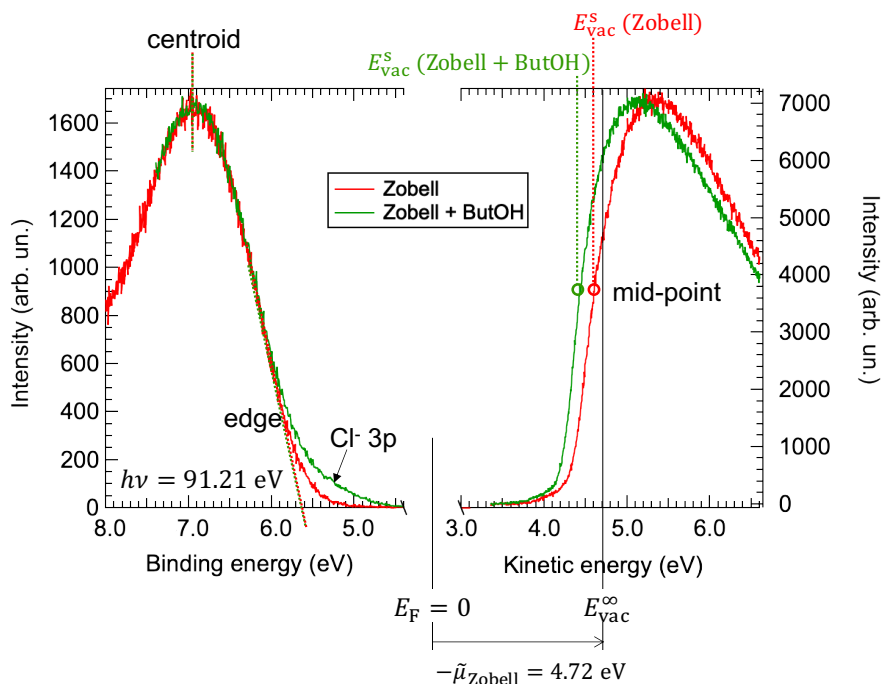


Fig. IV.13 Valence band maximum and secondary electron cutoff of the Zobell solution (red) and the Zobell + butanol solution (green).

in I/K ratios from XPS experiments and MD simulations (see Figure 6 in [169]). The authors find two reasons to explain this effect: (i) the strong interaction between the 1-butanol molecules and both ions, (ii) the fact that alcohol molecules for the most part sit on the interface with their OH groups pointing toward the bulk of the solution, so that ions are displaced away from the organic-vapour interface to interact directly with the alcohol hydroxyl groups [169].

Despite the presence of the Cl 3p feature, the position of the $1b_1$ liquid peak remains constant, which confirms the fact that the electrochemical potential remains unchanged, as well. The calculated ionisation energy (edge) has now a value of 10.10 eV (-0.16 eV compared to pure Zobell) due to a decrease in the solution's work function. This was already observed by Dynarowicz [165], who measured the changes of the electric potential on the surface of several n-butyl alcohol isomers solutions with varying concentration. Using the dynamic jet method (described here [170]), Dynarowicz observed that all investigated compounds (including n-butanol) decrease the natural surface potential of water. For a concentration $\sim 64 \text{ mmol} \cdot \text{L}^{-1}$ of n-butanol, this decrease corresponds to ~ 200 mV (see Figure C.4 of Appendix C), a value comparable to what we obtain via photoemission if one considers the uncertainty limits ($\Delta q\Phi = -0.16 \pm 0.10$ eV, see Table IV.3). Dynarowicz also estimates the n-butanol surface density (total of molecules adsorbed on

1 cm²) corresponding to this surface potential to be more than 2×10^{12} cm⁻² (see Figure C.4 of Appendix C).

IV.3.3 Reorganisation energy

The valence photoemission spectrum of the Zobell solution is shown in Figure IV.14. Following the interpretation of Seidel et al. [161], the observed peaks can be assigned to the Fe 3d(t_{2g}) levels (see Section C.4 of Appendix C for a short description of the octahedral crystal field theory). The peak at $E_b = 1.54$ eV would correspond to the spin-paired Fe^{II}(CN)₆⁴⁻ complex (Fe²⁺ oxidation state), while the peak at $E_b = 2.95$ eV corresponds then to the Fe^{III}(CN)₆³⁻ one (Fe³⁺). As stated before in Section IV.2.6, the binding energy of the Fe^{II}(CN)₆⁴⁻ complex is equal to the free reorganisation energy of the oxidised state (necessary to go from the excited state Fe^{III}(CN)₆^{3-*} to the relaxed state Fe^{III}(CN)₆³⁻), so $\lambda_0 = 1.54$ eV.

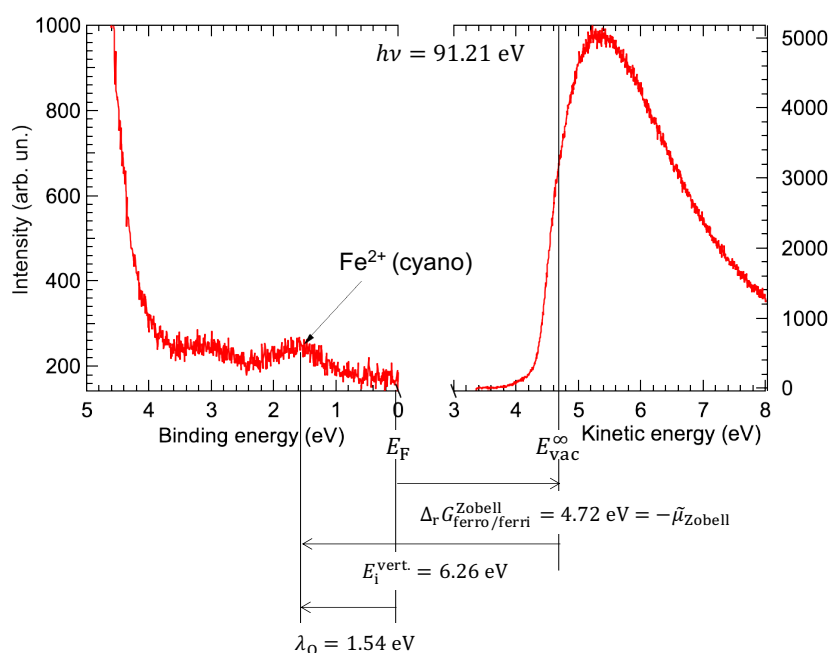


Fig. IV.14 Fe 3d valence level and secondary electron cutoff spectra of the Zobell solution.

Seidel and co-workers had already reported on the reorganisation free energies of the oxidised states in aqueous Fe^{2+/3+}-hexacyano redox pairs [161]. Via XPS, they report a value of the Fe^{II}(CN)₆⁴⁻ vertical ionisation energy (denoted ΔE_R in their case) equal to 6.11 eV. In their case, they use $\Delta G^\circ = 4.64$ eV for the absolute oxidation free energy (i.e. adiabatic ionisation energy), which is obtained by introducing the corresponding

standard redox potential of the ferro/ferri pair (0.36 eV) in equation (IV.11), although there is no well-defined redox couple in the solution, only the $\text{Fe}^{\text{II}}(\text{CN})_6^{4-}$ complex. The reorganisation parameter is simply deduced as the difference between both values as $\lambda_{\text{O}} = \Delta E_{\text{R}} - \Delta G^{\circ} = 1.47$ eV. Seidel's procedure, however, relies on an energy-scale calibration using the water $1b_1$ liquid peak at 11.16 eV as internal reference, which, in its turn, was determined using the $1b_1$ gas phase peak at 12.6 eV as external reference (see ref. [82]). This procedure assimilates E_{vac}^{∞} with $E_{\text{vac}}^{\text{s}}$ and does not take into account the contact potential difference between the liquid jet and the analyser (ΔE_{vac}), as already discussed in Section of Chapter II. Because E_{vac}^{∞} and $E_{\text{vac}}^{\text{s}}$ are close in energy (to 0.1 eV), the estimate given by Seidel et al. of λ_{O} is close to the value we measure directly from the XPS spectrum (to 0.1 eV) referenced to the Fermi level.

The reorganisation parameter is obtained in a more straightforward way by directly measuring the Fermi level of a metal electrode in contact with the analyser, as λ_{O} is simply the binding energy value of the Fe(II) valence state.

IV.4 Conclusion

The present experiment served to show that the measurement of core-level binding energies E_{b} of liquid solutions with respect to Fermi level can be performed, as it is commonly done for solids. For the first time, we have measured the binding energy of liquid water HOMO with respect to a solution redox/Fermi level; in other words, we have positioned the redox/Fermi level within the gap of water. We have illustrated the crucial importance of adding a known redox couple in the solution when XPS is performed. This is a breakthrough in the XPS approach, although well-known in electrochemistry.

Then, we have confirmed previous observations [92] concerning the shape of the secondary electron energy distribution cutoff. The step is wide ($\gamma = 0.5$ eV), much more than for solids. We have defined the position of the vacuum level in the vicinity of the surface by using the mid-point of the step. This approach seems valid as the ionisation energies calculated using it are very close (to 0.1 eV) to the ones determined using the $1b_1$ gas phase calibration method.

It is also remarkable that the mid-point of the SEEDC step is also close (to 0.1 eV) to the thermodynamic vacuum level E_{vac}^{∞} calculated using the measured electrode potential and the reference Gibbs energy of the H^+/H_2 couple given by Isse and Gennaro [155]. To our knowledge, it is the first time that the position of surface electrostatic potential is compared to the thermodynamic reference level for a given redox couple.

The advantage of using the $\text{Fe}^{\text{II}}(\text{CN})_6^{4-}/\text{Fe}^{\text{III}}(\text{CN})_6^{3-}$ couple is even more visible when we look for the determination of the reorganisation energy of the Fe^{III} species, as λ_{O} is simply equal to the binding energy of the reduced state $\text{Fe}^{\text{II}}(\text{CN})_6^{4-}$ with respect to E_{F} . This circumvents approximations that one must make in the absence of the Fe^{III} partner (a guess on the adiabatic ionisation energy) based on the standard energy of oxidation, and the assimilation of the surface vacuum level $E_{\text{vac}}^{\text{s}}$ with the thermodynamic reference E_{vac}^{∞} .

Using a commercial ORP reference standard, the Zobell solution, we were able to illustrate how two different phenomena, namely, (i) a change on the electrochemical potential, (ii) a change on the surface dipole, can affect the measured ionisation energies.

Inspired by the work of Bard et al. [93], this work illustrates that uncontrolled changes in the HOMO E_{b} of liquid water during XPS measurements of solutions in electrical contact with spectrometer (equilibrium) are eliminated by the presence of a well-defined redox couple. This is the first attempt to apply the common calibration methodology of solid samples to liquid samples in thermodynamic equilibrium with a metal electrode (in equilibrium with the analyser as well). The hypothesis earlier developed in Chapter II referring to the inconvenience of using $E_{\text{vac}}^{\text{s}}$ as reference given by the gas phase valence ionisation energy of water is confirmed, as $E_{\text{vac}}^{\text{s}}$ can be affected by adsorbates that modify the surface dipole energy barrier in liquid water (and, thus, the contact potential difference between the sample and the analyser). Although this has been known long ago [92], it was demonstrated in the present experiment when a small quantity of a surfactant (butanol) was added to the Zobell solution, inducing a change in the work function of the sample as a result of the surface dipole modification (although it has been known long ago).

Chapter V

A Model Surface to Study Hydrogen Bonding and Energy Shifts

Silicon is a group-IV element extensively used to fabricate solid-state devices in the industry of computers and microelectronics. Its dominant presence in the semiconductor industry can be attributed to its abundance and low cost, but mostly due to the high quality of the Si/SiO₂ interface (this is, its chemical and electrical stability). Much work has been devoted to the modification of SiO₂ surface by grafting molecules via OH groups in order to functionalise Si substrates. However, practical issues affect the homogeneity and stability of many organic layers grafted on SiO₂ [171]. This is why, later efforts have been focusing in grafting functional molecules on oxide-free Si surfaces. Although much of the attention has been given to H-terminated Si(001)-2×1, water-terminated Si(001)-2×1 offers alternative features.

(H,OH)-Si(100)-2×1 has strong similarities with H-terminated Si(001)-2×1 due to the presence of monohydrides and dangling bonds. However, it is the presence of hydroxyls that opens the way to interesting possibilities for grafting organic molecules [172, 173] or for reacting organometallic molecules [171, 174–176] to ensure the growth of high-permittivity oxides directly on the silicon substrate, in the context of atomic layer deposition (ALD). The key step in ALD is the formation of the first layer of organometallic adsorbates that systematically involves the breaking of the O-H bond of the surface hydroxyl. To facilitate the completion of the first layer, ammonia and amines must be considered as catalysts of the reaction, as the O-H bond is weakened by the ammonia/amine making an acceptor H bond with the surface hydroxyl. This scheme is widely used in silica deposition by ALD [177–179].

These practical considerations led us to perform studies on the reactivity of the water-saturated Si(001) surface by exposing it to two Lewis bases, trimethylamine (TMA) and ammonia (NH_3), at cryogenic temperatures. By combining experimental and ab initio core-level photoelectron spectroscopy (quantum chemistry calculations), the nature of the bonding of each molecule with the surface is revealed. It was expected to observe distinctive features among the two cases given the fact TMA is a tertiary amine that can only make acceptor H bonds, and it has a greater basicity than NH_3 as well.

V.1 The clean Si(100)- 2×1 surface

Silicon crystallises in a face centred cubic (fcc) structure with a two atom basis, also known as the diamond structure. If the silicon crystal is cleaved along the (100) crystal plane, two dangling bonds are left exposed in a highly unstable configuration. To minimise the surface energy, the dangling bonds of adjacent surface atoms pair to create a dimerised, row-ordered surface. This rearrangement was first observed by Schlier and Farnsworth in 1959 in a low energy electron diffraction (LEED) experiment [180], and is known as the Si(100)- 2×1 reconstruction.

One interesting feature of the reconstructed surface is that, due to electronic effects, the dimers are buckled, meaning that one of the atoms is raised slightly above and the other one moved slightly below [181], as shown in Figure V.1. There is a redistribution of the electron density making the up atom negatively charged (nucleophilic silicon atom) and the down atom positively charged (electrophilic silicon atom). It is now accepted that each asymmetric surface dimer has a bond length of $2.24 \pm 0.08 \text{ \AA}$ and an angle of $19 \pm 2^\circ$ to the surface plane [182]. This buckling is observable at 0 K by STM as the dimers are said to be “frozen” [183]. At room temperature, the buckling is dynamic.

V.2 The water-terminated Si(100)- 2×1 surface

The water-terminated Si(001) surface, denoted (H,OH)-Si(001), results from the dissociative adsorption of water on the clean dimerised surface. The Si-Si dimer remains intact when the exposure is made at room temperature [123, 185], as the oxygen insertion process in dimer bonds or in back bonds is only effective at a higher temperature (as shown by scanning tunnelling microscopy (STM) [186]), while the dangling bonds are decorated by OH and H fragments, each having a coverage of half a monolayer (ML) (one ML corresponds to $6.8 \times 10^{14} \text{ atoms} \cdot \text{cm}^{-2}$). The spatial arrangement of the SiOH

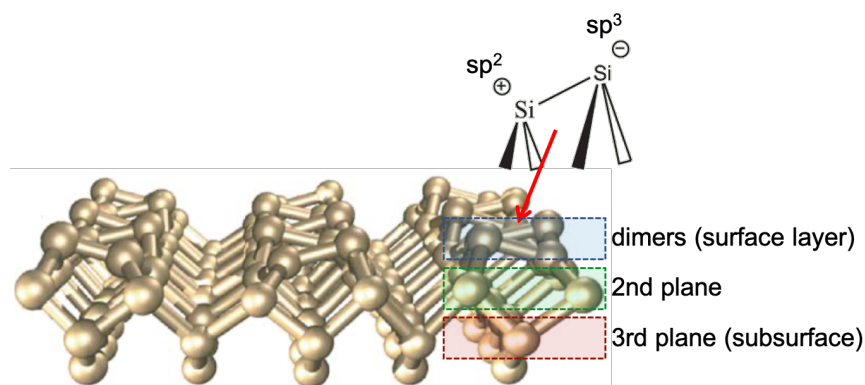


Fig. V.1 The dimers of the $\text{Si}(100)\text{-}2\times 1$ surface reconstruction. Modified with permission from [184]. Copyright 2020 Elsevier.

and SiH moieties has been extensively studied using STM [186–189]. The hydroxyls can be found aligned along the same side of the dimer row in “striped patterns” (SP), or can form checkerboard patterns (CBP), as shown in Figure V.2. Due to the competition between on-dimer and intra-row (inter-dimer) dissociation paths [190–192], two OH (and conversely two H) can also sit on the same dimer (ODIM paired OHs); this occurs on the average every five or six dimers in a row [188]. Nevertheless, the chemical passivation of the surface is not entirely perfect. About a few hundredths of a monolayer ($\sim 4.0 \pm 0.4 \times 10^{-2}$ ML on n^+ -doped $\text{Si}(001)$ [189]) of trivalent silicon atoms are left [112, 186–189], even after prolonged exposures to water at room temperature. These so-called isolated dangling bonds (IDB) are electrically active defects responsible for fixing the Fermi level in the silicon surface gap [112, 189].

The choice of the two molecules to study the reactivity of the water-saturated $\text{Si}(001)$ surface was first motivated by their different basicities; TMA is a stronger base than ammonia. Indeed, the gas basicity of NH_3 and TMA are 819.0 and 918.1 kJ mol^{-1} , respectively [193], and the calculated O-H distance in $\text{NH}_3/\text{H}_2\text{O}$ and $\text{TMA}/\text{H}_2\text{O}$ dimers is 0.992 Å and 0.997 Å respectively [179]. Thus a similar effect on the SiO-H bond length could be expected. Second, TMA can only make an acceptor H bond with a surface SiOH, while NH_3 can make both an acceptor H bond with a first SiOH and a donor H bond with a second adjacent SiOH.

When the H-bond pairing of surface hydroxides is of concern, or the H bonding of probe molecules with the latter ones, both the distance between OHs and their topological distribution matter. In this respect, (H,OH)- $\text{Si}(001)$ has clear advantages over hydroxylated vitreous/amorphous silica surfaces for which the OH coverage and bonding is highly dependent on the history of the material. For (H,OH)- $\text{Si}(001)$, the striped (SP)

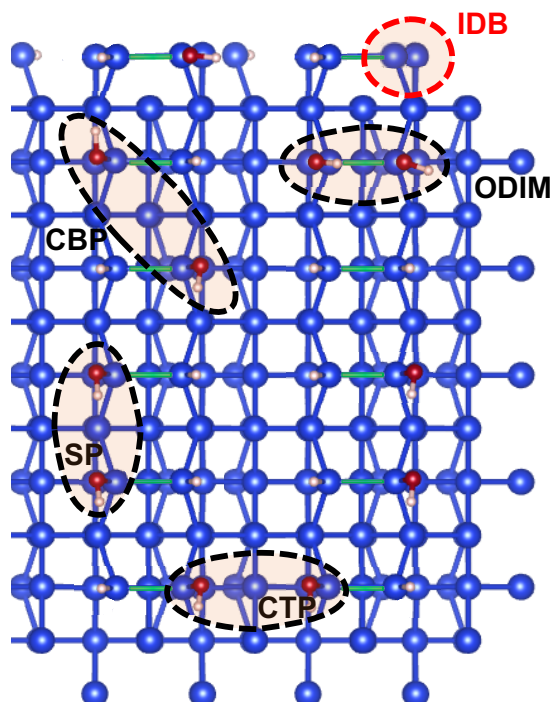


Fig. V.2 Ball and stick views of $(H,OH)\text{-Si}(001)$. Silicon, oxygen and hydrogen atoms are in blue, red and white, respectively. Dimer bonds of surface layer silicon atoms are highlighted in green. The OHs can form checkerboard patterns (CBP) and striped patterns (SP). On dimer (ODIM) and “cross-trench pattern” (CTP) OH pairs are also shown. Tri-coordinated silicon atoms, bearing an “isolated dangling bond” (IDB), are also depicted.

or checkerboard (CBP) patterns, can be theoretically modelled by periodic calculations in a way that is not too expensive in terms of cell size [194], and questions related to the realism [195] of modelling hydrated amorphous SiO_2 surfaces can be removed. Water-terminated $\text{Si}(001)\text{-}2\times 1$, which presents well-identified OH patterns, is the ideal surface to study molecular adsorption via H-bond formation both at experimental and theoretical levels.

V.3 Methods

To draw a complete picture of the molecule/surface interactions synchrotron radiation x-ray photoelectron spectroscopy (XPS) was combined with theoretical calculations. Using a cluster-type density function theory (DFT) quantum chemistry approach, core-level binding energies were simulated, and compared with the corresponding measured data. More especially for NH_3 adsorption, a periodic slab DFT calculation was undertaken fol-

lowing the Car-Parinello approach, and the adsorption energy of representative geometries were calculated, as well as their relative photoemission binding energies.

V.3.1 DFT slab periodic calculations

The periodic DFT calculations use plane waves in conjunction with norm-conserving and ultrasoft (for N and O) pseudopotentials. We used a cutoff of 35 Ry for the electron wave functions and of 280 Ry for the electron density. The calculations have been carried out using the CPMD code [196]. The exchange correlation is described through the semilocal functional proposed by Perdew, Becke and Ernzerhof (PBE) [197]. The model consists of a silicon slab of 6 layers with a $\sqrt{8} \times \sqrt{8}$ surface repeat unit resulting in a total number of 48 Si atoms. The Si lattice parameter (5.49 Å) corresponds to the lattice constant of bulk Si equilibrated at the PBE level. The Brillouin zone of the simulation cell is sampled at the Γ point only. The Si dangling bonds of the bottom layer are saturated with H atoms. The slabs are separated by 10 Å, which ensures that the images do not have any effect on the result.

In this study, we also performed Car–Parrinello molecular dynamics [198] to explore possible bonding configurations. We used a fictitious mass of 400 a.u., a time-step of 0.12 fs. The temperature was controlled by a Nosé–Hoover thermostat and set to 150 K. The adsorbates were allowed to evolve freely, and the structures obtained were monitored. In the different molecular dynamics simulation runs, we considered 1, 3 and 5 NH₃ molecules per supercell. The molecular dynamics simulations globally lasted up to 14 ps. The adsorption energies (E_{ads}) per molecule are total energy differences. They do not take into account any entropic effects nor any zero-point energy contributions.

For the core-level shifts (CLS_{per}th), a modified N pseudopotential was constructed corresponding to a N atom with a hole in the 1s shell. The method is similar to the one used in a series of papers by Rignanese and Pasquarello [199,200]. We considered various adsorbates configurations fully relaxed to equilibrium.

V.3.2 Cluster quantum chemistry (QC) DFT calculation of N 1s core ionisation potentials

We follow here a well-proven approach to calculate the excitation energies of the atomic core levels of adsorbates on silicon [201,202]. The calculation procedure, making use of the GAMESS (US) [203] software, is the same as that described in detail in previous stud-

ies [201, 202, 204, 205]. The clean silicon substrate is mimicked by a “one-dimer cluster” containing nine silicon atoms and 12 termination hydrogens (Si_9H_{12}), a “two-dimer-in-a-row” cluster containing 15 silicon atoms and 16 termination hydrogens ($\text{Si}_{15}\text{H}_{16}$), or a “three-dimer-in-a-row” cluster containing 21 silicon atoms and 20 termination hydrogens ($\text{Si}_{21}\text{H}_{20}$). The (H,OH)-Si(001) surface is mimicked by a bare dimer decorated by the (H,OH) fragments (Si_9H_{12} (OH,H)). Two non-adjacent dangling bonds on the (H,OH)-Si(001) surface are represented by a “three-dimer-in-a-row” cluster, $\text{Si}_{21}\text{H}_{20}$ (1H,3OH). The calculated configurations (cluster + fragments or adsorbate) for each molecule (ammonia and TMA), are indicated in sections V.4.1.2 and V.4.2.1.

Ground-state optimised geometries have been calculated using the Becke3 Lee–Yang–Parr (B3LYP) functional and effective core potentials (SBKJ + d polarisation) for the substrate silicon atoms, using a 6-311G+* basis sets for carbon, nitrogen and oxygen including polarisation (*) and diffuse functions (+), and 6-31G* for hydrogen. Theoretical N 1s or O 1s ionisation energies ($\Delta E_{i,\text{QC}}^{\text{th}}$) were calculated as the energy difference between the core-ionised and the ground state within the Δ Kohn–Sham approach and where the 6-311G+* basis set is substituted by the IGLOO III basis set on the core-hole site.

Relativistic corrections (0.3 eV for N 1s and 0.4 eV for O 1s) are included in the calculation. The N 1s $E_{i,\text{QC}}^{\text{th}}$ values (405.7 eV for NH_3 and 404.7 eV for TMA) are found within ± 0.1 eV of the measured ones [206], which is a good validation test for the method.

The question of the energy reference requires a comment. In cluster QC calculations, the E_i^{th} reference energy is the vacuum level at infinity E_{vac}^∞ , where the electron has zero energy. Therefore, the N 1s or O 1s E_i^{th} is that of a “gas phase molecule” consisting in the surface-mimicking cluster plus NH_3 or TMA. However, in XPS studies of a solid, the energy reference of ionisation energies (called in this case binding energies, E_b) is the Fermi level energy, E_F (common to the sample and spectrometer). Unfortunately, E_{vac}^∞ is inaccessible to measurement, and hence no common reference exists between XPS and cluster calculations. What is measurable is the work function $q\Phi$, that is by definition $q\Phi = E_{\text{vac}}^{\text{av},s} - E_F$, the difference between the energy position of the vacuum level “immediately” out of the solid surface $E_{\text{vac}}^{\text{av},s}$ (a surface-cell averaged value that depends on the surface dipole electrostatic potential), and E_F . Considering different adsorption geometries also forces us to consider different local work functions on the surface. With a local vacuum level $E_{\text{vac}}^{\text{loc},s}$, we can define as well a local work function, $q\Phi_{\text{loc}} = E_{\text{vac}}^{\text{loc},s} - E_F$ (E_F is considered not to vary over the surface). We pin the $E_{i,\text{QC}}^{\text{th}}$ to the local vacuum level. The same concept is used in photoelectron spectroscopy of adsorbed xenon [207]. Then the $E_{i,\text{QC}}^{\text{th}}$ of the configuration of interest is related to the binding energy E_b (referenced to E_F) by the following equation:

$$E_{i,\text{QC}}^{\text{th}} = E_{\text{b}} + q\Phi_{\text{loc}}. \quad (\text{V.1})$$

When we compare two different adsorption geometries, we calculate their difference in $E_{i,\text{QC}}^{\text{th}}$. One gets:

$$\Delta E_{i,\text{QC}}^{\text{th}} = \Delta E_{\text{b}} + \Delta q\Phi_{\text{loc}}. \quad (\text{V.2})$$

Therefore $E_{i,\text{QC}}^{\text{th}} = \Delta E_{\text{b}}$ only when $\Delta q\Phi_{\text{loc}}$ is negligible in equation (V.1). This caveat should always be kept in mind.

V.3.3 Real-time core-level XPS

V.3.3.1 Sample preparation

For XPS experiments, we used the same procedure described in preceding publications [173, 201, 208]. Heavily phosphorus-doped silicon wafers (n^+) of resistivity $0.003 \Omega \cdot \text{m}$ were first carefully degassed at 650°C for 20 h, and then cleaned from their native oxide by flash annealing (Joule effect) at 1100°C (measured by an infrared pyrometer) under ultra-high vacuum (UHV). The sample was then slowly cooled down to room temperature. To prepare the water-terminated Si(100)- 2×1 surface, water was purified by several freeze-pump-thaw cycles and dosed onto the clean Si(100)- 2×1 surface at room temperature through a leak-valve under a constant pressure of 5×10^{-9} mbar for 15 min; this corresponds to a dose Q of 3.4 L (or 1.7×10^{15} H_2O molecules cm^{-2} , i.e. 2.5 ML). Under these conditions, the surface is saturated by water. Finally, after cooling down to 130 K, the surface can be exposed to either NH_3 or TMA gas.

V.3.3.2 Synchrotron radiation XPS at BACH beamline

Electron spectroscopy measurements were performed at BACH Beamline, ELETTRA synchrotron facility (Trieste, Italy). Linearly polarised light in the 175–600 eV range is provided by a high-energy APPLE II helical undulator. The photon dispersion system is based on a Padmore variable angle spherical grating monochromator. Photoemission spectra were measured by means of a modified 150 mm VSW hemispherical electron analyser with a 16-channel detector. In the adopted geometry, the photon beam direction was perpendicular to the sample surface (polarisation was contained in the surface plane) and the photoelectron emission angle was at 60° from the sample surface.

The N 1s and O 1s spectra were measured at 455 eV and 595 eV, respectively. The spectra, after Shirley background subtraction, are fitted with sums of Gaussians. The Si 2p core level spectrum of (H,OH)-Si(001), measured at $h\nu = 175$ eV, and shown in Figure D.1 of the Appendix D (Section D.1), indicates that the surface is saturated by water fragments H and OH. The “up dimer atom” component is quenched and a $\text{Si}^{1+}/\text{SiOH}$ component shows up. Few isolated dangling bonds may remain on the surface ($\sim 4.0 \pm 0.4 \times 10^2$ ML [189]); these are doubly occupied and hence negatively charged [112]. The bulk Si $2p_{3/2}$ binding energy is measured at 99.41 eV at 300 K. After cooling down to 130 K, the Si 2p spectrum moves slightly to higher binding energy, because of a surface photovoltage effect that decreases the upward band bending at the surface. Therefore, all spectra acquired at low temperature (N 1s and O 1s) are corrected for this shift, keeping the Si $2p_{3/2}$ position at 99.41 eV. However, we will analyse the band bending changes both due to surface photovoltage and due to the probing molecule adsorption that can be measured from XPS/Auger spectroscopy.

V.4 Results

V.4.1 Ammonia (NH_3) as probing molecule

V.4.1.1 DFT slab periodic calculations

The ammonia molecule was placed at SP, CBP and CTP sites indicated in Figure V.2 (the ODIM paired OHs site was not examined). Here and in the following, we adopt a systematic nomenclature to identify hydroxyls and ammonia molecules accepting (denoted A or a) or donating (denoted D or d) a hydrogen atom. Capital letters mean that the H bond is strong (H-bond length below 2.2 Å). Lower case letters are used when the H bond is considered weak (H-bond length greater than 2.2 Å).

After Car–Parrinello molecular dynamics, the initial SP- $\text{NH}_3(\text{A},\text{D})$ and (A,A) configurations were preserved. However, initial CBP- $\text{NH}_3(\text{A},\text{D})$, (D,D) and (A,A) configurations ended up as CBP- $\text{NH}_3(\text{A},\text{d})$, CBP- $\text{NH}_3(\text{d},\text{d})$ and CBP- $\text{NH}_3(\text{A},\text{d})$. Initial CTP- $\text{NH}_3(\text{A},\text{D})$, (D,D) and (A,A) configurations all ended up as CTP- $\text{NH}_3(\text{A},\text{d})$. Minimum energy geometries in SP and CBP sites are shown in Figure V.4.

The negative of the adsorption energies $-E_{\text{ads}}$ obtained from structural relaxation in the periodic DFT set-up (corresponding to $T=0$ K) are given in Table V.1 together with

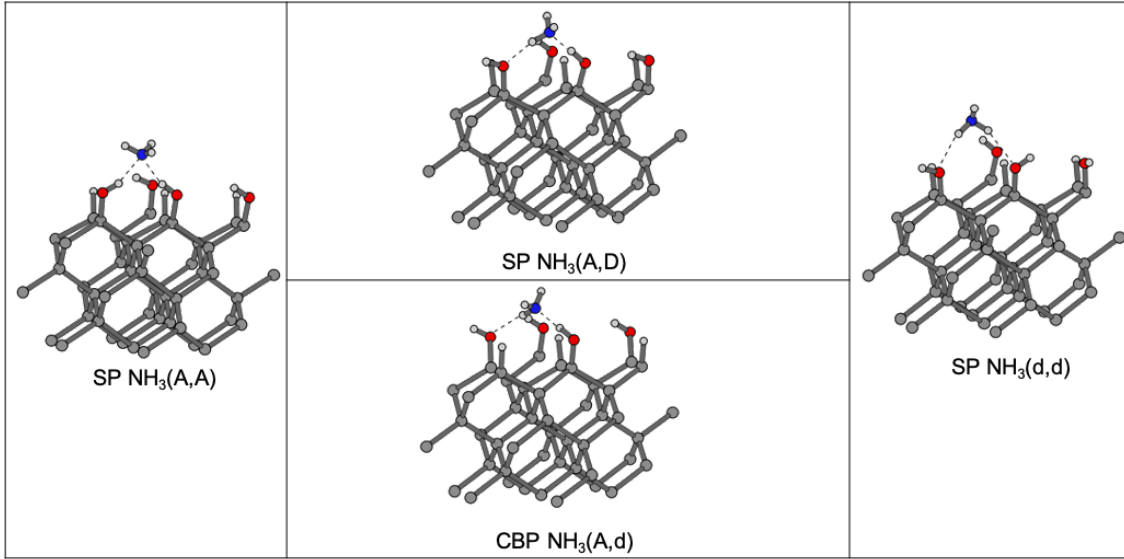


Fig. V.3 NH_3/OH equilibrium geometries calculated via the periodic DFT approach: silicon, oxygen, nitrogen, and hydrogen atoms are in grey, red, blue, and white, respectively. Nomenclature: striped pattern (SP), checkerboard pattern (CBP). A is for strong acceptor; D (d) is for strong (weak) donor (see text). We give in Table V.1 the adsorption energies of structurally relaxed molecules (E_{ads}) (calculated at 0 K) and their corresponding binding energy shifts ($\text{CLS}_{\text{per}}^{\text{th}}$), as obtained by the periodic DFT approach. Most strongly bonded geometries are of the type $\text{NH}_3(\text{A},\text{D})$ or $\text{NH}_3(\text{A},\text{d})$. These are observed experimentally (see text).

the N 1s core-level shift relative to that of the H–Si–Si–NH₂ moiety, $\text{CLS}_{\text{per}}^{\text{th}}$ ¹. The Si–NH₂ fragment is used as a benchmark of the XPS binding energies, because it is well documented [202]. The most stable configurations ($-E_{\text{ads}} > 0.56$ eV) are the SP-NH₃(A,D), CBP-NH₃(A,d), and cross-trench pattern (CTP) NH₃(A,d). All these configurations have a $\text{CLS}_{\text{per}}^{\text{th}}$ in the range 1.41 to 1.51 eV (see Table V.1).

The other adsorption geometries have $-E_{\text{ads}}$ values significantly smaller than that of the acceptor–donor ones. The SP NH₃(A,A) geometry has an $-E_{\text{ads}}$ value of 0.42 eV, and thus is less strongly attached to the OH pairs than the (A,D) or (A,d) geometries. Its calculated $\text{CLS}_{\text{per}}^{\text{th}}$ of 2.2 eV with respect to the dissociated H–Si–Si–NH₂ configuration is also noticeably greater than that of the acceptor/donor geometries by about +0.8 eV. Molecules adopting the NH₃(d,d) geometries are still more weakly bound to the surface with $-E_{\text{ads}}$ equal to 0.18 eV (SP) and 0.03 eV (CBP). Their calculated N 1s binding energy difference is small (less than 0.2 eV) with respect to that of Si–NH₂. Finally, from a spectroscopic viewpoint, the fact that the mixed NH₃(A,D) or NH₃(A,d) adsorption geometries lead to N 1s binding energies intermediate between that of NH₃(d,d) and that

¹ $\text{CLS}_{\text{per}}^{\text{th}}$ stand for the theoretical ('th') core-level shift calculated using the slab periodic ('per') method.

Table V.1: Periodic DFT Geometries, Adsorption Energies (E_{ads}), and N 1s Binding Energy Core-Level Shifts ($\text{CLS}_{\text{per}}^{\text{th}}$) with Respect to Si-NH₂ for Structurally Relaxed Configurations (at 0 K).^α

Configuration	H bond lengths (Å)	$-E_{\text{ads}}$ (eV)	$\text{CLS}_{\text{per}}^{\text{th}}$ N 1s core level shift with respect to Si-NH ₂ (eV)
H-Si-Si-NH ₂	NA	3.29	0
NH ₃ -Si-Si	NA	2.38	3.02
SP NH ₃ (A,D)	A: 1.64; D: 2.00	0.69	1.41
CBP NH ₃ (A,d)	A: 1.74; d: 2.45	0.61	1.44
CTP NH ₃ (A,d)	A: 1.67; d: 2.56	0.56	1.51
SP NH ₃ (A,A)	A: 2.00; A: 2.01	0.42	2.2
CBP NH ₃ (d,d)	d: 2.46; d: 2.49	0.18	0.29
SP NH ₃ (d,d)	d: 2.36; d: 2.47	0.06	0.15

^α Nomenclature: striped pattern (SP), checkerboard pattern (CBP), and cross-trench (CTP). The configurations are listed (from top to bottom) according to decreasing $-E_{\text{ads}}$ i.e. decreasing binding strength. A capital letter corresponds to a strong H bond, a lower case to a weak H bond (a H bond is considered weak when its length is longer than 2.2 Å).

of NH₃(A,A) is consistent. In fact, acceptor bonding shifts the N 1s binding energy to higher values while donor bonding counterweights this effect.

V.4.1.2 Cluster quantum chemistry (QC) DFT calculation of N 1s core ionisation potentials

For their part, the cluster QC DFT calculations have addressed ammonia bonding on SP and CBP patterns mimicking those of the periodic DFT calculations. We have also considered ammonia bonded on ODIM OHs pairs. Some optimised geometries are shown in Figure V.4. In the following, the reference species for N 1s $\Delta E_{i,\text{QC}}^{\text{th}}$ will be the amine (HSi-SiNH₂). For the O 1s $\Delta E_{i,\text{QC}}^{\text{th}}$ the isolated hydroxyl, see Appendix D, section D.3.

Absolute N 1s $E_{i,\text{QC}}^{\text{th}}$ are reported in Table V.2. First it is convenient to compare the $E_{i,\text{QC}}^{\text{th}}$ of the various configurations with that of gas phase ammonia (405.7 eV). All purely acceptor geometries have $E_{i,\text{QC}}^{\text{th}}$ higher by ~ 0.7 eV than the isolated molecule. In contrast, all purely donor geometries have $E_{i,\text{QC}}^{\text{th}}$ lower than that of isolated ammonia by ~ 1.1 eV. Dual acceptor/donor geometries have $E_{i,\text{QC}}^{\text{th}}$ nearly equal to that of isolated ammonia. This observation strongly suggests the electrostatic origin of the changes in $E_{i,\text{QC}}^{\text{th}}$ for the molecule, the presence of protons rising the ionisation energy and that of the electron lone pair decreasing it. Acceptor/donor bonds result in a quasi-cancellation of these opposite

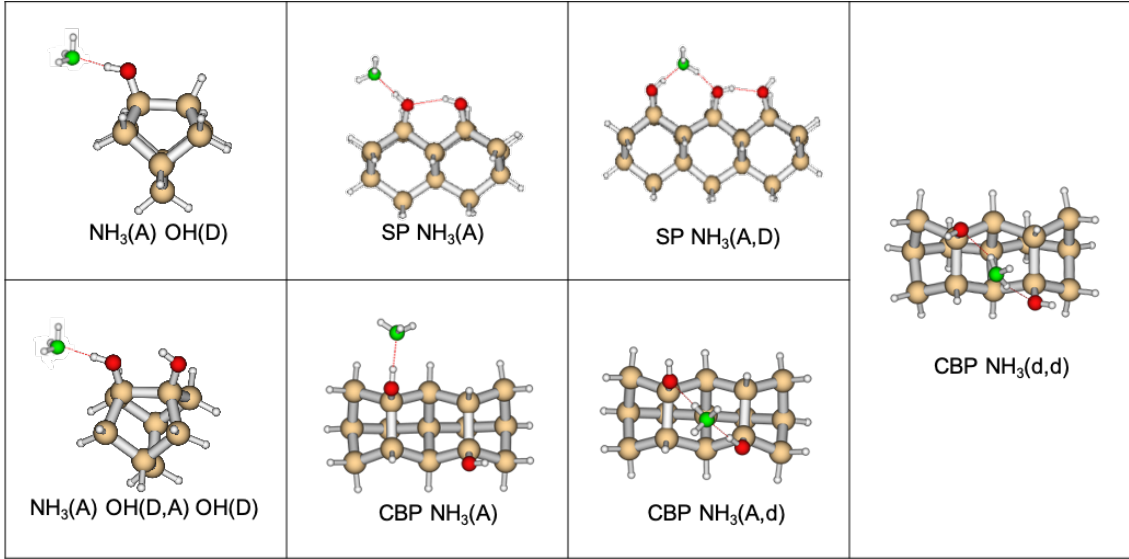


Fig. V.4 NH_3/OH equilibrium geometries calculated via the cluster QC DFT approach: silicon, oxygen, nitrogen, and hydrogen atoms are in brown, red, green, and white, respectively. Nomenclature is the same as in Figure V.3 (see also text). N Is calculated ionisation potentials ($E_{i,\text{QC}}^{\text{th}}$) of the cluster are given in Table V.2.

effects. The same trends were observed in periodic DFT.

To enable a comparison with the periodic DFT core-level shifts $\text{CLS}_{\text{per}}^{\text{th}}$, we calculate the $\Delta E_{i,\text{QC}}^{\text{th}}$ values referenced to dissociated ammonia (SiNH_2). The $E_{i,\text{QC}}^{\text{th}}$ of SiNH_2 is 404.0 eV for a Si_9H_{12} (NH_2, H) cluster, a value identical to that found for a CBP $\text{Si}_{15}\text{H}_{16}$ ($2\text{H}, 2\text{NH}_2$) cluster (Figure 1 in ref [202]). Purely acceptor bonds have $\Delta E_{i,\text{QC}}^{\text{th}}$ in the 2.3–2.5 eV range. $\text{NH}_3(\text{A})$ geometries with a single H bond of 1.84 ± 0.02 Å have practically the same $E_{i,\text{QC}}^{\text{th}}$ of a double H-bond SP- $\text{NH}_3(\text{A}, \text{A})$ geometry with two longer H bonds, of 2.05 ± 0.03 Å. The QC calculation $\Delta E_{i,\text{QC}}^{\text{th}}$ are in close agreement with the $\text{CLS}_{\text{per}}^{\text{th}}$ of SP- $\text{NH}_3(\text{A}, \text{A})$, equal to 2.2 eV. The SP- $\text{NH}_3(\text{A}, \text{D})$ and CBP- $\text{NH}_3(\text{A}, \text{D})$ have both the same $\Delta E_{i,\text{QC}}^{\text{th}}$ equal to 1.48 eV. The $\Delta E_{i,\text{QC}}^{\text{th}}$ of the ODIM $\text{NH}_3(\text{A}, \text{D})$ configuration is somewhat larger, 1.68 eV, because of the shorter A bond (1.77 Å). Again, the $\Delta E_{i,\text{QC}}^{\text{th}}$ values are remarkably close to the $\text{CLS}_{\text{per}}^{\text{th}}$ found for the corresponding geometries (1.41–1.44 eV, Table V.1). Considering the donor geometries, $\Delta E_{i,\text{QC}}^{\text{th}}$ is in the 0.48–0.76 eV range. If we consider specifically the CBP- $\text{NH}_3(\text{d}, \text{d})$ configuration, the most strongly adsorbed donor geometry according to periodic DFT, $\Delta E_{i,\text{QC}}^{\text{th}}$ is 0.48 eV, close to the $\text{CLS}_{\text{per}}^{\text{th}}$ of 0.29 eV for the same geometry.

Table V.2: Theoretical N 1s ionisation potential energies $E_{i,\text{QC}}^{\text{th}}$ calculated via a DFT QC silicon cluster approach for ammonia adsorption.^α

Configuration	Cluster plus fragments or adsorbate	H-bond lengths (Å)	N 1s $E_{i,\text{QC}}^{\text{th}}$ (eV)	$\Delta E_{i,\text{QC}}^{\text{th}}$ SiNH ₂ reference (eV)
Free ammonia molecule NH ₃		NA	405.70	
<i>Benchmark adsorption geometries</i>				
Single dimer H-Si-Si-NH ₂	Si ₉ H ₁₂ (NH ₂ ,H)	NA	404.00	0
CBP H-Si-Si-NH ₂	Si ₁₅ H ₁₆ (2H,2NH ₂)	NA	403.99	0
Si-Si-NH ₃ datively bonded	Si ₁₅ H ₁₆ (NH ₃)	NA	406.98	2.99
<i>H-bonding</i>				
ODIM OH(d)···OH(a,D)···NH ₃ (A)	Si ₉ H ₁₂ (2OH,NH ₃)	O-H···OH 2.64; O-H···NH ₃ 1.84	406.50	2.51
SP OH(D)···OH(A,D)···NH ₃ (A)	Si ₁₅ H ₁₆ (2OH,2H,NH ₃)	O-H···OH 2.15; O-H···NH ₃ 1.82	406.47	2.48
SP OH(D)···NH ₃ (A,A)···OH(D)	Si ₁₅ H ₁₆ (2OH,2H,NH ₃)	OH···NH ₃ 2.08; H ₃ N···HO 2.03	406.45	2.46
Single dimer OH(D)···NH ₃ (A)	Si ₉ H ₁₂ (OH,H,NH ₃)	O-H···NH ₃ 1.84	406.38	2.39
CBP OH(D)···NH ₃ (A)	Si ₁₅ H ₁₆ (2OH,2H,NH ₃)	OH···NH ₃ 1.86	406.28	2.29
ODIM OH(D)···NH ₃ (A,D)···OH(A)	Si ₉ H ₁₂ (2OH,NH ₃)	O-H···HNH ₂ 1.77; H ₂ NH···O-H 2.11	405.67	1.68
CBP OH(D)···NH ₃ (A,D)···OH(A)	Si ₁₅ H ₁₆ (2OH,2H,NH ₃)	OH···NH ₃ 1.82; H ₂ NH···OH 2.17	405.47	1.48
SP OH(D)···NH ₃ (A,D)···OH(A)	Si ₂₁ H ₂₀ (3OH,3H,NH ₃)	OH···NH ₃ 1.78; H ₂ NH···OH 2.04	405.47	1.48
Single dimer OH(A)···NH ₃ (D)	Si ₉ H ₁₂ (OH,H,NH ₃)	H-O···H-NH ₂ 2.17	404.75	0.76
SP OH(d)···OH(a,D)···NH ₃ (D)	Si ₁₅ H ₁₆ (2OH,2H,NH ₃)	H-O···H-NH ₂ 2.14	404.56	0.57
CBP OH(a)···NH ₃ (d,d)···OH(a)	Si ₁₅ H ₁₆ (2OH,2H,NH ₃)	OH···HNH ₂ 2.35; H ₂ NH···OH(a) 2.35	404.47	0.48

^α $\Delta E_{i,\text{QC}}^{\text{th}}$ is the ionisation energy referenced to that of the Si-NH₂ fragment. Si₉H₁₂, Si₁₅H₁₆ and Si₂₁H₂₀ are the “one-bare-dimer”, “two-bare-dimer-in-a-row” and “three-bare-dimer-in-a-row” clusters, respectively. (···) denotes a H bond. We use the following nomenclature: on-dimer (ODIM), striped pattern (SP), checkerboard pattern (CBP). OH and NH₃ can donate (D or d) or accept (A or a) H atoms. A capital letter corresponds to a strong H bond, a lower case to a weak H bond (a H bond is considered weak when its length is longer than 2.2 Å).

V.4.1.3 Real-time core-level XPS

During real-time N 1s XPS measurements (at $h\nu = 455$ eV), the water-covered surface described in section V.3.3.1 is exposed to NH_3 at 120 K by filling the analysis chamber up to a pressure of 5×10^{-9} mbar. Considering a gas temperature of 300 K, the flux F of molecules impinging on the surface is 1.85×10^{12} molecules $\text{cm}^{-2} \text{s}^{-1}$, equivalent to 2.72×10^{-3} ML s^{-1} , where one monolayer (ML) is the number of silicon atoms per unit surface ($6.8 \times 10^{14} \text{ cm}^{-2}$). The dose $Q = F \times t$ (where t is the exposure time) is expressed in ML in the following. After dosing for 865 s ($Q = 2.35$ ML), the X-ray spot was displaced to probe another area, to check for possible beam-induced chemistry. Then after an overall exposure of 1150 s ($Q = 3.2$ ML), ammonia was pumped down.

The question of co-adsorption of molecular water during cooling and then exposure to ammonia was examined by measuring the normalised O 1s intensity (see Appendix D, section D.2). The oxygen coverage at room temperature is 0.50 ML, because almost all silicon atoms are covered by an equal number of H and OH. The surface sample at 130 K before ammonia exposure has an oxygen surface coverage of 0.57 ML (known with a precision of 8%). The increase may be attributed to water co-adsorption (see Appendix D sections D.3 and D.4). However, after exposure to ammonia, we find an oxygen coverage of 0.50 ML again. Ammonia likely displaces the water molecules adsorbed on the surface. Therefore, we exclude the formation of $\text{NH}_3/\text{H}_2\text{O}$ H bonds; the probe molecule only binds to surface hydroxyls.

The time-resolved N 1s spectra (each spectrum is the sum of 5 individual spectra obtained in the so-called swept mode of the analyser) are given in Figure V.5(a). An illustrative N 1s spectra, with the corresponding fit by a sum of Gaussians, is given in Figure V.5(b). The N 1s intensity is normalised with respect to the (H, NH_2)-Si(001) standard surface (N coverage of 0.5 ML), as shown in section D.2 of Appendix D. In Figure V.5(c), we plot against time the normalised coverages (in ML) of the various chemical components resulting from the fit of the N 1s spectra.

The N 1s spectrum in Figure V.5(b) is recorded just before the onset of saturation. It is fitted with three components. The lowest binding energy component at 398.87 eV is attributed to dissociated ammonia Si- NH_2 . We base our attribution on previous XPS studies on the adsorption of ammonia on clean Si(001)- 2×1 [202,209]. The highest binding energy component at 401.73 eV, +2.86 eV above the Si NH_2 component, is attributed to ammonia datively bonded to a silicon dimer, as the predicted $\text{CLS}_{\text{per}}^{\text{th}}$ and $\Delta E_{\text{i,QC}}^{\text{th}}$ values (Tables V.1 and V.2) are both equal to 3.0 eV.

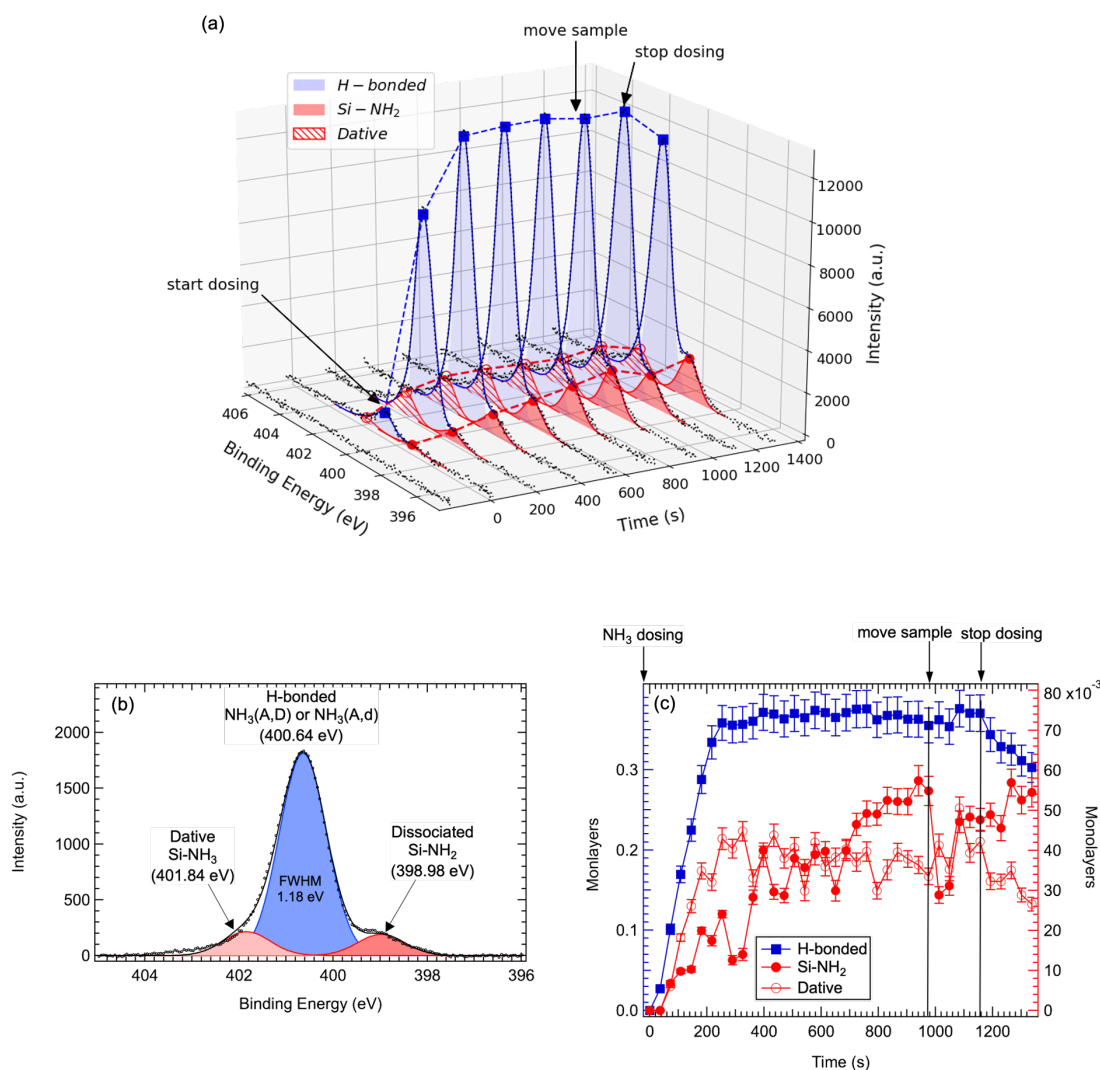


Fig. V.5 (a) Time-resolved $N 1s$ spectra measured during NH_3 adsorption on (H,OH) -Si(001)- 2×1 at 120 K (under 5×10^{-9} mbar of ammonia) with a photon energy of 455 eV (each spectrum shown here is the sum of 5 individual spectra). Baseline measured before NH_3 dosing was subtracted. All binding energies are aligned to a common position of the $Si 2p_{3/2}$ core level at 99.41 eV (the $Si 2p_{3/2}$ binding energy of n^+ (H,OH) -Si(001) at room temperature). (b) Illustrative spectrum measured while dosing at $t = 180$ s ($Q = 0.5$ ML), and corresponding fittings with three Gaussian components, datively bonded NH_3 , H-bonded NH_3 , and dissociated $Si-NH_2$ species. Full width at half-maximum is 1.8 eV for all peaks; binding energy is also indicated. (c) Nitrogen coverage (in ML) as a function of time for H-bonded NH_3 , datively bonded NH_3 , and dissociated $Si-NH_2$ species.

The third (middle) component found at 400.53 eV, is shifted by +1.66 eV with respect to the Si–NH₂ component. Looking to the periodic (cluster QC) DFT values in Table V.1 (Table V.2), we see that the NH₃(A,D) and NH₃(A,d) configurations have CLS_{per}th ($\Delta E_{i,QC}^{\text{th}}$) values in the 1.41–1.51 eV range (1.5–1.7 eV range). Therefore, the main central component is attributed to ammonia making acceptor/donor bonds with two hydroxyls. Formation of purely acceptor configurations is excluded because the theoretical chemical shifts with respect to SiNH₂ (2.2 eV in periodic DFT, and 2.3 ± 0.2 eV in cluster QC DFT) are much larger than the experimental ~ 1.6 eV shift.

The presence of acceptor–donor geometries is explained simply by the binding strength of the molecule on the surface. The $-E_{\text{ads}}$ values in Table V.1 show that the SP-NH₃(A,D) and the CBP-NH₃(A,d) geometries (Figure V.4) correspond to ammonia molecules that are the most firmly bound to the hydroxyls. Indeed, the $-E_{\text{ads}}$ value of the SP-NH₃(A,A) geometry is 0.3 eV lower. Neither single nor double donor geometries enter into consideration, as their $-E_{\text{ads}}$ values are much too low (0.06–0.18 eV), making them unobservable at 130 K.

In Section D.3 of Appendix D, we give a detailed theoretical account of the effect of H-bond formation on the O 1s $E_{i,QC}^{\text{th}}$ of the hydroxyls, and discuss the O 1s $\Delta E_{i,QC}^{\text{th}}$ taking the isolated SiOH as a reference. In Section D.4 of Appendix D we show the modifications of the O 1s after ammonia adsorption at 130 K. The experimental O 1s spectrum is significantly broadened and shifted to lower binding energy with respect to that of the pristine (H,OH)-Si(001) surface at 300 K, where the effects of H-bonding are supposed to be negligible. Theory explains qualitatively the experimental shift to lower binding energy, because the donor bond, OH(D) leads to a negative variation in $\Delta E_{i,QC}^{\text{th}}$ significantly greater in magnitude than that of the acceptor bond, OH(A or a), which is positive.

a) Adsorption Kinetics of H-bonded ammonia and saturation coverage Figure V.5(c) shows that the rate of adsorption of H-bonded ammonia, NH₃(A,D) or NH₃(A,d), is constant (1.52×10^{-3} ML s⁻¹) up to 216 s ($Q = 0.59$ ML), corresponding to an initial sticking coefficient of 0.6. Above that critical dose the rate goes to zero and the maximum coverage reached is 0.36 ML. This kinetic behaviour suggests the presence of a molecular precursor [210]. The saturation coverage is larger than 0.25 ML, the value expected for a configuration in which one ammonia is bonded to two OHs and each OH to only one ammonia. Some OHs are necessarily bonded to two ammonia molecules. Ammonia and OHs likely form strings of the type $\cdots \text{NH}_3 \cdots \text{OH} \cdots \text{NH}_3 \cdots$, where OHs are both donor and acceptor (see also D, section D.3 and D.4). We note also that the maximum coverage

of H-bonded ammonia is not affected by synchrotron beam damage (see below for the other species): when a fresh area is probed by moving the sample, the H-bonded coverage remains the same.

b) Desorption Kinetics at 130 K As shown in Figure V.5(c), once ammonia dosing is stopped (after 1150 s), the chamber is pumped down. We see that the H-bonded ammonia coverage starts to decrease. Assuming a first order reaction, the normalised coverage will be proportional to $\exp(-\frac{t}{\tau})$, where τ is the time constant. We find $\tau = 817$ s for an initial coverage of 0.37 ML (red squares in Figure V.6) This experience has been repeated from a coverage of about 0.25 ML (blue squares in Figure V.6) and we have found a characteristic time τ of 1371 s. A Gibbs energy of activation ΔG^\ddagger of 0.39–0.40 eV is obtained, using the Eyring–Polanyi–Evans equation valid for unimolecular desorption (the transmission coefficient is assumed to be one)

$$\tau^{-1} = \frac{k_B T}{h} \exp\left(-\frac{\Delta G^\ddagger}{k_B T}\right), \quad (\text{V.3})$$

where k_B is the Boltzmann constant and h the Planck constant ($k_B T/h$ is $2.7 \times 10^{12} \text{ s}^{-1}$ at 130 K). Assuming that adsorption is barrierless, $\Delta G^\ddagger = -\Delta G_{\text{ads}} = -(\Delta H_{\text{ads}} - T\Delta S_{\text{ads}})$. The increase of τ when the starting coverage is lower may indicate that the magnitude of ΔG_{ads} increases when the adsorption sites are less crowded. We recall that the calculated $-E_{\text{ads}} (= -\Delta H_{\text{ads}})$ values are in the range 0.56–0.69 eV (with PBE calculation errors of the order of 0.1 eV) for dual H-bonded geometries.

c) Probing the silicon dangling bonds with datively bonded ammonia The adsorption kinetics of the dative species (component at 402 eV) is shown in Figure V.5(c). We observe an initial linear regime up to 216 s ($Q = 0.59$ ML), with an adsorption rate of $2.06 \times 10^{-4} \text{ ML s}^{-1}$, corresponding to a sticking coefficient of 0.075, one order of magnitude smaller than that of the H-bonded species. Then a maximum coverage 4.4×10^{-2} ML is reached at 400 s ($Q = 1$ ML), after which the surface density of Si–NH₃ tends to decrease. This decrease is due, in part, to the exposure to the beam: when the beam spot is moved, we recover a coverage of 4.6×10^{-2} ML in the freshly analysed area. Considering the observed maximum coverage of datively bonded species (also around 4×10^{-2} ML), most of the silicon dangling bond sites should be occupied by ammonia.

We emphasise that the dative bonding of other Lewis bases than ammonia on n^+ -doped (H,OH)-Si(001) is also observed. Trimethylamine (a tertiary amine) does bond this way at 130 K, as proven by its N 1s spectrum given in Figure V.8. The coverage is

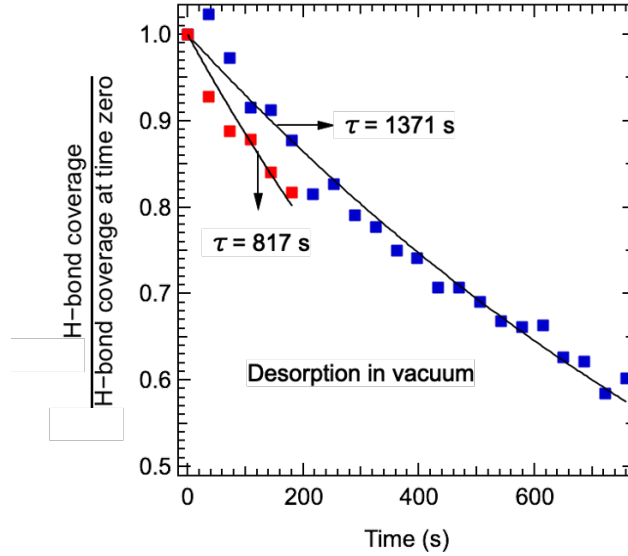


Fig. V.6 Desorption curves in vacuum plotted against time (time zero is the time at which the spectra start to be acquired). Coverages are divided by the value at time zero. Red square curve corresponds to desorption from a coverage of 0.37 ML, and blue square corresponds to a coverage estimated to be 0.25 ML. Curves are fitted by a decaying exponential ($\exp(-\frac{t}{\tau})$).

0.03 ML, a value comparable to the surface density of IDBs. However, the observation of a datively bonded species on an isolated tri-coordinated silicon atom may seem surprising. Indeed, in a simple acid–base reaction scheme, the formation of a Lewis adduct requires that the base (ammonia or trimethylamine) inserts its nitrogen lone-pair into an acidic site (an empty, positively charged silicon dangling bond). For instance, this applies to the case of the buckled clean surface [211, 212]. However, for an n^+ substrate, the dangling bond is doubly occupied, i.e., negatively charged [188]. Therefore, one would expect the ammonia to be repelled when it approaches the tri-coordinated silicon adsorption site. As a dative bonding is observed, this means that the electron charge on the silicon defect is delocalised into the substrate when the tri-coordinated silicon atom is attacked by the ammonia molecule. We recall that the adsorption of ammonia molecules and amines on n -type H-terminated Si(111) silicon-on-insulator (SOI) induces a strong electron-accumulation layer [213]. Adsorption likely takes place at silicon dangling bonds on that surface. Indeed, calculations [214] addressed the electronic structure of NH_3 bonded to the isolated dangling bonds of the H-terminated $\sqrt{3} \times \sqrt{3}$ Si(111) surface (the latter one mimics mesoporous Si). It was shown first that the molecule is bonded to the surface with $-E_{\text{ads}} = 0.45$ eV, and second, a shallow donor state appears just below the conduction band of silicon.

d) Dissociation Figure V.5(c) shows that the initial rate of the Si-NH₂ is also approximately constant and equal to $\sim 0.7 \times 10^{-4}$ ML s⁻¹. The synchrotron beam has a clear effect on breaking the ammonia molecule. After moving the spot (at 865 s), the Si-NH₂ coverage diminishes from ~ 0.06 ML to ~ 0.03 ML. This coverage is not zero; therefore dissociation may also occur in the absence of the beam, but the exposure to the beam multiplies the rate by at least a factor of ~ 2 .

We first consider a mechanism leading to dissociation of a molecule datively bonded to an IDB into Si-NH₂ and Si-H moieties without the assistance of the beam. In the case of the clean dimerised surface [209,212], two adjacent silicon dangling bonds (e.g., on the same dimer) are necessary. Such a situation is not encountered on (H,OH)-Si(001), as the IDBs, immobile at 130 K [215], are too far apart (2 nm on average for a coverage of 0.04 ML). The proton relay mechanism, which has a low activation barrier, could be a solution to the problem [209,216,217]. One could imagine that a string of H-bonded moieties (ammonia-hydroxyl-ammonia-hydroxyl...) connects the Si-NH₃ precursor to a distant second dangling bond. Once a proton leaves the ammonia molecule, another proton is transferred to the uncapped silicon atom far away.

Concerning ammonia dissociation due to the beam, the effect of light is indirect. In fact, electrons matter. Under X-ray irradiation photoelectrons and Auger electrons traveling in the silicon substrate suffer inelastic losses. Secondary electrons that have sufficient kinetic energies escape into the vacuum (the “tail” of the secondary electrons extends several electronvolts above the vacuum level [218]) and then can interact with the adsorbates. For NH₃ in the gas phase, a dissociative attachment resonant state is observed at 5.5 eV [219] above the vacuum level. Attachment-dissociation can lead to breaking of the adsorbed molecule into NH₂[•] + H⁻ or NH₂⁻ + H[•]. If a molecule datively bonded to an IDB breaks after attaching an electron, a Si-NH₂ moiety will form and the leaving H will react further apart, forming a new bond, e.g., abstracting another H from a Si-H, breaking a Si-Si bond, etc. For H-bonded or physisorbed molecules, formation of a Si-NH₂ moiety may need two steps, as in the mechanism proposed by Guizot *et al.* [220]. In a first instance, a radical (H[•] or NH₂[•]) abstracts one H from a surface hydride (regenerating a H₂ or an NH₃ molecule). This leaves a Si[•], which, in a second instance, captures another NH₂[•] radical. In any case, Si-NH₂ formation via a mechanism involving an NH₂[•] radical does not necessarily require the occurrence of two adjacent silicon dangling bonds.

V.4.2 Trimethylamine (TMA) as probing molecule

V.4.2.1 Cluster quantum chemistry (QC) DFT calculation of N 1s core ionisation potentials

For the TMA case, only “one-dimer clusters” were used. The clusters plus TMA molecule are shown in Figure V.7. As discussed in Section V.3.2, the comparison between the $E_{i,\text{QC}}^{\text{th}}$ values of various geometries and the experimental binding energies can only be made when $q\Phi_{\text{loc}}$ (which depends ultimately on the outer electrostatic potential close to the surface, $q\phi_{\text{out}}$) is a constant.

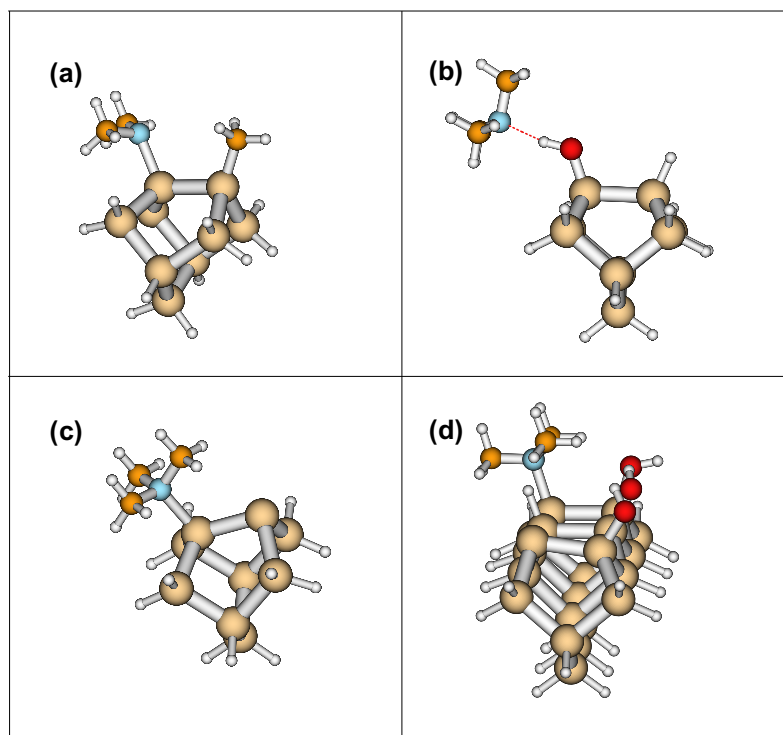


Fig. V.7 Cluster QC DFT optimised geometries: (a) TMA dissociated over a bare dimer, (b) TMA making an acceptor H bond with the hydroxyl of the (H,OH)-decorated dimer, (c) TMA bonded datively to a dangling bond of the bare dimer, (d) TMA bonded datively to a dangling bond of a H/OH decorated cluster with a non-adjacent dangling bond left free. Silicon, oxygen, nitrogen and hydrogen atoms are in brown, red, blue and white, respectively. N 1s calculated ionisation potentials ($E_{i,\text{QC}}^{\text{th}}$) of the cluster are given in Table V.3.

Table V.3: Theoretical N 1s ionisation potential energies $E_{i,\text{QC}}^{\text{th}}$ calculated via a DFT QC silicon cluster approach for TMA adsorption.^α

Species	Cluster type	Bond lengths (Å)	$E_{i,\text{QC}}^{\text{th}}$ (eV)	$E_{i,\text{QC}}^{\text{th}} - q\Phi^{\text{H,OH}}$ (eV)
Isolated N(CH ₃) ₃	–	–	404.7	400.3
NH(CH ₃) ₃ ⁺	–	N–H 1.0055	414.4	410.0
Dative bond on bare dimer	Si ₉ H ₁₂ (N(CH ₃) ₃)	–	406.8	402.4
H-bonded TMA OH(D)···N(CH ₃) ₃ (A)	Si ₉ H ₁₂ (H,OH,N(CH ₃) ₃)	N···H 1.7755 O–H 0.9973	405.3	400.9
Dissociated TMA on bare dimer	Si ₉ H ₁₂ (CH ₃ ,N(CH ₃) ₂)	–	403.7	399.3

^α We calculate $E_{i,\text{QC}}^{\text{th}} - q\Phi^{\text{H,OH}}$ to have comparable values of theoretical ionisation energies and experimental binding energies. $q\Phi^{\text{H,OH}}$ is the average experimental work function of the pristine (H,OH)-Si(001) (4.40 eV [112]).

V.4.2.2 Real-time core-level XPS

During the real-time XPS experiment, (H,OH)-Si(001)-2×1 was first exposed to TMA at 130 K under a measured pressure of 5×10^{-9} mbar. This corresponds to a molecular flux of 10^{12} molecules $\text{cm}^{-2} \text{s}^{-1}$. The surface was exposed for 140 s, corresponding to a total dose Q of 1.4×10^{14} molecules cm^{-2} (or 0.2 ML), after which the leak valve was closed, and TMA was pumped down.

The N 1s spectra (measured at $h\nu = 455$ eV) were continuously recorded (in swept mode). The time-resolved N 1s spectra are given in Figure V.8(a). The principal events (start dosing, stop dosing) are indicated. Due to the small nitrogen coverage, the N 1s spectra are integrated over the 140 s of dosing time (box #1 in panel V.8(a)). The corresponding spectrum is shown in panel V.8(b), top curve. It exhibits two components at 402.35 eV and 400.45 eV, respectively. In panel V.8(a), the band at 400.45 eV, decreases in intensity and shifts apparently to lower binding with increasing measurement time once TMA dosing is stopped and the chamber is pumped down. The shift is simply explained by the appearance of a new component at 399.25 eV. The latter clearly shows up in the middle spectrum of panel V.8(b), which is the sum of the spectra within box #2 in panel V.8(a) (spectra are measured after stopping the dosing). To examine possible cumulative synchrotron beam damage during real-time experiments, we have exposed a (H,OH)-Si(001) surface to a TMA dose of 1.3 ML, “in the dark”, after positioning the shutter of the beamline. Then when we have measured the N 1s spectrum, top curve in panel V.8(b) immediately after exposure and pumping. In this control experiment,

the N 1s spectrum shows a main line at 400.5 eV, two small components at 402.4 (8% of the spectral weight) and 401.3 eV (13% of the spectral weight), but no component at ~ 399 eV. This is a strong indication that the low binding energy component is due to the X-ray beam damage. In Figure V.8(c), we plot against time the total nitrogen coverage (expressed in ML), as well as those of the various chemical components (at 402.4 eV, 400.5 eV and 399.3 eV, resulting from the fit of the N 1s spectra shown in panel V.8(a)).

We will now proceed to the identification of the chemical species present at the surface based on the measured bond energies, the calculated N 1s ionisation energies summarised in Table V.3, and the nitrogen coverages versus measurement time deduced from the fits of the spectra measured in real time.

We can consider two extreme theoretical cases, TMA making no H-bond with the hydroxyls (this is simulated by the isolated molecule) and TMA making a strong H-bond (TMA(A)), of length 1.78 Å (the H-bond length is significantly shorter than that of ammonia making a single acceptor bond, 1.86 Å). The $E_{i,QC}^{\text{th}}$ increases from 404.7 eV (isolated TMA, the experimental value is 404.8 eV [206]) to 405.3 eV (TMA(A)). The large increase of +0.6 eV is due to the positively charged H at a short distance. Thus, considering the experimental work function of (H,OH)-Si(001) ($q\Phi^{\text{H,OH}} = 4.4$ eV), the expected binding energies of TMA adsorbed molecularly on the surface should range between 400.3 eV and 400.9 eV. This binding energy interval makes us confident that the component centred at a binding energy of 400.5 eV is due to molecular TMA. The question of H-bonding with the SiOH is more complex. The experimental peak centroid is 0.4 eV lower in energy than that we expect from the calculation for TMA(A), but the peak width (1.5 eV) is sufficiently large to encompass various configurations. For instance TMA may make multiple acceptor configurations with longer H-bonds (as it is the case for ammonia with two OHs in a stripped), which would lead to a smaller $E_{i,QC}^{\text{th}}$. The existence of adsorbed molecular TMA is confirmed by the peak at 286.50 eV in the experimental C 1s spectrum of panel V.8(d). Indeed, the measured gas phase C 1s ionisation energy of TMA is 291.26 eV [206], and subtracting $q\Phi^{\text{H,OH}}$ we find an estimated binding energy of 286.8 eV, close to the experimental one. The kinetics in Figure V.8(c) shows that for Q of 0.2 ML (140 s), the coverage reached by the molecular species is 0.08 ML. This will correspond to an approximate sticking probability of ~ 0.4 (pressure gauges are not corrected). If the sticking probability remains the same, the estimated coverage of molecularly adsorbed TMA (top curve in panel V.8(b)) could reach 0.5 ML at $Q = 1.3$ ML. When the TMA pressure goes to zero after stopping the dosing, the coverage decreases by 0.04 ML between 140 s and 1600 s (see panel V.8(c)). The total nitrogen coverage also diminishes by the same value during the same duration. Therefore,

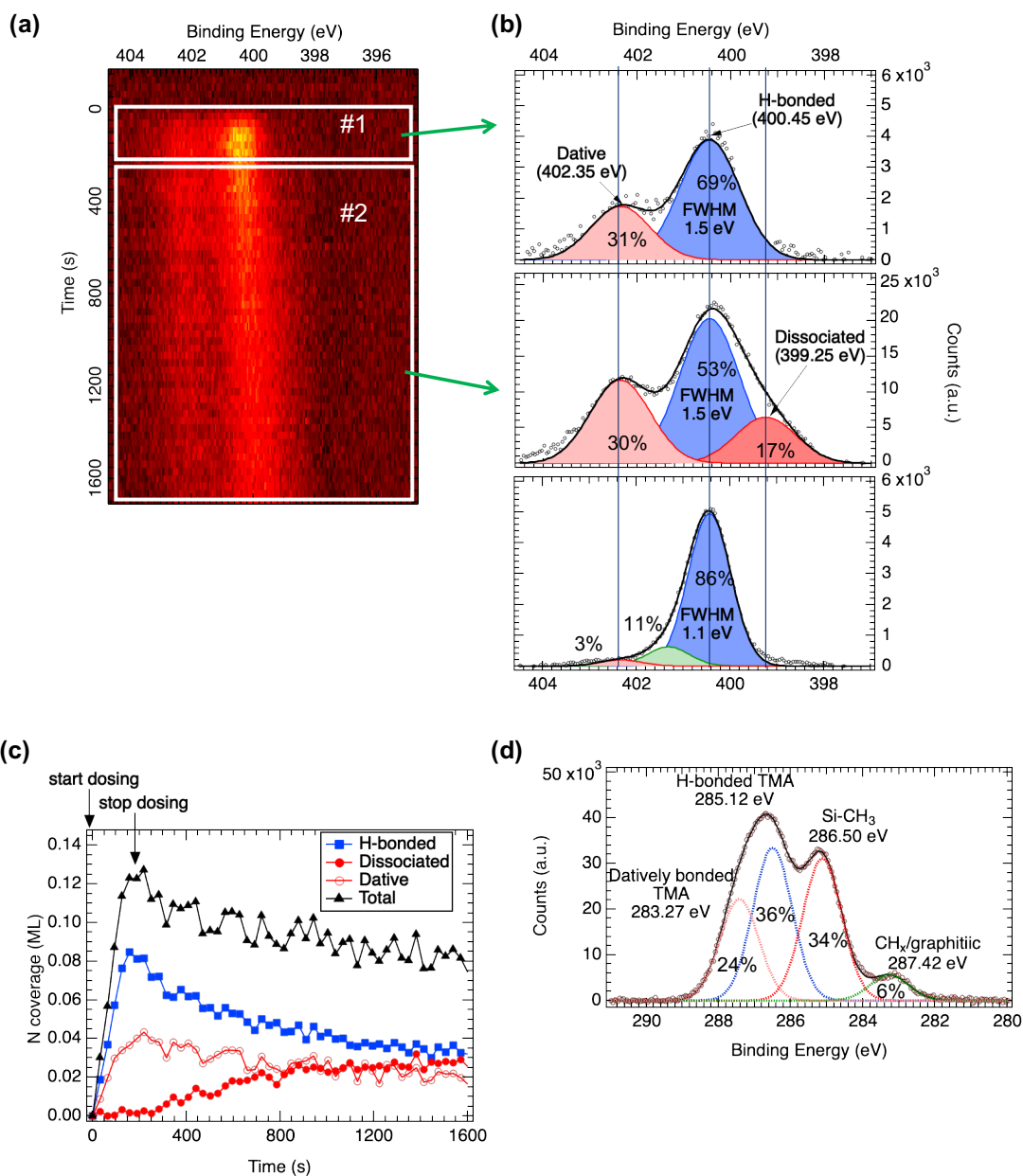


Fig. V.8 (a) Real-time $N\ 1s$ spectra measured at 130 K with a photon energy $h\nu$ of 455 eV over a total duration of 1200 s. TMA dosing (5×10^{-9} mbar) is interrupted after 140 s (Q is equal to 9×10^{14} molecules cm^{-2} , or 0.2 ML). (b) The top curve is the sum of the $N\ 1s$ spectra (box #1 in panel (a)) recorded during the first 140 s, the middle one is the sum of $N\ 1s$ spectra measured after pumping the gas (box #2 in panel (a)), and the bottom curve corresponds to a TMA exposure of 900 s in the absence of the X-ray beam (Q is equal to 1.4×10^{14} molecules cm^{-2} , or 1.3 ML). (c) Normalised surface nitrogen coverage (total) and of the three species deduced from the fitting of the $N\ 1s$ spectra in panel (a). (d) Control $C\ 1s$ spectrum ($h\nu = 350$ eV) measured immediately after the real-time $N\ 1s$ XPS monitoring of panel (a). All binding energies are referenced to a common $\text{Si}\ 2p_{3/2}$ binding energy at 99.41 eV. In panels (b) and (d) the curves are fitted with sum of Gaussians whose FWHM, binding energies and spectral weights are indicated.

molecularly adsorbed TMA leaves the surface under vacuum.

We will now consider the component at a high binding energy of 402.4 eV. At $Q = 0.2$ ML (140 s of dosing), the coverage of this species is 0.04 ML. The bottom curve in panel V.8(b) obtained for the maximum dose Q of 1.3 ML shows also a small but sizeable spectral contribution (3% of the spectral weight) at 402.4 eV. Thus, the coverage of this species remains in the 10^{-2} ML range (about 0.08×0.4 ML, that is 0.03 ML) even for a large Q of 1.3 ML. This coverage is close to the surface density of the IDBs (~ 0.04 ML), we can first consider that TMA molecules can bind to these uncapped silicon atoms via a dative bond. Indeed, the observed binding energy (400.4 eV) matches exactly that of tertiary amines (TMA [221] and triethylamine [212]) datively bonded on clean Si(001)- 2×1 . Moreover, the higher binding energy peak at 287.4 eV in the C 1s spectrum (panel V.8(d)) matches also that of the methyl moieties of datively bonded TMA on the clean surface [221]. The $E_{i,QC}^{\text{th}}$ of TMA adsorbed on a bare dimer (using a Si_9H_{12} cluster mimicking the adsorption on the clean surface, see Figure V.7(c)) is 406.8 eV, which corresponds to an expected binding energy of 402.4 eV after subtraction of $q\Phi^{\text{H,OH}}$, which is in excellent agreement with the experimental value. However, on the clean surface two paired dangling bonds are available, the negatively charged up dimer atom, and the positively charged down dimer atom that acts as the Lewis acid site in the dative bond formation. The adsorption geometry depicted in Figure V.7(d) shows that the IDB of the water-covered surface are not necessarily adjacent (as it is the case of the clean surface). Figure V.7(d) shows also interesting features that are a manifestation of the local charge density. One can note that the H atom of the hydroxyl facing the adsorbed molecule is repelled. This indicates that the molecule is electron-poor (in a Lewis scheme, the datively bonded species bears a positive formal charge). On the contrary, the hydrogen of the hydroxyl placed in front of the unoccupied silicon dangling bond is attracted to the latter. This shows that the remaining dangling bond is electron-rich (indeed the dimer buckles, with the “negative” silicon moving up). This calculation simply suggests that dative bonding on an IDB is feasible only when an electron “sink” is available. On a small “molecular cluster” the sink is the uncapped silicon atom. On the real, extended surface, the electronic charge could be pushed away from the surface into bulk silicon by the insertion of the Lewis base lone-pair into IDB.

The low binding energy component at 399.25 eV, which, we suspect, is due to beam decomposition, is absent during the gas exposure, but gradually increases with time reaching 0.03 ML after 1600 s of measurement. The binding energy matches indeed that of the Si-N(CH₃)₂ moiety, resulting from the dissociative adsorption of TMA via N-C bond cleavage on the bare dimer of the clean surface (see Figure V.7(a)) [221]. The cluster

QC DFT calculation predicts an $E_{i,\text{QC}}^{\text{th}}$ of 403.7 eV for Si-N(CH₃)₂, which leads to an expected binding energy of 399.3 eV, after subtraction of the work function of the pristine water-covered surface, in good accord with the observed value. At the end of the real-time N 1s XPS monitoring, without moving the X-ray spot, we have immediately recorded a control C 1s spectrum, shown in Figure V.8(d). If we exclude the one at 283.42 eV that is a CH_x/graphitic contamination [222], the spectrum is fitted with three components related to the TMA molecule, among which the component at 285.0 eV is representative of the Si-CH₃ moiety [221]. This is not only a further proof of the breaking of the N-C bond. It shows that the CH₃ fragment attaches to a silicon atom (indeed the CH₃ could recombine with a surface hydride to form a volatile methane molecule, or with an OH to produce a methanol molecule). The kinetics in Figure V.8(d) show also that the increase in coverage of dissociated TMA (0.02 ML at 1600 s) mirrors the decrease of the datively bonded species. This may mean that the dissociated species results from the dissociation of the datively bonded species under the beam.

Contrary to ammonia, the breaking of TMA on two distant IDBs is obviously impossible as there are no H bonds between these tertiary amine molecules. Thus N-C bond cleavage is certainly due to the beam. As for the case of NH₃, the effect of light is indirect involving secondary electrons induced by the X-ray beam. For TMA in the gas phase, a dissociative attachment resonant state is observed at about 6 eV above the vacuum level [223]. Attachment-dissociation can lead to the breaking of the adsorbed molecule into N(CH₃)₂[•] + CH₃⁻ or N(CH₃)₂⁻ + CH₃[•]. If a TMA molecule datively bonded to an IDB breaks after attaching an electron, a Si-N(CH₃)₂ moiety will form, and the leaving CH₃ will react further apart forming a new bond, e.g. abstracting another H from a Si-H to form a methane molecule, or breaking a Si-Si bond to form Si-CH₃, etc.

A second hypothesis may be that for H-bonded or physisorbed molecules, the formation of a Si-N(CH₃)₂ moiety may need two steps. In a first instance, a radical (CH₃[•] or N(CH₃)₂[•]) abstracts one H from a surface hydride (generating a CH₄ or a NH(CH₃)₂ molecule). This leaves a Si[•] which, in a second instance, captures other N(CH₃)₂[•] or CH₃[•] radicals. In any case, Si-N(CH₃)₂/Si-CH₃ formation via a mechanism involving the considered radicals does not necessarily require the occurrence of two adjacent silicon dangling bonds.

V.5 Conclusion

The combination of cluster quantum chemistry DFT calculations with core-electron (XPS) spectroscopy was effective to determine the adsorption geometries of NH_3 and trimethylamine probing surface hydroxyls and isolated dangling bonds of the water-reacted (H,OH)-Si(001) surface (n^+ substrate) at cryogenic temperatures (130 K).

For the case of ammonia, periodic DFT was used to calculate adsorption energies E_{ads} and N 1s core-level binding energy shifts relative to dissociated ammonia (SiNH_2), while Quantum Chemistry DFT was adopted to calculate N 1s and O 1s ionisation energies ($\Delta E_{i,\text{QC}}^{\text{th}}$) using ad-hoc clusters describing the adsorption geometries. We find that the periodic DFT N 1s core-level binding energy shifts $\text{CLS}_{\text{per}}^{\text{th}}$ and the cluster quantum chemistry N 1s $\Delta E_{i,\text{QC}}^{\text{th}}$ are in excellent agreement, supporting of the validity of the approaches applied.

The theory-assisted interpretation of the N 1s spectra leads to the conclusion that each ammonia molecule sticks molecularly to the surface at 130 K, making one H-acceptor and one H-donor bonds with a pair of OHs. Under a pressure of 5×10^{-9} mbar, the maximum coverage achieved is ~ 0.35 ML. However, when ammonia is pumped down, the H-bonded ammonia coverage diminishes due to desorption. The estimated barrier energy for desorption is $\Delta G^\ddagger \approx 0.4$ eV. This value can be compared to the “binding strength” $-E_{\text{ads}}$ of acceptor-donor geometries that are comprised between 0.56 eV and 0.69 eV, according to periodic DFT calculations (at $T = 0$ K).

Besides the non-covalent, reversible attachments, XPS shows that about 4×10^{-2} monolayers of ammonia molecules are datively bonded to the silicon dangling bonds present on the surface. Molecular dissociation is also observed (Si-NH₂ fragments are detected by XPS), largely due to beam damage.

The adsorption of trimethylamine shows strong similarities with that of ammonia. Trimethylamine molecules make acceptor H-bonds with the surface OH. This results in an N 1s binding energy in good agreement with the calculations. Other species are observed on the surface. Trimethylamine can bond molecularly to the isolated dangling bonds remaining on the surface, reaching a surface coverage of a few hundredth of a monolayer. XPS shows also that the synchrotron beam favours the dissociation of trimethylamine via N-C bond cleavage, the mechanism of which remains elusive.

Until now, the (large) effects of H-bonding on nitrogen and oxygen 1s core-level binding energies have been insufficiently addressed in the XPS literature, probably because of the

lack of theoretical support. We hope that the present work will stimulate further XPS studies, in contexts where H-bonding is of primary importance, from water/solid interfaces to supramolecular chemistry.

Conclusion and Perspectives

Throughout this thesis, the outstanding capabilities of X-ray photoemission spectroscopy for the study of several interfaces have been displayed. It has been shown how the use of modern XPS techniques, like Near-Ambient Pressure XPS and liquid-jet XPS, has allowed to overcome the two main challenges associated to interface characterisation nowadays, namely, the aim to emulate “real-life” conditions and the need for a comprehensive view that relates both the chemical and the electronic-structure related information of a particular reaction. Indeed, although the first challenge was surmounted a decade ago via instrumental improvements of the conventional technique, the second one has driven me to revisit the basic elements underlying thermodynamic equilibrium and correctly apply them for a proper understanding of the electronic band alignment during interfacial phenomena. The major objective of this theoretical review was to clarify the difference between the so-long mixed up concepts of electrochemical potential $\tilde{\mu}$ and work function $q\Phi$, due to a confusion between the thermodynamic vacuum level E_{vac}^{∞} and the vacuum level local to a sample $E_{\text{vac}}^{\text{s}}$, despite the illuminating review made by Egelhoff in 1979 [11].

During my PhD, I made use of *in situ* real time XPS to study varied interfacial phenomena and understand (i) the chemical processes taking place at the atomic scale, (ii) the electronic level alignment which drive these chemical reactions.

The first project treated the electronic level alignment at a metal/oxide/gas interface during the oxidation of the Al(111) surface in O₂ atmosphere. By following the growth of the oxide via NAP-XPS the aim was to relate the kinetics of the oxidation of the Al(111) surface under an O₂ atmosphere with changes in the band energies. After considering the thermodynamic basis of the Cabrera-Mott model for metal oxidation and having discussed the observed changes in the band bending with pressure and thickness, it was possible to validate the main hypothesis of the model; this is, the existence of an electric field that facilitates the transport of ionic species. The methodology presented here is effective and can be generalised beyond the specific case of aluminium oxidation. Indeed, one could go

long way off bulk materials and refer, for example, to the case of the enhanced oxidation of Fe nanoparticles which are seen as promising candidates for applications within the fields of data storage and ground water remediation [224]. This kind of systems could surely benefit from the detailed chemical and electronic-related description that XPS offers.

The second project studied the alignment of electronic energy levels at a metal/liquid interface in the presence of redox couple. This was a follow-up of the prospect previously proposed by Anthony Boucly in this PhD thesis [225], who was intrigued by the question of the band alignment in electrochemical solutions and laid the groundwork of the liquid-jet experiment done here. The experiment was based on this simple principle: that the Fermi level and the redox potential in solution denote the same thing and they must be aligned when thermodynamic equilibrium is reached. The use of a well-defined redox couple was, thus, essential to fix the Fermi level of the system which was used as reference for the energy scale calibration. The ionisation energy associated to the water $1b_1$ liquid phase peak was determined and compared with the results previously obtained by other authors. It was proved that the surface dipole of a solution could be deliberately modified and that this inevitably led to a modification of the position of the vacuum level of the sample. This demonstrated the initial hypothesis of considering $E_{\text{vac}}^{\text{s}}$ as an inconvenient reference for liquid-phase measurements. The calibration procedure presented here can be used for further research of complex electrochemical systems that requires the analysis of the interfacial electronic structure and the determination of other relevant thermodynamic parameters.

The third and last project was focused on the studying the reactivity of well-known model surface, the water-saturated Si(001)- 2×1 , exposed to two Lewis bases, trimethylamine (TMA) and ammonia (NH_3), at cryogenic temperatures. The investigation made use of experimental (XPS) and theoretical (DFT calculations) tools to elucidate the nature of the bonding of each molecule with the surface, which can be summarised as hydrogen bonding with surface hydroxyls and dative bonding with the silicon isolated dangling bonds present on the surface. Adsorption and desorption kinetics were also discussed for the case of ammonia. This last chapter highlights the competency of photoemission spectroscopy in terms of chemical specificity and points out to the advantages of having a combined view of experimental data with quantum chemistry calculations, as both kinds of information can be complementary in any type of study. This is an approach that should be given to most of the atomic-scale surface phenomena, when possible.

Appendix A

A.1 A Small Review in Thermodynamics

The First Law of thermodynamics applies the conservation of energy principle to systems where heat transfer and work can take place. It states that every thermodynamic system possesses a characteristic property known as the internal energy, U , and any net change dU is either due to heat exchanged or work done [226]. This can be expressed mathematically as

$$dU = \bar{d}q + \bar{d}w, \quad (\text{A.1})$$

where the symbol \bar{d} is used to represent an inexact differential, as it is the case for path dependent quantities like heat and work.

Let us consider a closed system of one chemical component (e.g. a pure substance) in a single homogeneous phase where changes are brought reversibly¹. In this case, the only kind of possible work is expansion work expressed as $\bar{d}w_{\text{rev}} = -pdV$. The reversible change in heat is given by the Second Law of thermodynamics derived from Clausius inequality [228], which states that $\bar{d}q_{\text{rev}} = TdS$. Thus, equation (A.1) can be rewritten as

$$dU = TdS - pdV. \quad (\text{A.2})$$

One may think that this formula only applies for reversible processes. Remember,

¹According to Sommerfeld [227], ‘reversible processes’ are not, in fact, processes at all. They are sequences of states of equilibrium so that the system and surroundings can be restored to the initial state from the final state without producing any changes elsewhere in the universe.

however, that dU is a state function independent of path (a perfect differential). This means that $dU_{\text{rev}} = dU_{\text{irrev}} = dU$. Therefore, equation (A.2) applies irrespective of whether the change is brought about reversibly or irreversibly, and is usually known as the *Gibbs equation*.

A.1.1 The Chemical Potential

From the form that equation (A.2) appears, the most sensible way of considering U is as a function of S and V . The mathematical consequence of this is that we can identify the coefficients of dS and dV as²

$$T = \left(\frac{\partial U}{\partial S} \right)_V, \quad (\text{A.3})$$

$$-p = \left(\frac{\partial U}{\partial V} \right)_S. \quad (\text{A.4})$$

In a similar fashion, we can then consider a one-phase-one-substance open system where the amount n of components (particles, moles) may vary. The expression for dU now becomes a function of three independent variables, S , V and n , and can be written as

$$dU = \left(\frac{\partial U}{\partial S} \right)_{V,n} dS + \left(\frac{\partial U}{\partial V} \right)_{S,n} dV + \left(\frac{\partial U}{\partial n} \right)_{S,V} dn, \quad (\text{A.5})$$

where the third partial derivative $(\partial U/\partial n)_{S,V}$ is represented by the symbol μ and is a state function known as the **chemical potential** [229]. One may think of it as a ‘chemical work’ related to changing the number of components in a system. With these substitutions, equation (A.5) becomes

$$dU = TdS - pdV + \mu dn. \quad (\text{A.6})$$

It appears to be that an expression for the chemical potential subjected to constant V and S while the number of particles changes is not very convenient when treating condensed matter systems, where volume and entropy are, in fact, not easy to control. Although the internal energy is a natural variable and leads to various equations between the thermodynamic properties of a system, another set of variables can be introduced by

²By Euler’s reciprocity relation.

making transforms³ [230]. One of these variables is the Gibbs energy G , defined as

$$G = U + pV - TS. \quad (\text{A.7})$$

Taking its derivative and combining it with equation (A.6), it is possible to get

$$dG = Vdp - SdT + \mu dn. \quad (\text{A.8})$$

This expression can be extended to systems containing a mixture of substances where the amount of each substance can vary independently. This extended form is usually known as the *Gibbs fundamental equation* and is written as

$$dG = Vdp - SdT + \sum_i \mu_i dn_i, \quad (\text{A.9})$$

where

$$\mu_i = \left(\frac{\partial G}{\partial n_i} \right)_{T,p,n_{j \neq i}}. \quad (\text{A.10})$$

This last formula gives a definition of the chemical potential easier to use experimentally [231].

A.1.2 The Electrochemical Potential

We shall now think of a system where component i is no longer electrically neutral. One mol of that i -th component carries a charge $z_i F$, where F denotes the Faraday constant, a number that represents the magnitude of electric charge per mole of electrons ($\sim 96494 \text{ C mol}^{-1}$)⁴. The system under consideration is said to have an electrical potential ϕ with respect to an hypothetical ‘ground’ at potential zero. The introduction of dn_i moles of charged particles into the system entails the realisation of an electrical work $\phi z_i F dn_i$ in addition to the already defined ‘chemical work’ $\mu_i dn_i$. The expression for internal energy becomes

³Legendre transforms define new thermodynamic potentials, such as enthalpy H , Helmholtz energy A , and Gibbs energy G by subtracting one or more products of conjugate variables from the internal energy [230].

⁴The Faraday constant is just the product between the elementary charge, $e = 1.602176634 \cdot 10^{-19} \text{ C}$ and the Avogadro constant, $N_A = 6.0221407610 \cdot 10^{23} \text{ mol}^{-1}$.

$$dU = TdS - pdV + \sum_i \mu_i dn_i + \sum_i z_i F \phi dn_i, \quad (\text{A.11})$$

or, combining the two last summations,

$$dU = TdS - pdV + \sum_i \tilde{\mu}_i dn_i, \quad (\text{A.12})$$

where

$$\tilde{\mu}_i = \mu_i + z_i F \phi. \quad (\text{A.13})$$

Guggenheim [232] defined this term as the **electrochemical potential**. Bear in mind that “the conception of splitting the electrochemical potential $\tilde{\mu}_i$ into the sum of a chemical term μ_i and an electrical term $z_i \phi$ has no physical significance”. All forces between atoms and charged entities are fundamentally electrical in nature. However, it is a useful conceptual tool (as many of the notions that will be viewed in this chapter). Finally, it can be easily proved that

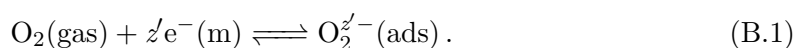
$$\tilde{\mu}_i = \left(\frac{\partial G}{\partial n_i} \right)_{T,p,n_{j \neq i}}. \quad (\text{A.14})$$

Hence, we have a quantity which depends on the chemical constitution of the material, and on the electron density, but not on the electrostatic potential.

Appendix B

B.1 A thermodynamic approach of the Cabrera-Mott potential

We consider the non-dissociative adsorption of an O_2 molecule from the gas phase ($O_2(\text{gas})$) onto the surface of the oxide. The adsorbed molecule has charge $z'q$ (z' is a positive integer equal to 1 or 2, $q < 0$ is the electron charge) depending on the oxide thickness (see e.g. ref [102]). Thus, the adsorption reaction can be written



At thermodynamic equilibrium we get an equation between the chemical potential of $O_2(\text{gas})$, $\mu_{O_2(\text{gas})}$, the electrochemical potentials of the electron in the metal $\tilde{\mu}_m$ (for simplicity $m\mu_m$ includes the electrostatic term due to the attraction of the nuclei, see Egelhoff [11]) and the electrochemical potential of $O_2^{z'-}(\text{ads})$, $\tilde{\mu}_{O_2^{z'-}(\text{ads})}$.

$$\mu_{O_2(\text{gas})} + z'\tilde{\mu}_m = \tilde{\mu}_{O_2^{z'-}(\text{ads})}. \quad (\text{B.2})$$

The metal is at potential $qV_{m/o}$ and the oxide surface where the molecular anions are sitting is at potential $qV_{o/g}$. As

$$\mu_{O_2(\text{gas})} + z'\mu_m + z'qV_{m/o} = \mu_{O_2^{z'-}(\text{ads})} + z'qV_{o/g}. \quad (\text{B.3})$$

Then the Cabrera-Mott potential qV_{CM} is:

$$z'q(V_{\text{o/g}} - qV_{\text{m/o}}) = \mu_{\text{O}_2(\text{gas})} + z'\mu_{\text{m}} - \mu_{\text{O}_2^{z'-}(\text{ads})} = -\Delta G_{\text{ads}} \quad (\text{B.4})$$

where $-\Delta G_{\text{ads}}$ is the Gibbs adsorption energy (per molecule). Equation (B.4) is simply the usual Nernst equation of electrochemistry.

From (B.4) one gets the Cabrera-Mott potential qV_{CM} (an upward band bending $qV_{\text{bb}} > 0$):

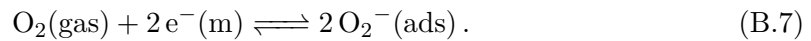
$$qV_{\text{CM}} = q(V_{\text{o/g}} - qV_{\text{m/o}}) = -\frac{\Delta G_{\text{ads}}}{z'}, \quad (\text{B.5})$$

or

$$qV_{\text{CM}} = z'^{-1} \cdot \left(\mu_{\text{O}_2(\text{gas})} - \mu_{\text{O}_2^{z'-}(\text{ads})} \right) - (-\mu_{\text{m}}), \quad (\text{B.6})$$

Cabrera and Mott have assimilated $-\mu_{\text{m}}$ with the clean metal work function ($q\Phi_{\text{m}}$) and $\mu_{\text{O}_2(\text{gas})} - \mu_{\text{O}_2^{z'-}(\text{ads})}$ with the electron affinity energy of the O_2 molecule at the surface of the oxide. The work function and the affinity are measured with respect to the vacuum level local to the sample $E_{\text{vac}}^{\text{s}}$, the one which is accessible to measurement (Kelvin probe, or SEEDC cutoff). Not being referred to E_{vac}^{∞} , they can not be thermodynamic entities [11]. In the original Cabrera-Mott model, qV_{CM} is independent from the O_2 pressure p_{O_2} . In fact, the dependence of qV_{CM} on p_{O_2} stems naturally from equation (B.5), as ΔG_{ads} is pressure dependent.

If now we consider the following dissociative absorption reaction assumed to be at equilibrium:



then qV_{CM} writes as

$$2qV_{\text{CM}} = \mu_{\text{O}_2(\text{gas})} + 2\mu_{\text{m}} - 2\mu_{\text{O}_2^{z'-}(\text{ads})} = -\Delta G_{\text{ads}} \quad (\text{B.8})$$

Therefore, also in the case of dissociative adsorption:

$$qV_{\text{CM}} = -\frac{\Delta G_{\text{ads}}}{z'}, \quad (\text{B.9})$$

where z' is the number of transferred electrons. In (B.7), thermodynamic equilibrium requires that two $\text{O}_2^-(\text{ads})$ ions can recombine to reform an O_2 molecule that escapes in the gas phase.

B.2 Data treatment

B.2.1 Photon energies, inelastic mean free paths according to kinetic energy

Two different runs of experiments were performed at photon energies of 150 eV and 600 eV respectively. Table B.1 reports the inelastic mean free paths (as calculated from Tanuma's TPP-2 predictive IMFP formula [124]) in metallic Al and in Al_2O_3 for kinetic energies that correspond to the Al 2p core-level.

Table B.1: Inelastic mean free path values for metallic Al (λ_{m}) and Al_2O_3 (λ_{ox}) calculated with Tanuma's TPP-2 formula [124].

$h\nu$ (eV)	E_{kin}	λ_{m} (nm)	λ_{ox} (nm)
150	77.6	0.48	0.70
600	526.3	1.46	1.58

B.2.2 Curve fitting

The following describes the whole curve fitting procedure for each Al 2p spectra. After a Shirley-type background subtraction, the Al 2p_{1/2} component is stripped of the Al 2p doublet, following the method given in ref. [123]; we consider a 2p_{1/2}:2p_{3/2} branching ratio of 0.5 and a spin-orbit splitting of 0.41 eV [233] (see Figure B.1).

Then, all spectra were numerically fit with 5 components whose interpretation is based on previous peak assignments [125, 126, 234]. The components corresponding to Al atoms in the bulk (72.68 eV), and surface aluminium atoms bound to one (+0.45 eV), two (+0.88 eV), or three (+1.42 eV) chemisorbed oxygen atoms are fitted with Voigt curves, i.e. the convolution of a Gaussian (of full width at half maximum GW) by a Lorentzian

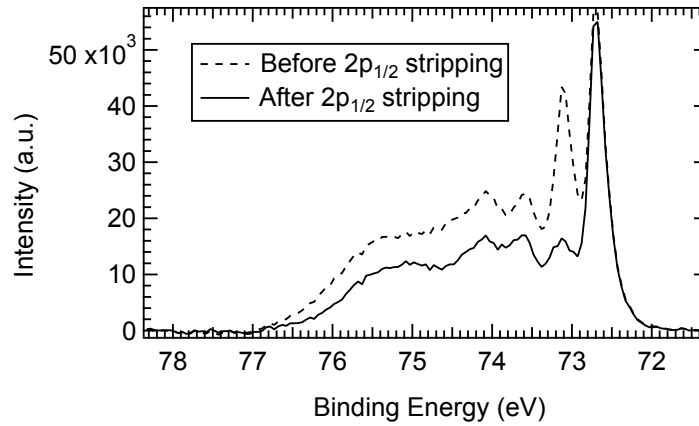


Fig. B.1 *Al 2p_{1/2} spin-orbit stripping.*

(of full-width at half maximum LW). The LW was fixed at a value of 48 meV while the GW varied for each component. Only the oxide component related to amorphous Al_2O_3 was fitted using a Gaussian curve. A fit example is shown in Figure B.2, along with the corresponding fitting parameters in Table B.2. All components remained fixed in position along oxygen exposure except for the stoichiometric Al_2O_3 component whose position varied between 74.84–75.49 eV (with a precision of ± 0.15 eV).

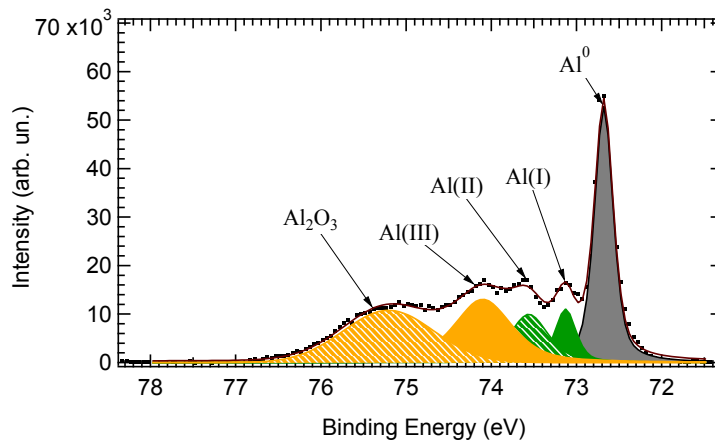


Fig. B.2 *Al 2p spectrum of the Al(111) surface during exposure to 10^{-6} mbar of O_2 , after background subtraction and stripping of the $2p_{1/2}$ component.*

Table B.2: Binding energy positions (eV), Lorentzian and Gaussian widths of each component shown in Figure B.2.

Component	Al 2p _{3/2} binding energy (eV)	Core-level shifts (eV)	LW (eV)	GW (eV)
Al ⁰	72.68	0	0.480	0.261
Al(I)	73.13	+0.45	0.480	0.290
Al(II)	73.56	+0.88	0.480	0.530
Al(III)	74.10	+1.42	0.480	0.800
Al ₂ O ₃	74.84-75.49	+2.16 – 2.81	0.480	1.252

B.2.3 Calculation of thicknesses

In XPS, the intensity (I_A) of a photoelectron peak from element A in a solid is given in a simplified form, by:

$$dI_A = J(h\nu) \cdot n_A \sigma_A L_A \cdot \exp\left(-\frac{z}{\lambda_A \cos\theta}\right) dz, \quad (\text{B.10})$$

where $J(h\nu)$ is the photon flux, n_A is the number of atoms per volume unit, σ_A is the cross section, L_A the anisotropy factor, λ_A the inelastic mean free path of element A, z the depth and θ the emission angle. If separately integrating the formula for a layer of Al₂O₃ of thickness X , and for an infinite solid Al under this layer, considering normal emergence ($\theta = 0$), same photon flux, same geometry and same cross section, one can find the ratio of intensities to be:

$$\frac{I_{\text{Al}_2\text{O}_3}}{I_{\text{Al}}} = \frac{n_{\text{Al}_2\text{O}_3} \lambda_{\text{Al}_2\text{O}_3} \left[\exp\left(\frac{X}{\lambda_{\text{Al}_2\text{O}_3}}\right) - 1 \right]}{n_{\text{Al}} \lambda_{\text{Al}}}. \quad (\text{B.11})$$

So, it is possible to calculate the thickness of the oxide layer as

$$X = \lambda_{\text{Al}_2\text{O}_3} \left(\ln \left(1 + \frac{I_{\text{Al}_2\text{O}_3} n_{\text{Al}} \lambda_{\text{Al}}}{I_{\text{Al}} n_{\text{Al}_2\text{O}_3} \lambda_{\text{Al}_2\text{O}_3}} \right) \right) \quad (\text{B.12})$$

Values for inelastic mean free paths are found in Table B.1. n_{Al} and $n_{\text{Al}_2\text{O}_3}$ are calculated as:

$$n_{\text{Al}} = \frac{\rho_{\text{Al}}}{M_{\text{Al}}/N_{\text{Al}}} = \frac{2.70 \times 6.022 \cdot 10^{23}}{27} = 6.022 \cdot 10^{22} \text{ at} \cdot \text{cm}^{-3} \quad (\text{B.13})$$

$$n_{\text{Al}_2\text{O}_3} = \frac{\rho_{\text{Al}_2\text{O}_3}}{M_{\text{Al}_2\text{O}_3}/N_{\text{Al}_2\text{O}_3}} = \frac{2.70 \times 6.022 \cdot 10^{23}}{27} = 6.022 \cdot 10^{22} \text{ at} \cdot \text{cm}^{-3} \quad (\text{B.14})$$

I_{Al} corresponds to the intensity of the bulk metal component while $I_{\text{Al}_2\text{O}_3}$ is the sum of all oxide component intensities.

B.3 Measurement of $E_{\text{b,Al}2\text{p}_{3/2}}^{\text{Al}_2\text{O}_3} - E_{\text{bVBM}}$

$E_{\text{b,Al}2\text{p}_{3/2}}^{\text{Al}_2\text{O}_3} - E_{\text{bVBM}}$ is plotted against thickness in Figure B.3. Note that this difference is a constant (worth 70.70 eV with a standard deviation of $\sigma = 0.04$ eV) once a continuous film is formed ($X = 1.4$ nm). Indeed changes in E_{b} can be translated into E_{F} changes in the oxide gap provided the oxide is not n-type degenerated [235]. For ultra-thin films below 1.4 nm, dielectric discontinuity effects could be considered [236,237]. The core-hole created in Al_2O_3 is stabilised by its image force in the metal, especially since it is produced closer to the metal/oxide interface. Therefore, the relaxation energy decreases for oxide layers close to the oxide/gas interface, and the E_{b} increases. Taking into consideration the short IMFP, the E_{b} should increase with increasing oxide thicknesses.

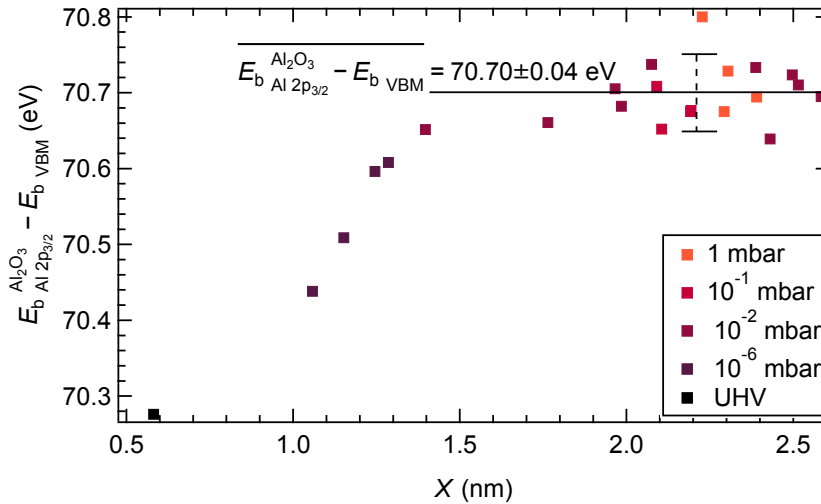


Fig. B.3 Measurement of $E_{\text{b,Al}2\text{p}_{3/2}}^{\text{Al}_2\text{O}_3} - E_{\text{bVBM}}$ against oxide thickness (the O_2 pressure program). Pressures are also given. The average value is calculated for $X > 1.4$ nm.

B.4 Measurement of the oxide gap

The oxide band gap was experimentally determined following the method proposed by Miyazaki [121], which consists in measuring the energy losses of the O 1s core-level (see Figure B.4). Electronic excitations such as plasmons and band-to-band transitions in dielectric thin films appear at lower kinetic energy than the primary core-line peak. For alumina, the plasmon energy (centroid at ~ 23.5 eV, see also Perevalov et al. [238]) is much larger than that of the valence-to-conduction band excitation. Therefore, the band-gap energy values can be determined from the threshold energy of the energy-loss spectrum, as shown in Figure B.4. The onset of the energy-loss spectrum is obtained by linearly extrapolating the segment of maximum negative slope to the background level. The band-gap value determined for Al_2O_3 films of thickness ~ 3 nm is 7.10 ± 0.11 eV, in excellent agreement with the experimental finding of Miyazaki et al. (6.95 eV). These two experimental values are close to the gap of amorphous Al_2O_3 calculated using a hybrid functional, i.e. 6.64 eV [239]. Note that the gap of amorphous alumina is notably smaller than that of crystalline $\alpha\text{-Al}_2\text{O}_3$ (9.13 eV [240]).

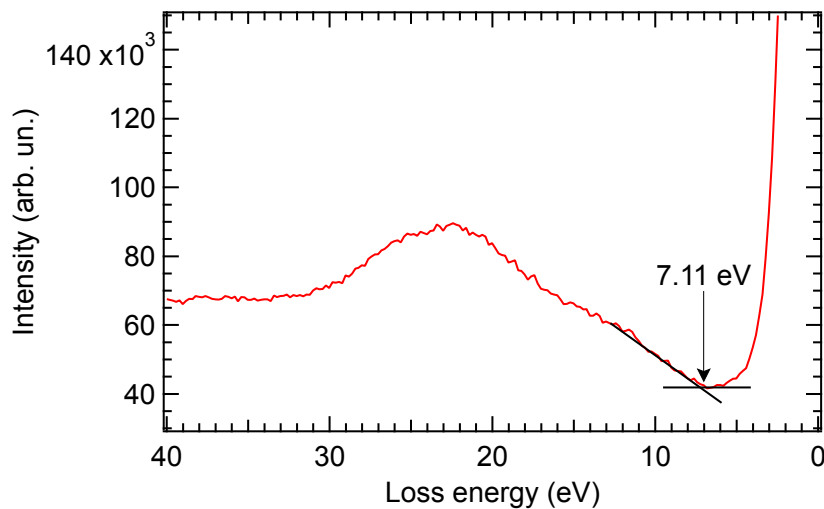


Fig. B.4 O 1s energy-loss spectra for a 3.0-nm-thick Al_2O_3 oxide film. The zero energy is the centroid of the O 1s peak. The vertical arrow indicates the onset of the valence-to-conduction band transitions. The valence electron plasmon loss occurs at 23.4 eV.

B.5 Weight of the oxide surface plane in the O 1s spectrum

For the O 1s spectrum, measured at $h\nu = 600$ eV ($E_{\text{kin}} \sim 70$ eV), the spectral contribution R_{surf} of the surface plane is estimated from the formula [123]:

$$R_{\text{surf}} = 1 - \exp\left(-\frac{d_{\text{layer}}}{\lambda_{\text{ox}}}\right), \quad (\text{B.15})$$

where d_{layer} is the distance between two Al_2O_3 planes (~ 0.2 nm [102]) and λ_{ox} is 0.7 nm [124]. We find $R_{\text{surf}}=0.25$.

B.6 Effect of band bending on the measured binding energies

The x axis is oriented from the oxide/gas interface ($x = 0$) to the metal/oxide interface ($x = X$). λ_{ox} is the inelastic mean free path of the photoelectrons in the oxide. E_{bVBM} is assumed to follow a linear relationship with x ($qV_{\text{bb}} = E_{\text{bVBM}}^{\text{m/o}} - E_{\text{bVBM}}^{\text{o/g}}$):

$$E_{\text{bVBM}}(x) = E_{\text{bVBM}}^{\text{o/g}} + \frac{E_{\text{bVBM}}^{\text{m/o}} - E_{\text{bVBM}}^{\text{o/g}}}{X}x, \quad (\text{B.16})$$

where $E_{\text{bVBM}}^{\text{m/o}} - E_{\text{bVBM}}^{\text{o/g}}$ is the “true” qV_{bb} .

Then the measured value E_{bVBM} is the averaged value of $E_{\text{bVBM}}(x)$:

$$E_{\text{bVBM}} = \langle E_{\text{bVBM}}(x) \rangle = E_{\text{bVBM}}^{\text{o/g}} + \frac{\int_0^X \left(\frac{E_{\text{bVBM}}^{\text{m/o}} - E_{\text{bVBM}}^{\text{o/g}}}{X} \right) x e^{-\frac{x}{\lambda_{\text{ox}}}} dx}{\lambda_{\text{ox}}}, \quad (\text{B.17})$$

$$\langle E_{\text{bVBM}}(x) \rangle = E_{\text{bVBM}}^{\text{o/g}} + \left(E_{\text{bVBM}}^{\text{m/o}} - E_{\text{bVBM}}^{\text{o/g}} \right) \times \left(\frac{\lambda_{\text{ox}} - (\lambda_{\text{ox}} + X)e^{-\frac{X}{\lambda_{\text{ox}}}}}{X} \right). \quad (\text{B.18})$$

E_{bVBM} is measured experimentally (for $\lambda_{\text{ox}} = 0.7$ nm). Then the “corrected” value $E_{\text{bVBM}}^{\text{o/g}}$ can be estimated as

$$E_{\text{bVBM}}^{\text{o/g}} = \frac{\langle E_{\text{bVBM}}(x) \rangle - G(X, \lambda_{\text{ox}}) \times E_{\text{bVBM}}^{\text{m/o}}}{1 - G(X, \lambda_{\text{ox}})}, \quad (\text{B.19})$$

$$\text{with } G(X, \lambda_{\text{ox}}) = \frac{\lambda_{\text{ox}} - (\lambda_{\text{ox}} + X)e^{-\frac{X}{\lambda_{\text{ox}}}}}{X}$$

This value is used in equation (III.7) of chapter III.

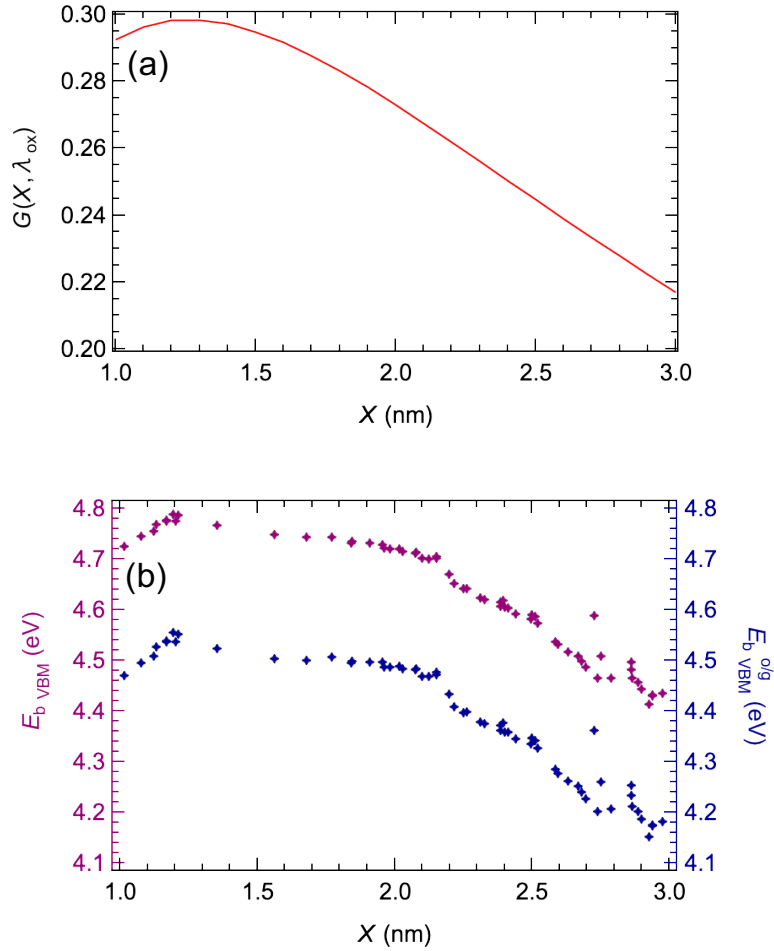


Fig. B.5 (a) Plot of the $G(X, \lambda_{\text{ox}})$ function for $\lambda_{\text{ox}} = 0.7$ nm, (b) comparison of $E_{\text{bVBM}}^{\text{o/g}}$ and the averaged measured E_{bVBM} versus X .

B.7 Uniform E and limit concentration of donors in the oxide

For a built-in potential V_{bb} , the depletion width w_{d} in a semiconductor of dopant (donor) charge concentration ρ_i is [241]:

$$w_d \ll \sqrt{\frac{2\varepsilon_0\varepsilon_r V_{bb}}{\rho_i}}, \quad (\text{B.20})$$

where ε_0 and ε_r are the vacuum permittivity and the relative dielectric constant (9.6), respectively.

The condition $w_d \gg X$, with X in the range 1 to 3 nm means that:

$$\rho_i \ll \frac{2\varepsilon_0\varepsilon_r V_{bb}}{X^2}, \quad (\text{B.21})$$

Taking $X = 2 \times 10^{-9}$ m and $V_{bb} = 1$ V, $\rho_i \ll 4.25 \times 10^7$ C · m⁻³.

For 2+ ionised donors (e.g. O vacancies), their density should be much less than 1.33×10^{26} m⁻³ (1.33×10^{20} cm⁻³).

An ionised donor density in the 10^{20} cm⁻³ range (a rather high value) means an equal density of electrons in the conduction band. We now examine the density of electrons in the conduction band that can be deduced from the positions of the Fermi level (E_F) within the band gap. The effective density of states in the conduction band of alumina is given by [241]:

$$N_C = 2 \left(\frac{2\pi m^* k_B T}{h^2} \right)^{3/2} M_C, \quad (\text{B.22})$$

where m^* is the effective mass of conduction electrons in alumina ($m^* = 0.4m$, see ref [238]), and M_C the number of equivalent minima (taken as 1). For alumina we calculate that N_C is 0.63×10^{19} cm⁻³. The density n of free electrons in the conduction band is:

$$n = N_C \exp\left(-\frac{E_{b\text{CBM}}}{k_B T}\right), \quad (\text{B.23})$$

where $E_{b\text{CBM}}$ is the binding energy of the conduction band minimum (CBM) (referred, of course, to E_F).

$E_{b\text{CBM}}$ writes as:

$$E_{b\text{CBM}} = E_g - E_{b\text{VBM}}, \quad (\text{B.24})$$

with $E_g = 7.1$ eV (see Section B.4).

E_{bCBM} is ~ 1.7 eV (at the metal/oxide interface) and varies between 2.9 and 2.6 eV at the oxide/gas surface. E_{bCBM} being always much greater than $k_{\text{B}}T$ (0.025 eV), the Boltzmann factor is $< e^{-68}$, that is $\sim 10^{-30}$. Thus, given a N_{C} of 10^{19} cm^{-3} , n is always vanishingly small.

We conclude that given the position of E_{F} in the gap it is not possible to get a density of ionised dopants as high as 10^{20} cm^{-3} . Therefore, the space charge width w_{d} is always much greater than the film thickness X and the Cabrera-Mott assumption is applicable in the case of aluminium oxidation at room temperature. Consequently, the extra charge is distributed at the oxide/gas interface (negative charge due the acceptor levels associated to the adsorbed oxygen) and at the metal/oxide interface (positive charge). Then the electric field is uniform throughout the film.

In their ab initio periodic DFT simulation, Baran and coworkers [102] have considered O_2 molecules sitting on the undercoordinated Al atoms at the surface of (0001)-oriented $\alpha\text{-Al}_2\text{O}_3$ layers supported on Al(111). For this particular form of alumina, calculations confirm the Cabrera-Mott assumption of the absence of space charge. Indeed the extra charge, calculated from differences in Bader charges, *is limited to the metal/oxide and oxide/gas interface*, which points to a uniform electric field within the oxide at a given thickness X .

B.8 Kirk and Huber data (Kelvin probe measurement, 1968)

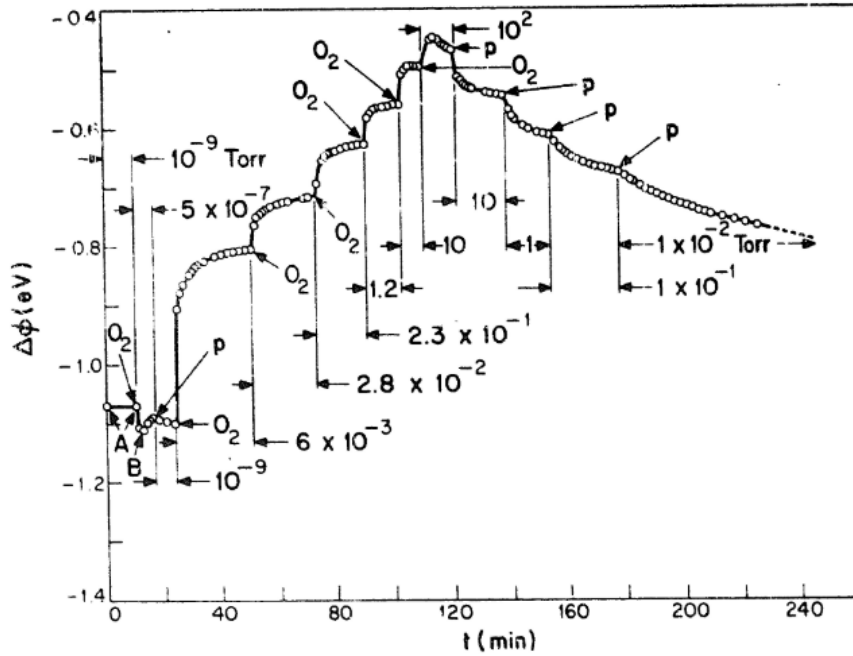


Fig. B.6 Plot of contact potential difference ($\Delta\phi$ in the figure) between an aluminium film and a gold reference electrode in an oxygen atmosphere versus time, t , with oxygen pressure as a parameter. Points A establish the vacuum value of $\Delta\phi$ (for a freshly deposited aluminium film). Point B is the value of $\Delta\phi$ (a minimum) associated with the formation of the first monolayer of oxide). Oxygen gas is admitted to the system, and to the pressure indicated, at points labeled, O_2 . Oxygen is pumped from the system to the pressure indicated at the points labeled P. Note that the work function of gold is 5.22 ± 0.05 eV. Reprinted with permission from [117]. Copyright 2020 Elsevier.

B.9 Fitting the oxide growing rate in the low-pressure regime

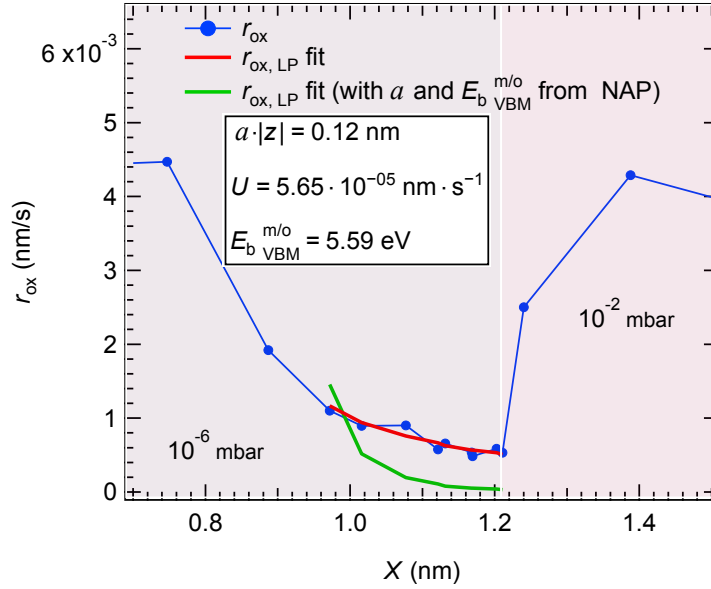


Fig. B.7 Blue dots: oxide growth rate r_{ox} plotted against thickness X . Red line: fit of the growth rate in the low-pressure regime using the Cabrera-Mott rate law (the three independent fit parameters $E_{\text{b VBM}}^{\text{m/o}}$, $|z| \times a$, and U are shown in the box). Green line: calculated growth rate using the same fit parameters $E_{\text{b VBM}}^{\text{m/o}}$ (5.34 eV) and $|z| \times a$ (0.69 nm) as those of the NAP domain, but a U parameter (4.89×10^{-9} nm/s) three orders of magnitude smaller than the one obtained under NAP conditions (2.72×10^{-6} nm \cdot s $^{-1}$).

Appendix C

C.1 Cyclic voltammetry measurements of the Zobell solution after XPS experiments

To verify that the composition of the solution was not modified after having passed through the liquid jet and suffered irradiation, cyclic voltammetry (CV) measurements were carried on the Zobell and Zobell + butanol samples. The principle is relatively simple; current is recorded as a varying potential is applied to the system. For this purpose, three electrodes are inserted into the solution. A working electrode, where the reduction/oxidation reaction of interest takes place, a reference electrode with a known potential, used as a reference point against which the potential of other electrodes can be measured, and a counter electrode to complete the circuit. Naturally, the working electrode must be composed of a redox-inert material in the potential range of interest. The usual procedure is to record the current as the potential is swept back and forth (from positive to negative and negative to positive) between some chosen limits. The information obtained from CV can be used to learn about the electrochemical behaviour of the material.

Aside from illustrating the general electrochemical behaviour of the material, two key informations can be obtained from a voltammogram: (i) the open circuit potential (OCP), which corresponds to the situation where the potential of the electrode equilibrates with the solution (so no current flows) and (ii) the position of the two current plateaus observed at extreme potentials, which give the cathodic and anodic limiting current. Comparing these values for the solutions before and after passing through the liquid jet makes it

possible to check whether the solution has been modified during the measurements, since the intensity of the plate currents is directly proportional to the concentration of the ions.

The voltammograms obtained for unused Zobell solution compared to used Zobell and used Zobell + butanol solution are represented in Figures C.1 and C.2, respectively. The measurements were done at a room temperature of 22°C. The corresponding results are reported in Table C.1. In each case, the measured value of the OCP is in good agreement with the expected redox potential for the working temperature [159]. Additionally, the cathodic and anodic limiting currents remain relatively constant, as well, so it is reasonable to consider that our solutions have, for the most part, not reacted or been degraded by passing through the liquid jet.

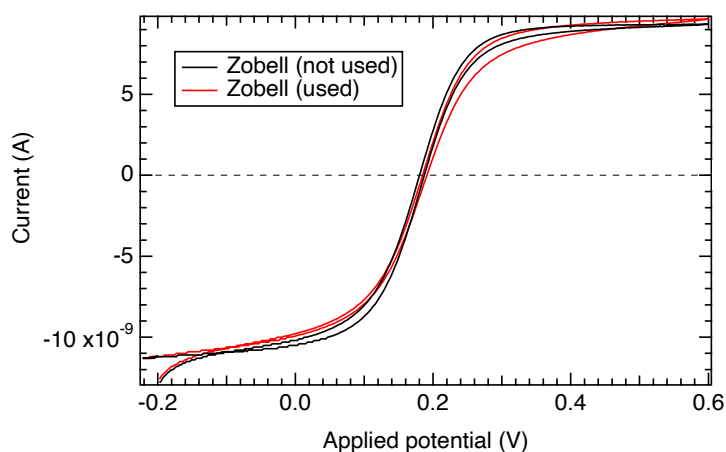


Fig. C.1 Voltammogram of an unused Zobell solution compared to a Zobell solution recovered after liquid-jet measurements.

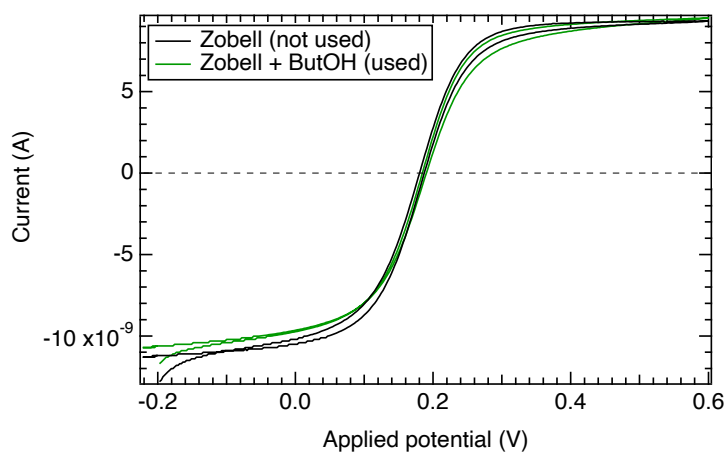


Fig. C.2 Voltammogram of an unused Zobell solution compared to a Zobell + butanol solution recovered after liquid-jet measurements.

Table C.1: Results from cyclic voltammetry measurements.

Solution	Cathodic limiting current (A)	Anodic limiting current (A)	OCP SCE ¹ (V)	OCP SHE ² (V)
Zobell (not used)	9.29×10^{-9}	-1.13×10^{-8}	0.194	0.439
Zobell (used)	9.30×10^{-9}	-1.13×10^{-8}	0.195	0.440
Zobell + ButOH (used)	9.34×10^{-9}	-1.07×10^{-8}	0.195	0.440

¹ Referenced to the standard calomel electrode.

² Referenced to the standard hydrogen electrode.

C.2 Effect of applied bias on a liquid jet

The magnitude of the shift in the O 1s gas phase ionisation energy observed in Figure IV.8 Section IV.2.4 is caused by two reasons: (i) the vacuum level offset between the aqueous solution and the analyser ($q\Phi_a - q\Phi_s$), ii) a geometric factor, c that accounts for the size of the ionisation source sampling a finite gas volume somewhere between the liquid and the analyser. In this volume, gas phase molecules experience a gradient in the electric field that affects their E_i to different extents depending on their distance from the liquid jets surface. Thus, c can be determined by quantifying the response (slope) of the measured O 1s gas phase ionisation energy when the liquid jet is subject to controlled applied bias [242].

In the example depicted in Figure C.3, the grounded liquid is assumed to have a higher vacuum level than the analyser, $q\Phi_{\text{water}} > q\Phi_{\text{ana}}$. The vacuum level of the liquid is varied by applying an external bias to the liquid jet. A positive applied bias shifts the vacuum level of the liquid down, whereas a negative applied bias shifts it up relative to that of the analyser. The full width at half the maximum (FWHM) of the O 1s gas phase peak is proportional to the slope in its vacuum level.

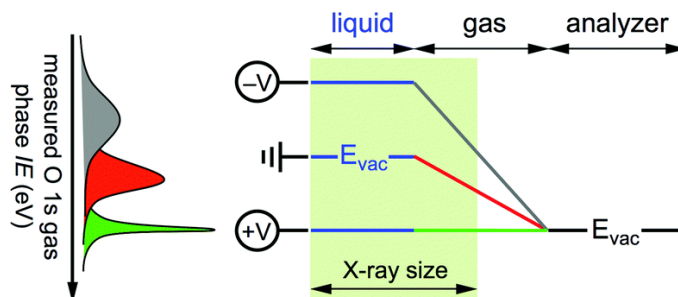


Fig. C.3 Energy level diagram depicting the effect of applied bias on the liquid jet and the corresponding response in the gas phase O 1s spectra. Reprinted from [87].

C.3 Electrical properties of n-butyl alcohol isomers at the free surface of water Solution

Figure C.4 shows the changes of the electric surface potential (ΔV) of aqueous solutions of several n-butyl alcohol isomers as a function of concentration and surface density. An extensive discussion can be found in Dynarowicz article [165].

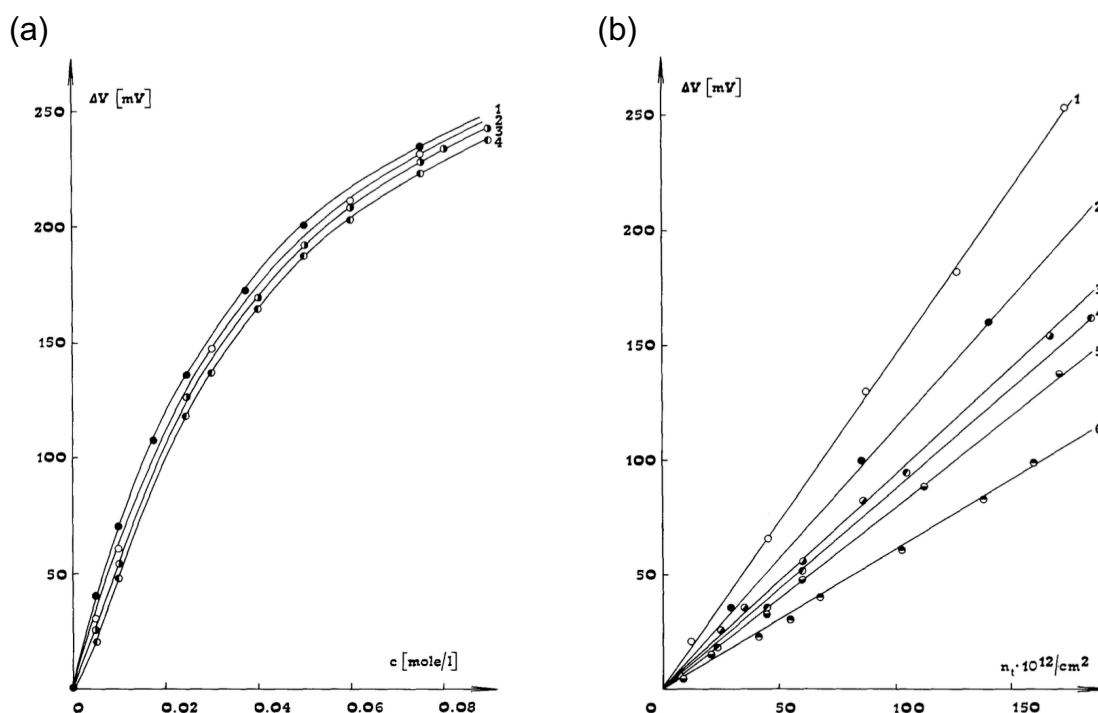


Fig. C.4 (a) ΔV vs concentration for n-butyl alcohol isomers: *tert*-butanol (1), *sec*-butanol (2), *n*-butanol (3) and *iso*-butanol(4). (b) Surface potential versus the total number of molecules adsorbed on 1 cm^2 of surface: *pi*-valaldehyde (1) *tert*-butanol (2), *sec*-butanol (3), *n*-butanol (4), *iso*-butanol (5) and butandiol (6). Reprinted with permission from [165]. Copyright 2020 Elsevier.

C.4 Crystal field theory applied to ferricyanide and ferrocyanide complexes

Crystal field theory (CFT) is a bonding model that explains many important properties of transition-metal complexes. It focuses on the interaction of the transition-metal d orbitals with ligands arranged in a regular array around it, assuming that these interactions are only electrostatic in nature. If examining a single transition metal ion, the five d -orbitals

have the same energy (they are degenerate). However, when ligands approach the metal ion, there is a splitting in the energy levels of the d orbitals. In the case of octahedral complexes, the energies of the d_{z^2} and $d_{x^2-y^2}$ orbitals (denoted e_g) increase with respect to the normal energy level while the energies of the d_{xy} , d_{xz} and d_{yz} (denoted t_{2g}) decrease. This crystal field splitting is denoted Δ_o .

How electrons are filled within this orbitals depends on the ligand. In fact, taking the example of a d^4 octahedral complex, one could expect to begin filling the first three low-energy d orbitals (d_{xy} , d_{xz} , d_{yz}) following the Aufbau principle; the position of the fourth electron depends on whether the spin pairing energy is higher or lower than the crystal field splitting Δ_o . “Weak-field ligands” cause a transition metal to have a small crystal field splitting (lower than the spin pairing energy), which leads to a high-spin configuration. “Strong-field ligands” cause a transition metal to have a big crystal field splitting (higher than the spin pairing energy), which leads to a low-spin configuration. One can determine whether a ligand is weak or strong by following the electrochemical series.

In the case of ferri and ferrocyanide complexes, the CN^- groups create a strong-field ligand, leading to a low-spin configuration for both cases, as shown in Figure C.5. The only difference is that $\text{Fe}^{\text{II}}(\text{CN})_6^{4-}$ is a spin-paired complex, while $\text{Fe}^{\text{II}}(\text{CN})_6^{3-}$ is not.

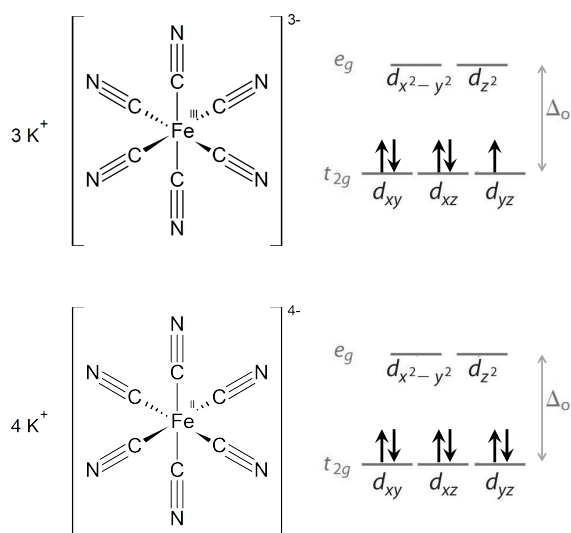


Fig. C.5 Octahedral CFT splitting and configuration of ferricyanide (top) and ferrocyanide (bottom) ligands.

Appendix D

D.1 XPS characterisation of the water-covered Si(100) surface

The Si 2p core level of the (H,OH)-Si(001) surface (shown in Figure D.1) is measured at $h\nu=175$ eV. At a kinetic energy of ~ 75 eV, the inelastic mean free path λ is ~ 4.8 nm. Considering the exit angle of the photoelectrons with respect to the surface normal (60°), the effective escape depth $\cos(60^\circ)$ is small (~ 2.4 Å), which ensures a good surface sensitivity (a surface plane is worth 46% of the spectral weight). The spectrum is very similar to those shown in previous publications [188, 243]. It is fitted with five doublets (the spin-orbit splitting is 0.602 eV and the $2p_{1/2}:2p_{3/2}$ branching ratio is 0.5). We use Voigt functions with a Lorentzian width (LW) of 0.045 eV. Gaussian widths (GW) are indicated in Table D.1. We find the Si $2p_{3/2}$ component of bulk silicon Si^0 component at 99.41 eV. The “SiH plus 2nd plane” component is at +0.27 eV from Si^0 , the SiOH (Si^{1+}) component at +0.98 eV. As the SiOH coverage is 0.5 ML, 48% of the spectral weight corresponds to the surface plane, which shows the high surface sensitivity. Note the absence of the Si^{2+} oxidation state at about +1.8 eV from Si^0 (and of higher oxidation states). This proves the absence of subsurface oxidation. Only OHs are present on the surface. Two more small subsurface components are needed to obtain a good fit. The S1 component at -0.30 eV, distinct from that of the “up” dimer atom component of the clean surface that appears at -0.57 eV [188, 243], and the “S2” component at $+0.64$ eV.

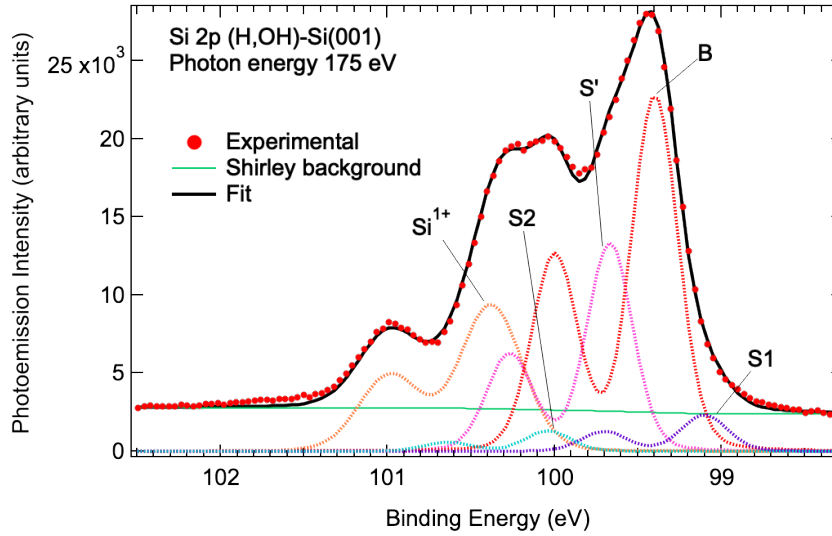


Fig. D.1 XPS Si 2p spectrum ($h\nu = 175$ eV) of the (H,OH)-Si(001)-2 \times 1 surface.

Table D.1: Surface core-level shifts (SCLS) referenced to the bulk component binding energy, widths, and spectral weights of the Voigt components used to fit the Si 2p experimental spectrum of the water-covered Si(001) surface shown in Figure D.1.

Component	SCLS (eV)	GW (eV)	Weight (%)	Attribution
S1	-0.30	0.30	4.5	Subsurface
B	0	0.30	44.63	Bulk
S'	+0.30	0.30	24.60	2nd plane + SiH
S2	+0.64	0.30	2.4	Subsurface
S ¹⁺	+0.93	0.414	23.90	SiOH

D.2 O 1s and N 1s normalisation with respect to Si LVV

Figure D.2 presents the N 1s spectra of a Si(001)-2 \times 1 surface after saturation with NH₃ at a pressure of 5×10^{-9} mbar (blue), and a silicon surface after 10 minutes of water dosing ($P = 5 \times 10^{-9}$ mbar) plus approximately 20 minutes of ammonia dosing ($P = 5 \times 10^{-9}$ mbar) (red). The spectra are normalised using the Si LVV Auger edge to evaluate the variation of ammonia quantities on the surface, reasonably assuming that the Auger peak does not vary significantly after adsorption of NH₃. The area under the N 1s peak of the blue curve, measured from the (H,NH₂)-Si(001) surface [202], corresponds to 0.5 ML. Taking this as a standard, we find that the calculated area under the N 1s peak of the red curve is 0.40 ML. Since the red spectrum is taken just after the end of the ammonia

dosing process given in Figure V.5 of Chapter V, we deduce from the normalised N 1s intensity the nitrogen coverages as a function of time for the different species.

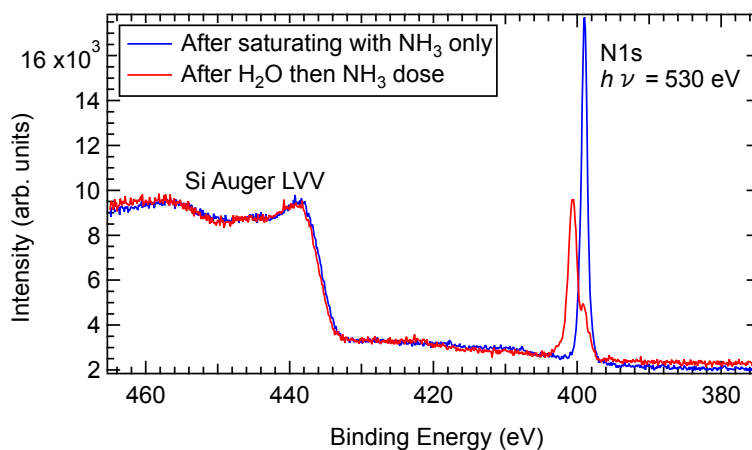


Fig. D.2 Si Auger LVV and N 1s core level peak recorded at $h\nu = 530$ eV from the NH_3 -covered silicon surface and the NH_3 -(H,OH)-covered surface.

Figure D.3 shows the O 1s spectra of the silicon surface after 10 minutes of water dosing at room temperature ($P = 5 \times 10^{-9}$) (blue), after cooling down to 130 K (red), and, finally, after 20 minutes of NH_3 dosing at $P = 5 \times 10^{-9}$ (green) at 130 K. Given that the dissociation of water on the silicon dimers at room temperature leads to the formation of half a monolayer (ML) of SiH and half a monolayer of SiOH, the area under the O 1s peak of the blue curve correspond to 0.5 ML of OH species exactly. The (H,OH)-Si(001) surface formed at 300 K serves as standard to estimate the oxygen coverages. Therefore, the calculated oxygen coverage after cooling down in UHV is 0.57 ML, and after ammonia dosing is 0.50 ML.

Both for N and O coverages, the relative uncertainty due to adjusting the Si LVV edges is about 5% and that due to measuring the spectral intensity is 3%. The overall error in measuring is estimated to be $\sim 8\%$.

D.3 Cluster QC DFT O 1s ionisation energies ($E_{i,QC}^{th}$)

D.3.1 Single dimer clusters

The results of the O 1s cluster QC DFT calculations obtained for single-dimer clusters, Si_9H_{12} (OH,H) (single OH) and Si_9H_{12} (2OH) (ODIM OH pairs), are collected in Table

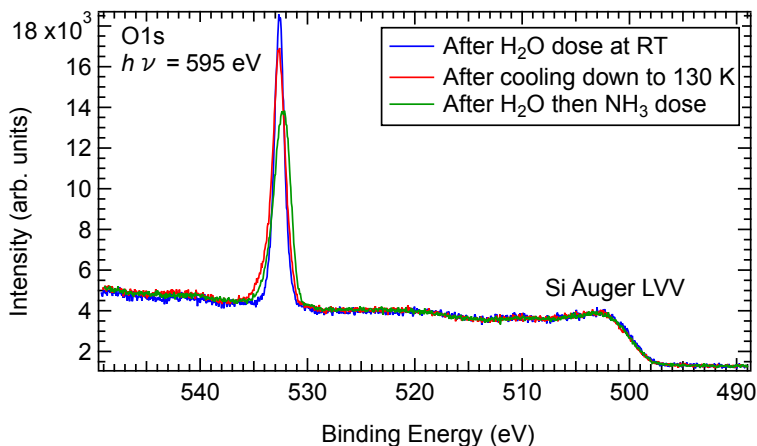


Fig. D.3 Si Auger LVV and O 1s core level peak recorded at $h\nu = 595$ eV from the silicon surface after water saturation at room temperature (blue), then cooling down to 130 K (red), and after NH₃ dosing under a pressure of 5×10^{-9} mbar (green).

D.2 for various configurations. Calculations of O 1s ionisation energies $E_{i,QC}^{\text{th}}$ were limited to this small cluster. While such an approach obviously cannot represent the variety of configurations encountered on the real surface, trends can be highlighted that are useful for interpreting the experimental spectra.

The $E_{i,QC}^{\text{th}}$ of isolated the isolated hydroxyl is found at 537.86 eV. It is used as an energy reference to calculate $\Delta E_{i,QC}^{\text{th}}$ of other configurations.

Pairs of OH sitting on the same dimer establish strong H bonds. Indeed, the optimised O–O distance is 2.60 Å (the Si–Si dimer bond length is 2.35 Å). The short H–O···H–O H-bond length (1.64 Å) means that the effect on O 1s $E_{i,QC}^{\text{th}}$ is large. The $E_{i,QC}^{\text{th}}$ of the OH(A) and OH(D) species are 538.20 eV and 536.28 eV, respectively. This corresponds to an energy splitting of 1.92 eV: the acceptor shifts by $\Delta E_{i,QC}^{\text{th}} = +0.34$ eV and the donor by $\Delta E_{i,QC}^{\text{th}} = -1.58$ eV, with respect to the isolated OH case (Table D.1). This situation is reminiscent of that of the (H₂O)₂ dimer, see Carniato et al. [201] and Table 1, where the acceptor moves by +0.56 eV and the donor by 1.17 eV with respect to the case of the isolated water molecule. The same trend in sign for the core level shifts and a larger shift magnitude for the donor than for the acceptor were also calculated by Garcia-Gil and coworkers in the case intermolecular H-bond in organic molecules [244].

Table D.2: Theoretical O 1s ionisation potential energies $E_{i,\text{QC}}^{\text{th}}$ calculated via a DFT QC silicon cluster approach (Si_9H_{12} , the “one-bare-dimer” cluster). $\Delta E_{i,\text{QC}}^{\text{th}}$ values are referenced to the $E_{i,\text{QC}}^{\text{th}}$ of the isolated OH (537.86 eV). (\cdots) denotes a H bond. OH and NH_3 can donate (D or d) or accept (A or a) H atoms. A capital letter corresponds to a strong H bond, a lower case to a weak H bond (the “proxy” of the H bond strength is its length given in the table).

Configuration	Cluster	H-bond lengths (\AA)	O 1s $E_{i,\text{QC}}^{\text{th}}$ (eV)	$\Delta E_{i,\text{QC}}^{\text{th}}$ (eV)
Free H_2O	NA	NA	405.70	1.92
Single OH	Si_9H_{12}	NA	537.86	0
Single OH(D) \cdots NH ₃ (A)	Si_9H_{12} (H,OH,NH ₃)	O–H \cdots NH ₃ 1.84	536.55	–1.31
Single OH(a) \cdots NH ₃ (d)	Si_9H_{12} (H,OH,NH ₃)	H–O \cdots H–NH ₂ 2.17	537.84	–0.02
ODIM pair OH(D) \cdots OH(A)	Si_9H_{12} (2OH)	O–H \cdots O–H 1.64	536.28	–1.58
ODIM pair OH(D) \cdots OH(A)			536.28	0.34
ODIM OH(D) \cdots NH ₃ (A,d) \cdots OH(A)	Si_9H_{12} (2OH,NH ₃)	O–H \cdots NH ₃ 1.77	536.50	–1.36
ODIM OH(D) \cdots NH ₃ (A,d) \cdots OH(A)		H ₂ NH \cdots O–H 2.10	538.00	0.14
ODIM OH(d) \cdots OH(a,D) \cdots NH ₃ (A)	Si_9H_{12} (2OH,NH ₃)	O–H \cdots NH ₃ 1.84	536.84	–1.02
ODIM OH(d) \cdots OH(a,D) \cdots NH ₃ (A)		O–H \cdots OH 2.64	537.36	–0.5

D.3.2 Adsorption on Si_9H_{12} (H,OH)

The ammonia molecule can be attached to the single OH of the Si_9H_{12} (OH,H) cluster. In the OH(D) \cdots NH₃(A) configurations the H-bond length is 1.84 \AA , and $\Delta E_{i,\text{QC}}^{\text{th}} = -1.31$ eV. A minimum energy configuration can also be achieved by presenting one hydrogen of the molecule in front of the oxygen of the hydroxyl. The hydrogen bond is then weak (HO(a) \cdots HNH₂(d) is 2.17 \AA long) and $\Delta E_{i,\text{QC}}^{\text{th}}$ is zero.

D.3.3 Adsorption on Si_9H_{12} (2OH)

We then investigated the adsorption of an ammonia molecule on Si_9H_{12} (2OH). Ammonia can be inserted between the two hydroxides, to make a OH(D) \cdots NH₃(A,D) \cdots OH(A) configuration. The “D” and “A” H-bond lengths are 1.77 and 2.10 \AA . The $\Delta E_{i,\text{QC}}^{\text{th}}$ of OH(D) is worth -1.36 eV and that of OH(A) is $+0.14$ eV. The energy shifts are again non symmetric with respect to the $E_{i,\text{QC}}^{\text{th}}$ of the isolated OH.

The ammonia molecule can also be placed in an end-on position, to make a OH(d)···OH(a,D)···NH₃(A) configuration, with a “d” bond length of 2.64 Å and a “D” one of 1.84 Å. Interestingly we have produced a OH(a,D) hydroxyl making a double H bond. The $\Delta E_{i,\text{QC}}^{\text{th}}$ of OH(a,D) is = -1.02 eV, smaller in magnitude than that of OH(D) in the previous, bridge configuration.

D.4 Experimental O 1s XPS spectra and their interpretation

We present in Figure D.4 the experimental O 1s spectra of the (H,OH)-Si(001) surface at 300 K, at 130 K under vacuum, and then exposed to ammonia. The spectrum of (H,OH)-Si(001) recorded at 300 K (bottom curve) is fitted by a single Gaussian component positioned at a binding energy of 532.62 eV. The FWHM is 1.15 eV. H bonds are not expected to be stabilised at this temperature [245]. Therefore the line at 532.62 eV is characteristic of “isolated” OHs.

When the temperature drops to 130 K (middle curve), the main component remains at the same position (532.64 eV) but broadens (FWHM= 1.46 eV). The broadening may be due to stabilisation of H bonds between hydroxyls. The effect OH pairing in SP patterns leads to a theoretical splitting of 0.25 eV between OH(a) and OH(d) [201]. The OH pairing in CBP should lead to a still smaller splitting. The pairing of ODIM OH pairs leads to very large change in $E_{i,\text{QC}}^{\text{th}}$ (see Section D.3), but we see no clear reflection of it in the experimental spectrum (we recall that the effect is asymmetric as the magnitude of the donor shift is greater than that of the acceptor one). In fact, complex H-bonded OH patterns are likely to form on the surface, that are difficult to take into account with cluster methods. In addition, relatively long-distance electrostatic effects between OHs can also complicate the picture. In addition to the main OH component, we need to introduce a Gaussian component at 534.30 eV. The binding energy shift is 1.70 eV with respect to the OH component at 532.62 eV, and this value is close to the $\Delta E_{i,\text{QC}}^{\text{th}}$ of molecular water (1.9 eV). H₂O coming from the residual gas in the chamber is likely co-adsorbed on the surface during cooling in UHV. The component represents 9% of the spectral weight (i.e. ~0.05 ML). This is in good agreement with the increase in oxygen coverage to 0.57 ML.

When the (H,OH)-Si(001) surface is covered by molecular ammonia at 130 K, we observe sizeable changes in the spectrum (top curve of Figure D.4). The coverage of H bonded ammonia is in the range 0.22–0.37 ML. The spectrum can always be fitted by two Gaussians, but the small peak that accounts for the asymmetry at high binding

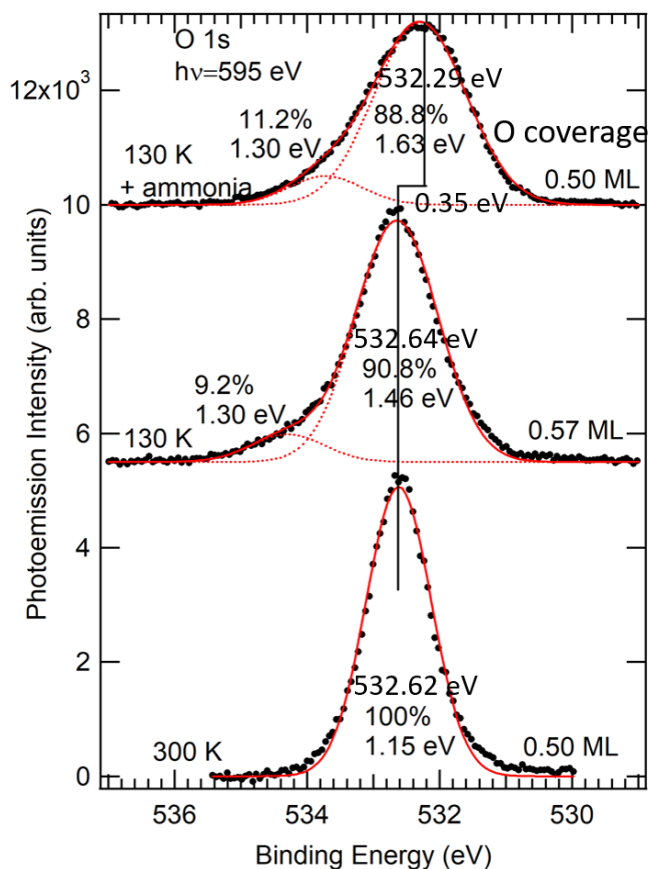


Fig. D.4 O 1s spectra measured at $h\nu=595$ eV. The spectra are normalised with respect to the O 1s intensity of the (H,OH)-Si(001) surface at 300 K. The oxygen coverage is indicated. Fits (solid red line) are also shown. The spectral weights (%) and FWHM of the Gaussian components (dotted red lines) are indicated.

energy is now positioned at 533.7 eV¹. In fact, the peak attributed to H₂O (at 534.3 eV) has disappeared. This suggests that the water molecules have been displaced by the ammonia molecules and is in line with the fact that the oxygen coverage has returned to 0.5 ML. Concerning the main component, it is strongly broadened (FWHM= 1.63 eV) and significantly shifted to lower binding energy (532.30 eV). The large FWHM, much greater than that at 300 K (1.15 eV), suggests it encompasses two or more contributions. The spectrum can be fitted again by substituting the broad main component at 532.29 eV by a doublet consisting in two components of equal intensity, with a FWHM of 1.17 eV each. The resulting fit is shown in Figure D.5. The high binding energy component of the doublet is only at +0.1 eV from that of the “isolated” OH, while the low binding energy

¹One could attribute this peak to an OH sitting close to a datively bonded ammonia which bears a Lewis charge of +1.

one is at -0.72 eV. The QC calculations have shown that the magnitude of $\Delta E_{i,\text{QC}}^{\text{th}}$ is much less for OH(A) than for OH(D) in the $\text{OH(D)}\cdots\text{NH}_3(\text{A,D})\cdots\text{OH(A)}$ configuration (see Table V.3). To ease the comparison between theory and experiment, the theoretical energy positions of OH(A) and OH(D) are indicated by a fuchsia and a violet vertical bar, respectively. However, the large $E_{i,\text{QC}}^{\text{th}}$ splitting of 1.5 eV is greater than that obtained from the experimental fit (0.82 eV). This suggests that the H-bonding pattern of OHs is much more complex than the assumption of singly H-bonded OH(A) and OH(D). The green bar in Figure D.5 represents the OH(a,D) component and the orange one that of a OH(d) component (see Table V.3). To sum up, the global shift of the peak maximum to lower binding energy and its broadening can be explained qualitatively by the QC calculations, assuming a distribution of OH(D), OH(d), OH(a,D) and OH(A) hydroxyls.

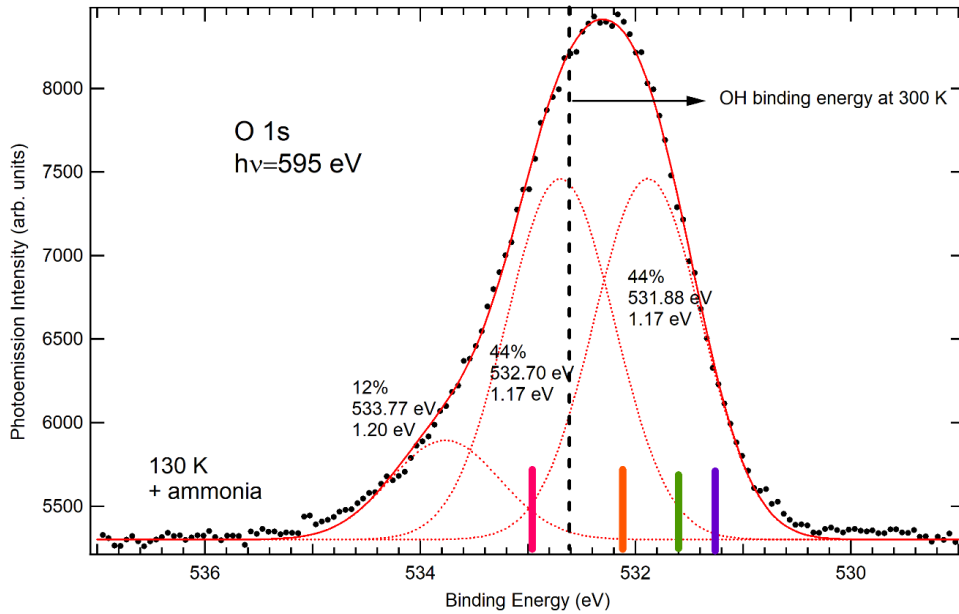


Fig. D.5 Normalised $O\ 1s$ spectra of the $(\text{H,OH})\text{-Si}(001)$ surface at 130 K covered by ammonia. The dashed vertical line corresponds to the binding energy of the OHs at 300 K (non-interacting OHs). Fits (solid red line) are also shown. The spectral weights (%), energy positions and FWHM of the Gaussian components (dotted red lines) are indicated. The violet and fuchsia vertical bars indicate the $\Delta E_{i,\text{QC}}^{\text{th}}$ of the OH(D) and OH(A) in a $\text{OH(D)}\cdots\text{NH}_3(\text{A,d})\cdots\text{OH(A)}$ configuration (the reference is the dashed vertical line). Similarly, the orange and the green bars indicate the $\Delta E_{i,\text{QC}}^{\text{th}}$ of the OH(d) and OH(a,D) in a $\text{OH(d)}\cdots\text{OH(a,D)}\cdots\text{NH}_3(\text{A})$ configuration (see Table V.3).

Bibliography

- [1] S. Succi, “Mesoscopic modeling of slip motion at fluid-solid interfaces with heterogeneous catalysis,” *Physical review letters*, vol. 89, no. 6, p. 064502, 2002. 1
- [2] Y. P. Zhu, C. Guo, Y. Zheng, and S.-Z. Qiao, “Surface and interface engineering of noble-metal-free electrocatalysts for efficient energy conversion processes,” *Accounts of chemical research*, vol. 50, no. 4, pp. 915–923, 2017. 1
- [3] E. A. Noor and A. H. Al-Moubaraki, “Thermodynamic study of metal corrosion and inhibitor adsorption processes in mild steel/1-methyl-4 [4’(-x)-styryl pyridinium iodides/hydrochloric acid systems,” *Materials Chemistry and Physics*, vol. 110, no. 1, pp. 145–154, 2008. 1
- [4] K. Wandelt and S. Thurgate, *Solid-Liquid Interfaces: Macroscopic Phenomena—Microscopic Understanding*, vol. 85. Springer Science & Business Media, 2002. 1
- [5] Y. Zhao and M. H. White, “Modeling of direct tunneling current through interfacial oxide and high-k gate stacks,” *Solid-State Electronics*, vol. 48, no. 10-11, pp. 1801–1807, 2004. 1
- [6] D.-B. Ruan, P.-T. Liu, Y.-C. Chiu, P.-Y. Kuo, M.-C. Yu, K.-Z. Kan, T.-C. Chien, Y.-H. Chen, and S. M. Sze, “Effect of interfacial layer on device performance of metal oxide thin-film transistor with a multilayer high-k gate stack,” *Thin Solid Films*, vol. 660, pp. 578–584, 2018. 1
- [7] S. Tiquia-Arashiro and D. Rodrigues, “Application of nanoparticles,” in *Extremophiles: Applications in Nanotechnology*, pp. 163–193, Springer, 2016. 1
- [8] W. J. Stark, P. R. Stoessel, W. Wohlleben, and A. Hafner, “Industrial applications of nanoparticles,” *Chemical Society Reviews*, vol. 44, no. 16, pp. 5793–5805, 2015. 1

- [9] K. C. Ko, S. T. Bromley, J. Y. Lee, and F. Illas, "Size-dependent level alignment between rutile and anatase TiO_2 nanoparticles: implications for photocatalysis," *The Journal of Physical Chemistry Letters*, vol. 8, no. 22, pp. 5593–5598, 2017. 2
- [10] C.-H. M. Chuang, P. R. Brown, V. Bulović, and M. G. Bawendi, "Improved performance and stability in quantum dot solar cells through band alignment engineering," *Nature materials*, vol. 13, no. 8, pp. 796–801, 2014. 2
- [11] W. Egelhoff Jr, "Core-level binding-energy shifts at surfaces and in solids," *Surface Science Reports*, vol. 6, no. 6-8, pp. 253–415, 1987. 3, 6, 18, 28, 30, 42, 46, 111, 117, 118
- [12] N. Cabrera and N. F. Mott, "Theory of the oxidation of metals," *Reports on progress in physics*, vol. 12, no. 1, pp. 163–184, 1949. 4, 40, 54
- [13] R. A. Marcus, "On the theory of oxidation-reduction reactions involving electron transfer. i," *The Journal of chemical physics*, vol. 24, no. 5, pp. 966–978, 1956. 4
- [14] H. Hertz, "Über sehr schnelle elektrische schwingungen," *Annalen der Physik*, vol. 267, no. 7, pp. 421–448, 1887. 5
- [15] A. Einstein, "Über einen die erzeugung und verwandlung des liches betreffenden heuristischen gesichtspunkt," *Annalen der physik*, vol. 322, no. 6, pp. 132–148, 1905. 5
- [16] H. Robinson and W. Rawlinson, "Xxxiii. the magnetic spectrum of the β rays excited in metals by soft x rays," *The London, Edinburgh, and Dublin Philosophical Magazine and Journal of Science*, vol. 28, no. 164, pp. 277–281, 1914. 5
- [17] S. Hagström, C. Nordling, and K. Siegbahn, "Electron spectroscopy for chemical analyses," *Physics Letters*, vol. 9, pp. 235–236, 1964. 5
- [18] K. Siegbahn and C. Nordling, "Esca, atomic, molecular and solid state structure studied by means of electron spectroscopy," *Nov. act. uppsaliensis*, 1967. 5
- [19] T. Carlson, *Photoelectron and Auger spectroscopy*. Springer Science & Business Media, 2013. 5
- [20] T. L. Barr, *Modern ESCA The Principles and Practice of X-Ray Photoelectron Spectroscopy*. CRC press, 1994. 6
- [21] H. C. Mastwijk, P. V. Bartels, and H. L. Lelieveld, "The origin of the work function," *arXiv preprint arXiv:0704.3797*, 2007. 6

- [22] A. Kahn, “Fermi level, work function and vacuum level,” *Materials Horizons*, vol. 3, no. 1, pp. 7–10, 2016. 6
- [23] V. Dose, “Image potential surface states,” *Physica Scripta*, vol. 36, no. 4, p. 669, 1987. 6
- [24] R. Culver and F. Tompkins, “Surface potentials and adsorption process on metals,” in *Advances in Catalysis*, vol. 11, pp. 67–131, Elsevier, 1959. 6
- [25] J. Hölzl and F. K. Schulte, “Work function of metals,” in *Solid surface physics*, pp. 1–150, Springer, 1979. 6
- [26] G. Friedbacher and H. Bubern, *Surface and Thin Film Analysis: A Compendium of Principles, Instrumentation, and Applications*. John Wiley & Sons, 2011. 7
- [27] S. Tougaard, “Surface analysis | x-ray photoelectron spectroscopy,” in *Encyclopedia of Analytical Science (Second Edition)* (P. Worsfold, A. Townshend, and C. Poole, eds.), pp. 446 – 456, Oxford: Elsevier, second edition ed., 2005. 7
- [28] C. J. Powell, A. Jablonski, I. Tilinin, S. Tanuma, and D. R. Penn, “Surface sensitivity of auger-electron spectroscopy and x-ray photoelectron spectroscopy,” *Journal of electron spectroscopy and related phenomena*, vol. 98, pp. 1–15, 1999. 7
- [29] D. J. O’Connor, B. A. Sexton, and R. S. Smart, *Surface analysis methods in materials science*, vol. 23. Springer Science & Business Media, 2013. 8
- [30] M. P. Seah and W. Dench, “Quantitative electron spectroscopy of surfaces: A standard data base for electron inelastic mean free paths in solids,” *Surface and interface analysis*, vol. 1, no. 1, pp. 2–11, 1979. 8
- [31] Omicron NanoTechnology GmbH, Limburger Strasse 75, 65232 Taunusstein, Germany, *EA 125 Energy Analyser User’s Guide*, 2.1 ed., 7 2002. 9, 12
- [32] H. Seyama, M. Soma, and B. Theng, “Chapter 2.5 - x-ray photoelectron spectroscopy,” in *Handbook of Clay Science* (F. Bergaya and G. Lagaly, eds.), vol. 5 of *Developments in Clay Science*, pp. 161 – 176, Elsevier, 2013. 9
- [33] S. Zhang, L. Li, and A. Kumar, *Materials characterization techniques*. CRC press, 2008. 9, 10, 12
- [34] J. Cazes, *Analytical instrumentation handbook*. CRC Press, 2004. 9
- [35] G. Mamantov and R. Marassi, *Molten salt chemistry: an introduction and selected applications*, vol. 202. Springer Science & Business Media, 2012. 10

- [36] Y. Farge, “Les dix premières années du lure: 1971 à 1980,” *Histoire de la recherche contemporaine. La revue du Comité pour l’histoire du CNRS*, vol. 3, no. 1, pp. 28–32, 2014. [10](#)
- [37] F. C. Adams, “X-ray absorption and diffraction | overview,” in *Encyclopedia of Analytical Science (Third Edition)* (P. Worsfold, C. Poole, A. Townshend, and M. Miró, eds.), pp. 391 – 403, Oxford: Academic Press, third edition ed., 2019. [11](#)
- [38] W. Clegg, “2.4 - x-ray diffraction,” in *Comprehensive Coordination Chemistry II* (J. A. McCleverty and T. J. Meyer, eds.), pp. 57 – 64, Oxford: Pergamon, 2003. [11](#)
- [39] D. H. Bilderback, P. Elleaume, and E. Weckert, “Review of third and next generation synchrotron light sources,” *Journal of Physics B: Atomic, molecular and optical physics*, vol. 38, no. 9, p. S773, 2005. [11](#)
- [40] C. Brundle, A. Baker, and T. D. Thomas, “Electron spectroscopy: Theory, techniques, and applications, volume 2.,” *Physics Today*, vol. 32, p. 62, 1979. [12](#)
- [41] J. Helmer and N. Weichert, “Enhancement of sensitivity in esca spectrometers,” *Applied Physics Letters*, vol. 13, no. 8, pp. 266–268, 1968. [13](#)
- [42] D. Briggs and J. T. Grant, *Surface analysis by Auger and X-ray photoelectron spectroscopy*. SurfaceSpectra, 2012. [13](#)
- [43] J. F. Watts and J. Wolstenholme, *An introduction to surface analysis by XPS and AES*. Wiley Online Library, 2003. [14](#)
- [44] S. S. N. A. GmbH, “Phoibos 150 wal hemispherical energy analyzer with wide angle lens,” 7 2010. [14](#), [22](#)
- [45] C. N. Berglund and W. E. Spicer, “Photoemission studies of copper and silver: theory,” *Physical Review*, vol. 136, no. 4A, p. A1030, 1964. [14](#)
- [46] J. Pendry, “Theory of photoemission,” *Surface Science*, vol. 57, no. 2, pp. 679–705, 1976. [14](#)
- [47] S. Tougaard, “Energy loss in xps: Fundamental processes and applications for quantification, non-destructive depth profiling and 3d imaging,” *Journal of Electron Spectroscopy and Related Phenomena*, vol. 178, pp. 128–153, 2010. [14](#), [16](#)
- [48] A. Damascelli, “Probing the electronic structure of complex systems by arpes,” *Physica Scripta*, vol. 2004, no. T109, p. 61, 2004. [15](#)
- [49] S. Hüfner, *Photoelectron spectroscopy: principles and applications*. Springer Science & Business Media, 2013. [15](#), [18](#)

- [50] J. Fuggle, D. Fabian, and L. Watson, "Electron energy loss processes in x-ray photoelectron spectroscopy," *Journal of Electron Spectroscopy and Related Phenomena*, vol. 9, no. 2, pp. 99–109, 1976. 16
- [51] K. Garg, N. David, *et al.*, *X-ray Absorption In Bulk And Surfaces-Proceedings Of The International Workshop*. World Scientific, 1994. 16
- [52] X.-T. Wu, *Controlled assembly and modification of inorganic systems*, vol. 133. Springer, 2009. 16
- [53] W. Eberhardt *et al.*, *Applications of synchrotron radiation: high-resolution studies of molecules and molecular adsorbates on surfaces*. Springer, 1995. 16
- [54] K. Norrman, S. Cros, R. de Bettignies, M. Firon, and F. C. Krebs, "Lifetime and stability studies," in *Polymer Photovoltaics*, pp. 155–227, SPIE-International Society for Optical Engineering, 2008. 18
- [55] C. Wagner, "Chemical shifts of auger lines, and the auger parameter," *Faraday Discussions of the Chemical Society*, vol. 60, pp. 291–300, 1975. 19
- [56] H. Reiss, "The fermi level and the redox potential," *The Journal of Physical Chemistry*, vol. 89, no. 18, pp. 3783–3791, 1985. 19, 28, 29, 30, 62
- [57] Z. Zhang and J. T. Yates Jr, "Band bending in semiconductors: chemical and physical consequences at surfaces and interfaces," *Chemical reviews*, vol. 112, no. 10, pp. 5520–5551, 2012. 19, 40, 59
- [58] D. F. Ogletree, H. Bluhm, E. D. Hebenstreit, and M. Salmeron, "Photoelectron spectroscopy under ambient pressure and temperature conditions," *Nuclear Instruments and Methods in Physics Research Section A: Accelerators, Spectrometers, Detectors and Associated Equipment*, vol. 601, no. 1-2, pp. 151–160, 2009. 20, 23
- [59] J. Knudsen, J. N. Andersen, and J. Schnadt, "A versatile instrument for ambient pressure x-ray photoelectron spectroscopy: The lund cell approach," *Surface Science*, vol. 646, pp. 160–169, 2016. 20, 23
- [60] M. Salmeron and R. Schlögl, "Ambient pressure photoelectron spectroscopy: A new tool for surface science and nanotechnology," *Surface Science Reports*, vol. 63, no. 4, pp. 169–199, 2008. 21
- [61] D. Starr, Z. Liu, M. Hävecker, A. Knop-Gericke, and H. Bluhm, "Investigation of solid/vapor interfaces using ambient pressure x-ray photoelectron spectroscopy," *Chemical Society Reviews*, vol. 42, no. 13, pp. 5833–5857, 2013. 23

- [62] H. Siegbahn and K. Siegbahn, "Esca applied to liquids," *Journal of Electron Spectroscopy and Related Phenomena*, vol. 2, no. 3, pp. 319–325, 1973. [23](#)
- [63] M. Faubel, S. Schlemmer, and J. Toennies, "A molecular beam study of the evaporation of water from a liquid jet," *Zeitschrift für Physik D Atoms, Molecules and Clusters*, vol. 10, no. 2-3, pp. 269–277, 1988. [24](#)
- [64] M. Faubel, "Photoelectron spectroscopy at liquid surfaces," in *Photoionization And Photodetachment: (In 2 Parts)*, pp. 634–690, World Scientific, 2000. [24](#)
- [65] M. Faubel and B. Steiner, "Strong bipolar electrokinetic charging of thin liquid jets emerging from 10 μm ptir nozzles," *Berichte der Bunsengesellschaft für physikalische Chemie*, vol. 96, no. 9, pp. 1167–1172, 1992. [24](#)
- [66] P. Hiemenz and R. Rajagopalan, "Electrophoresis and other electrokinetic phenomena," *Principles of colloid and surface chemistry*, vol. 3, pp. 544–547, 1977. [25](#)
- [67] N. Preissler, F. Buchner, T. Schultz, and A. Lübcke, "Electrokinetic charging and evidence for charge evaporation in liquid microjets of aqueous salt solution," *The Journal of Physical Chemistry B*, vol. 117, no. 8, pp. 2422–2428, 2013. [25](#)
- [68] R. H. Fowler, *Statistical thermodynamics*. CUP Archive, 1939. [28](#)
- [69] C. Herring and M. Nichols, "Thermionic emission," *Reviews of Modern Physics*, vol. 21, no. 2, p. 185, 1949. [28](#), [29](#)
- [70] J. Bardeen, "Surface states and rectification at a metal semi-conductor contact," *Physical Review*, vol. 71, no. 10, p. 717, 1947. [28](#)
- [71] E. Lange, "Über elektrochemische grundbegriffe, insbesondere der elektrode metall/lösung," *Zeitschrift für Elektrochemie und angewandte physikalische Chemie*, vol. 55, no. 2, pp. 76–92, 1951. [28](#)
- [72] C. A. Domenicali, "Irreversible thermodynamics of thermoelectricity," *Reviews of Modern Physics*, vol. 26, no. 2, p. 237, 1954. [28](#)
- [73] R. Parsons, "Equilibrium properties of electrified interfaces in "modern aspects of electrochemistry", vol. 1, j. o'm. bockris and b. conway," 1954. [28](#)
- [74] D. Keller Jr, "A simple model for surface energy and various metal interfaces," *SAE Transactions*, pp. 191–199, 1966. [28](#)
- [75] N. D. Lang, "The density-functional formalism and the electronic structure of metal surfaces," in *Solid state physics*, vol. 28, pp. 225–300, Elsevier, 1974. [29](#)

- [76] A. Groß, “Theoretical surface science: A microscopic perspective,” 2007. 29
- [77] J. Broughton and D. Perry, “Electron binding energies in the study of adsorption by photoelectron spectroscopy: The reference level problem,” *Surface Science*, vol. 74, no. 1, pp. 307–317, 1978. 30
- [78] H. Gerischer and W. Ekardt, “Fermi levels in electrolytes and the absolute scale of redox potentials,” *Applied physics letters*, vol. 43, no. 4, pp. 393–395, 1983. 30, 62
- [79] A. Cros, “Charging effects in x-ray photoelectron spectroscopy,” *Journal of electron spectroscopy and related phenomena*, vol. 59, no. 1, pp. 1–14, 1992. 32
- [80] M. Faubel, B. Steiner, and J. P. Toennies, “Photoelectron spectroscopy of liquid water, some alcohols, and pure nonane in free micro jets,” *The Journal of chemical physics*, vol. 106, no. 22, pp. 9013–9031, 1997. 34, 35
- [81] O. Björneholm, M. H. Hansen, A. Hodgson, L.-M. Liu, D. T. Limmer, A. Michaelides, P. Pedevilla, J. Rossmeisl, H. Shen, G. Tocci, *et al.*, “Water at interfaces,” *Chemical reviews*, vol. 116, no. 13, pp. 7698–7726, 2016. 35
- [82] B. Winter, R. Weber, W. Widdra, M. Dittmar, M. Faubel, and I. Hertel, “Full valence band photoemission from liquid water using euv synchrotron radiation,” *The Journal of Physical Chemistry A*, vol. 108, no. 14, pp. 2625–2632, 2004. 35, 36, 76, 82
- [83] M. Banna, B. McQuaide, R. Malutzki, and V. Schmidt, “The photoelectron spectrum of water in the 30 to 140 ev photon energy range,” *The Journal of chemical physics*, vol. 84, no. 9, pp. 4739–4744, 1986. 35
- [84] B. Winter and M. Faubel, “Photoemission from liquid aqueous solutions,” *Chemical reviews*, vol. 106, no. 4, pp. 1176–1211, 2006. 36
- [85] K. Nishizawa, N. Kurahashi, K. Sekiguchi, T. Mizuno, Y. Ogi, T. Horio, M. Oura, N. Kosugi, and T. Suzuki, “High-resolution soft x-ray photoelectron spectroscopy of liquid water,” *Physical Chemistry Chemical Physics*, vol. 13, no. 2, pp. 413–417, 2011. 36
- [86] N. Kurahashi, S. Karashima, Y. Tang, T. Horio, B. Abulimiti, Y.-I. Suzuki, Y. Ogi, M. Oura, and T. Suzuki, “Photoelectron spectroscopy of aqueous solutions: Streaming potentials of NaX ($\text{x} = \text{Cl}, \text{Br}, \text{and I}$) solutions and electron binding energies of liquid water and x^- ,” *The Journal of chemical physics*, vol. 140, no. 17, p. 174506, 2014. 36

- [87] G. Olivieri, A. Goel, A. Kleibert, D. Cvetko, and M. A. Brown, “Quantitative ionization energies and work functions of aqueous solutions,” *Physical Chemistry Chemical Physics*, vol. 18, no. 42, pp. 29506–29515, 2016. [36](#), [70](#), [77](#), [133](#)
- [88] M. N. Pohl, E. Muchová, R. Seidel, H. Ali, Š. Sršeň, I. Wilkinson, B. Winter, and P. Slavíček, “Do water’s electrons care about electrolytes?,” *Chemical science*, vol. 10, no. 3, pp. 848–865, 2019. [36](#), [37](#)
- [89] C. F. Perry, P. Zhang, F. B. Nunes, I. Jordan, A. von Conta, and H. J. Wörner, “Ionization energy of liquid water revisited,” *The Journal of Physical Chemistry Letters*, vol. 11, no. 5, pp. 1789–1794, 2020. [37](#), [76](#)
- [90] J. Nishitani, S. Karashima, C. W. West, and T. Suzuki, “Surface potential of liquid microjet investigated using extreme ultraviolet photoelectron spectroscopy,” *The Journal of Chemical Physics*, vol. 152, no. 14, p. 144503, 2020. [37](#)
- [91] D. Cahen and A. Kahn, “Electron energetics at surfaces and interfaces: concepts and experiments,” *Advanced Materials*, vol. 15, no. 4, pp. 271–277, 2003. [37](#)
- [92] H. Tissot, J.-J. Gallet, F. Bournel, G. Olivieri, M. G. Silly, F. Sirotti, A. Boucly, and F. Rochet, “The electronic structure of saturated nacl and nai solutions in contact with a gold substrate,” *Topics in Catalysis*, vol. 59, no. 5-7, pp. 605–620, 2016. [37](#), [77](#), [82](#), [83](#)
- [93] S. J. Percival and A. J. Bard, “Ultra-sensitive potentiometric measurements of dilute redox molecule solutions and determination of sensitivity factors at platinum ultramicroelectrodes,” *Analytical chemistry*, vol. 89, no. 18, pp. 9843–9849, 2017. [37](#), [63](#), [64](#), [76](#), [83](#)
- [94] F. P. Fehlner and N. F. Mott, “Low-temperature oxidation,” *Oxidation of metals*, vol. 2, no. 1, pp. 59–99, 1970. [39](#), [40](#), [42](#), [44](#), [52](#), [57](#)
- [95] A. Atkinson, “Transport processes during the growth of oxide films at elevated temperature,” *Reviews of Modern Physics*, vol. 57, no. 2, p. 437, 1985. [39](#), [40](#)
- [96] K. R. Lawless, “The oxidation of metals,” *Reports on Progress in Physics*, vol. 37, no. 2, p. 231, 1974. [39](#), [44](#)
- [97] N. Cai, G. Zhou, K. Müller, and D. E. Starr, “Tuning the limiting thickness of a thin oxide layer on al (111) with oxygen gas pressure,” *Physical Review Letters*, vol. 107, no. 3, p. 035502, 2011. [39](#), [44](#), [55](#), [56](#)

- [98] N. Cai, G. Zhou, K. Müller, and D. E. Starr, "Effect of oxygen gas pressure on the kinetics of alumina film growth during the oxidation of al (111) at room temperature," *Physical Review B*, vol. 84, no. 12, p. 125445, 2011. [39](#)
- [99] N. Cai, G. Zhou, K. Müller, and D. E. Starr, "Temperature and pressure dependent mott potentials and their influence on self-limiting oxide film growth," *Applied Physics Letters*, vol. 101, no. 17, p. 171605, 2012. [39](#), [55](#)
- [100] L. Nguyen, T. Hashimoto, D. N. Zakharov, E. A. Stach, A. P. Rooney, B. Berkels, G. E. Thompson, S. J. Haigh, and T. L. Burnett, "Atomic-scale insights into the oxidation of aluminum," *ACS applied materials & interfaces*, vol. 10, no. 3, pp. 2230–2235, 2018. [39](#), [43](#), [44](#), [49](#)
- [101] C. Lanthony, J. M. Ducéré, M. D. Rouhani, A. Hémercyck, A. Estève, and C. Rossi, "On the early stage of aluminum oxidation: An extraction mechanism via oxygen cooperation," *The Journal of Chemical Physics*, vol. 137, no. 9, p. 094707, 2012. [39](#), [40](#)
- [102] J. D. Baran, H. Grönbeck, and A. Hellman, "Mechanism for limiting thickness of thin oxide films on aluminum," *Physical review letters*, vol. 112, no. 14, p. 146103, 2014. [39](#), [40](#), [56](#), [57](#), [117](#), [124](#), [127](#)
- [103] C. M. Lousada and P. A. Korzhavyi, "The first stages of oxide growth at the low index al surfaces (100),(110),(111): clusters and stripes vs. homogeneous growth," *Physical Chemistry Chemical Physics*, vol. 20, no. 46, pp. 29549–29557, 2018. [39](#)
- [104] C. M. Lousada and P. A. Korzhavyi, "First stages of oxide growth on al (1 1 0) and core-level shifts from density functional theory calculations," *Applied Surface Science*, vol. 441, pp. 174–186, 2018. [39](#), [40](#)
- [105] P. Xu, S. Sun, S. Sun, X. Tan, Y. Ren, and H. Jia, "First-principles study of the initial stage of aluminum oxidation," *Chemical Physics Letters*, vol. 744, p. 137237, 2020. [39](#), [40](#)
- [106] S. K. Sankaranarayanan, E. Kaxiras, and S. Ramanathan, "Atomistic simulation of field enhanced oxidation of al (100) beyond the mott potential," *Physical review letters*, vol. 102, no. 9, p. 095504, 2009. [39](#), [40](#)
- [107] M. E. Trybula and P. A. Korzhavyi, "Atomistic simulations of al (100) and al (111) surface oxidation: Chemical and topological aspects of the oxide structure," *The Journal of Physical Chemistry C*, vol. 123, no. 1, pp. 334–346, 2018. [39](#), [40](#)

- [108] A. Fromhold Jr and E. L. Cook, “Kinetics of oxide film growth on metal crystals: Thermal electron emission and ionic diffusion,” *Physical Review*, vol. 163, no. 3, p. 650, 1967. [40](#)
- [109] S. V. Lamberts, T. Visart de Bocarmé, D. E. Perea, and N. Kruse, “Directional gateway to metal oxidation: 3d chemical mapping unfolds oxygen diffusional pathways in rhodium nanoparticles,” *The Journal of Physical Chemistry Letters*, vol. 11, no. 8, pp. 3144–3151, 2020. [40](#)
- [110] L. Qin, Y. Huang, F. Xia, L. Wang, J. Ning, H. Chen, X. Wang, W. Zhang, Y. Peng, Q. Liu, *et al.*, “5 nm nanogap electrodes and arrays by super-resolution laser lithography,” *Nano letters*, vol. 20, no. 7, pp. 4916–4923, 2020. [40](#)
- [111] M. W. Roberts, “Metal oxidation,” *Quarterly Reviews, Chemical Society*, vol. 16, no. 1, pp. 71–99, 1962. [42](#), [43](#)
- [112] D. Pierucci, J.-J. Gallet, F. Bournel, F. Sirotti, M. Silly, H. Tissot, A. Naitabdi, and F. Rochet, “Real-time x-ray photoemission spectroscopy study of si (001)-2×1 exposed to water vapor: Adsorption kinetics, fermi level positioning, and electron affinity variations,” *The Journal of Physical Chemistry C*, vol. 120, no. 38, pp. 21631–21641, 2016. [42](#), [43](#), [87](#), [92](#), [104](#)
- [113] F. Himpsel, G. Hollinger, and R. Pollak, “Determination of the fermi-level pinning position at si (111) surfaces,” *Physical Review B*, vol. 28, no. 12, p. 7014, 1983. [43](#)
- [114] D. F. Ogletree, H. Bluhm, G. Lebedev, C. S. Fadley, Z. Hussain, and M. Salmeron, “A differentially pumped electrostatic lens system for photoemission studies in the millibar range,” *Review of Scientific Instruments*, vol. 73, no. 11, pp. 3872–3877, 2002. [43](#)
- [115] L. Trotochaud, A. R. Head, O. Karshoğlu, L. Kyhl, and H. Bluhm, “Ambient pressure photoelectron spectroscopy: Practical considerations and experimental frontiers,” *Journal of Physics: Condensed Matter*, vol. 29, no. 5, p. 053002, 2016. [43](#)
- [116] E. Huber Jr and C. Kirk Jr, “Work function changes due to the chemisorption of water and oxygen on aluminum,” *Surface Science*, vol. 5, no. 4, pp. 447–465, 1966. [43](#), [46](#), [49](#)
- [117] C. Kirk Jr and E. Huber Jr, “The oxidation of aluminum films in low-pressure oxygen atmospheres,” *Surface Science*, vol. 9, no. 2, pp. 217–245, 1968. [43](#), [44](#), [53](#), [57](#), [128](#)

- [118] M. Roberts and B. Wells, "Surface rearrangement involving chemisorbed oxygen; the aluminium-oxygen system," *SurSci*, vol. 8, no. 4, pp. 453–457, 1967. [43](#)
- [119] Y. Enta, B. S. Mun, M. Rossi, P. N. Ross Jr, Z. Hussain, C. S. Fadley, K.-S. Lee, and S.-K. Kim, "Real-time observation of the dry oxidation of the si (100) surface with ambient pressure x-ray photoelectron spectroscopy," *Applied Physics Letters*, vol. 92, no. 1, p. 012110, 2008. [43](#)
- [120] Z. Novotny, B. Tobler, L. Artiglia, M. Fischer, M. Schreck, J. Raabe, and J. Osterwalder, "Kinetics of the thermal oxidation of ir (100) toward iro₂ studied by ambient-pressure x-ray photoelectron spectroscopy," *The Journal of Physical Chemistry Letters*, vol. 11, no. 9, pp. 3601–3607, 2020. [43](#)
- [121] S. Miyazaki, "Photoemission study of energy-band alignments and gap-state density distributions for high-k gate dielectrics," *Journal of Vacuum Science & Technology B: Microelectronics and Nanometer Structures Processing, Measurement, and Phenomena*, vol. 19, no. 6, pp. 2212–2216, 2001. [44](#), [123](#)
- [122] C. Ocal, S. Ferrer, and N. Garcia, "Cabreramott mechanism for oxidation of metals explains diffusion of metallic atoms through thin defective oxide layers," *Surface Science*, vol. 163, no. 2-3, pp. 335–356, 1985. [44](#), [49](#), [53](#)
- [123] F. Himpsel, F. McFeely, A. Taleb-Ibrahimi, J. Yarmoff, and G. Hollinger, "Microscopic structure of the sio₂/si interface," *Physical review B*, vol. 38, no. 9, p. 6084, 1988. [46](#), [86](#), [119](#), [124](#)
- [124] S. Tanuma, C. J. Powell, and D. R. Penn, "Calculations of electron inelastic mean free paths (imfps). iv. evaluation of calculated imfps and of the predictive imfp formula tpp-2 for electron energies between 50 and 2000 ev," *Surface and interface analysis*, vol. 20, no. 1, pp. 77–89, 1993. [vii](#), [46](#), [119](#), [124](#)
- [125] C. McConville, D. Seymour, D. Woodruff, and S. Bao, "Synchrotron radiation core level photoemission investigation of the initial stages of oxidation of al (111)," *Surface Science*, vol. 188, no. 1-2, pp. 1–14, 1987. [46](#), [119](#)
- [126] M. G. Yazdi, C. M. Lousada, J. Evertsson, L. Rullik, M. Soldemo, F. Bertram, P. A. Korzhavyi, J. Weissenrieder, E. Lundgren, and M. Göthelid, "Structure dependent effect of silicon on the oxidation of al (111) and al (100)," *Surface Science*, vol. 684, pp. 1–11, 2019. [46](#), [49](#), [119](#)
- [127] J. Grepstad, P. Gartland, and B. Slagsvold, "Anisotropic work function of clean and smooth low-index faces of aluminium," *Surface Science*, vol. 57, no. 1, pp. 348–362, 1976. [46](#)

- [128] R. Eastment and C. Mee, "Work function measurements on (100),(110) and (111) surfaces of aluminium," *Journal of Physics F: Metal Physics*, vol. 3, no. 9, p. 1738, 1973. [46](#)
- [129] P. Hofmann, W. Wyrobisch, and A. Bradshaw, "The interaction of oxygen with aluminium single crystal surfaces: Mainly $\delta\varphi$ aspects," *Surface Science*, vol. 80, pp. 344–351, 1979. [46](#)
- [130] X. Deng, T. Herranz, C. Weis, H. Bluhm, and M. Salmeron, "Adsorption of water on cu₂o and al₂o₃ thin films," *The Journal of Physical Chemistry C*, vol. 112, no. 26, pp. 9668–9672, 2008. [48](#)
- [131] B. Winter, S. Berkebile, J. Ivanco, G. Koller, F. Netzer, and M. Ramsey, "Oxygen induced molecular reorientation on aluminum," *Applied physics letters*, vol. 88, no. 25, p. 253111, 2006. [49](#)
- [132] A. Kiejna and B. I. Lundqvist, "First-principles study of surface and subsurface o structures at al (111)," *Physical Review B*, vol. 63, no. 8, p. 085405, 2001. [49](#)
- [133] A. Kiejna and B. I. Lundqvist, "Stability of oxygen adsorption sites and ultrathin aluminum oxide films on al (111)," *Surface science*, vol. 504, pp. 1–10, 2002. [49](#)
- [134] N. Cabrera, "Xiv. on the oxidation of metals at low temperatures and the influence of light," *The London, Edinburgh, and Dublin Philosophical Magazine and Journal of Science*, vol. 40, no. 301, pp. 175–188, 1949. [50](#), [56](#)
- [135] R. Ghez, "On the mott-cabrera oxidation rate equation and the inverse-logarithmic law," *The Journal of Chemical Physics*, vol. 58, no. 5, pp. 1838–1843, 1973. [55](#)
- [136] P. Capdevielle, A. Lavigne, D. Sparfel, J. Baranne-Lafont, K. C. Nguyen, and M. Maumy, "Mechanism of primary aliphatic amines oxidation to nitriles by the cuprous chloride-dioxygen-pyridine system.," *Tetrahedron letters*, vol. 31, no. 23, pp. 3305–3308, 1990. [55](#)
- [137] O. Guise, J. Levy, and J. T. Yates Jr, "Direct measurement of the direction of interface motion in the oxidation of metals and covalent solids—al (111) and si (100) oxidation with o₂ at 300 k," *Thin solid films*, vol. 496, no. 2, pp. 426–430, 2006. [55](#)
- [138] D. Starodub, T. Gustafsson, and E. Garfunkel, "The reaction of o₂ with al (1 1 0): a medium energy ion scattering study of nano-scale oxidation," *Surface science*, vol. 552, no. 1-3, pp. 199–214, 2004. [55](#)

- [139] J. Davies, B. Domeij, J. Pringle, and F. Brown, "The migration of metal and oxygen during anodic film formation," *Journal of the Electrochemical Society*, vol. 112, no. 7, p. 675, 1965. [56](#)
- [140] W. Lee and S.-J. Park, "Porous anodic aluminum oxide: anodization and templated synthesis of functional nanostructures," *Chemical reviews*, vol. 114, no. 15, pp. 7487–7556, 2014. [56](#)
- [141] R. Nakamura, T. Toda, S. Tsukui, M. Tane, M. Ishimaru, T. Suzuki, and H. Nakajima, "Diffusion of oxygen in amorphous Al_2O_3 , Ta_2O_5 , and Nb_2O_5 ," *Journal of applied Physics*, vol. 116, no. 3, p. 033504, 2014. [56](#)
- [142] A. Stoneham and P. Tasker, "Image charges and their influence on the growth and the nature of thin oxide films," *Philosophical Magazine B*, vol. 55, no. 2, pp. 237–252, 1987. [56](#)
- [143] X. Liu, J. Cheng, and M. Sprik, "Aqueous transition-metal cations as impurities in a wide gap oxide: The $\text{Cu}^{2+}/\text{Cu}^+$ and $\text{Ag}^{2+}/\text{Ag}^+$ redox couples revisited," *The Journal of Physical Chemistry B*, vol. 119, no. 3, pp. 1152–1163, 2015. [59](#)
- [144] J. Cheng and M. Sprik, "Alignment of electronic energy levels at electrochemical interfaces," *Physical Chemistry Chemical Physics*, vol. 14, no. 32, pp. 11245–11267, 2012. [59](#)
- [145] A. C. Meng, J. Cheng, and M. Sprik, "Density functional theory calculation of the band alignment of $(10\bar{1}0)$ in $\text{x Ga}_{1-x}\text{N}/\text{water}$ interfaces," *The Journal of Physical Chemistry B*, vol. 120, no. 8, pp. 1928–1939, 2016. [59](#)
- [146] H. Ishii, K. Sugiyama, E. Ito, and K. Seki, "Energy level alignment and interfacial electronic structures at organic/metal and organic/organic interfaces," *Advanced materials*, vol. 11, no. 8, pp. 605–625, 1999. [59](#)
- [147] S. Narioka, H. Ishii, D. Yoshimura, M. Sei, Y. Ouchi, K. Seki, S. Hasegawa, T. Miyazaki, Y. Harima, and K. Yamashita, "The electronic structure and energy level alignment of porphyrin/metal interfaces studied by ultraviolet photoelectron spectroscopy," *Applied physics letters*, vol. 67, no. 13, pp. 1899–1901, 1995. [59](#)
- [148] M. A. Brown, Z. Abbas, A. Kleibert, R. G. Green, A. Goel, S. May, and T. M. Squires, "Determination of surface potential and electrical double-layer structure at the aqueous electrolyte-nanoparticle interface," *Physical Review X*, vol. 6, no. 1, p. 011007, 2016. [59](#)

- [149] M. A. Brown, R. Seidel, S. Thürmer, M. Faubel, J. C. Hemminger, J. A. van Bokhoven, B. Winter, and M. Sterrer, "Electronic structure of sub-10 nm colloidal silica nanoparticles measured by in situ photoelectron spectroscopy at the aqueous-solid interface," *Physical Chemistry Chemical Physics*, vol. 13, no. 28, pp. 12720–12723, 2011. [59](#)
- [150] G. Olivieri and M. A. Brown, "Structure of a core-shell type colloid nanoparticle in aqueous solution studied by xps from a liquid microjet," *Topics in Catalysis*, vol. 59, no. 5-7, pp. 621–627, 2016. [59](#)
- [151] M. Faubel, B. Steiner, and J. Toennies, "Measurement of he i photoelectron spectra of liquid water, formamide and ethylene glycol in fast-flowing microjets," *Journal of electron spectroscopy and related phenomena*, vol. 95, no. 2-3, pp. 159–169, 1998. [59](#)
- [152] R. Gomer and G. Tryson, "An experimental determination of absolute half-cell emf's and single ion free energies of solvation," *The Journal of chemical physics*, vol. 66, no. 10, pp. 4413–4424, 1977. [62](#)
- [153] H. Gerischer, "Physical chemistry: An advanced treatise," by H. Eyring et al., *Academic Press, New York*, pp. 487–489, 1970. [62](#)
- [154] S. Trasatti, "The absolute electrode potential: an explanatory note," *Pure Appl. Chem*, vol. 58, no. 7, pp. 955–966, 1986. [63](#)
- [155] A. A. Isse and A. Gennaro, "Absolute potential of the standard hydrogen electrode and the problem of interconversion of potentials in different solvents," *The Journal of Physical Chemistry B*, vol. 114, no. 23, pp. 7894–7899, 2010. [63](#), [76](#), [82](#)
- [156] M. Seah, "Summary of iso/tc 201 standard: Vii iso 15472: 2001–surface chemical analysis–x-ray photoelectron spectrometers–calibration of energy scales," *Surface and Interface Analysis: An International Journal devoted to the development and application of techniques for the analysis of surfaces, interfaces and thin films*, vol. 31, no. 8, pp. 721–723, 2001. [67](#)
- [157] A. W. Bier, "Introduction to oxidation reduction potential measurement," *Hach Company, Lit*, no. 2072, 2009. [68](#)
- [158] D. K. Nordstrom and F. D. Wilde, "Chapter a6. section 6.5. reduction-oxidation potential (electrode method)," tech. rep., US Geological Survey, 2005. [68](#)
- [159] D. K. Nordstrom, "Thermochemical redox equilibria of zobell's solution," *Geochimica et Cosmochimica Acta*, vol. 41, no. 12, pp. 1835–1841, 1977. [68](#), [132](#)

- [160] J. Stöhr, *NEXAFS spectroscopy*, vol. 25. Springer Science & Business Media, 2013. 72
- [161] R. Seidel, S. Thürmer, J. Moens, P. Geerlings, J. Blumberger, and B. Winter, “Valence photoemission spectra of aqueous $\text{Fe}^{2+}/\text{Fe}^{3+}$ and $[\text{Fe}(\text{CN})_6]^{4-}/\text{Fe}^{3+}$ and their interpretation by dft calculations,” *The Journal of Physical Chemistry B*, vol. 115, no. 40, pp. 11671–11677, 2011. 72, 81
- [162] J. Werner, *Exploring the Surface of Aqueous Solutions: X-ray photoelectron spectroscopy studies using a liquid micro-jet*. PhD thesis, Acta Universitatis Upsaliensis, 2015. 78
- [163] N. Ottosson, M. Faubel, S. E. Bradforth, P. Jungwirth, and B. Winter, “Photoelectron spectroscopy of liquid water and aqueous solution: Electron effective attenuation lengths and emission-angle anisotropy,” *Journal of Electron Spectroscopy and Related Phenomena*, vol. 177, no. 2-3, pp. 60–70, 2010. 78
- [164] B. Chen, J. I. Siepmann, and M. L. Klein, “Vapor-liquid interfacial properties of mutually saturated water/1-butanol solutions,” *Journal of the American Chemical Society*, vol. 124, no. 41, pp. 12232–12237, 2002. 79
- [165] P. Dynarowicz, “Surface orientation and electrical properties of n-butyl alcohol isomers at the free surface of water solution,” *Colloids and surfaces*, vol. 42, no. 1, pp. 39–48, 1989. 79, 80, 134
- [166] B. V. Crist, “Handbook of the elements and native oxides,” *XPS International Inc., Iowa, USA*, 1999. 79
- [167] P. Jungwirth and D. J. Tobias, “Specific ion effects at the air/water interface,” *Chemical reviews*, vol. 106, no. 4, pp. 1259–1281, 2006. 79
- [168] H. Tissot, G. Olivieri, J.-J. Gallet, F. Bournel, M. G. Silly, F. Sirotti, and F. Rochet, “Cation depth-distribution at alkali halide aqueous solution surfaces,” *The Journal of Physical Chemistry C*, vol. 119, no. 17, pp. 9253–9259, 2015. 79
- [169] M. J. Krisch, R. D’Auria, M. A. Brown, D. J. Tobias, C. Hemminger, M. Ammann, D. E. Starr, and H. Bluhm, “The effect of an organic surfactant on the liquid-vapor interface of an electrolyte solution,” *The Journal of Physical Chemistry C*, vol. 111, no. 36, pp. 13497–13509, 2007. 80
- [170] M. Paluch and P. Dynarowicz, “Electrical properties of the mixed films of 2, 2, 2-trifluoroethanol—ethanol at the water/air interface,” *Journal of colloid and interface science*, vol. 98, no. 1, pp. 131–137, 1984. 80

- [171] P. Thissen, O. Seitz, and Y. J. Chabal, "Wet chemical surface functionalization of oxide-free silicon," *Progress in surface science*, vol. 87, no. 9-12, pp. 272–290, 2012. [85](#)
- [172] K. Ihm, T.-H. Kang, J. H. Han, S. Moon, C. C. Hwang, K.-J. Kim, H.-N. Hwang, C.-H. Jeon, H.-D. Kim, B. Kim, *et al.*, "Hydroxyl group-induced adsorptions of 4-nitro benzoic acid on the si (1 0 0) surface," *Journal of electron spectroscopy and related phenomena*, vol. 144, pp. 397–400, 2005. [85](#)
- [173] F. Bournel, J.-J. Gallet, U. Köhler, B. B. Ellakhmissi, S. Kubsky, S. Carniato, and F. Rochet, "Propanoate grafting on (h, oh)-si (0 0 1)-2× 1," *Journal of Physics: Condensed Matter*, vol. 27, no. 5, p. 054005, 2014. [85](#), [91](#)
- [174] B. Willis, A. Mathew, L. Wielunski, and R. Opila, "Adsorption and reaction of hfcl4 with h2o-terminated si (100)-2× 1," *The Journal of Physical Chemistry C*, vol. 112, no. 6, pp. 1994–2003, 2008. [85](#)
- [175] S. McDonnell, R. C. Longo, O. Seitz, J. B. Ballard, G. Mordi, D. Dick, J. H. Owen, J. N. Randall, J. Kim, Y. J. Chabal, *et al.*, "Controlling the atomic layer deposition of titanium dioxide on silicon: dependence on surface termination," *The Journal of Physical Chemistry C*, vol. 117, no. 39, pp. 20250–20259, 2013. [85](#)
- [176] R. Longo, J. Owen, S. McDonnell, D. Dick, J. Ballard, J. Randall, R. Wallace, Y. Chabal, and K. Cho, "Toward atomic-scale patterned atomic layer deposition: Reactions of al2o3 precursors on a si (001) surface with mixed functionalizations," *The Journal of Physical Chemistry C*, vol. 120, no. 5, pp. 2628–2641, 2016. [85](#)
- [177] J. Klaus and S. George, "Atomic layer deposition of sio2 at room temperature using nh3-catalyzed sequential surface reactions," *Surface Science*, vol. 447, no. 1-3, pp. 81–90, 2000. [85](#)
- [178] J. Ferguson, E. Smith, A. Weimer, and S. George, "Ald of sio2 at room temperature using teos and h 2 o with nh 3 as the catalyst," *Journal of The Electrochemical Society*, vol. 151, no. 8, p. G528, 2004. [85](#)
- [179] T. R. Mayangsari, J.-M. Park, L. L. Yusup, J. Gu, J.-H. Yoo, H.-D. Kim, and W.-J. Lee, "Catalyzed atomic layer deposition of silicon oxide at ultralow temperature using alkylamine," *Langmuir*, vol. 34, no. 23, pp. 6660–6669, 2018. [85](#), [87](#)
- [180] R. Schlier and H. Farnsworth, "Structure and adsorption characteristics of clean surfaces of germanium and silicon," *The Journal of Chemical Physics*, vol. 30, no. 4, pp. 917–926, 1959. [86](#)

- [181] K. Wandelt, *Surface and Interface Science, Volume 5 and 6: Volume 5-Solid Gas Interfaces I; Volume 6-Solid Gas Interfaces II*. John Wiley & Sons, 2016. 86
- [182] H. Over, J. Wasserfall, W. Ranke, C. Ambiatello, R. Sawitzki, D. Wolf, and W. Moritz, "Surface atomic geometry of si (001)-(2× 1): A low-energy electron-diffraction structure analysis," *Physical Review B*, vol. 55, no. 7, p. 4731, 1997. 86
- [183] Y. Jung, Y. Shao, M. S. Gordon, D. J. Doren, and M. Head-Gordon, "Are both symmetric and buckled dimers on si (100) minima? density functional and multireference perturbation theory calculations," *The Journal of chemical physics*, vol. 119, no. 20, pp. 10917–10923, 2003. 86
- [184] M. A. Filler and S. F. Bent, "The surface as molecular reagent: organic chemistry at the semiconductor interface," *Progress in surface science*, vol. 73, no. 1-3, pp. 1–56, 2003. 87
- [185] C. Poncey, F. Rochet, G. Dufour, H. Roulet, F. Sirotti, and G. Panaccione, "Adsorption of water on si (001)-2× 1 and si (111)-7× 7 surfaces at 90 and 300 k: A si 2p core-level and valence band study with synchrotron radiation," *Surface science*, vol. 338, no. 1-3, pp. 143–156, 1995. 86
- [186] D. B. Skliar and B. G. Willis, "The role of dangling bonds in h₂o-induced oxidation of si (100)-2× 1," *The Journal of Physical Chemistry C*, vol. 112, no. 25, pp. 9434–9442, 2008. 86, 87
- [187] L. Andersohn and U. Köhler, "In situ observation of water adsorption on si (100) with scanning tunneling microscopy," *Surface science*, vol. 284, no. 1-2, pp. 77–90, 1993. 87
- [188] J.-J. Gallet, F. Bournel, F. Rochet, U. Köhler, S. Kubsky, M. Silly, F. Sirotti, and D. Pierucci, "Isolated silicon dangling bonds on a water-saturated n^+ -doped si (001)-2× 1 surface: An xps and stm study," *The Journal of Physical Chemistry C*, vol. 115, no. 15, pp. 7686–7693, 2011. 87, 101, 137
- [189] D. Pierucci, *The electronic structure and reactivity of tri-coordinated silicon atoms on water-covered Si (001) surface: time-resolved XPS and STM studies*. PhD thesis, Paris 6, 2013. 87, 92
- [190] J.-H. Cho, K. S. Kim, S.-H. Lee, and M.-H. Kang, "Dissociative adsorption of water on the si (001) surface: A first-principles study," *Physical Review B*, vol. 61, no. 7, p. 4503, 2000. 87

- [191] J.-Y. Lee and J.-H. Cho, "Two dissociation pathways of water and ammonia on the si (001) surface," *The Journal of Physical Chemistry B*, vol. 110, no. 37, pp. 18455–18458, 2006. [87](#)
- [192] S.-Y. Yu, Y.-S. Kim, H. Kim, and J.-Y. Koo, "Influence of flipping si dimers on the dissociation pathways of water molecules on si (001)," *The Journal of Physical Chemistry C*, vol. 115, no. 50, pp. 24800–24803, 2011. [87](#)
- [193] E. P. Hunter and S. G. Lias, "Evaluated gas phase basicities and proton affinities of molecules: an update," *Journal of Physical and Chemical Reference Data*, vol. 27, no. 3, pp. 413–656, 1998. [87](#)
- [194] F. Giustino and A. Pasquarello, "First-principles theory of infrared absorption spectra at surfaces and interfaces: Application to the si (100): H₂O surface," *Physical Review B*, vol. 78, no. 7, p. 075307, 2008. [88](#)
- [195] F. Tielens, C. Gervais, J. F. Lambert, F. Mauri, and D. Costa, "Ab initio study of the hydroxylated surface of amorphous silica: A representative model," *Chemistry of Materials*, vol. 20, no. 10, pp. 3336–3344, 2008. [88](#)
- [196] "Cpmd." <https://www.cpmd.org/>. [89](#)
- [197] J. P. Perdew, K. Burke, and M. Ernzerhof, "Generalized gradient approximation made simple," *Physical review letters*, vol. 77, no. 18, p. 3865, 1996. [89](#)
- [198] R. Car and M. Parrinello, "Unified approach for molecular dynamics and density-functional theory," *Physical review letters*, vol. 55, no. 22, p. 2471, 1985. [89](#)
- [199] G.-M. Rignanese, A. Pasquarello, J.-C. Charlier, X. Gonze, and R. Car, "Nitrogen incorporation at si (001)- SiO₂ interfaces: Relation between N 1s core-level shifts and microscopic structure," *Physical review letters*, vol. 79, no. 25, p. 5174, 1997. [89](#)
- [200] G.-M. Rignanese and A. Pasquarello, "First-principles study of NH₃ exposed si (001) 2×1: Relation between N 1s core-level shifts and atomic structure," *Applied Physics Letters*, vol. 76, no. 5, pp. 553–555, 2000. [89](#)
- [201] S. Carniato, J.-J. Gallet, F. Rochet, G. Dufour, F. Bournel, S. Rangan, A. Verdini, and L. Floreano, "Characterization of hydroxyl groups on water-reacted si (001)-2×1 using synchrotron radiation O 1s core-level spectroscopies and core-excited state density-functional calculations," *Physical Review B*, vol. 76, no. 8, p. 085321, 2007. [89](#), [90](#), [91](#), [140](#), [142](#)

- [202] C. Mathieu, X. Bai, F. Bournel, J.-J. Gallet, S. Carniato, F. Rochet, F. Sirotti, M. Silly, C. Chauvet, D. Krizmancic, *et al.*, “Nitrogen 1 s nexafs and xps spectroscopy of nh₃-saturated si (001)-2×1: Theoretical predictions and experimental observations at 300 k,” *Physical Review B*, vol. 79, no. 20, p. 205317, 2009. [89](#), [90](#), [93](#), [95](#), [97](#), [138](#)
- [203] “Gordon group/gamess homepage.” <http://www.msg.chem.iastate.edu/gamess/index.html>. Accessed Jun 7, 2013). [89](#)
- [204] S. Rangan, F. Bournel, J.-J. Gallet, S. Kubsky, K. Le Guen, G. Dufour, F. Rochet, F. Sirotti, S. Carniato, and V. Ilakovac, “Experimental and theoretical nexafs/xps study of the room-temperature adsorption of acetonitrile on si (001)- 2 × 1,” *Physical Review B*, vol. 71, no. 16, p. 165319, 2005. [90](#)
- [205] C. Mathieu, X. Bai, J.-J. Gallet, F. Bournel, S. Carniato, F. Rochet, E. Magnano, F. Bondino, R. Funke, and U. Köhler, “Molecular staples on si(001)-2 × 1: Dual-head primary amines,” *The Journal of Physical Chemistry C*, vol. 113, no. 26, pp. 11336–11345, 2009. [90](#)
- [206] W. Jolly, K. Bomben, and C. Eyermann, “Core-electron binding energies for gaseous atoms and molecules,” *Atomic Data and Nuclear Data Tables*, vol. 31, no. 3, pp. 433–493, 1984. [90](#), [105](#)
- [207] K. Wandelt, “The local work function: Concept and implications,” *Applied surface science*, vol. 111, pp. 1–10, 1997. [90](#)
- [208] D. Pierucci, A. Naitabdi, F. Bournel, J.-J. Gallet, H. Tissot, S. Carniato, F. Rochet, U. Köhler, D. Laumann, S. Kubsky, *et al.*, “Benzaldehyde on water-saturated si (001): reaction with isolated silicon dangling bonds versus concerted hydrosilylation,” *The Journal of Physical Chemistry C*, vol. 118, no. 19, pp. 10005–10016, 2014. [91](#)
- [209] M. Satta, R. Flammini, A. Goldoni, A. Baraldi, S. Lizzit, and R. Larciprete, “Fundamental role of the h-bond interaction in the dissociation of nh₃ on si (001)-(2×1),” *Physical review letters*, vol. 109, no. 3, p. 036102, 2012. [97](#), [102](#)
- [210] M. Lipponer, M. Reutzler, M. Dürr, and U. Höfer, “Energy dependent sticking coefficients of trimethylamine on si (001)–influence of the datively bonded intermediate state on the adsorption dynamics,” *Surface Science*, vol. 653, pp. 118–122, 2016. [99](#)
- [211] M. Z. Hossain, S.-i. Machida, Y. Yamashita, K. Mukai, and J. Yoshinobu, “Purely site-specific chemisorption and conformation of trimethylamine on si (100) c (4×

- 2),” *Journal of the American Chemical Society*, vol. 125, no. 31, pp. 9252–9253, 2003. [101](#)
- [212] A. Naitabdi, F. Bournel, J.-J. Gallet, A. Markovits, F. Rochet, Y. Borensztein, M. G. Silly, and F. Sirotti, “Triethylamine on si (001)-(2× 1) at 300 k: molecular adsorption and site configurations leading to dissociation,” *The Journal of Physical Chemistry C*, vol. 116, no. 31, pp. 16473–16486, 2012. [101](#), [102](#), [107](#)
- [213] G. Dubey, F. Rosei, and G. P. Lopinski, “Molecular modulation of conductivity on h-terminated silicon-on-insulator substrates,” *small*, vol. 6, no. 24, pp. 2892–2899, 2010. [101](#)
- [214] Á. Miranda-Durán, X. Cartoixà, M. Cruz Irisson, and R. Rurali, “Molecular doping and subsurface dopant reactivation in si nanowires,” *Nano letters*, vol. 10, no. 9, pp. 3590–3595, 2010. [101](#)
- [215] A. Vittadini, A. Selloni, and M. Casarin, “Binding and diffusion of hydroxyl radicals on si (100): A first-principles study,” *Physical Review B*, vol. 52, no. 8, p. 5885, 1995. [102](#)
- [216] X. Huang, R.-Y. Tian, Y.-J. Zhao, *et al.*, “Complexity of h-bonding between polar molecules on si (100)-2×1 and ge (100)-2×1 surfaces,” *Surface Science*, vol. 651, pp. 187–194, 2016. [102](#)
- [217] H. S. Kato, K. Akagi, S. Tsuneyuki, and M. Kawai, “Long-range proton transport for the water reaction on si (001): Study of hydrogen-bonded systems with a model liquid- solid interface,” *The Journal of Physical Chemistry C*, vol. 112, no. 33, pp. 12879–12886, 2008. [102](#)
- [218] J. Cazaux, “Calculated influence of work function on se escape probability and secondary electron emission yield,” *Applied surface science*, vol. 257, no. 3, pp. 1002–1009, 2010. [102](#)
- [219] N. B. Ram and E. Krishnakumar, “Dissociative electron attachment resonances in ammonia: A velocity slice imaging based study,” *The Journal of chemical physics*, vol. 136, no. 16, p. 164308, 2012. [102](#)
- [220] J.-L. Guizot, P. Alnot, F. Wyczisk, J. Perrin, and B. Allain, “Kinetics of deposition and electrical properties of silicon nitride films obtained by 185 nm photolysis of sih4-nh3 mixtures,” *Semiconductor science and technology*, vol. 6, no. 7, p. 582, 1991. [102](#)

- [221] X. Cao and R. J. Hamers, “Silicon surfaces as electron acceptors: dative bonding of amines with si (001) and si (111) surfaces,” *Journal of the American Chemical Society*, vol. 123, no. 44, pp. 10988–10996, 2001. [107](#), [108](#)
- [222] F. Rochet, F. Jolly, F. Bournel, G. Dufour, F. Sirotti, and J.-L. Cantin, “Ethylene on si (001)- 2×1 and si (111)- 7×7 : X-ray photoemission spectroscopy with synchrotron radiation,” *Physical Review B*, vol. 58, no. 16, p. 11029, 1998. [108](#)
- [223] C. Mulcahy, A. Aquino, J. Rogers, and T. Jones, “Resonant vibrational excitation in high-resolution electron energy-loss spectroscopy studies of trimethylamine chemisorbed on gaas (100),” *The Journal of chemical physics*, vol. 104, no. 22, pp. 9120–9126, 1996. [108](#)
- [224] A. Pratt, L. Lari, O. Hovorka, A. Shah, C. Woffinden, S. P. Tear, C. Binns, and R. Kröger, “Enhanced oxidation of nanoparticles through strain-mediated ionic transport,” *Nature materials*, vol. 13, no. 1, pp. 26–30, 2014. [112](#)
- [225] A. Boucly, *Catalytical reactions and environmental chemistry modifications as seen by synchrotron radiation NAP-XPS*. PhD thesis, 2017. [112](#)
- [226] I. Müller, *A history of thermodynamics: the doctrine of energy and entropy*. Springer Science & Business Media, 2007. [113](#)
- [227] A. Sommerfeld, *Lectures on Theoretical Physics: Thermodynamics and statistical mechanics*, vol. 5. Academic press, 2012. [113](#)
- [228] R. Clausius, “Über eine veränderte form des zweiten hauptsatzes der mechanischen wärmetheorie,” *Annalen der Physik*, vol. 169, no. 12, pp. 481–506, 1854. [113](#)
- [229] H. DeVoe, “Thermodynamics and chemistry, 2nd edn version 8,” 2016. [114](#)
- [230] Y. Demirel, “Chapter 1 - fundamentals of equilibrium thermodynamics,” in *Nonequilibrium Thermodynamics (Third Edition)* (Y. Demirel, ed.), pp. 1 – 74, Amsterdam: Elsevier, third edition ed., 2014. [115](#)
- [231] H. H. Girault, *Analytical and physical electrochemistry*. CRC Press, 2004. [115](#)
- [232] E. A. Guggenheim, “The conceptions of electrical potential difference between two phases and the individual activities of ions,” *The Journal of Physical Chemistry*, vol. 33, no. 6, pp. 842–849, 1929. [116](#)
- [233] W. Theis and K. Horn, “Temperature-dependent line broadening in core-level photoemission spectra from aluminum,” *Physical Review B*, vol. 47, no. 23, p. 16060, 1993. [119](#)

- [234] C. Berg, S. Raaen, A. Borg, J. Andersen, E. Lundgren, and R. Nyholm, "Observation of a low-binding-energy peak in the 2p core-level photoemission from oxidized al (111)," *Physical Review B*, vol. 47, no. 19, p. 13063, 1993. [119](#)
- [235] A. Klein, C. Körber, A. Wachau, F. Säuberlich, Y. Gassenbauer, S. P. Harvey, D. E. Proffit, and T. O. Mason, "Transparent conducting oxides for photovoltaics: Manipulation of fermi level, work function and energy band alignment," *Materials*, vol. 3, no. 11, pp. 4892–4914, 2010. [122](#)
- [236] A. Pasquarello, M. S. Hybertsen, and R. Car, "Theory of si 2p core-level shifts at the si (001)-sio 2 interface," *Physical Review B*, vol. 53, no. 16, p. 10942, 1996. [122](#)
- [237] D. Flötotto, Z. Wang, and E. J. Mittemeijer, "On the structural development during ultrathin amorphous al₂o₃ film growth on al (111) and al (100) surfaces by thermal oxidation," *Surface Science*, vol. 633, pp. 1–7, 2015. [122](#)
- [238] T. Perevalov, V. Gritsenko, and V. Kaichev, "Electronic structure of aluminum oxide: ab initio simulations of α and γ phases and comparison with experiment for amorphous films," *The European physical journal applied physics*, vol. 52, no. 3, p. 30501, 2010. [123](#), [126](#)
- [239] Z. Guo, F. Ambrosio, and A. Pasquarello, "Oxygen defects in amorphous al₂o₃: A hybrid functional study," *Applied physics letters*, vol. 109, no. 6, p. 062903, 2016. [123](#)
- [240] R. H. French, "Electronic band structure of al₂o₃, with comparison to alon and ain," *Journal of the American Ceramic Society*, vol. 73, no. 3, pp. 477–489, 1990. [123](#)
- [241] S. M. Sze and K. K. Ng, *Physics of semiconductor devices*. John wiley & sons, 2006. [125](#), [126](#)
- [242] A. Chaudhuri, T. Lerotholi, D. Jackson, D. Woodruff, and V. Dhanak, "Local methylthiolate adsorption geometry on au (111) from photoemission core-level shifts," *Physical review letters*, vol. 102, no. 12, p. 126101, 2009. [133](#)
- [243] F. Bournel, J.-J. Gallet, D. Pierucci, A. Khaliq, F. Rochet, and A. Pietzsch, "Hydrosilylation of styrene on water-saturated si (001)-2 \times 1 at room temperature," *The Journal of Physical Chemistry C*, vol. 115, no. 30, pp. 14827–14833, 2011. [137](#)
- [244] S. García-Gil, A. Arnau, and A. Garcia-Lekue, "Exploring large o 1s and n 1s core level shifts due to intermolecular hydrogen bond formation in organic molecules," *Surface science*, vol. 613, pp. 102–107, 2013. [140](#)

- [245] C. Larsson, A. Johnson, A. Flodström, and T. Madey, “Adsorption of h₂o on planar and stepped si (100): Structural aspects,” *Journal of Vacuum Science & Technology A: Vacuum, Surfaces, and Films*, vol. 5, no. 4, pp. 842–846, 1987. [142](#)